UNIVERSIDAD
DE GRANADA

STUDYING AN UNBALANCED TWO-ION CRYSTAL IN A PENNING TRAP: TOWARDS THE QUANTUM REGIME IN A HIGH MAGNETIC FIELD

TESIS DOCTORAL

MANUEL JESÚS GUTIÉRREZ TORRES

PROGRAMA DE DOCTORADO EN
FÍSICA Y CIENCIAS DEL ESPACIO

Granada, Mayo de 2021

Editor: Universidad de Granada. Tesis Doctorales
Autor: Manuel Jesús Gutiérrez Torres
ISBN: 978-84-1306-937-1
URI: http://hdl.handle.net/10481/69660

Studying an unbalanced two-ion crystal in a Penning trap: towards the quantum regime in a high magnetic field

REALIZADO POR:

Manuel Jesús Gutiérrez Torres

DIRIGIDO POR:

Daniel Rodríguez Rubiales

DEPARTAMENTO:

Departamento de Física Atómica, Molecular y Nuclear

UNIVERSIDAD DE GRANADA

PROGRAMA DE DOCTORADO EN FÍSICA Y CIENCIAS DEL ESPACIO

Granada, Mayo de 2021

Acknowledgements

First of all I would like to thank my supervisor, Daniel, for his extraordinary support during the course of this Thesis, especially during the writing of this manuscript. My coworkers, Joaquin and Fran, also deserve my heartfelt thanks – both for their help and for the distended work environment we were able to create. I hope this becomes a trademark of our lab! I am also very grateful to Juanma, who taught me so much when I started, Raúl and Jesús, who were always willing to talk and help me see things with perspective, and all other former members of the lab (Jaime, Martín, Javi, and everyone else). Thank you as well to Stefan and Íñigo. Both were always nice and ready to help. Gracias también a Pablo, de quien he aprendido a pensar en los procesos de fabricación, en lugar de *dibujar alegremente* y dejar que otros se preocupen.

During my stay at GSI I had the opportunity to interact with many people, and I sincerely enjoyed all of it. I felt welcome by all and I learned a lot. An exhaustive list of names would be way too long, but I must thank Michael, Francesca, Brankica, Oliver and Tobias.

En un terreno más personal me gustaría agradecer a mis padres y hermana, que siempre me han apoyado, incluso cuando no era fácil hacerlo. Lo mismo se puede decir de mis amigos, especialmente Eli y los *gudboiz*, con los que siempre he podido desconectar. Dejando lo más importante para el final, muchísimas gracias a Cristina, quien me ha apoyado en mis momentos más bajos y empujado a avanzar. Sin ella, esta tesis no existiría.

This Thesis has been carried out under the FPU fellowship FPU15/04679 from the Spanish Ministry of Education.

Abstract

This Thesis has been devoted to study a new technique based on two simultaneously trapped ions with prospects for high-accuracy Penning-trap mass spectrometry. One of the two ions (called sensor) can be laser cooled, either to the Doppler limit or to the ground state. The other ion (called target), although not directly interacting with any laser, is *sympathetically* cooled to the same temperature by the Coulomb interaction. In this scenario, a crystal is formed. Information about the oscillations of the crystal is read out through photons scattered by the sensor ion.

The unbalanced two-ion crystal has been theoretically studied for the first time in a Penning trap in the course of this Thesis. A detailed study and analysis of the motional frequencies of the crystal has been carried out. The implications of the anharmonicities introduced by the Coulomb interaction in the frequency measurement process, quantifying shifts in the classical and in the quantum regime, have been studied. Part of these results have been published in Physical Review A and the software package built for this is available to the ion-trapping community.

The experimental component of this thesis has two parts: i) the implementation of a new control and data acquisition system based on ARTIQ (Advanced Real-Time Infrastructure for Quantum physics), and ii) the study, modifications and improvements around the open-ring Penning trap, where the crystal is formed. The work with ARTIQ has integrated the devices needed for ion trapping, dipolar/quadrupolar driving and image collection. The work on the open-ring Penning trap started by implementing a custom Laplace-solver program to stablish a tuning procedure that minimizes anharmonic terms. After that, technical issues related to ion production and lasers were overcome. The results, including the first evidence of laser cooling of $^{40}Ca^{+}$ under 7 Tesla, have been published in New Journal of Physics. The Thesis ends by showing our first two-ion crystal, an unique experimental platform for the envisaged studies.

Resumen

Esta Tesis doctoral ha estado dedicada al estudio de una nueva técnica basada en dos iones atrapados de forma simultánea, de cara a la realización de espectrometría de masas de alta precisión con trampas Penning. Uno de los iones (*sensor*) puede enfriarse mediante láseres hasta el límite Doppler, o incluso hasta su estado fundamental. El otro ion (*de interés*) es enfriado al mismo nivel gracias a la interacción de Coulomb. En este escenario se forma un cristal. La información sobre las oscilaciones del cristal se obtiene a través de los fotones dispersados por el ion sensor.

En esta Tesis se ha estudiado el cristal asimétrico de dos iones en una trampa Penning, con especial atención a los modos de movimiento del mismo, así como a los corrimientos en frecuencia que surgen debido a la no-armonicidad de la interacción de Coulomb. Parte de estos resultados se han publicado en la revista Physical Review A, y el paquete informático construido para este estudio está disponible para todos los grupos que trabajan con iones atrapados.

La parte experimental de la Tesis tiene dos componentes importantes: i) la implementación de un nuevo sistema de control y adquisición de datos basado en ARTIQ (Advanced Real-Time Infrastructure for Quantum physics) y ii) el estudio y mejoras en torno a la trampa de anillos abierta, donde se forma dicho cristal. En el trabajo llevado a cabo con ARTIQ se han integrado los dispositivos necesarios para atrapar, aplicar campos dipolares o cuadrupolares y registrar la imagen del ion sensor. El trabajo sobre la trampa Penning comenzó instaurando un protocolo de sintonización, basado en un programa de resolución de potenciales electrostáticos propio, para establecer un procedimiento de sintonización que minimice términos no armónicos. También se ha trabajado en mejoras técnicas como la producción de iones y en el sistema de láseres. Los resultados, incluyendo enfriamiento láser de $^{40}Ca^{+}$ en 7 Tesla, se publicaron en la revista New Journal of Physics. La Tesis termina presentando un cristal de dos iones, que constituye una plataforma única para llevar a cabo los estudios aquí propuestos.

Contents

List of Figures

Chapter 1

Introduction

When attempting to measure a physical magnitude, it is often advantageous to map it to a frequency [1]. Two oscillations with very close frequencies can be discriminated if left to evolve for a long enough time, so that their relative phase changes. The phenomenon of interference can also be exploited to large gains, allowing e.g. an optical frequency measurement into a radiofrequency or microwave measurement, as it is done in a frequency comb [2]. Many experiments have used frequency measurements to determine other quantities, such as the proton radius (where the results obtained from spectroscopy of electronic [3] and muonic [4] hydrogen result in uncertainties significantly lower than those obtained from other methods [5]), the proton [6], antiproton [7] and electron [8] magnetic moments, fundamental constants (such as the Rydberg constant, one of the most precisely determined) and limits to their temporal variation [9].

Mass measurements in Penning traps are also a prime example [10]. The mass-to-charge ratio of the trapped particle is measured through its cyclotron frequency, that is, the frequency of the particle's motion in the presence of a magnetic field B, $\omega_c = qB/m$. The trapping electrostatic field perturbs the particle's motion, but the cyclotron frequency can nevertheless be reconstructed by measuring the resulting motional frequencies [11, 12], or a linear combination of the radial ones [13].

There are many reasons to measure masses precisely, with precisions that depend on the goal in question. For example, a comparison of the proton and antiproton masses provides a test of CPT (Charge, Parity and Time reversal) symmetry [14]. In the realm of nuclear physics, since nuclei are composite systems, mass measurements enable a direct measurement of their binding energy. This is done, thanks to the mass-energy equivalence, by comparing the difference between the mass of the

nucleus and the sum of the masses of its components. The values of some masses provide insight into certain stellar nucleosynthesis processes [15, 16]. Nuclear masses are also used to perform fundamental tests, such as the unitarity of the Cabibbo-Kobayashi-Maskawa matrix [17]. They have been used for studies on double-beta or double-electron capture decays (see Ref. [18] and references therein). Especially interesting are the ongoing efforts to pin down the neutrino mass through the study of different decays [19]. One of these experiments, KATRIN [20], which studies the beta decay of tritium, has already halved the previous upper bound of the neutrino mass, down to 1.1 eV [21]. Other decays are also been studied, such as the electron capture decay of ^{163}Ho, within the ECHo project [22].

The main motivation of this work, however, are the so-called SuperHeavy Elements (SHEs). Also known as *transactinides*, SHEs are produced in minute rates in a few facilities worldwide [23, 24, 25, 26]. Currently known SHEs are unstable – however, the existence of an *island of stability*, a region of the nuclide chart where nuclear shell effects greatly increase stability, was first postulated as early as 1926 [27]. There are several proposed locations of the island of stability. There is an ongoing effort by the SHIPTRAP collaboration at GSI to map the binding energies of the SHEs through precise Penning trap mass measurements [28, 29, 30], which will shed light on the location of the island.

The technique currently in use for Penning-trap mass spectrometry of SHEs is Phase-Imaging Ion-Cyclotron-Resonance (PI-ICR). It measures the radial frequencies (or their sum) by projecting the ion motion into a position sensitive micro-channel plate detector. It has already been proven with success for the first SHE ever measured directly [30]. However, this detection process is destructive, and around ten ions are needed for a measurement. This fact, coupled to the rapidly dropping production cross section of the SHEs, makes this technique impractical for the heaviest ones. Another technique, based on the detection of the minute image currents the ion induces in the trap electrodes, is capable of single ion sensitivity, and has provided the highest precisions for stable elements [31]. However, it has two major drawbacks in this context: the time required for a measurement (which directly determines the achievable precision) and, most importantly, the signal-to-noise ratio of the induced image current, which goes down with the ion's mass-to-charge ratio – so far, measurements above $\sim 65\,\mathrm{u/e}$ have not been performed [32]. Since the electronic charge of the SHEs that can be delivered to a Penning trap is limited [33], new stopping techniques [34] or faster, more sensitive detection setups based on quartz

resonators and radial pick-up [35, 36, 37], or perfection of more traditional setups using superconducting coils [38] are needed before induced image current techniques can be applied to SHEs.

In other areas of physics, laser-cooled ions (which can be detected through the photons they scatter) are being used as auxiliary systems to cool [39] or study [40, 41] other species that do not have suitable transitions, even with the ultimate goal of using these for quantum information processing [42]. Similarly, a proposal was made to use a laser-cooled $^{40}Ca^{+}$ ion as a detector for mass spectrometry, sensitive to a single ion regardless of its mass-to-charge ratio [43]. This technique would have the two ions (which in this work will be referred to as *target* and *sensor* ions) stored in physically separated traps with a common endcap, so that the interaction takes place through the current the ions induce in the shared electrode. A first prototype was designed and constructed [44], fluorescence from an ion cloud under operation as a Paul trap was observed [45]. A second prototype is in the design phase right now.

This Thesis sets out to study the feasibility of an alternative approach. Instead of storing the two ions in physically separated traps, a single trap is used. Both ions form a crystal when the sensor ion is laser cooled. The interaction between both ions is much stronger, so much so that it is no longer possible to speak of the individual ions' motion – instead, a description of the dynamics of the whole system is required. The strong anharmonicity of the Coulomb interaction introduces amplitude dependent shifts that must be characterized and taken into account if any sort of measurement is to be carried out, either in the classical or quantum regime.

The layout of this work, around three pillars comprising theory and experiment, is as follows. Chapter 2 presents an overview of the Penning trap and the related techniques relevant to this work, namely, the interaction of the trapped ion with additional radiofrequency fields and laser cooling. Chapter 3 presents the existing Penning-trap mass spectrometry techniques in detail. Chapter 4, which constitutes a large parte of this Thesis, presents the analysis of the dynamics of the Coulomb crystal formed by the target and sensor ions when laser cooled. Such a system is referred to as an *unbalanced two-ion crystal*, to distinguish it from the case where the ions conforming the crystal are of the same species. Chapter 5 presents the integration of the devices required for unbalanced crystal experiments into a new control and data acquisition system. Finally, Chapter 6 presents the modifications and experimental progress in the facility carried out in the course of this work until

the creation of the first two-ion crystals, underlining a first possible measurement. Chapter 7 analyzes the work carried out during this Thesis, as well as the future work that lays ahead.

Chapter 2

The Penning trap

When one wants to study the properties of a particle, confining it to a small region of space makes any manipulation or observation process much easier. To achieve confinement, a restoring force of some sort is required. In the case of ion traps, the electric charge of the ion is exploited for this purpose.

As a starting point, a hypothetical restoring electrostatic field in free space, $\mathbf{E}(\mathbf{r})$, is assumed. Due to its restoring nature, the force it exerts on a particle with charge q in any small displacement around the equilibrium position, $\mathbf{r}_0$, must point towards $\mathbf{r}_0$. This gives rise to a non-vanishing flux of the electric field vector through a surface S enclosing $\mathbf{r}_0$,

$$\oint_S \mathbf{E}(\mathbf{r}) \cdot \mathrm{d}\mathbf{S} \neq 0 \,.$$

However, by virtue of Gauss's flux theorem, the flux of the electric field through any closed surface S is determined by the net charge it encloses, i.e.,

$$\oint_S \mathbf{E}(\mathbf{r}) \cdot \mathrm{d}\mathbf{S} = \frac{Q}{\varepsilon} \,.$$

Therefore, the hypothetical restoring electrostatic field $\mathbf{E}$ cannot exist in free space. This result, known as *Earnshaw's theorem* (see Ref. [46]), implies that a charged particle cannot be trapped by means of a purely electrostatic field. Two well-known ways have been developed to work around this restriction, namely,

- *Paul* or *RF traps*, which use a time-varying electric field that gives rise to net confinement of the charged particle (see e.g. Ref. [47]), and
- *Penning traps*, which combine electro- and magnetostatic fields, also giving

rise to overall confinement.

This Chapter will elaborate on the latter. First, the creation of the electromagnetic field of a Penning trap will be discussed. The electrostatic field creation will be discussed at length, since it is relevant for the discussion about trap geometries. The equations of motion of a single trapped ion in the Penning trap's electromagnetic field will then be solved. After the trap geometries are presented, the ion manipulation techniques used in this Thesis, including cooling of the ion's motion, will be introduced.

2.1 Generation of the electromagnetic field

A Penning trap is created by superimposing an electrostatic field to a uniform magnetic field. The means by which both are created will be outlined in the following.

Electrostatic field

The potential inside the trap must follow the differential form of Gauss's law, that is,

$$\nabla^2 \varphi = \frac{\rho_q}{\varepsilon} , \tag{2.1}$$

where ρ_q is the electric charge density and ε is the electric permittivity of the medium. Since this is a particular case of Poisson's equation,

$$\nabla^2 \varphi = f(\mathbf{r}) ,$$

it must comply with the uniqueness theorem (see e.g. Ref. [48]), that can be summed up in the phrase *the electrostatic potential inside a given volume is uniquely determined by the potential on a closed surface bounding that volume.* Therefore, the simplest way to generate a given electric field starts by identifying a set of equipotential surfaces that define a closed region of space. Metal pieces (called *electrodes*) can be machined to conform to these surfaces. If the potential on the electrodes is set to those of the equipotential surfaces, a boundary condition is set, and the electric field within the trap must conform to the desired one.

In order to make the ion's motion easy to characterize, a harmonic field is desirable. The associated potential can be written as

$$\varphi(\mathbf{r}) = \left(\alpha x^2 + \beta y^2 + \gamma z^2\right) . \tag{2.2}$$

This potential must fulfill the differential form of Gauss' law (Eq. 2.1), which, in free space ($\rho_q = 0$), leads to

$$\nabla^2\varphi(\mathbf{r}) = \frac{\partial^2\varphi}{\partial x^2} + \frac{\partial^2\varphi}{\partial y^2} + \frac{\partial^2\varphi}{\partial z^2} = \alpha + \beta + \gamma = 0 . \tag{2.3}$$

This implies that at least one of the constants (α, β or γ) must be negative, resulting in a repulsive force along the direction corresponding to the constant. In Penning traps, the common choice is to make the electrostatic potential confining in the axial direction ($\gamma > 0$) as well as imposing revolution symmetry around the axial direction ($\alpha = \beta$). The electrostatic potential within the trap can then be written as

$$\varphi(\mathbf{r}) = \gamma\left(z^2 - \frac{1}{2}x^2 - \frac{1}{2}y^2\right) = \gamma\left(z^2 - \frac{1}{2}r^2\right) . \tag{2.4}$$

The equipotential surfaces can be found by forcing the potential to be constant:

$$\varphi(\mathbf{r}) = \gamma\left(z^2 - \frac{1}{2}x^2 - \frac{1}{2}y^2\right) = \varphi_0 \implies \frac{x^2}{\left|\frac{2\varphi_0}{\gamma}\right|} + \frac{y^2}{\left|\frac{2\varphi_0}{\gamma}\right|} - \frac{z^2}{\left|\frac{\varphi_0}{\gamma}\right|} = -\frac{\frac{2\varphi_0}{\gamma}}{\left|\frac{2\varphi_0}{\gamma}\right|} = -\operatorname{sgn}\varphi_0 . \tag{2.5}$$

Here, sgn is the *sign function*. This equation is that of a hyperboloid,

$$\frac{x^2}{A^2} + \frac{y^2}{B^2} - \frac{z^2}{C^2} = \pm 1 , \tag{2.6}$$

where the + sign corresponds to the *hyperboloid of one sheet*, and the − sign to the *hyperboloid of two sheets*. A, B and C are the distances from the surface to the center of coordinates in the x, y and z direction, respectively. The hyperboloids of one and two sheets with the same parameters are asymptotic to the same cone – therefore, it is clear that they define a closed region of space. The first Penning traps were machined with electrodes following these surfaces, as shown in Fig. 2.1.

If voltages are applied to the ring and endcap electrodes so that the potential difference between them is U, the potential

$$\varphi(\mathbf{r}) = \frac{U}{2z_0^2 + r_0^2}\left(2z^2 - r^2\right) = \frac{U}{4d_0^2}\left(2z^2 - r^2\right) , \tag{2.7}$$

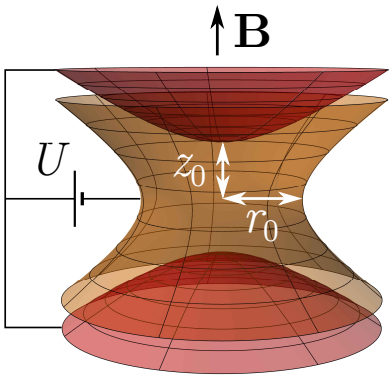

Figure 2.1: Sketch of the original geometry of a Penning trap, with a *ring* electrode (depicted in orange) and two *endcap* electrodes (depicted in red). The electrodes follow the shape of a one and two-sheet hyperboloid, respectively, therefore creating a quadrupolar potential when voltages are applied.

which fulfills the boundary conditions at the electrodes's surfaces, must be the potential at any point within the trap. Here, z_0 and r_0 are the distances from the trap center to the endcaps and ring electrodes, respectively, and $d_0 = \sqrt{2z_0^2 + r_0^2}/2$ is the so-called *characteristic distance* of the trap.

Magnetic field

The magnetic field used in an ideal Penning trap is uniform and oriented along the trap's symmetry axis, i.e., $\mathbf{B} = B\hat{\mathbf{z}}$. It is common to specify the field homogeneity as parts-per-million (or similar) of variation in the field intensity B in a given volume, usually $1\,\mathrm{cm}^3$, around the trap center. Creating such a field with high homogeneity is only viable in limited regions of space.

Although permanent magnets have been used, and are in some cases preferable (see e.g. Ref. [49]), superconducting electromagnets are widely extended. A more in-depth discussion on electromagnet geometries can be found in Ref. [50] and references therein. Superconducting electromagnets are quite complex to design, requiring several *shimming* coils used to correct field inhomogeneities to very high orders. For example, the superconducting magnet used in the present Thesis (see Ref. [51]) has eight shim coils, whose currents are adjusted individually on installation. Besides the coils, some passive elements are also added to shape the field with the desired specifications at a fixed intensity.

2.2 Eigenmotions of a single trapped ion

The motion of a single ion in a Penning trap is defined by the Lorentz force, $\mathbf{F} = q\left(\mathbf{E} + \mathbf{v} \times \mathbf{B}\right)$. In this work the Lagrangian formalism will be used, as this treatment is more adequate to analyze the dynamics of the unbalanced two-ion crystal.

The potential energy of the trapped particle due to the trap's electric and magnetic fields is[1]

$$V = q\varphi - q\mathbf{v}\cdot\mathbf{A} = \frac{qU}{4d_0^2}\left(2z^2 - x^2 - y^2\right) - q\left(\dot{x}\hat{\mathbf{x}} + \dot{y}\hat{\mathbf{y}} + \dot{z}\hat{\mathbf{z}}\right)\cdot\left(\frac{1}{2}\mathbf{B}\times\mathbf{r}\right) = \\ = \frac{qU}{4d_0^2}\left(2z^2 - x^2 - y^2\right) + \frac{qB}{2}\left(\dot{x}y - \dot{y}x\right)\,, \quad (2.8)$$

resulting in the Lagrangian function

$$\mathcal{L} = K - V = \frac{1}{2}m\left(\dot{x}^2 + \dot{y}^2 + \dot{z}^2\right) - \frac{qU}{4d_0^2}\left(2z^2 - x^2 - y^2\right) - \frac{qB}{2}\left(\dot{x}y - \dot{y}x\right)\,. \quad (2.9)$$

The equations of motion can be readily obtained by using the Euler-Lagrange equation:

$$\frac{\partial\mathcal{L}}{\partial r_i} - \frac{\mathrm{d}}{\mathrm{d}t}\frac{\partial\mathcal{L}}{\partial\dot{r}_i} = 0\,,\ r_i \in \{x, y, z\} \implies \begin{cases} \ddot{x} - \frac{qB}{m}\dot{y} - \frac{1}{2}\frac{qU}{md_0^2}x = \ddot{x} - \omega_c\dot{y} - \frac{1}{2}\omega_z^2 x = 0 \\ \ddot{y} + \frac{qB}{m}\dot{x} - \frac{1}{2}\frac{qU}{md_0^2}y = \ddot{y} + \omega_c\dot{x} - \frac{1}{2}\omega_z^2 y = 0 \\ \ddot{z} + \frac{qU}{md_0^2}z = \ddot{z} + \omega_z^2 z = 0 \end{cases}. \quad (2.10)$$

Here, ω_c is the *free cyclotron frequency* (the frequency of the circular motion a particle of charge q and mass m would follow when moving perpendicular to a uniform magnetic field of intensity B), and $\omega_z = \sqrt{qU/md_0^2}$ is the frequency of the (harmonic) axial motion.

The motions in the radial plane are coupled. The usual way to work around this is to introduce the variable $u = x + iy$ – this yields a single equation for the radial motion ($\ddot{u} + i\omega_c\dot{u} - \frac{1}{2}\omega_z^2 u = 0$) that is trivial to solve. However, since this work is

[1] The equivalency $\mathbf{A} = \frac{1}{2}\mathbf{B}\times\mathbf{r}$ holds true as long as $(\mathbf{r}\cdot\nabla)\,\mathbf{B} = 0$. This can be proven using $\mathbf{B} = \nabla\times\mathbf{A}$ and the properties of the curl of a vector product. Our case (uniform $\mathbf{B}$) trivially verifies this condition. Note that a choice of gauge was made by using this particular value of $\mathbf{A}$.

devoted to study a two-ion crystal, the motion of the single ion will be studied using the same tools that will be utilized later. To proceed, the equations are written in matrix form

$$\begin{pmatrix} \ddot{x} \\ \ddot{y} \\ \ddot{z} \end{pmatrix} - \omega_c \begin{pmatrix} 0 & 1 & 0 \\ -1 & 0 & 0 \\ 0 & 0 & 0 \end{pmatrix} \begin{pmatrix} \dot{x} \\ \dot{y} \\ \dot{z} \end{pmatrix} - \frac{1}{2}\omega_z^2 \begin{pmatrix} 1 & 0 & 0 \\ 0 & 1 & 0 \\ 0 & 0 & -2 \end{pmatrix} \begin{pmatrix} x \\ y \\ z \end{pmatrix} = \mathbb{O}_{3\times 1}\,. \tag{2.11}$$

Here, $\mathbb{O}$ is the zero matrix. If the *ansatz* $\mathbf{r} = \boldsymbol{\rho} e^{-i\omega t}$ is introduced and the equation is divided by ω_c^2, the algebraic matrix equation

$$\left[\left(\frac{\omega}{\omega_c}\right)^2 \begin{pmatrix} 1 & 0 & 0 \\ 0 & 1 & 0 \\ 0 & 0 & 1 \end{pmatrix} - i \left(\frac{\omega}{\omega_c}\right) \begin{pmatrix} 0 & 1 & 0 \\ -1 & 0 & 0 \\ 0 & 0 & 0 \end{pmatrix} + \frac{1}{2} \left(\frac{\omega_z}{\omega_c}\right)^2 \begin{pmatrix} 1 & 0 & 0 \\ 0 & 1 & 0 \\ 0 & 0 & -2 \end{pmatrix} \right] \begin{pmatrix} \rho_x \\ \rho_y \\ \rho_z \end{pmatrix} = $$

$$= Q\left(\frac{\omega}{\omega_c}\right) \begin{pmatrix} \rho_x \\ \rho_y \\ \rho_z \end{pmatrix} = \mathbb{O}_{3\times 1} \tag{2.12}$$

is obtained. This is known as a *quadratic eigenvalue problem* [52], which is a generalization of the usual eigenvalue problems found in undergraduate Linear Algebra courses. There are two main solving strategies:

- Find the eigenvalues by solving $\det\left[Q\left(\omega\right)\right] = 0$ and the eigenvectors by solving $Q\left(\omega\right) \cdot \boldsymbol{\rho} = 0$, or
- Linearize the original differential equations by introducing the additional variables $\mathbf{v} = \dot{\mathbf{r}}$; this is a particular case of a *linearization of the first companion form* [52]. A standard eigenvalue problem results after some transformations.

The first approach will be used here. The eigenvalues are

$$\det\left[Q\left(\omega\right)\right] = 0 \implies \omega = \begin{cases} \pm\frac{\omega_c}{2}\left(1 \pm \sqrt{1 - 2\left(\frac{\omega_z}{\omega_c}\right)^2}\right) = \pm\frac{1}{2}\left(\omega_c \pm \omega_1\right) = \pm\omega_\pm \\ \pm\omega_z \end{cases}. \tag{2.13}$$

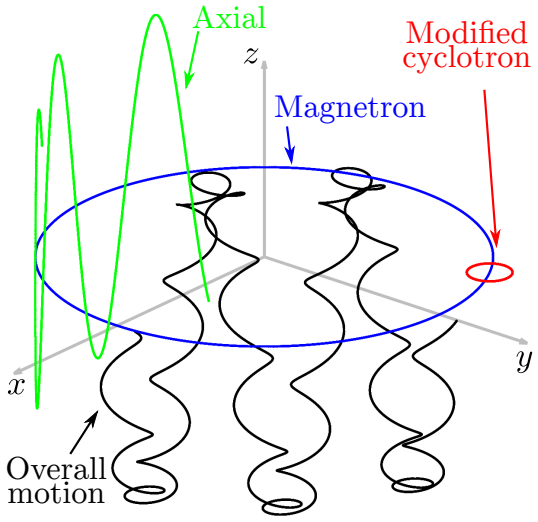

Figure 2.2: Trajectory of a single ion confined in a Penning trap. The individual modes are highlighted in color to illustrate the results obtained in this section.

The associated eigenvectors are shown in Tab. 2.1. Note that each radial eigenvector is associated with both radial eigenvalues. It is possible to obtain the trajectories from either of the radial eigenvectors – in both cases, the y coordinate has an additional $\pi/2$ phase with respect to the x coordinate.

The frequency ω_+ is known as *reduced-cyclotron* frequency, since for normal operation conditions ($\omega_z \ll \omega_c$) ω_+ is slightly below the cyclotron frequency ω_c. On the other hand, ω_- is known as *magnetron frequency*. The frequency $\omega_1 = \omega_+ - \omega_- = \sqrt{\omega_c^2 - 2\omega_z^2}$ is introduced here, since it will appear often in later calculations.

Returning to the cartesian coordinate system, the trajectory is given by

$$\begin{cases} x = \rho_+ \cos(\omega_+ t + \phi_+) + \rho_- \cos(\omega_- t + \phi_-) \\ y = -\rho_+ \sin(\omega_+ t + \phi_+) - \rho_- \sin(\omega_- t + \phi_-) \\ z = \rho_z \cos(\omega_z t + \phi_z) \end{cases} . \tag{2.14}$$

Note that $\omega_\pm$ have the same sign as $\omega_c \propto q$. Therefore, a charge reversal results in a

Table 2.1: Eigenvalues and eigenvectors of the quadratic eigenvalue problem given by Eq. 2.12.

Eigenvalue	$+\omega_+$	$-\omega_+$	$+\omega_-$	$-\omega_-$	$+\omega_z$	$-\omega_z$
Eigenvector	$\frac{1}{\sqrt{2}}\begin{pmatrix}1\\-i\\0\end{pmatrix}$	$\frac{1}{\sqrt{2}}\begin{pmatrix}1\\i\\0\end{pmatrix}$	$\frac{1}{\sqrt{2}}\begin{pmatrix}1\\-i\\0\end{pmatrix}$	$\frac{1}{\sqrt{2}}\begin{pmatrix}1\\i\\0\end{pmatrix}$	$\begin{pmatrix}0\\0\\1\end{pmatrix}$	$\begin{pmatrix}0\\0\\1\end{pmatrix}$

sign change for the y coordinate – in other words, the trajectory in the radial plane changes from clockwise to counterclockwise. Figure 2.2 illustrates the individual modes of motion of the trapped ion, as well as their superposition.

A stability condition can be derived from the frequencies (Eq. 2.13). Given the ansatz, $\mathbf{r} = \boldsymbol{\rho} e^{-i\omega t}$, an imaginary component in ω results in an unbound mode. For the confinement to be stable, therefore,

$$\frac{\omega_z}{\omega_c} < \frac{1}{\sqrt{2}}\,. \tag{2.15}$$

Note that at the edge of stability ($\omega_z/\omega_c = 1/\sqrt{2}$) the radial frequencies become $\omega_+ = \omega_- = \omega_c/2$.

The stability condition is usually seen as a way to judge the maximum axial frequency (i.e. the maximum trapping potential U) that can be used in a given experiment, that is, for a given magnetic field intensity B and a certain species with charge q and mass m. There is another way to look at it that will be useful in Chapter 4: for a fixed trap configuration (fixed values of B and U), the range of mass-to-charge ratios that can be confined is

$$\frac{\omega_z}{\omega_c} = \frac{\sqrt{\frac{qU}{md_0^2}}}{\frac{q}{m}B} < \frac{1}{\sqrt{2}} \implies \frac{m}{q} < \frac{1}{2}\frac{U}{B^2 d_0^2}\,. \tag{2.16}$$

This will be revisited when discussing the stability of the two-ion crystal.

Expanding the radial frequencies (Eq. 2.13) as a function of the ratio ω_z/ω_c yields

$$\omega_+ = \omega_c - \frac{\omega_z^2}{2\omega_c} + O\left(\left[\frac{\omega_z}{\omega_c}\right]^4\right) \text{ and } \omega_- = \frac{\omega_z^2}{2\omega_c} + O\left(\left[\frac{\omega_z}{\omega_c}\right]^4\right) = \frac{U}{2Bd_0^2} + O\left(\left[\frac{\omega_z}{\omega_c}\right]^4\right). \tag{2.17}$$

The very low mass sensitivity of the magnetron frequency has become apparent. This feature can be exploited to discriminate among a variety of species trapped simultaneously (resulting e.g. from fusion-evaporation nuclear reactions) with fairly high resolving power (see Ref. [53]).

Some frequency relationships of great value can be obtained by operating on Eq. 2.13, namely

$$\omega_c = \omega_+ + \omega_- \tag{2.18a}$$

$$\omega_c^2 = \omega_+^2 + \omega_z^2 + \omega_-^2 \tag{2.18b}$$

$$\omega_z^2 = 2\omega_+\omega_- \,. \tag{2.18c}$$

Equations 2.18a and 2.18b are commonly used in Penning-Trap Mass Spectrometry, since they allow the determination of the free cyclotron frequency from the actual motional frequencies. Equation 2.18b, known as *invariance theorem* (see Ref. [12]), is of special significance. Trap imperfections will, in general, shift the motional frequencies; however, if the imperfections are of a certain kind[2] the resulting motional frequencies still verify the invariance theorem. This makes it very useful in high-precision mass measurements – measuring all three of the ion's motional frequencies makes the resulting mass value robust against those kinds of imperfections.

It is very useful to know the energy content of each of the modes of motion. It can be done by calculating the Hamiltonian of the system via the Legendre transformation of the Lagrangian[3]. The canonical momenta associated with the cartesian coordinates are

$$p_i = \frac{\partial \mathcal{L}}{\partial \dot{r}_i} \,\forall i \in \{x, y, z\} \implies \begin{cases} p_x = m\dot{x} - \frac{1}{2}qBy \\ p_y = m\dot{y} + \frac{1}{2}qBx \\ p_z = m\dot{z} \end{cases} , \tag{2.19}$$

and the resulting Hamiltonian is

$$\mathcal{H} = \sum_i p_i \dot{r}_i - \mathcal{L} = \frac{1}{2}m\dot{\mathbf{r}}^2 + q\varphi = \frac{(\mathbf{p} - q\mathbf{A})^2}{2m} + q\varphi \,. \tag{2.20}$$

Note that the canonical momentum does not match the kinetic momentum for the radial coordinates.

Finding the energy of the ion is a matter of substituting the ion's trajectories (Eq. 2.14) into the Hamiltonian. This is easiest if the second to last expression (involving velocities instead of canonical momenta) is used:

[2] The imperfections considered in Ref. [12] are misalignments between the electric and magnetic fields or harmonic electrostatic fields that lack revolution symmetry (e.g. a trapping potential with a certain degree of elipticity).

[3] The Lagrangian of this system fulfills the conditions stated in Ref. [54] to verify $\mathcal{H} = E$.

$$
\begin{aligned}
E &= \frac{1}{2}m\dot{\mathbf{r}}^2 + \frac{qU}{4d_0^2}\left(2z^2 - x^2 - y^2\right) = \\
&= \frac{1}{2}m\left(\omega_+^2 - \frac{1}{2}\omega_z^2\right)\rho_+^2 + \frac{1}{2}m\left(\omega_-^2 - \frac{1}{2}\omega_z^2\right)\rho_-^2 + \\
&\qquad + m\left(\omega_+\omega_- - \frac{1}{2}\omega_z^2\right)\rho_+\rho_-\cos\left(\left[\omega_+ - \omega_-\right]t + \left[\phi_+ - \phi_-\right]\right) + \frac{1}{2}m\omega_z^2\rho_z^2 = \\
&= \frac{1}{2}m\omega_+\omega_1\rho_+^2 - \frac{1}{2}m\omega_-\omega_1\rho_-^2 + \frac{1}{2}m\omega_z^2\rho_z^2\,,
\end{aligned}
\tag{2.21}
$$

where the identity $\omega_z^2 = 2\omega_+\omega_-$ and the definition of ω_z have been used. The average energy content of each mode can be found simply by zeroing out the amplitudes of the remaining ones.

It is important to remark that the total energy of the magnetron motion is negative. This illustrates its most fundamental property: instability. Any source of dissipation results in an increase of the magnetron radius. Eventually, the ion would either collide with the trap electrodes. However, if the vacuum in the trap is good enough, the damping time will be on the order of years [11] or longer, so it does not play a role in the experiments.

It is useful to present the system's Hamiltonian in a different coordinate system to study the ion behavior under additional, time-dependent electromagnetic fields (*drivings*). The canonical transformation is (see Ref. [55])

$$
\begin{aligned}
q_+ &= \tfrac{1}{\sqrt{2}}\left(\sqrt{\tfrac{m\omega_1}{2}}x - \sqrt{\tfrac{2}{m\omega_1}}p_y\right) \quad & p_+ &= \tfrac{1}{\sqrt{2}}\left(\sqrt{\tfrac{m\omega_1}{2}}y + \sqrt{\tfrac{2}{m\omega_1}}p_x\right) \\
q_- &= \tfrac{1}{\sqrt{2}}\left(\sqrt{\tfrac{m\omega_1}{2}}x + \sqrt{\tfrac{2}{m\omega_1}}p_y\right) \quad & p_- &= \tfrac{1}{\sqrt{2}}\left(-\sqrt{\tfrac{m\omega_1}{2}}y + \sqrt{\tfrac{2}{m\omega_1}}p_x\right). \\
q_3 &= \sqrt{m\omega_z}z & p_3 &= \tfrac{1}{\sqrt{m\omega_z}}p_z
\end{aligned}
\tag{2.22}
$$

The canonical nature of this transformation can be verified by calculating the corresponding *Poisson brackets* (see e.g. Ref. [54]) and verifying that

$$
[q_i, q_j] = [p_i, p_j] = 0 \text{ and } [q_i, p_j] = \delta_{ij}\,,
\tag{2.23}
$$

where δ_{ij} is the Kronecker delta.

By isolating the old coordinates as a function of the new ones in Eq. 2.22 and substituting in the original Hamiltonian (Eq. 2.20), it becomes [55]

$$
\mathcal{H} = \frac{1}{2}\omega_+\left(p_+^2 + q_+^2\right) - \frac{1}{2}\omega_-\left(p_-^2 + q_-^2\right) + \frac{1}{2}\omega_z\left(p_3^2 + q_3^2\right)\,.
\tag{2.24}
$$

Solving Hamilton's equations is now easier – q_+, q_- and q_3, unlike the eigenvectors shown in Tab. 2.1, oscillate only with ω_+, ω_- and ω_z, respectively. Therefore, from this point onwards they will be referred to as the *eigenmode basis*. Furthermore, since the coordinates and momenta verify Eq. 2.23, i.e. they are canonical conjugates, it is easy to move on to a quantum-mechanical description of the motion [55]. The associated operators verify

$$[\hat{q}_i, \hat{q}_j] = [\hat{p}_i, \hat{p}_j] = 0 \text{ and } [\hat{q}_i, \hat{p}_j] = i\hbar\delta_{ij} \,, \tag{2.25}$$

and the *annihilation* and *creation* operators for each mode are

$$\hat{a}_i = \frac{1}{\sqrt{2\hbar}} (q_i + ip_i) \text{ and } \hat{a}_i^\dagger = \frac{1}{\sqrt{2\hbar}} (q_i - ip_i) \,. \tag{2.26}$$

Using this definition and Eq. 2.25 the Hamiltonian operator of the single ion can be written as

$$\hat{\mathcal{H}} = \hbar\omega_+ \left(\hat{a}_+^\dagger \hat{a}_+ + \frac{1}{2}\right) - \hbar\omega_- \left(\hat{a}_-^\dagger \hat{a}_- + \frac{1}{2}\right) + \hbar\omega_z \left(\hat{a}_3^\dagger \hat{a}_3 + \frac{1}{2}\right) \,, \tag{2.27}$$

which, except for the sign in the magnetron contribution, is the sum of three harmonic oscillators. The eigenstates of each of the terms of the Hamiltonian are the eigenstates of $\hat{a}^\dagger \hat{a} = \hat{N}$ (the *number* operator), which are known as *Fock states* and have a well-defined number of quanta,

$$\hat{N}_\lambda |n_\lambda\rangle = n_\lambda |n_\lambda\rangle \,, \lambda \in \{+, -, 3\} \,, \tag{2.28}$$

and energy $\hbar\omega_\lambda (n_\lambda + 1/2)$. The overall state will be of the form $|n_+\rangle \otimes |n_-\rangle \otimes |n_z\rangle$ (or a combination of these).

2.3 Electromagnetic driving of trapped ions

One of the most useful manipulation techniques in ion traps is the driving of the charged particles using electromagnetic fields. These allow for manipulation of the ion's motion, controlling the amplitudes and phases of the different eigenmotions, or even transferring energy between modes. In this Section, the effects of dipolar and quadrupolar driving on the trapped ions will be presented.

Drivings consist of oscillating potentials superimposed to the static trapping poten-

tials on suitable electrodes. For example, to drive the axial motion, the correction or endcap electrodes of an open-endcap cylindrical trap can be used (marked in red in Fig. 2.3). By superimposing an oscillating voltage, an additional electric field approximating $\mathbf{E}_{RF} = E_{RF}\cos(\omega_{RF}t + \phi_{RF})\,\hat{\mathbf{z}}$ appears at the trap center and its surroundings, modifying the ion's motion. The driving electric field will have higher order components; for example, if the ion is off-axis it will experiment a radial force. Nevertheless, these higher order components can be neglected, since the ion will react to small driving amplitudes [50]. The relationship between E_{RF} and V_{RF} is usually approximated by that of a pair of infinite parallel plates, corrected with a geometrical constant α such that $E_{RF} = \alpha V_{RF}/d_{elec}$ (where d_{elec} is the distance from the electrode to the trap center) to quantify the deviation from the parallel plate shape.

In the case of the radial motion, since the trap has revolution symmetry, segmentation of the electrodes is needed. Figure 2.3 shows a sketch with a typical cylindrical trap with segmented electrodes, together with the configuration used for different driving schemes.

2.3.1 Dipolar driving

Each of the three modes of motion of the trapped ion is a harmonic oscillator (see Sec. 2.2). Therefore, to study the effect of a dipolar driving on the ion's motion, it suffices to study the transient behavior of the driven harmonic oscillator; this is described in Appendix A.1. The results presented there are directly applicable to the driven axial motion. The differential equation for the axial coordinate while driven is

$$\ddot{z} + \omega_z^2 z = \frac{q}{m}\frac{\alpha V_{RF}}{d_{elec}}\sin(\omega_{RF}t)\ . \tag{2.29}$$

The amplitude of an ion, initially at rest, that is driven near resonance, is given by (see Eq. A.11)

$$\rho_z \simeq \frac{q}{m}\frac{\alpha V_{RF} T_{RF}}{2\omega_z d_{elec}}\mathrm{sinc}\left(\frac{\Delta\omega}{2}T_{RF}\right) \tag{2.30}$$

and the energy gained by the ion is

$$E \simeq \frac{1}{8m}\left(\frac{\alpha q V_{RF} T_{RF}}{d_{elec}}\right)^2 \mathrm{sinc}^2\left(\frac{\Delta\omega}{2}T_{RF}\right)\ , \tag{2.31}$$

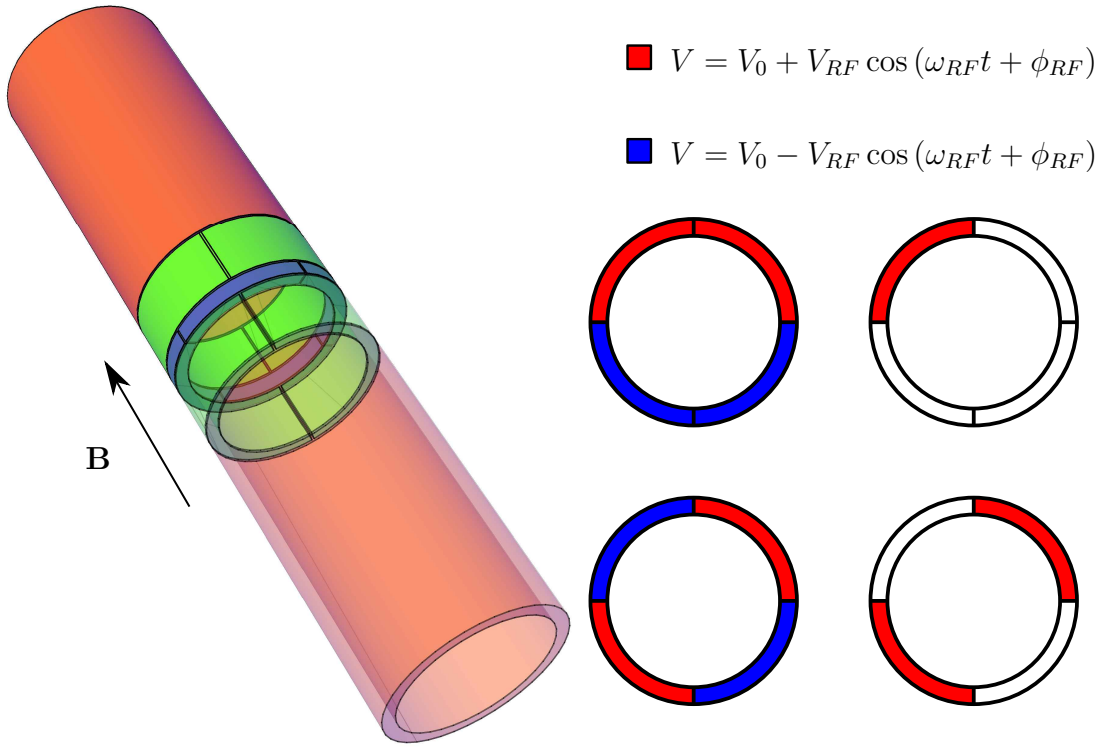

Figure 2.3: Left panel: cylindrical trap showing the four-fold segmentation of the ring electrode (blue) and two-fold segmentation of the correction electrodes (green). The electrodes closer to the reader are made transparent to improve visibility of the ring electrode segmentation. Right panel: electrodes' configurations used in the different driving schemes. Top: two possible configurations to apply dipolar driving to the radial motions. The configurations will differ in the geometrical parameter α (Eq. 2.29). Bottom: two possible configurations to apply quadrupolar driving to the radial motions. Again, they will differ on the geometrical parameter α. The configurations on the right will also modulate the potential at the trap center slightly, since there is no out-of-phase counterpart (blue).

where $\Delta\omega = \omega_{RF} - \omega_z$. Figure A.1 is a graphical representation of the amplitude (and phase) after the dipolar driving. When the ion starts with non-vanishing amplitude, Eq. A.19 should be used instead of Eq. A.11, and Fig. A.2 shows the amplitude and phase under those conditions.

In the case of the radial motions, the simpler way to describe the effect of the driving is to use the Hamiltonian as shown in Eq. 2.24. One possible electric potential to originate the electric field $\mathbf{E}_{RF} = \frac{\alpha V_{RF}}{d_{elec}} \sin(\omega_{RF} t)\, \hat{\mathbf{x}}$ is $\varphi_{RF} = -x \frac{\alpha V_{RF}}{d_{elec}} \sin(\omega_{RF} t)$. This can be written in the eigenmode basis and inserted into the Hamiltonian, yielding

$$\mathcal{H} = \frac{1}{2}\omega_+ \left(q_+^2 + p_+^2\right) - \frac{1}{2}\omega_- \left(q_-^2 + p_-^2\right) + \frac{1}{2}\omega_z \left(q_3^2 + p_3^2\right) - \frac{\alpha q V_{RF}}{d_{elec}\sqrt{m\omega_1}} (q_+ + q_-) \sin(\omega_{RF} t) \ . \tag{2.32}$$

Using the Hamilton equations of motion one obtains

$$\begin{cases} \frac{\partial \mathcal{H}}{\partial q_i} = \mp \dot{p}_i \\ \frac{\partial \mathcal{H}}{\partial p_i} = \pm \dot{q}_i \end{cases} \implies \begin{cases} \dot{p}_\pm = \mp\omega_\pm q_\pm + \frac{\alpha q V_{RF}}{d_{elec}} \frac{1}{\sqrt{m\omega_1}} \sin(\omega_{RF} t) \\ \dot{q}_\pm = \pm\omega_\pm p_\pm \end{cases} \implies$$

$$\implies \ddot{q}_\pm + \omega_\pm^2 q_\pm = \pm \frac{\alpha q V_{RF} \omega_\pm}{d_{elec}\sqrt{m\omega_1}} \sin(\omega_{RF} t) \ . \tag{2.33}$$

In this case, two eigenmotions are driven. However, their frequencies under normal operating conditions ($\omega_z \ll \omega_c$) are far apart. Since the full solution for the driven harmonic oscillator (Eq. A.4) vanishes when the driving is far from resonance, only one of the radial modes is affected. If the ion is initially at rest, the amplitude after driving near resonance is

$$A_\pm \simeq \frac{\alpha q V_{RF} T_{RF}}{2 d_{elec}\sqrt{m\omega_1}} \mathrm{sinc}\left(\frac{\Delta\omega}{2} T_{RF}\right) , \tag{2.34}$$

which in cartesian coordinates translates into the radii

$$\rho_\pm \simeq \frac{\alpha q V_{RF} T_{RF}}{2 d_{elec} m \omega_1} \mathrm{sinc}\left(\frac{\Delta\omega}{2} T_{RF}\right) . \tag{2.35}$$

This is consistent with the radii shown in Ref. [56] for on-resonance excitation (since $\mathrm{sinc}(x) \xrightarrow[x\to 0]{} 1$). The overall $\pm$ sign in Eq. 2.33 can be accounted for with an additional phase of π for the magnetron mode.

The energy gained by the ion is

$$E = \frac{1}{2}m\omega_{\pm}^2\rho_{\pm}^2 \simeq \frac{1}{8m}\left(\frac{\alpha q V_{RF} T_{RF}}{d_{elec}}\frac{\omega_{\pm}}{\omega_1}\right)^2 \mathrm{sinc}^2\left(\frac{\Delta\omega}{2}T_{RF}\right) . \tag{2.36}$$

The resulting amplitude and phase of the radial motions after the driving are also the ones shown in Fig. A.1 (or Fig. A.2 if the ion is not initially at rest).

2.3.2 Quadrupolar driving

A quadrupolar potential in the radial plane originates an electric field $\mathbf{E}$ such that $\mathbf{E}\cdot\hat{\mathbf{x}} \propto y$ and $\mathbf{E}\cdot\hat{\mathbf{y}} \propto x$. One possible potential that fulfills these is $\varphi_{RF} = -xy\frac{2\alpha V_{RF}}{d_{elec}^2}\cos\left(\omega_{RF}t + \phi_{RF}\right)$, where again α quantifies the deviation with respect to the ideal geometry (in this case, a quadrupole). The modified Hamiltonian in the eigenmode basis is then

$$\begin{aligned}\mathcal{H} = \frac{1}{2}\omega_+\left(q_+^2+p_+^2\right) - \frac{1}{2}\omega_-\left(q_-^2+p_-^2\right) + \frac{1}{2}\omega_z\left(q_3^2+p_3^2\right) \\ - k_0\cos\left(\omega_{RF}t+\phi_{RF}\right)\left(q_+ + q_-\right)\left(p_+ - p_-\right) ,\end{aligned} \tag{2.37}$$

where $k_0 = \frac{2\alpha q V_{RF}}{m\omega_1 d_{elec}^2}$. The resulting equations of motion can be solved under certain assumptions (see Appendix A.2). The radii of the radial motions are

$$\rho_{\pm}(t) = \rho_{\pm}(0)\cos\left(\omega_B t\right) \mp \frac{e^{i\pi/2}\Delta\omega\cdot\rho_{\pm}(0) + k_0 e^{\pm i\Delta\phi}\rho_{\mp}(0)}{2\omega_B}\sin\left(\omega_B t\right) , \tag{2.38}$$

where $\Delta\omega = \omega_{RF} - \omega_c$ is the detuning, $\omega_B = \sqrt{\Delta\omega^2 + k_0^2}/2$ is the *beat frequency* (frequency at which the radii oscilate) and $\Delta\phi = \phi_{RF} - \phi_+ - \phi_-$ depends on the relative phases of the driving and the initial modified-cyclotron and magnetron motions. There is also an overall phase $\phi = \pm\frac{\Delta\omega}{2}t$ that has been omitted, since it does not affect the actual attained radii.

Finally, it is also possible to couple the radial and axial motions. Ref. [57] shows that an electric field of the form

$$E \propto \cos\left(\omega_{RF}t+\phi_{RF}\right)\left(x\hat{z} + z\hat{x}\right) \tag{2.39}$$

with driving frequencies $\omega_{RF} \simeq |\pm\omega_{\pm} - \omega_z|$ couples the corresponding radial motion to the axial one. This is used in mass measurements featuring induced image current detection of the axial motion (see Sec. 3.2.1) to determine the frequencies of the radial motions.

2.4 Laser cooling of trapped ions

For most experiments involving ion traps, the initial energy of the ions is in the eV range. Such energies can complicate experiments because of e.g. Doppler broadening of any transitions of interest, frequency shifts due to the large oscillation amplitudes, short oscillation times, ...

There are a number of methods of ion cooling (see e.g. Ref. [58] and references therein). To choose a method one has to balance the experiment's features and needs, especially when it comes to the ionic species to be cooled. In the following the most common techniques are outlined.

Resistive cooling dampens the oscillation amplitude through the image current the ion induces in the trap electrodes, commonly using a resonant circuit. It also enables a non-destructive ion detection method by amplifying the induced image current. This method has been used with great success to perform precision measurements (see e.g. Refs. [6, 31] for two recent examples). However, since the current induced by the ion is proportional to the motional frequencies to be measured, and because of the way these frequencies scale with ion mass, these techniques have not been proven yet with heavier ions at low charge states. Nevertheless, recent results obtained by implementing quartz resonators instead of superconducting coils have yielded promising results (see Refs. [59, 35, 36, 37]).

Buffer gas cooling, on the other hand, can be applied to heavier particles, and it can even be used to remove unwanted species present in the trap (see Ref. [53]). It also has some drawbacks; collisions with the background gas perturb the particle's internal energy levels, affect its motion and reduce the storage time. In some cases collisions can also result in changes in the charge state of the ions. These issues are often circumvented by performing the cooling and measurement procedures in different traps (see e.g. Refs. [60, 61]).

The technique of interest for this Thesis, laser cooling, can reduce the energy to the µeV range and lower (*Doppler cooling*) or even reach the ground state of the ion's motion (*resolved sideband cooling*). Furthermore, it enables an additional method

of non-destructive, very sensitive method of detection (via imaging of the photons scattered by the laser-cooled ion). However, since it relies on the internal structure of the ion, only a few species can be used directly; sympathetic cooling, where the ion of interest is cooled by exchanging energy with a laser-cooled ion, can be used to extend the technique to other species (see e.g. Ref. [39]).

This Section will explore laser cooling with some detail, with the ultimate goal of being able to detect a generic ion's mass via the optical imaging of a laser-cooled ion.

2.4.1 Doppler cooling

Doppler cooling takes advantage of the change in momentum a particle experiences when it absorbs a photon of energy $\hbar\omega$ – the particle must therefore have some internal structure. The absorption can either increase or decrease the particle's kinetic energy, depending on the direction of motion with respect to the laser beam at the time of absorption. The latter is favored if the photons are red-detuned, that is, their energy is slightly below that of the transition between the two levels, $\hbar\omega_{ge}$. The *detuning* is $\Delta = \omega - \omega_{ge}$. In this case, absorption will happen preferably when the laser photons and the trapped particle are moving in opposite directions, since the apparent photon frequency will shift towards resonance.

The de-excitation process (spontaneous or stimulated emission) limits the minimum energy achievable via Doppler cooling. If the ion decays to its ground state via stimulated emission, the momentum kick due to emission balances the one due to absorption, since the absorbed and emitted photons are identical. Therefore, momentum and kinetic energy remain the same. If the emission happens spontaneously, however, the momentum kicks will average to zero, since spontaneous emission patterns are usually symmetric; the kinetic energy change, however, will not. This gives rise to *recoil heating*, which balances the cooling at a certain temperature; the lowest possible value of the equilibrium temperature is referred to as *Doppler limit*. The spontaneously emitted photons can be detected with a suitable optical system. This provides a non-destructive detection method that is single ion sensitive. Figure 2.4 depicts the process of Doppler cooling.

A mathematical description that summarizes the cooling mechanism is given in the following. Refs. [47, 58, 62] present more accurate descriptions of the process.

The wavevectors of the absorbed and spontaneously emitted photons are represented

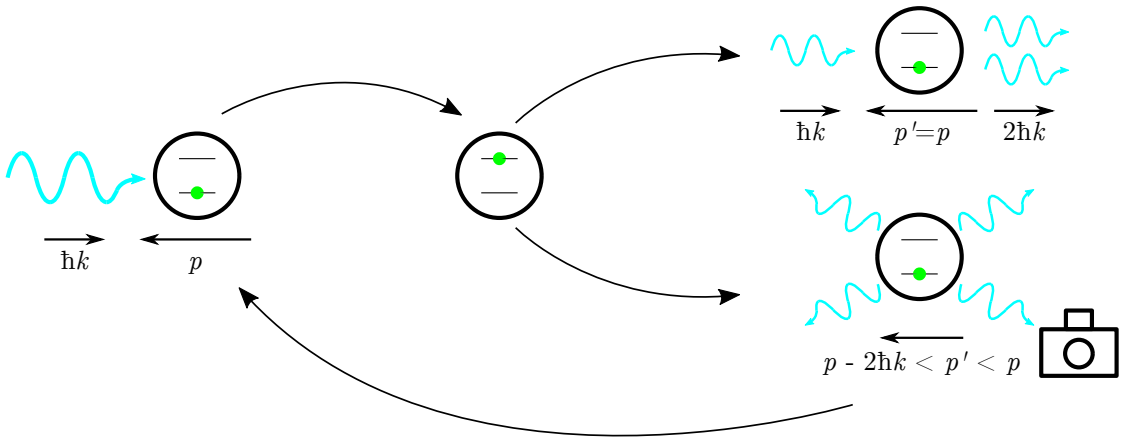

Figure 2.4: Schematic explanation of the Doppler cooling process. See text for details.

by $\mathbf{k}$ and $\mathbf{k}'$, respectively, and the velocities of the trapped particle before and after the absorption-emission cycle, in turn, are $\mathbf{v}$ and $\mathbf{v}'$. If the system is in the weak binding regime, where the natural linewidth of the transition, Γ, is much larger than the motional frequencies of the trapped particle, $\Gamma \gg \omega_m$ (*weak binding regime*), no significant change in the particle speed happens between absorption and emission. In that case, imposing the conservation of energy and momentum, the change in kinetic energy is

$$\begin{cases} m\mathbf{v} + \hbar\mathbf{k} = m\mathbf{v}' + \hbar\mathbf{k}' \\ \frac{1}{2}m\mathbf{v}^2 + \hbar\omega = \frac{1}{2}m\mathbf{v}'^2 + \hbar\omega' \end{cases} \implies \Delta K = \hbar\mathbf{v}\cdot(\mathbf{k}-\mathbf{k}') + R\left(\hat{\mathbf{k}}^2 - 2\hat{\mathbf{k}}\cdot\hat{\mathbf{k}}' + \hat{\mathbf{k}}'^2\right), \tag{2.40}$$

where $R = (\hbar k)^2/2m$ and $\hat{\mathbf{k}}$ and $\hat{\mathbf{k}}'$ are the unit vectors with the same direction as $\mathbf{k}$ and $\mathbf{k}'$. The wavevectors can be assumed to verify $|\mathbf{k}| \simeq |\mathbf{k}'| \simeq k$, since the maximum frequency shift of the emitted photon with respect to the absorbed one is twice the frequency shift due to the Doppler effect, much smaller than the frequency of the transition, which usually lies in the optical regime. Separating the different components,

$$\Delta K_i = \hbar v_i (k_i - k_i') + R\left(\hat{k}_i^2 - 2\hat{k}_i\hat{k}_i' + \hat{k}_i'^2\right) \tag{2.41}$$

where k_i and $\hat{k}_i$ are the i component of $\mathbf{k}$ and $\hat{\mathbf{k}}$, respectively.

The cooling process requires many absorption-emission cycles, so one has to take

into account the direction of the spontaneously emitted photons. These are emitted randomly, following a certain probability distribution, $P\left(\hat{\mathbf{k}}'\right)$[4]. Since the emission patterns are symmetric for dipole transitions, that is, $P\left(\hat{\mathbf{k}}'\right) = P\left(-\hat{\mathbf{k}}'\right)$, the average value of the terms k_i' and $\hat{k}_i\hat{k}_i'$ vanish over many cycles, while the average of the $\hat{k}_i'^2$ terms does not. The constants $f_{si} = \left\langle \hat{\mathbf{k}}_i'^2 \right\rangle$, characteristic of the type of transition involved, are introduced. The average change in the energies due to the motion in each direction are then

$$\langle \Delta K_i \rangle = R\left(\hat{k}_i^2 + f_{si}\right) + \hbar k_i v_i \,. \tag{2.42}$$

If the coordinate system is chosen so that the cooling beam is aligned with one of the axes,

$$\langle \Delta K_i \rangle = R\left(1 + f_{si}\right) + \hbar k_i v_i \tag{2.43a}$$

$$\langle \Delta K_j \rangle = R f_{sj} \,,\; j \neq i \tag{2.43b}$$

.

The overall energy change rate over each direction will be equal to Eqs. 2.43 multiplied by the rate at which the absorption-emission cycles take place. This is equal to the spontaneous decay rate (i.e. the linewidth of the transition, Γ) times the probability of the trapped particle to be in the excited state; the underlying assumption is that decays are much faster than absorptions. This probability is given by

$$P\left(\text{exc}\right) = \frac{s/2}{1 + s + \left(2\Delta_{app}/\Gamma\right)^2} \,. \tag{2.44}$$

Here, $\Delta_{app} = \Delta - k v_i$ is the *apparent* detuning experienced by the trapped particle, and s is the saturation parameter. The latter is given by $s = 2\Omega_r^2/\Gamma^2$, where Ω_r is the *Rabi frequency*[5]. Thus, in the direction of the cooling beam,

$$\left\langle \dot{K}_i \right\rangle = \left[R\left(1 + f_{si}\right) + \hbar k v_i\right]\Gamma \frac{s/2}{1 + s + \left[2\left(\Delta - k v_i\right)/\Gamma\right]^2} \,. \tag{2.45}$$

Close to the Doppler limit, the velocity of the trapped particle is small. Expanding Eq. 2.45 to first order in v_i and averaging over many absorption-emission cycles (so

[4] These are given by the electric dipole moment of the transition between the two internal states, $\langle g \left|\mathbf{d}\right| e \rangle$ (see Ref. [62]).

[5] The Rabi frequency is the frequency at which the populations of a two-level system oscillate when the transition is driven on resonance. See e.g. Ref. [47] for a more complete discussion.

that all terms proportional to v_i vanish, remaining only the term proportional to v_i^2), the equilibrium energy is

$$\left\langle \dot{K}_i \right\rangle \simeq \left\langle \dot{K}_i\Big|_{v=0} + v_i \left.\frac{\partial \dot{K}_i}{\partial v_i}\right|_{v=0} \right\rangle = 0 \implies$$
$$\implies \langle K_i \rangle_\infty = \frac{1}{2} m \left\langle v_i^2 \right\rangle_\infty = \frac{\hbar\Gamma}{16}\left(1+f_{si}\right)\left[(1+s)\frac{\Gamma}{2\Delta}+\frac{2\Delta}{\Gamma}\right] . \quad (2.46)$$

The equilibrium temperature, understood as a quantity proportional to the energy stored in a given mode of motion, is then

$$T = \frac{m\langle v^2\rangle}{k_B} = \frac{\hbar\Gamma}{8k_B}\left(1+f_s\right)\left[(1+s)\frac{\Gamma}{2\Delta}+\frac{2\Delta}{\Gamma}\right] . \quad (2.47)$$

The detuning Δ that minimizes this temperature is readily found to be $\Gamma/2\cdot\sqrt{1+s}$. The resulting temperature

$$T_{min} = \frac{\hbar\Gamma}{4k_B}\left(1+f_s\right)\sqrt{1+s}\,, \quad (2.48)$$

is the aforementioned Doppler limit.

In the remaining directions of motion, the average rate of energy change is given by

$$\left\langle \dot{K}_j \right\rangle = R f_{sj}\Gamma \frac{s/2}{1+s+\left[2\left(\Delta - k v_i\right)/\Gamma\right]^2} . \quad (2.49)$$

Since all the quantities are positive, $\left\langle \dot{K}_j \right\rangle > 0$, that is, the trapped particle is heated along these directions of motion. The laser beam provides no cooling in these directions, unless the associated modes of motion are coupled in some way to a mode with a component in the direction of the laser beam.

2.4.2 Ground state cooling

There are several ways to use the interaction between the trapped ion and the laser field to achieve cooling to the ground state with high probability. A well known one is resolved sideband cooling [63], although cooling by Electromagnetically Induced Transparency [64, 65] or resolved-sideband Raman Cooling [66] are in some cases more advantageous.

The first report of the use of sideband cooling to reach the ground state [63] summed up the process with an energetic argument. If the trapped particle oscillates with frequency ω_m, its absorption/emission profile as seen in the laboratory frame will have sidebands at $\omega_{ge} \pm n\omega_m$. If the laser is tuned to the *first red sideband*, $\omega = \omega_{ge} - \omega_m$, the photons absorbed by the particle have energy $\hbar(\omega_{ge} - \omega_m)$, while those that are re-emitted will average to $\hbar\omega_{ge}$. Therefore, on average, each absorption-emission cycle reduces the particle energy by a motional quantum, $\hbar\omega_m$.

The absorption profile is calculated in a semiclassical picture in Ref. [58]. The ion is assumed to be in the strong binding regime (i.e. $\omega_m \gg \Gamma$ – in other words, that the absorption-emission cycles are slower than the oscillation of the trapped particle, unlike what was assumed to Doppler cooling). Further, the particle is assumed to be in the Lamb-Dicke regime, i.e. the Lamb-Dicke parameter verifies $\eta = 2\pi\rho/\lambda \ll 1$. This means that the oscillation amplitude ρ must be smaller than the laser wavelength λ. This condition is usually achieved with a previous Doppler cooling stage. The spectral absorption cross-section then reads [58]

$$\sigma(\omega) = \sigma_0 \sum_{n=-\infty}^{+\infty} |J_n(\eta)|^2 \frac{(\Gamma/2)^2}{(\Gamma/2)^2 + [\omega_{ge} - (\omega + n\omega_m)]^2}, \tag{2.50}$$

where J_n are the Bessel functions of the first kind. The trapped particle is thus able to absorb radiation at $\omega_{ge} \pm n\omega_m$, with a probability weighted by $|J_n(\eta)|^2$. Since the asymptotic behavior of the Bessel functions for $\eta \ll 1$ is $|J_n(\eta)| \sim \eta^{|n|}$, the carrier ($n = 0$) line dominates, and only the first few sidebands have a significant contribution. It is possible to obtain the temperature from the relative amplitude of the sidebands. Note that the Bessel functions have zeros for certain values of η; this means that the cooling using a given sideband can stop at certain oscillation amplitudes (or phonon numbers).

The speed of the process is limited by the strong binding condition, $\omega_m \gg \Gamma$, i.e., by the long de-excitation times. To circumvent this, the excited state can be depopulated by other means, e.g. by coupling it to a different state with a lower lifetime.

This semiclassical picture will not be sufficient when the number of quanta is small. It is possible to obtain an approximate, but accurate, explanation, in terms of rate equations for the population of the different states of the motional degree of freedom. Such an analysis can be found e.g. in Ref. [47]. Two heating processes play a role, with similar probabilities: absorption at the carrier frequency followed by emission

at the first blue sideband and absorption at the first blue sideband followed by emission at the carrier frequency. The cooling and heating rates are again given by the average change in energy multiplied by the rate at which the cycles take place. At the final stages of the cooling process the study may be restricted to the ground and first excited states, whose occupation probabilites follow the rate equations[6]

$$\begin{cases} \dot{p}_0 = p_1 \frac{\left(\eta\Omega_r^2\right)}{\Gamma} - p_0 \left[\left(\frac{\Omega_r \tilde{\eta}}{2\omega_m} \right)^2 \Gamma + \left(\frac{\eta\Omega_r}{4\omega_m} \right)^2 \Gamma \right] \\ \dot{p}_1 = -\dot{p}_0 \end{cases} . \tag{2.51}$$

In the steady state, $\dot{p}_i = 0 \,\forall\, i$ and $p_0 + p_1 = 1$. This yields an average occupation number

$$\langle n \rangle = \sum_n n p_n \simeq p_1 = \left(\frac{\Gamma}{2\omega_m} \right)^2 \left[\left(\frac{\tilde{\eta}}{\eta} \right)^2 + \frac{1}{4} \right] . \tag{2.52}$$

Since the particle is assumed to be in the strong binding regime ($\omega_m \gg \Gamma$) and the term in square brackets is $\sim$1, $\langle n \rangle \ll 1$, and the particle is cooled to the ground state with high probability.

In the case of $^{40}Ca^+$ the transition that will be used for sideband cooling is the one that from the $S_{1/2}$ state with $m_J = \pm 1/2$ to the $D_{5/2}$ state with $m_J = \pm 5/2$ or $m_J = \pm 3/2$. The orientation of the laser beam required to induce such a transition was studied in Ref. [67].

2.4.3 Laser cooling of the magnetron motion

In the previous sections the particle was assumed to be confined in a stable harmonic potential well. In a Penning trap, however, one of the motions is unstable – thus, cooling of the ion is more complex. Further, the strong magnetic field perturbs the internal states of the ion. This Section, as well as the following one, address these issues.

The total energy associated to a magnetron motion of radius ρ_- is $E_- = -\frac{1}{2} m \omega_- \omega_1 \rho_-^2$ (see Sec. 2.2). Since it is negative, cooling of the motion (reduce the amplitude of oscillation/speed) must be done by incresing its energy. There are two well-known ways to achieve this:

[6] $\tilde{\eta}$ is the Lamb-Dicke parameter of the emission at the first blue sideband. It appears in the heating term due to absorption at the carrier frequency.

- Spatial discrimination: instead of discriminating the relative direction of the ion and the laser photons by means of the Doppler effect, the laser beam is offset from the trap center. If the laser beam points in the same direction as the magnetron orbit, the change in magnetron energy is $\dot{E}_- = \mathbf{F}\cdot\mathbf{v}_- \sim \mathbf{k}\cdot\mathbf{v}_- > 0$. Since $\omega_+ \gg \omega_-$, it is reasonable to expect that for normal experimental conditions the initial radii verify $\rho_- \gg \rho_+$. Therefore, the laser can cover the full modified-cyclotron orbits while only within the favorable half of the magnetron orbit. Thus, cooling of the modified-cyclotron motion happens as described in Sec. 2.4.1. This approach was proposed in Ref. [62] and has been realized at several places [68, 69]. It is now considered less desirable than the second approach.

- The magnetron and modified-cyclotron motions are coupled by means of a quadrupolar drive (see Sec. 2.3.2). The working principle is similar to that of the technique presented in Ref. [53] – the magnetron motion, which cannot be cooled by itself, is coupled to the modified-cyclotron motion, which is being cooled. Therefore, there is a competition between the laser (which increases ρ_-) and the coupling (which, if the parameters are set correctly, decreases ρ_-). This can be written in terms of two coupled differential equations for the magnetron and modified-cyclotron radii [70],

$$\begin{cases} \dot{\rho}_+ = -\gamma_+\rho_+ + \delta\rho_- \\ \dot{\rho}_- = -\delta\rho_+ + \gamma_-\rho_- \end{cases} , \tag{2.53}$$

where $\gamma_\pm$ are the damping constants for each of the motions due to the laser and δ indicates the coupling strength. Note that $\dot{\rho}_- > 0$ in the absence of coupling) Introducing an ansatz of the form $\rho_\pm = \rho_\pm^{(0)} e^{-\gamma t}$, an eigenvalue problem is obtained,

$$\begin{pmatrix} \gamma - \gamma_+ & \delta \\ \delta & \gamma + \gamma_- \end{pmatrix} \begin{pmatrix} \rho_+^{(0)} \\ \rho_-^{(0)} \end{pmatrix} , \tag{2.54}$$

from which, by zeroing out the determinant, the overall damping constants are obtained:

$$\gamma = \frac{(\gamma_+ - \gamma_-) \pm \sqrt{(\gamma_+ - \gamma_-)^2 - 4\,(\delta^2 - \gamma_+\gamma_-)}}{2} . \tag{2.55}$$

To have cooling ($\gamma > 0$ for both signs of the square root) the individual damping constants must verify $\gamma_+ > \gamma_-$, and the square root must be smaller than $\gamma_+ + \gamma_-$. This is achieved if the coupling is strong enough that $\delta^2 > \gamma_+\gamma_-$. As in buffer gas cooling, if the coupling is too strong the square root becomes imaginary and the radii oscillate at a frequency $\omega_B = \mathrm{Im}(\gamma) = \sqrt{4(\delta^2 - \gamma_+\gamma_-) - (\gamma_+ - \gamma_-)^2}$, but overall $\rho_\pm \to 0$ with a damping constant $\mathrm{Re}(\gamma) = \gamma_+ - \gamma_-$, the maximum attainable value.

2.4.4 Zeeman splitting and J-mixing under intense magnetic fields

Since the laser cooling mechanisms rely on the internal structure of the trapped particle, the effects of the magnetic field on it need to be adressed. The electronic structure of the species in question, $^{40}Ca^+$, in absence of magetic field is presented in Fig. 2.5, and the precise parameters of the relevant transitions are given in Tab. 2.2. The presence of a magnetic field breaks the $2J + 1$-fold degeneracy of the levels; this is known as *Zeeman splitting*. For relatively low magnetic field intensities, the correction to any energy level is given by $\Delta E = \mu_B B g_J m_J$, where μ_B is Bohr's magneton, g_J is the Landé g-factor of the state in question and m_J is the third component of the total angular momentum. This results in a set of sublevels with equal spacing among them. However, this correction, obtained from first order perturbation theory, is not sufficient. In previous Penning-trap experiments using calcium ions ($B \sim 1$ T [68]) the size of the second order corrections are close to the linewidth of the transitions – this is of course far from the case when $B \sim 7$ T, where even the third order corrections are, in the worst case, barely within the power broadened linewidth. This Section will employ perturbation theory directly to calculate the second and third order energy shifts, and estimate those of the fourth order. The procedure is well described in Ref. [71]. Note that even though the initial levels are degenerate, the perturbation is diagonal within each of the degenerate subspaces. This simplifies the calculations, enabling the use of the expressions derived for non-degenerate perturbation theory.

As usual, the total Hamiltonian can be written as

$$\hat{\mathcal{H}} = \hat{\mathcal{H}}_0 + \hat{\mathcal{H}}', \tag{2.56}$$

where $\hat{\mathcal{H}}_0$ is the original Hamiltonian (including fine structure) and

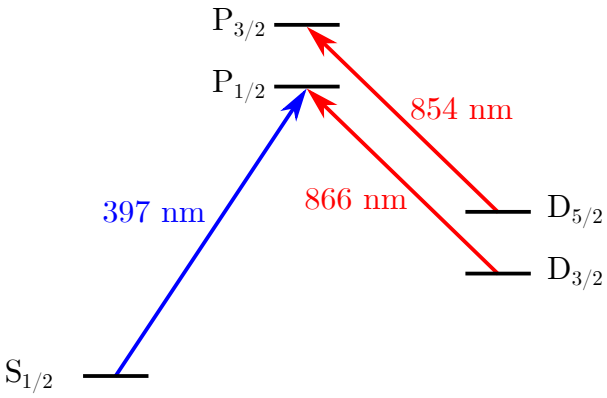

Figure 2.5: Atomic level scheme of $^{40}Ca^{+}$ in absence of magnetic field. The colored arrows are the transitions presented in Tab. 2.2. The transition used for Doppler cooling is $S_{1/2} \rightarrow P_{1/2}$. From the $P_{1/2}$ state, the ion can decay to the ground state $S_{1/2}$ or to the $D_{3/2}$ state (with a branching ratio $\sim 1:16$ [68]). Given the long lifetime of the metastable $D_{3/2}$ state (since $D_{3/2} \rightarrow S_{1/2}$ is dipole-forbidden), the level must be depopulated using the 866 nm transition. The presence of the magnetic field will make the 854 nm transition needed as well.

$$\hat{\mathcal{H}}' = \frac{\mu_B B}{\hbar}\left(\hat{L}_z + g\hat{S}_z\right) \tag{2.57}$$

is the term arising from the trapping magnetic field. Here, g is the electron's gyromagnetic ratio (see e.g. [79]). It is important to note that the eigenstates of $\hat{\mathcal{H}}_0$ have well-defined quantum numbers L, S, J and M_J, while the eigenstates of the perturbation $\hat{\mathcal{H}}'$ are characterized by L, M_L, S and M_S. The coefficients that are used to go from one base to another, $\langle LM_LSM_S|\, LS; JM_J\rangle$, are the well-known Clebsch-Gordan coefficients. The use of $g_L = 1$ and the free electron's gyromagnetic ratio instead of the experimentally measured g_J provides enough precision for the purposes of Doppler cooling.

The corrections to the energy can be written in a compact form if one uses the matrix representation of the perturbation, $\hat{\mathcal{H}}'$, in the base of the eigenstates of the original Hamiltonian, $\hat{\mathcal{H}}_0$, are used. Each of the matrix elements, represented by $h_{ij} = \langle i|\, \hat{\mathcal{H}}'\, |j\rangle$, is calculated in Appendix A.3. Note that the resulting matrix is

Table 2.2: Transitions in the internal structure of $^{40}Ca^{+}$ relevant for laser cooling [72, 73, 74, 75, 76, 77, 78] .

Transition	Frequency (MHz)	Γ (MHz)	Saturation intensity ($\mu W/mm^2$)
$S_{1/2} \rightarrow P_{1/2}$	755 222 766.2 (1.7)	21.57(8)	433
$D_{3/2} \rightarrow P_{1/2}$	346 000 234.867 (96)	1.482(8)	3.4
$D_{5/2} \rightarrow P_{3/2}$	350 862 882.830 (91)	1.350(6)	3.3

quite sparse, since for each state there is at most one non-zero element outside the diagonal. Using this notation, the first order correction to the energy of the state $|i\rangle = |LS; JM_J\rangle$ is simply given by $\Delta E^{(1)}_{L\,S\,J\,M_J} = h_{ii} = \langle LS; JM_J| \hat{\mathcal{H}}' |LS; JM_J\rangle$. For example, for the $D_{5/2}$ state with $M_J = +3/2$,

$$\Delta E^{(1)}_{2,\,1/2,\,5/2,\,+3/2} = + \left(\frac{6}{5} + \frac{3g}{10}\right) \mu_B B \,. \tag{2.58}$$

The result, as expected, matches the value obtained using the ubiquitous Zeeman splitting formula. The results for all states are presented in Tab. 2.3.

The second order energy correction to a level $|i\rangle$ is calculated as

$$\Delta E^{(2)} = \sum_{j: E^{(0)}_i \neq E^{(0)}_j} \frac{|h_{ij}|^2}{E^{(0)}_i - E^{(0)}_j} \,, \tag{2.59}$$

where the sum condition (non-degeneracy of $|i\rangle$ and $|j\rangle$ in the original Hamiltonian) means in this case that the initial and final states must differ either in J or in L. Appendix. A.3 shows that for a given state $|i\rangle = |LS; JM_J\rangle$ there is at most a state $|j\rangle \neq |i\rangle$ so that $h_{ij} \neq 0$. The condition for such a $|j\rangle$ to exist for an ion with $S = 1/2$ is that $L \neq 0$ and $|M_J| < L + 1/2$. Equation 2.59 can therefore be written as

$$\Delta E^{(2)}_{L\,S\,J\,M_J} = \begin{cases} \frac{|h_{JJ'}|^2}{E^{(0)}_J - E^{(0)}_{J'}} & \text{if } L \neq 0 \text{ and } |M_J| < L + 1/2 \\ 0 & \text{otherwise} \end{cases} . \tag{2.60}$$

Note that the labels i and j of the two states connected by the perturbation have been substituted on the right-hand side with J and J'. This has been done because J is the only quantum number that differs among two such states.

The correction to e.g. the $D_{5/2}$ state with $M_J = +3/2$ is

$$\Delta E^{(2)}_{2,\,1/2,\,5/2,\,+3/2} = \frac{\left|h_{5/2,\,3/2}\right|^2}{E_{5/2} - E_{3/2}} = \frac{4}{25} (g-1)^2 \frac{(\mu_B B)^2}{E_{5/2} - E_{3/2}} \,. \tag{2.61}$$

If the state $D_{3/2}$ with $M_J = +3/2$ had been considered instead, the only difference would be the order reversal in the denominator, resulting in an overall negative sign. This sort of *symmetry* applies to all other pairs with non-zero second order corrections. The results are presented in Tab. 2.3. While the first order corrections were proportional to $\mu_B B$, second order corrections are proportional to

$(\mu_B B)^2 / \left(E_J^{(0)} - E_{J'}^{(0)}\right) = (\mu_B B)^2 / \Delta E_{JJ'}^{(0)}$, that is, their weight is reduced by a factor $\mu_B B / \Delta E_{JJ'}^{(0)}$.

Third order corrections are given by [80]

$$\Delta E_i^{(3)} = \\ = \sum_{j:E_j^{(0)} \neq E_i^{(0)}} \sum_{k:E_k^{(0)} \neq E_i^{(0)}} \frac{h_{ij} h_{jk} h_{ki}}{\left(E_i^{(0)} - E_j^{(0)}\right)\left(E_i^{(0)} - E_k^{(0)}\right)} - \sum_{j:E_j^{(0)} \neq E_i^{(0)}} \frac{h_{ij} h_{ji} h_{ii}}{\left(E_i^{(0)} - E_j^{(0)}\right)^2} . \tag{2.62}$$

Making the same considerations as for the second order corrections regarding the sparseness of the $\hat{\mathcal{H}}'$, one obtains

$$\Delta E^{(3)}_{L\,S\,J\,M_J} = \begin{cases} \frac{|h_{JJ'}|^2}{\left(E_J^{(0)} - E_{J'}^{(0)}\right)^2}\left(h_{JJ} - h_{J'J'}\right) & \text{if } L \neq 0 \text{ and } |M_J| < L + 1/2 \\ 0 & \text{otherwise} \end{cases} . \tag{2.63}$$

Note that this expression can be rewritten in terms of the first and second order energy corrections as

$$\Delta E^{(3)}_{L\,S\,J\,M_J} = \begin{cases} \frac{\Delta E^{(2)}_{L\,S\,J\,M_J}}{E_J^{(0)} - E_{J'}^{(0)}}\left(\Delta E^{(1)}_{L\,S\,J\,M_J} - \Delta E^{(1)}_{L\,S\,J'\,M_J}\right) & \text{if } L \neq 0 \text{ and } |M_J| < L + 1/2 \\ 0 & \text{otherwise} \end{cases} . \tag{2.64}$$

The fraction on the right-hand side of the equation is always positive (see Eq. 2.60). Therefore, the magnitude of the correction is again the same for the states with $L = L'$, $S = S'$ and $|M_J| = |M_J'|$, but the sign is determined by the size of the first order corrections $\Delta E^{(1)}$, and not by the unperturbed energies $E^{(0)}$.

As an example, the third order correction the $D_{5/2}$ level with $M_J = +3/2$ is

Table 2.3: Zeeman shifts in $^{40}Ca^{+}$. The linear terms are divided by $\mu_B B$, quadratic terms by $(\mu_B B)^2/\left|\Delta E^{(0)}_{JJ'}\right|$ and the cubic terms by $(\mu_B B)^3/(\Delta E^{(0)}_{JJ'})^2$.

Level	Linear term	Quadratic term	Cubic term
$S_{1/2}$, $M_J = \pm 1/2$	$\pm g/2$	0	0
$P_{1/2}$, $M_J = \pm 1/2$	$\pm\,(2/3 - g/6)$	$-2/9 \cdot (g-1)^2$	$\mp 2/27 \cdot (g-1)^3$
$P_{3/2}$, $M_J = \pm 1/2$	$\pm\,(1/3 + g/6)$	$+2/9 \cdot (g-1)^2$	$\pm 2/27 \cdot (g-1)^3$
$P_{3/2}$, $M_J = \pm 3/2$	$\pm\,(1 + g/2)$	0	0
$D_{3/2}$, $M_J = \pm 1/2$	$\pm\,(3/5 - g/10)$	$-6/25 \cdot (g-1)^2$	$\mp 6/125 \cdot (g-1)^3$
$D_{3/2}$, $M_J = \pm 3/2$	$\pm\,(9/5 - 3g/10)$	$-4/25 \cdot (g-1)^2$	$\mp 12/125 \cdot (g-1)^3$
$D_{5/2}$, $M_J = \pm 1/2$	$\pm\,(2/5 + g/10)$	$+6/25 \cdot (g-1)^2$	$\pm 6/125 \cdot (g-1)^3$
$D_{5/2}$, $M_J = \pm 3/2$	$\pm\,(6/5 + 3g/10)$	$+4/25 \cdot (g-1)^2$	$\pm 12/125 \cdot (g-1)^3$
$D_{5/2}$, $M_J = \pm 5/2$	$\pm\,(2 + g/2)$	0	0

$$\Delta E^{(3)}_{2,1/2,5/2,+3/2} = \frac{\left|h_{5/2,3/2}\right|^2}{\left(E^{(0)}_{5/2} - E^{(0)}_{3/2}\right)^2}\left(h_{5/2,5/2} - h_{3/2,3/2}\right) =$$
$$= \frac{\left|-\frac{2}{5}\mu_B B\,(g-1)\right|^2}{\left(E^{(0)}_{5/2} - E^{(0)}_{3/2}\right)^2}\mu_B B\left(\frac{6}{5} + \frac{3g}{10} - \frac{9}{5} + \frac{3g}{10}\right) =$$
$$= +\frac{3}{5}(g-1)^3\,\frac{(\mu_B B)^3}{\left(E^{(0)}_{D_{5/2}} - E^{(0)}_{D_{3/2}}\right)^2}\,. \quad (2.65)$$

The weight of the correction is again lowered with respect to the previous term by a factor $\mu_B B/\Delta E^{(0)}_{JJ'}$. The results for all levels are presented in Tab. 2.3. The size of the third order corrections (in terms of frequency) for $B = 7$ T is ~ 1 MHz for the P states and ~ 10 MHz for the D states. These are of the same order as the linewidths of the transitions involved when power broadening is accounted for. The fourth order corrections, whose weights will be further reduced by an additional factor of $\mu_B B/\Delta E^{(0)}_{JJ'}$, would be about 0.01 MHz for the P states and 0.1 MHz, for the D states, irrelevant for Doppler cooling. Figure 2.6 shows the final energy of the levels of the $^{40}Ca^{+}$ ion in the magnetic field, with the intensity determined in Sec. 6.2.

There is a second effect of the magnetic field that must be taken into account: modification of the eigenstates, that gain small components along the other eigenstates of the unperturbed Hamiltonian. The first order correction to a state $|i\rangle$ reads [71]

$$\left|i^{(1)}\right\rangle = \sum_{j:E_i^{(0)}\neq E_j^{(0)}} \frac{h_{ji}}{E_i^{(0)} - E_j^{(0)}} \left|j^{(0)}\right\rangle . \tag{2.66}$$

Accounting again for the sparseness of the matrix, most of the sum elements vanish, as in the second and third order corrections:

$$\left|L\,S;J\,M_J\,^{(1)}\right\rangle = \begin{cases} \frac{h_{JJ'}}{E_J^{(0)}-E_{J'}^{(0)}} \left|L\,S;J'\,M_J\,^{(0)}\right\rangle & \text{if } L\neq 0 \text{ and } |M_J| < L+1/2 \\ 0 & \text{otherwise} \end{cases} . \tag{2.67}$$

Only the states with non-zero second order corrections will have corrections to the states themselves. In particular, the perturbed $D_{3/2}$ sublevels gain a small component in the $D_{5/2}$, that is, the perturbed states are of the form

$$\left|D_{3/2}, m_J\right\rangle = \left|D_{3/2}^{(0)}, m_J\right\rangle + \epsilon \left|D_{5/2}^{(0)}, m_J\right\rangle . \tag{2.68}$$

The same occurs to $P_{1/2}$ and $P_{3/2}$ states. This causes a non-vanishing probability of the ion in the modified $P_{1/2}$ state to decay to the modified $D_{5/2}$, as reported in Ref. [83]. The probability of a transition between two states $|i\rangle$ and $|j\rangle$ is quantified by the squared modulus of the electric-dipole matrix element,

$$M = \langle j|\,\mathbf{d}\cdot\mathbf{E}\,|i\rangle . \tag{2.69}$$

Studying which combinations result in non-zero values gives rise to the *selection rules*. In particular, since $\Delta J \neq 0, \pm 1$, M is identically zero for any pair of (unperturbed) $P_{1/2}$ and $D_{5/2}$ states,

$$M = \left\langle {P_{1/2}}^{(0)}, M_J' \right| \mathbf{d}\cdot\mathbf{E} \left| {D_{5/2}}^{(0)}, M_J \right\rangle = 0 . \tag{2.70}$$

However, if the states are perturbed, i.e. if

$$\left|D_{5/2}, M_J\right\rangle \simeq \left|{D_{5/2}}^{(0)}, M_J\right\rangle + \epsilon_D \left|{D_{3/2}}^{(0)}, M_J\right\rangle \tag{2.71}$$

and

$$\left|P_{1/2}, M_J'\right\rangle \simeq \left|{P_{1/2}}^{(0)}, M_J'\right\rangle + \epsilon_P \left|{P_{3/2}}^{(0)}, M_J'\right\rangle , \tag{2.72}$$

with

$$\epsilon_P = \frac{\sqrt{2}}{3}\frac{\mu_B B}{E^{(0)}_{\mathrm{P}_{1/2}} - E^{(0)}_{\mathrm{P}_{3/2}}} \quad \text{and} \quad \epsilon_D = \left\{\frac{2}{5}, \frac{\sqrt{6}}{5}\right\}\frac{\mu_B B}{E^{(0)}_{\mathrm{D}_{5/2}} - E^{(0)}_{\mathrm{D}_{3/2}}} \tag{2.73}$$

being two small numbers (note that ϵ_D takes either of the values between curly brackets depending on the value of M_J), the probability of the $\mathrm{P}_{1/2} \to \mathrm{D}_{5/2}$ transition scales as

$$\begin{aligned} P\left(\mathrm{P}_{1/2} \to \mathrm{D}_{5/2}\right) \sim |M'|^2 = \left|\left\langle \mathrm{P}_{1/2}, M'_J\right| \mathbf{d}\cdot\mathbf{E} \left|\mathrm{D}_{5/2}, M_J\right\rangle\right|^2 \simeq \\ \simeq \left|\epsilon_P \left\langle {\mathrm{P}_{3/2}}^{(0)}, M'_J\right| \mathbf{d}\cdot\mathbf{E} \left|{\mathrm{D}_{5/2}}^{(0)}, M_J\right\rangle + \epsilon_D \left\langle {\mathrm{P}_{1/2}}^{(0)}, M'_J\right| \mathbf{d}\cdot\mathbf{E} \left|{\mathrm{D}_{3/2}}^{(0)}, M_J\right\rangle\right|^2 \sim \\ \sim (\mu_B B)^2 \,, \end{aligned} \tag{2.74}$$

where a term in ϵ^2 is neglected, since $\epsilon \ll 1 \implies \epsilon^2 \ll \epsilon$, and only the non-zero electric-dipole matrix elements are shown. The branching ratio, obtained by evaluating the matrix elements in the previous expression for $^{40}\mathrm{Ca}^+$ [83], is

$$\frac{P\left(\mathrm{P}_{1/2} \to \mathrm{D}_{5/2}\right)}{P\left(\mathrm{P}_{1/2} \to \mathrm{S}_{1/2}\right)} \simeq 4.2 \times 10^{-7} B^2\,\mathrm{T}^{-2}\,. \tag{2.75}$$

The value at $B \sim 7$ T is $\sim 1/50\,000$. This means that, in average, an ion undergoing Doppler cooling will decay to the perturbed $\mathrm{D}_{5/2}$ state once every 50 000 absorption emission cycles. i.e. in $\sim 50\,000/\left(\Gamma/4\right) \sim 10$ ms. Given the long half-life of the $\mathrm{D}_{5/2}$ state, in the order of 1 s (since the transition $\mathrm{D}_{5/2} \to \mathrm{S}_{1/2}$ is forbidden even in the presence of the magnetic field) cooling will not take place during 99 % of the time. Pumping of the $\mathrm{D}_{5/2}$ state is therefore mandatory to successfully perform Doppler cooling of $^{40}\mathrm{Ca}^+$ in a Penning trap.

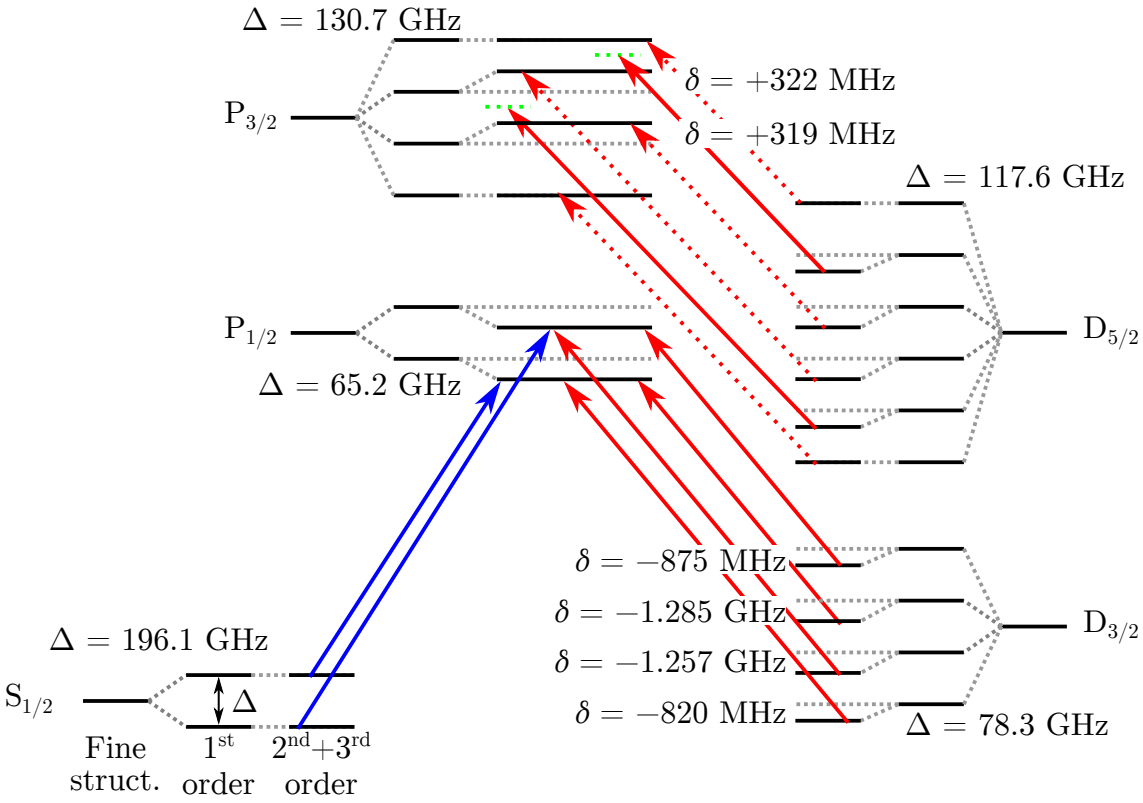

Figure 2.6: Atomic level scheme of $^{40}Ca^+$ in a $\sim 7\,T$ magnetic field. The exact value of B was obtained from a time-of-flight resonance for $^{40}Ca^+$ (see Chapter 6). Δ is the energy splitting due to the first order Zeeman effect, and δ is the size of the second and third order corrections. The magnitude of the latter is the same between P and D states with equal M_J (see Tab. 2.3). The blue arrows are the transitions used for Doppler cooling, whereas the red ones are the transitions driven to depopulate the metastable D states – in all cases, $\Delta M_J = \pm 1$ is chosen, so that the lasers can induce transitions regardless of the alignment of the beam with respect to the magnetic field [81, 82]. Solid arrows represent the transitions driven directly by lasers, while the dashed ones indicate transitions that are driven using sidebands generated by an Electro-Optic Modulator (see Sec. 6.1.2). The 854 nm lasers used to pump the $D_{5/2}$ state are detuned by +33 and +70 MHz (see Chapter 6 for details).

Chapter 3

Mass measurements with Penning traps

This Chapter provides an overview of the Penning-Trap Mass Spectrometry (PTMS) techniques that are currently in use. What all techniques have in common is that the quantities that are actually measured are motional frequencies. As a consequence, the achievable precisions are very high, regardless of the particular technique that is used. The goal in PTMS is to measure the ratio of the free cyclotron frequencies of the target particle with respect to a reference, which is related to the quotient of their mass-to-charge ratios (see Sec. 2.2). The different PTMS techniques differ in the method of determination of the free cyclotron frequency. Since the present work is oriented towards techniques with single ion sensitivity in the SuperHeavy Elements (SHE) region of the nuclear chart, whose production rate is very limited, the techniques will be grouped according to the nature of the detection method used (destructive/non-destructive).

3.1 Destructive detection techniques

Only two PTMS have been successfully applied to SHE so far, and both of them feature destructive detection. These are the Time-Of-Flight Ion-Cyclotron-Resonance (TOF-ICR) [13] and the Phase-Imaging Ion-Cyclotron-Resonance (PI-ICR) [84] techniques. This section will introduce both.

3.1.1 Time-Of-Flight Ion-Cyclotron-Resonance

The TOF-ICR technique exploits the force a non-uniform magnetic field exerts on a magnetic dipole,

$$V_{dipole} = -\boldsymbol{\mu} \cdot \mathbf{B} \implies \mathbf{F} = \nabla (\boldsymbol{\mu} \cdot \mathbf{B}) \,. \tag{3.1}$$

In the following, its use to determine the trapped ion's free cyclotron frequency will be shown. More details can be found in Ref. [85] and references therein.

In a TOF-ICR measurement, the trapped ion is ejected towards a detector placed outside the magnetic field, and its *time-of-flight* is recorded. When the potentials in the trap change to eject the ion, it no longer follows the equations of motion derived in Sec. 2.2. Instead, its motion can be seen as the superposition of pure cyclotron orbits, unaffected by the electric field, plus the axial motion. When the potential changes, position and speed must be continuous, and so must the kinetic energy:

$$K = \frac{1}{2} m\omega_c^2 \rho_c^2 = \frac{1}{2} m\omega_-^2 \rho_-^2 + \frac{1}{2} m\omega_+^2 \rho_+^2 \simeq \frac{1}{2} m\omega_+^2 \rho_+^2 \,. \tag{3.2}$$

The ion, now moving in circular trajectories within the magnetic field, can be seen as a current loop. The magnetic dipolar moment of such a loop is given by the current times the area enclosed by the loop. The direction of the dipolar moment is given by the right-hand rule. Therefore,

$$\boldsymbol{\mu} = I\mathbf{S} = q\nu_c \cdot \pi\rho_c^2 \, (-\hat{\mathbf{z}}) = -\frac{1}{2} q\omega_c \rho_c^2 \hat{\mathbf{z}} = -\frac{K}{B} \hat{\mathbf{z}} \,. \tag{3.3}$$

The energy of such a dipole in the magnetic field is

$$V = -\boldsymbol{\mu} \cdot \mathbf{B} = \frac{1}{2} q\omega_c \rho_c^2 B \,. \tag{3.4}$$

The same potential can be derived using $V = -q\mathbf{v} \cdot \mathbf{A}$ (see Sec. 2.2). This potential originates a force whose axial component,

$$\mathbf{F} \cdot \hat{\mathbf{z}} = -q\omega_c \rho_c^2 / 2 \frac{\partial B}{\partial z} \,, \tag{3.5}$$

accelerates the ion as it leaves the magnetic field ($\partial B/\partial z < 0 \implies \mathbf{F} \cdot \hat{\mathbf{z}} > 0$). The force (and therefore the time-of-flight reduction) is larger if the radius of the ion orbit (and therefore its magnetic dipole moment) is larger.

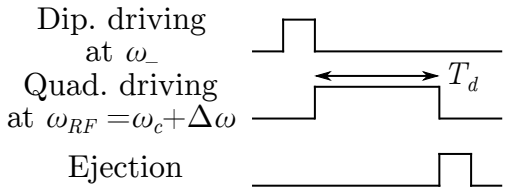

Figure 3.1: TOF-ICR measurement scheme. The ions must be centered before the dipolar driving at the magnetron frequency. The duration of the quadrupolar pulse that converts magnetron motion into modified-cyclotron motion determines the linewidth. See text for details.

The time of flight can be determined as [13]

$$t_{flight} = \int_{z_{trap}}^{z_{det}} \frac{\mathrm{d}z}{\dot{z}} = \int_{z_{trap}}^{z_{det}} \mathrm{d}z \sqrt{\frac{m}{2K}} = \int_{z_{trap}}^{z_{det}} \mathrm{d}z \sqrt{\frac{m}{2\left(E - qV\left(z\right) - \mu B\left(z\right)\right)}}, \tag{3.6}$$

where E is the total energy of the ion. Note that the magnetic moment has been assumed to be constant throughout the extraction process – this is an approximation, since the ion cannot have an orbital magnetic moment if there is no magnetic field to sustain its orbit.

The sequence to perform a TOF-ICR measurement is shown in Fig. 3.1. The ions must start at the trap center. This is usually achieved via cooling resonance in a Preparation Trap (PT). Once the ions are centered, they are driven to a certain magnetron radius ρ_- (see Sec. 2.3.1). The quadrupolar driving (see Sec. 2.3.2) is carried out with amplitude V_d and duration T_d such that full conversion is achieved if $\omega_{RF} = \omega_c$, and partial conversion otherwise. This results in a magnetic moment that depends on $\Delta\omega = \omega_{RF} - \omega_c$ as

$$|\boldsymbol{\mu}| = \frac{1}{2} q \omega_c \left(\rho_-^{ini}\right)^2 \cdot \frac{\pi^2}{4} \mathrm{sinc}\left(\frac{\pi}{2}\sqrt{\left(\frac{\Delta\omega \cdot T_d}{\pi}\right)^2 + 1}\right) \tag{3.7}$$

(see Eq. A.30). This, combined with Eq. 3.6 can be used to fit the datapoints and obtain the free cyclotron frequency of the ions. Figure 3.2 shows the typical line shape obtained after such a measurement.

Expanding Eq. 3.7 in a Taylor series allows for an approximate determination of the Full Width Half Maximum (FWHM) of the TOF curve:

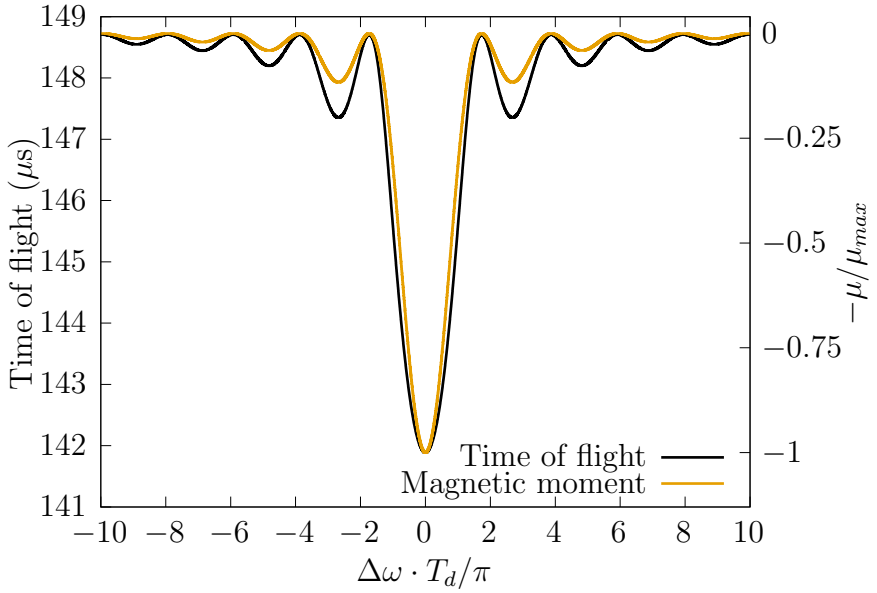

Figure 3.2: Theoretical line shape of a TOF-ICR measurement. The time-of-flight curve (dark line) is calculated inserting the magnetic moment after the quadrupolar driving (Eq. 3.7, presented in the light line) into Eq. 3.6 with reasonable $V(z)$ and $B(z)$ profiles.

$$\frac{|\boldsymbol{\mu}|}{|\boldsymbol{\mu}_{max}|} = \frac{\pi^2}{4}\mathrm{sinc}\left(\frac{\pi}{2}\sqrt{\left(\frac{\Delta\omega\cdot T_d}{\pi}\right)^2+1}\right) \simeq \left[1-\left(\frac{\Delta\omega\cdot T_d}{\pi}\right)^2\right] \implies$$
$$\implies \frac{|\boldsymbol{\mu}(\Delta\omega_{FWHM})|}{|\boldsymbol{\mu}_{max}|} = \frac{1}{2} \implies \Delta\omega_{FWHM} = \frac{\pi}{T_d\sqrt{2}} \implies$$
$$\implies FWHM = 2\Delta\nu_{FWHM} = \frac{\Delta\omega_{FWHM}}{\pi} = \frac{1}{T_d\sqrt{2}} \simeq \frac{0.8}{T_d}\,. \quad (3.8)$$

The actual statistical uncertainty of the resulting cyclotron frequency, however, is smaller than the linewidth. It is given by [86]

$$\Delta\nu_c \propto \frac{1}{T_d\sqrt{N}}\,, \quad (3.9)$$

where the exact value of the proportionality constant (around 0.9) is determined experimentally for a particular setup.

As per the resolving power, using the Rayleigh criterion for resolution (which states that the two spectra are resolved if their centers are further apart than the distance from either center to the first minimum [87]) it is given by

$$\mathcal{R} = \frac{m}{\Delta m} = \frac{\nu_c}{\Delta \nu} = \nu_c T_d \,. \tag{3.10}$$

These expressions would suggest that the performance may be increased arbitrarily by increasing the driving time T_d. However, there are experimental limits to T_d, such as the effects of collisions with any gas particles that remain in the trap, or even the disintegration of the ion in the case of radioactive species. However, the performance may be improved instead using other driving configurations:

1. Ramsey excitation: instead of a single quadrupolar RF driving pulse of length T_d, several equispaced pulses of the same length and phase coherent are applied [55]. The optimal number of pulses is two [88], and the smallest possible FWHM for a total measurement time T_d is $\sim 0.5/T_d$.

2. Octupolar excitation: if the radial electrode is split into eight segments instead of four (see Fig. 2.3), an octupolar RF driving ($V_{RF} \propto x^4 - 6x^2y^2 + y^4$) could be used to couple the magnetron and modified-cyclotron motions. The resonant frequency in this case can be shown to be $\omega_{RF} = 2\omega_c$, and the resolving power is improved by over a factor of 10 [89].

Regardless of the driving configuration, several tens of ions are needed to perform a mass measurement with TOF-ICR. Their times of flight have to be registered for a set of values of the driving frequency around the expected cyclotron frequency. This limits its applicability to SHEs, which are produced in minute quantities using fusion-evaporation reactions. The species with the lowest production rate that has been studied using this technique is ^{256}Lr [28, 29]. Due to the low production cross-section, $^{256}Lr^{2+}$ were detected at a rate of ~ 0.5 h^{-1}. With an excitation time of 200 ms, the resulting uncertainty in the cyclotron frequency was $\sim 3 \cdot 10^{-7}$.

3.1.2 Phase-Imaging Ion-Cyclotron-Resonance

The working principle of the PI-ICR technique relies on the revolution symmetry of the time-of-flight section. From that, it follows that two ions ejected from the trap at positions that form a relative angle ϕ will have detector hits that also form an angle ϕ. The *image* recorded by the detector will, however, be magnified by a factor G, that is sensitive to the configuration of the time-of-flight section. A position sensitive detector [90] can be used to determine these relative angles and, knowing

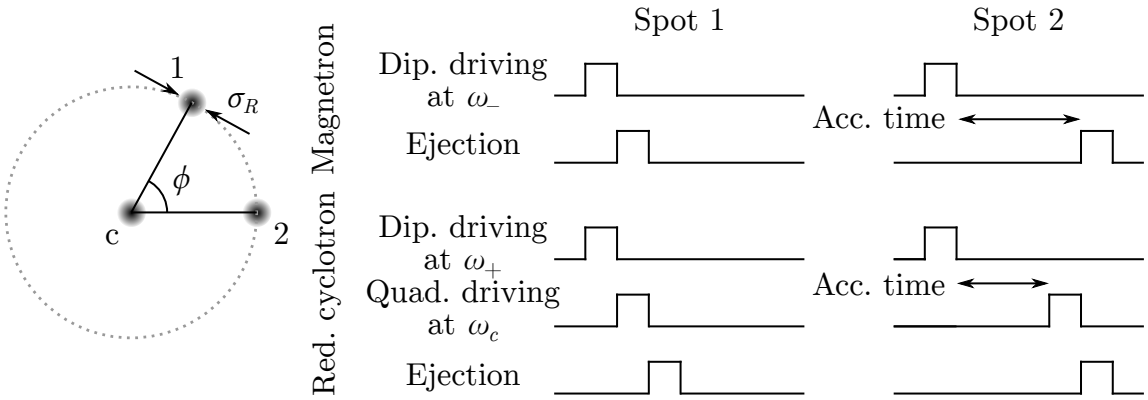

Figure 3.3: PI-ICR measurement scheme when the magnetron and reduced-cyclotron frequencies are measured separately. Left: typical image obtained for each of the frequencies. Right: measurement procedure for each of the frequencies. The center spot (which can be common) is obtained by ejecting the ion with no dipolar driving. A possible centering pulse at ω_- to compensate for e.g. misalignment between the preparation and measurement traps is omitted here.

the time difference between ejections (the *phase accumulation time* T) the frequency is then $\omega = (2\pi N + \phi)/T$, where ϕ is the *observed angle* and N is the number of full turns that the ion performs in the accumulation time. Some foreknowledge of ω is required in order to determine N. An initial measurement with a smaller accumulation time can be carried out to avoid errors in N.

In practice, the ions must be prepared consistently with the same initial radii and phase. The starting point are ions cooled at the preparation trap, as in the TOF-ICR technique. An additional pulse at ω_- could be used at the beginning of the measurement to eliminate some residual magnetron motion arising from e.g. a misalignment between traps. The ions are then driven with a dipolar RF field with well-defined amplitude, phase and duration. Since a reference is needed to determine the angle, some ions must be ejected with no driving applied. The spots recorded by the position sensitive detector are shown in the left part of Fig. 3.3.

A practical consideration has to be made when measuring the reduced-cyclotron frequency. Since $\omega_+ \gg \omega_-$, small changes in the accumulation time T can result in a wide angular distribution of ions that are otherwise prepared identically (i.e. *smearing* of the spots). Therefore, it is preferable to use a quadrupolar RF field to convert the modified-cyclotron motion to magnetron motion before ejecting the ion – the resulting magnetron phase is related to the original reduced-cyclotron phase as $\phi_- = \phi_{conv} - \phi_+$, where ϕ_{conv} is a constant (see Sec. A.2). Some foreknowledge of the free cyclotron frequency in order to perform the conversion is needed, although

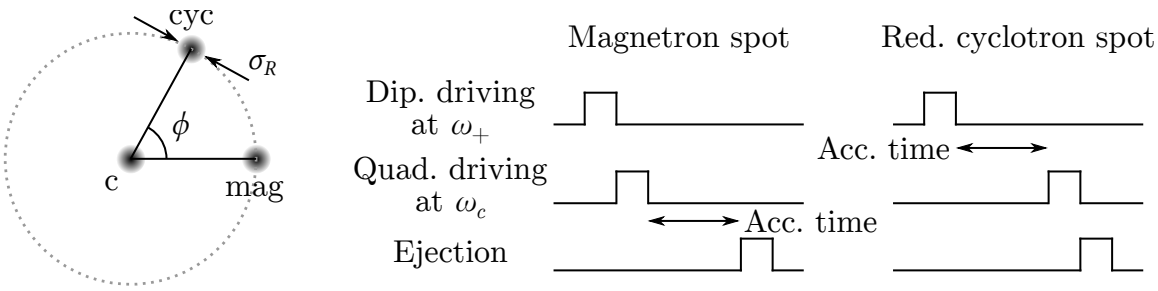

Figure 3.4: PI-ICR measurement scheme for direct free cyclotron determination. See text for details.

it does not have to be too precise, since the pulse can be made quite short, as long as the amplitude required for full conversion does not become too large.

The obvious way to use a position-sensitive detector to determine the free cyclotron frequency is to measure the magnetron and reduced-cyclotron frequencies separately, as shown in Fig. 3.3. In the case of the reduced-cyclotron frequency (bottom part of the same figure) the ϕ_{conv} term appears in both spots after the conversion, and will therefore result in a rotation that preserves the relative angle between the spots. However, an alternative exists that requires less ions.

The alternative procedure to directly determine the free cyclotron frequency was presented in Ref. [84]. In this case, the ions are driven at ω_+, and the conversion happens either soon after (*magnetron spot*) or after some accumulation time (*cyclotron spot*). In both cases, phase accumulation time is the same – the difference is in the eigenmotion that has non-zero amplitude during that time. The phase introduced by the quadrupolar pulse, ϕ_{conv}, again results in a rotation common to both spots. If the full number of turns for each of the spots is N_+ and N_-, respectively, the free cyclotron frequency is given by

$$\omega_c = \frac{2\pi\,(N_+ + N_-) + \phi_c}{T}\,, \tag{3.11}$$

where ϕ_c is the observed angle between the spots. This procedure needs half the *spots* compared to the previous one, so it is very advantageous for cases where the number of ions is limited, namely in SHEs.

Two spots can be resolved if their centers are further apart than two standard deviations, $2\sigma_R$ (see Fig. 3.4). The angle subtended by the arc $2\sigma_R$ at a radius R is $\delta\phi \simeq 2\sigma_R/R$ if $\sigma_R \ll R$. If two ions are close enough to be concerned about resolution, their magnetron frequencies will be identical, and only the spots associated to the modified-cyclotron motion will differ. The resolving power is then

$$\mathcal{R} = \frac{\omega_+}{\delta\omega_+} = \frac{2\pi N_+ + \phi_+}{\delta\phi} = \frac{2\pi N_+ + \phi_+}{2\sigma_R/R} = \frac{\omega_+ TR}{2\sigma_R} = \frac{\pi\nu_+ TR}{\sigma_R}\,, \tag{3.12}$$

which is related to that of TOF-ICR (Eq. 3.10) as

$$\frac{\mathcal{R}_{PI}}{\mathcal{R}_{TOF}} = \pi\frac{R}{\sigma_R} \tag{3.13}$$

(the difference between this value and the one given in Ref. [84] boils down to a different resolution criterion in TOF-ICR). Using the values given in the same reference ($\sigma_R \simeq 45$ µm and $R = 0.7$ mm), the improvement in resolving power is ~ 50.

Since each spot is the combination of several repetitions, ideally with a single ion each, the distribution of the *hits* will contribute to the uncertainty in the measured frequency values. Assuming that the spread in all directions is similar, i.e. $\sigma_x = \sigma_y = \sigma_R$, the uncertainty in the center coordinates of the spots scales with the number of counts as $\Delta x_i = \sigma_R/\sqrt{N}$. The coordinates of a spot with respect to the central spot are $(X_i, Y_i) = (x_i - x_c, y_i - y_c)$. Given that the center spot can be measured using the reference ion, for which the number of events is not a concern, its contribution to the uncertainty can be neglected, and $\Delta X_i \simeq \Delta x_i = \sigma_R/\sqrt{N}$. The uncertainty in the angle of each spot as obtained under quadratic error propagation is then

$$\phi = \operatorname{atan}\left(\frac{Y_i}{X_i}\right) \implies \Delta\phi = \frac{\sqrt{X_i^2\left(\Delta Y_i\right)^2 + Y_i^2\left(\Delta X_i\right)^2}}{R^2} = \frac{\Delta R}{R} = \frac{1}{\sqrt{N}}\frac{\sigma_R}{R}\,. \tag{3.14}$$

In terms of frequency, whose uncertainty is affected by both spots, this translates into

$$\Delta\omega_c = \frac{\Delta\phi_c}{T} = \frac{\sqrt{\left(\Delta\phi_1\right)^2 + \left(\Delta\phi_2\right)^2}}{T} = \frac{1}{\sqrt{N}}\frac{\sqrt{2}}{T}\frac{\sigma_R}{R}\,. \tag{3.15}$$

Comparing with the most favorable uncertainty possible in TOF-ICR (that of the two-pulse Ramsey scheme) it follows that PI-ICR can obtain the same uncertainty with reduced statistics, in particular, with $N_{TOF}/N_{PI} \simeq 25$ [84]. This is of course a great advantage when the ion of interest is a SHE.

3.2 Non-destructive detection techniques

A detection technique is *non-destructive* if a measurement does not require the ejection or otherwise loss of the ion in question. Up to date, only one non-destructive detection method has been applied in high-precision PTMS: the *induced image current detection* (of which several variants exist). It relies on the image current an ion moving within the trap induces in the trap electrodes. In the following, the method will be outlined.

3.2.1 Induced image current detection: FT-ICR

According to Ref. [91], the image charge $q_{ind}(\mathbf{r})$ induced by an ion of charge q at a position $\mathbf{r}$ on an electrode is given by

$$\frac{q_{ind}(\mathbf{r})}{q} = -\frac{\varphi(\mathbf{r})}{\Delta U} \tag{3.16}$$

(see Ref. [92] for proof), where $\Delta\varphi(\mathbf{r})$ is the change in potential at $\mathbf{r}$ when the electrode in question (the so-called *pick-up electrode*) experiences a voltage change ΔU. If a pair of infinite parallel plates, defined by $z = \pm D/2$, are assumed, the electrostatic potential between them is $\varphi(z) = U_- + (U_+ - U_+)(z + D/2)/D$, and the charge induced in e.g. the plate at $z = +D/2$ is

$$\frac{q_{ind}(\mathbf{r})}{q} = -\frac{\partial\varphi}{\partial U_+} = -\frac{z}{D} \implies Q(z) = -q\frac{z}{D}. \tag{3.17}$$

Real electrodes deviate from this geometry – a geometric factor α is introduced to account for the deviation. It is the ratio of the electric field E created by the pickup electrode and the field an infinite parallel plate at the same potential and distance would create, V/d: $\alpha = Ed/V$. The *effective distance*, defined as $D_{eff} = D/\alpha$, can be used to simplify later expressions. When the electrode geometry differs too much from the parallel-plate one, this correction does not suffice. In that case, non-linear terms in z may be needed (see e.g. Ref. [50]).

If the ion performs a harmonic motion, using Eq. 3.17, the induced current is

$$I_{ind} = \frac{\mathrm{d}q_{ind}}{\mathrm{d}t} = -q\frac{\dot{z}}{D_{eff}} = iq\omega\frac{z}{D_{eff}}, \tag{3.18}$$

where $\dot{z} = -i\omega z$ has been used in the last step. It is noteworthy that the induced

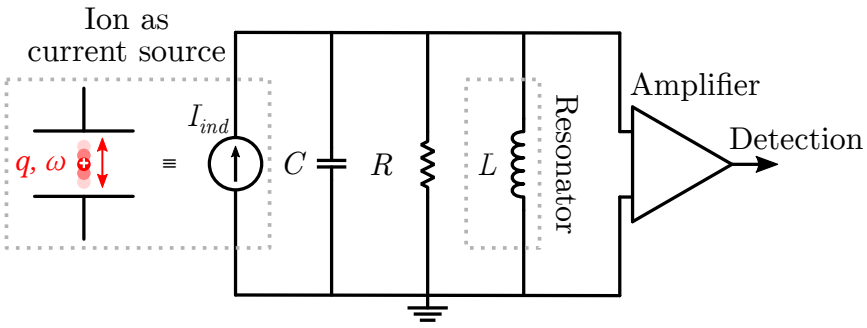

Figure 3.5: Simplified equivalent circuit for induced image current detection. The ion oscillating between the trap electrodes is modelled as a current source. The capacitance and resistor account for all parasitic capacities and losses in the system, respectively. See text for details.

current *amplitude* is proportional to the motional frequency involved.

Since α and the ratio between oscillation amplitude and trap size are bounded by one, $I \leq \omega q$. Even for the reduced-cyclotron frequency of $^{40}Ca^{+}$ in $B = 7$ T, $I_{max} \sim 3$ pA, scaling with q^2/m. Amplification is therefore crucial to be able to observe these minute currents.

Let us consider a setup where an amplifier is directly connected to the pick-up electrode. The parasitic capacitances of the trap electrodes and other elements are merged into an equivalent capacitance C, and losses also merged into an equivalent resistor R. Assuming an ideal amplifier (i.e. infinite input impedance) the equivalent impedance of the circuit is

$$\mathcal{Z} = \frac{1}{\frac{1}{R} + i\omega C}\,. \tag{3.19}$$

This is a low pass filter, since at high frequencies the capacitor acts as a shortcut. More precisely, the cutoff frequency (frequency at which the power dissipated at the resistor is half of the maximum, RI_{ind}^2) can be calculated as

$$P = VI_R = \frac{V^2}{R} = \frac{I_{ind}^2\,|\mathcal{Z}|^2}{R} = \frac{RI_{ind}^2}{2} \implies \frac{|\mathcal{Z}|^2}{R^2} = \frac{1}{2} \implies \omega = \frac{1}{RC}\,. \tag{3.20}$$

To avoid this suppression at higher frequencies, a *resonator* in the form of a coil of inductance L[1] is introduced [59, 93]. Now the circuit is that of Fig. 3.5, and the combined impedance is

[1]The actual physical component does not have to be a coil, see e.g. Refs. [35, 36, 37].

$$\mathcal{Z} = \frac{1}{\frac{1}{R} + i\left(\omega C - \frac{1}{\omega L}\right)}\,, \tag{3.21}$$

whose squared modulus has a maximum $|\mathcal{Z}|^2 = R^2$ at $\omega_{LC} = 1/\sqrt{LC}$.

The bandwidth $\delta\omega$ is usually defined, much as the cutoff frequency of the low-pass filter, as the distance between the frequencies at which the dissipated power is half of the maximum dissipated power:

$$\frac{|\mathcal{Z}(\omega)|^2}{R^2} = \frac{1}{2} \implies |\omega| = \frac{\sqrt{\frac{1}{R^2} + 4\frac{C}{L}} \pm \frac{1}{R}}{2C} \implies \delta\omega = \frac{1}{RC}\,, \tag{3.22}$$

The Q factor is then

$$Q = \frac{\omega}{\delta\omega} = \omega_{LC} RC = R\sqrt{\frac{L}{C}}\,. \tag{3.23}$$

The RMS voltage in resonance ($\mathcal{Z} = R$), that is, the *signal*, is

$$V_{RMS}^{(signal)} = \frac{R\,|I_{ind}|}{\sqrt{2}}\,. \tag{3.24}$$

The thermal noise at the resistor R in the relevant frequency band is calculated from the Johnson-Nyquist noise's Power Spectral Density (PSD) [94] as

$$V_{RMS}^{(noise)} = \sqrt{\int \mathrm{PSD}\,\mathrm{d}\nu} = \sqrt{\mathrm{PSD}\,\Delta\nu} = \sqrt{4k_B T R}\sqrt{\Delta\nu}\,, \tag{3.25}$$

since the PSD of thermal noise is constant (except at very high frequencies). Here, k_B is Boltzmann's constant, T is the temperature and $\Delta\nu$ is the width of the ion signal as seen in the resulting spectrum, that is, the largest value between the actual signal width or the resolution after performing the Fourier transform of the waveform. Assuming the latter dominates, $\Delta\nu$ is the inverse of the measurement time T_{meas}. The resulting Signal to Noise Ratio (SNR) is therefore

$$SNR = \frac{|I_{ind}|}{\sqrt{8k_B T}}\sqrt{R}\sqrt{T_{meas}} = \frac{|I_{ind}|}{\sqrt{8k_B T}}\sqrt{\frac{Q}{\omega_{LC} C}}\sqrt{T_{meas}}\,. \tag{3.26}$$

This gives an idea on how one can improve the sensitivity of the technique. Two very important factors are the temperature and the capacitance. This means that sensitivity can be improved with cryogenic amplification and with short distances

between electrodes and detection board.

None of this, however, has considered the effects of the detection on the ion itself. A simple energetic argument shows that, since the ion motion is the only source of energy in the circuit shown in Fig. 3.5, the amplitude of the ion's oscillation must go down over time. The voltage drop due to the presence of the detector creates a force on the ion that has two effects [93]: resistive cooling of the ion motion (caused by the real part of $\mathcal{Z}$) and a frequency shift, called *image current shift*, caused by the imaginary part of $\mathcal{Z}$. The ion's equation of motion, assuming axial pick-up and including the voltage drop, is

$$\ddot{z} + \omega_z^2 z = \frac{F_e}{m} = -q\frac{V}{mD_{eff}} = -q\frac{\mathcal{Z}I_{ind}}{mD_{eff}}\,. \tag{3.27}$$

Using Eq. 3.18,

$$\mathcal{Z}I_{ind} = -\frac{q\mathrm{Re}\left(\mathcal{Z}\right)}{D_{eff}}\dot{z} - \frac{q\omega\mathrm{Im}\left(\mathcal{Z}\right)}{D_{eff}}z\,, \tag{3.28}$$

and therefore

$$\ddot{z} + \frac{q^2\mathrm{Re}\left(\mathcal{Z}\right)}{mD_{eff}^2}\dot{z} + \left(\omega_z^2 + \frac{q^2\omega\mathrm{Im}\left(\mathcal{Z}\right)}{mD_{eff}^2}\right)z = 0\,, \tag{3.29}$$

which is the equation of a damped harmonic oscillator. The impedance can be rewritten as

$$\mathcal{Z} = \frac{1}{\frac{1}{R} + i\left(\omega C - \frac{1}{\omega L}\right)}\frac{\frac{1}{R} - i\left(\omega C - \frac{1}{\omega L}\right)}{\frac{1}{R} - i\left(\omega C - \frac{1}{\omega L}\right)} = \frac{\frac{1}{R} + i\left(\frac{1}{\omega L} - \omega C\right)}{\frac{1}{R^2} + \left(\omega C - \frac{1}{\omega L}\right)^2}\,. \tag{3.30}$$

Therefore, $\mathrm{Im}\left(\mathcal{Z}\right) \propto \left(\frac{1}{\omega L} - \omega C\right)$, and the direction of the frequency shift depends on whether $\omega \lessgtr \omega_{LC}$. On the other hand, $\mathrm{Re}\left(\mathcal{Z}\right) > 0\,\forall\,\omega$, that is, the ions are always cooled. Assuming that the oscillator is underdamped, the result is a harmonic oscillator whose amplitude decays[2] with time constant

$$T_c = \frac{2mD_{eff}^2}{q^2\mathrm{Re}\left(\mathcal{Z}\right)}\,. \tag{3.31}$$

Once the ion has been cooled (*thermalized*), the only remaining source of energy is the thermal noise of the resistor R. In order to study the behavior of the ion-

[2] At this point the equality $\dot{z} = -i\omega z$ used in Eq. 3.18 becomes an approximation (the speed due to the amplitude decay is neglected with respect to that of the oscillation itself.)

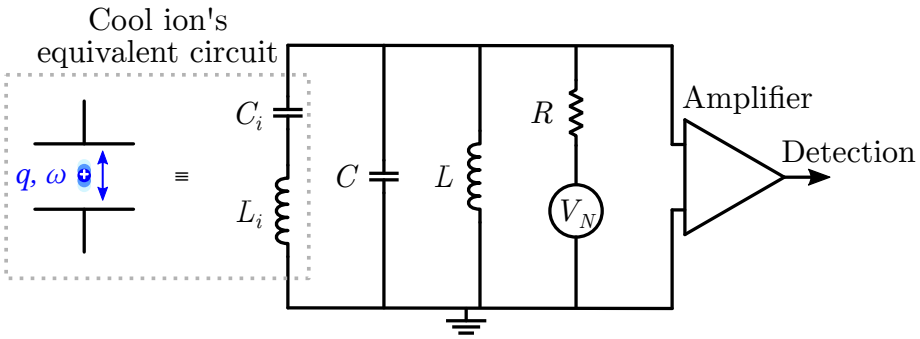

Figure 3.6: Simplified circuit for induced current detection including ion-detector interaction. The ion is substituted for a series LC circuit, and the thermal noise of the resistor R is explicitly shown. See text for details.

detector combined system, the ion can be modeled as an equivalent circuit [95]. Using Eq. 3.18 the equation of motion can be rewritten using the current as the dependent variable:

$$\frac{mD_{eff}^2}{q^2}\frac{\mathrm{d}I_{ind}}{\mathrm{d}t} + \omega_z^2\frac{mD_{eff}^2}{q^2}\int I_{ind}\mathrm{d}t = V\,. \tag{3.32}$$

The voltage drops at an inductance L and a capacitance C through which a current I flows are $L\mathrm{d}I/\mathrm{d}t$ and $Q/C = \int I\mathrm{d}t/C$, respectively. This allows the modeling of the ion as a series LC circuit with $L_i = mD_{eff}^2/q^2$ and $C_i = 1/\omega_z^2 L_i$. The full equivalent circuit is shown in Fig. 3.6. The impedance is

$$\mathcal{Z} = \frac{1}{\frac{1}{R} + i\left[\left(\omega C - \frac{1}{\omega L}\right) - \left(\omega L_i - \frac{1}{\omega C_i}\right)^{-1}\right]}\,. \tag{3.33}$$

At the ion's resonant frequency, $\omega_i = 1/\sqrt{L_i C_i} = \omega_z$, $\left(\omega L_i - \frac{1}{\omega C_i}\right) = 0$. The amplifier input is shorted by the ion's equivalent LC circuit. This is known as a *dip*. Its width for a single ion is [95]

$$\Delta\nu = \frac{R}{L_i}\,. \tag{3.34}$$

There is an additional way to observe a dip in the signal without the attainment of equilibrium between the ion and the oscillator. If the oscillator is energized, energy will be transferred to the ion and a dip will still form until the oscillator's energy is dissipated in the circuit [37].

Both of the detection methods outlined before only allow the direct detection of one

of the eigenfrequencies (usually the axial). There are several methods to translate this into a mass measurement (see e.g. Ref. [96]). Most often, the two radial eigenfrequencies are determined through the axial motion by driving them to a certain radius and then coupling to the axial motion using a quadrupolar drive. The free cyclotron frequency can then be calculated from the three eigenfrequencies using the invariance theorem (Eq. 2.18b).

Mass measurements obtained using induced image current detection are the most precise to date (see e.g. Ref. [31] for a recent measurement with parts-per-trillion relative uncertainty). The main issue when it comes to SHEs, however, is sensitivity – the technique has not been applied so far to mass measurements of single ions with mass-to-charge ratios above ∼65 u/e (see e.g. Ref. [32]). This is not enough to study species in the SHE region of the nuclear chart, since the charge state distribution after cooling and trapping is not expected to reach higher than 2+ or 3+ [33]. Developments on this front are, however, ongoing, both in terms of more sensitive detectors [35, 36, 37, 38] or alternative cooling methods [39, 34].

Chapter 4

The unbalanced two-ion crystal

The previous chapter showed how different PTMS techniques determine a mass value by measuring a trapped ion's motional frequencies (or linear combinations). The detection methods employed are either destructive or have not been proven for single ions with mass-to-charge ratios over $\sim 65\,\mathrm{u/e}$. Doppler cooling enables the detection of a single ion through the photons it scatters – however, only a few species can be observed in this way. There has been significant work devoted to the use of one of these ions as an auxiliary system to cool [39] and/or study the properties [40, 41] of an ion that cannot be observed optically in a direct manner.

In the same spirit, Ref. [43] proposed the use of a laser-cooled ion (the *sensor ion*) as a detector to measure the motional frequencies (and therefore the mass) of a generic *target ion*. This method would have the ions stored in physically separated traps and interacting through the current induced in a common electrode. The resulting coupling is small, which comes with advantages (the target ion's motion is not perturbed), but also requires an extremely well controlled setup, in particular, with very low heating rates. Progress on the construction and commissioning of the first prototype of the dual trap system was reported in Refs. [44, 45]. A new concept is currently being studied.

In this Chapter an alternative to the previous technique is developed. The target and sensor ions are stored in the same trap, experiencing an interaction of the same magnitude as the trapping field. When the sensor ion is laser cooled, an *unbalanced*[1] Coulomb crystal is formed. The eigenmotions of the crystal will be characterized (generalizing the results that were presented in Ref. [97]), and a relationship between the crystal's eigenfrequencies and the individual ions' free cyclotron frequencies will

[1] This Chapter refers to *unbalanced* two-ion crystals when the ions are of different species.

be presented.

The work presented in this Chapter rests on several previous studies. For example, Ref. [98], where the dynamics of *balanced* Coulomb crystals of two or three ions were studied. Some mass measurement techniques based on induced current detection also use two simultaneously trapped ions, in this case with the goal of minimizing the systematic uncertainties due to magnetic field fluctuations (see Ref. [99]). In this case the ions are placed at opposite ends of a common magnetron orbit with a large radius, so that the distance among them makes the frequency shifts arising from the Coulomb interaction negligible. Ref. [100] studies two-dimensional Penning trap arrays, where a single ion is placed on each trap, and the interaction among these is studied. The mathematical description is often equivalent to that of the unbalanced two-ion crystal. Furthermore, the *generalized invariance theorem* derived for the array also holds for the case studied here. Last, but not least, Ref. [101] presents a technique to use optical detection for mass measurements in Paul traps. Its applicability in Penning traps was discussed in Ref. [102].

4.1 Modes of motion of an unbalanced two-ion crystal

The Lagrangian function of the unbalanced two-ion crystal is comprised of the Lagrangian functions of the two individual ions (Eq. 2.9), which will be referred to as 'target' and 'sensor' ions, minus the interaction potential. If the charge and mass ratios ($\kappa = q_t/q_s$ and $\mu = m_t/m_s$, respectively) are introduced, the crystal's Lagrangian function can be written in terms of the sensor ion's axial (ω_{zs}) and free cyclotron (ω_{cs}) frequencies as

$$\begin{aligned}\mathcal{L}_{crystal} = &\frac{1}{2}\mu m_s \dot{\mathbf{r}}_t^2 - \kappa\frac{1}{4}m_s\omega_{zs}^2\left(2z_t^2 - x_t^2 - y_t^2\right) - \kappa\frac{1}{2}m_s\omega_{cs}\left(\dot{x}_t y_t - \dot{y}_t x_t\right)\\ &+ \frac{1}{2}m_s\dot{\mathbf{r}}_t^2 - \frac{1}{4}m_s\omega_{zs}^2\left(2z_s^2 - x_s^2 - y_s^2\right) - \frac{1}{2}m_s\omega_{cs}\left(\dot{x}_s y_s - \dot{y}_s x_s\right)\\ &- \frac{1}{4\pi\varepsilon_0}\frac{\kappa q_s^2}{|\mathbf{r}_t - \mathbf{r}_s|}\,. \qquad (4.1)\end{aligned}$$

Using the sensor ion's eigenfrequencies instead of the trap parameters (U, B and d_0) is convenient to link the crystal's eigenfrequencies with those of the individual

ions.

The resulting equations of motion, obtained using the Euler-Lagrange equation, are

$$\mu\ddot{x}_t = \kappa\frac{1}{2}\omega_{zs}^2 x_t + \kappa\omega_{cs}\dot{y}_t + \kappa\frac{1}{m_s}\frac{q_s^2}{4\pi\varepsilon_0}\frac{(x_t - x_s)}{|\mathbf{r}_t - \mathbf{r}_s|^3} \tag{4.2a}$$

$$\ddot{x}_s = \frac{1}{2}\omega_{zs}^2 x_s + \omega_{cs}\dot{y}_s - \kappa\frac{1}{m_s}\frac{q_s^2}{4\pi\varepsilon_0}\frac{(x_t - x_s)}{|\mathbf{r}_t - \mathbf{r}_s|^3} \tag{4.2b}$$

$$\mu\ddot{y}_t = \kappa\frac{1}{2}\omega_{zs}^2 y_t - \kappa\omega_{cs}\dot{x}_t + \kappa\frac{1}{m_s}\frac{q_s^2}{4\pi\varepsilon_0}\frac{(y_t - y_s)}{|\mathbf{r}_t - \mathbf{r}_s|^3} \tag{4.2c}$$

$$\ddot{y}_s = \frac{1}{2}\omega_{zs}^2 y_s - \omega_{cs}\dot{x}_s - \kappa\frac{1}{m_s}\frac{q_s^2}{4\pi\varepsilon_0}\frac{(y_t - y_s)}{|\mathbf{r}_t - \mathbf{r}_s|^3} \tag{4.2d}$$

$$\mu\ddot{z}_t = \kappa\omega_{zs}^2 z_t + \kappa\frac{1}{m_s}\frac{q_s^2}{4\pi\varepsilon_0}\frac{(z_t - z_s)}{|\mathbf{r}_t - \mathbf{r}_s|^3} \tag{4.2e}$$

$$\ddot{z}_s = \omega_{zs}^2 z_s - \kappa\frac{1}{m_s}\frac{q_s^2}{4\pi\varepsilon_0}\frac{(z_t - z_s)}{|\mathbf{r}_t - \mathbf{r}_s|^3}\,. \tag{4.2f}$$

These equations can be partially solved if the two ions are identical ($\mu = \kappa = 1$). Introducing the center of mass coordinates, $\mathbf{R} = \mathbf{r}_t - \mathbf{r}_s$[2], the Coulomb term cancels out, and the equations of motion are identical to those of the single ion (Eq. 2.10). The relative motion, however, remains unsolved, as does the general case $\mu \neq 1$. Some approximations will be needed to find the crystal's modes of motion.

In order to simplify the Coulomb interaction, an equilibrium configuration of the crystal needs to be found. The electrostatic potential can then be expanded to second order around this configuration. This approximated model of the crystal can be solved, and the effects of the neglected terms can be considered afterwards as a perturbation.

There are three equilibrium configurations for a two-ion crystal, depending on the trap parameters (specified through ω_{zs} and ω_{cs} in this case) and, to a lesser extent, the angular momentum of the crystal. A given trap configuration can be specified for the purposes of this work through the frequency ratio $r = \omega_{zs}/\omega_{cs}$ (see Sec. 4.1.4). For a balanced two-ion crystal [98]

[2]In general, to improve readability, this Thesis will differentiate quantities that refer to a single ion from those that refer to the crystal as a whole with capitalization. For example, individual ions' positions, amplitudes and frequencies have been labeled using $\mathbf{r}$, ρ and ω, respectively. The crystal's coordinates (e.g. center of mass coordinates), amplitudes and frequencies will be labeled as R, P and Ω. Greek letters will be used to label quantities of the crystal's modes of motion, and Latin letters to label quantities of the individual ions.

- The ions line up with the z axis if $\omega_{zs} < \omega_1 = \sqrt{\omega_{cs}^2 - 2\omega_{zs}^2} \implies \omega_{zs}/\omega_{cs} < 1/\sqrt{3}$, or

- they orbit within the radial plane if $\omega_{zs} > \omega_1 \implies \omega_{zs}/\omega_{cs} > 1/\sqrt{3}$, or

- the crystal is tilted if $\omega_{zs} < \omega_1$ and the ions have some rotational energy.

If the crystal is comprised of two ions with charge $q_t = \kappa q_s$ and mass $m_t = \mu m_s$, the orientation criterion is instead $r \lessgtr \sqrt{\kappa/\mu}/\sqrt{3}$. If the crystal is unbalanced, it is only logical to assume that the change of orientation occurs somewhere in between $r = 1/\sqrt{3}$ and $r = \sqrt{\kappa/\mu}/\sqrt{3}$. The point is moot, however, because it will be shown that a new stability criterion, stricter than both, will arise.

To perform laser cooling it is desirable that the equilibrium configuration keeps the ions stationary; therefore, the axial orientation is chosen, and the trap potentials will be tuned in consequence. All that remains to determine the equilibrium positions is to zero out the electrostatic field's gradient:

$$\nabla V_{crystal}\big|_{eq} = 0 \implies \begin{cases} m_s\omega_{zs}^2 z_s + \frac{\kappa q_s^2}{4\pi\varepsilon_0}\frac{z_t - z_s}{|z_t - z_s|^3} = 0 \\ \kappa m_s\omega_{zs}^2 z_t - \frac{\kappa q_s^2}{4\pi\varepsilon_0}\frac{z_t - z_s}{|z_t - z_s|^3} = 0 \end{cases} \implies$$

$$\implies \begin{cases} z_s = -\kappa z_t \\ d = |z_t - z_s| = \left[\frac{q_s^2/4\pi\varepsilon_0}{m_s\omega_{zs}^2}(\kappa + 1)\right]^{1/3} \end{cases} . \quad (4.3)$$

The ions are separated by a distance d, with the sensor ion a factor κ further away from the trap center. Abusing the notation, from this point onwards all coordinates are relative to the equilibrium configuration, i.e., $z_t := z_t - d/(\kappa + 1)$ and $z_s := z_s + d\kappa/(\kappa + 1)$. The constants accompanying the Coulomb interaction will also be rewritten as $\kappa q_s^2/4\pi\varepsilon_0 = m_s\omega_{zs}^2 d^3\kappa/(\kappa + 1)$.

Around this equilibrium position the potential can be approximated by its expansion to second order. The zero order term (a shift in potential) can be ignored, and the first order vanishes at the equilibrium position. Therefore, only the second order term contributes. It can be written in terms of the Hessian matrix of the potential at the equilibrium position, $\mathbf{H}V_{crystal}\big|_{eq}$ ($\mathbf{H}$ in short), as

$$
\begin{aligned}
V_{crystal} &\simeq \frac{1}{2}\begin{pmatrix} x_t & x_s & y_t & y_s & z_t & z_s \end{pmatrix} \mathbf{H} \begin{pmatrix} x_t & x_s & y_t & y_s & z_t & z_s \end{pmatrix}^{\top} \\
&\simeq \frac{1}{4} m_s \omega_{zs}^2 \left\{ - \left[\left(\kappa + \frac{2\kappa}{\kappa+1} \right) x_t^2 - \frac{2\kappa}{\kappa+1} 2 x_t x_s + \left(1 + \frac{2\kappa}{\kappa+1} \right) x_s^2 \right] \right. \\
&\qquad - \left[\left(\kappa + \frac{2\kappa}{\kappa+1} \right) y_t^2 - \frac{2\kappa}{\kappa+1} 2 y_t y_s + \left(1 + \frac{2\kappa}{\kappa+1} \right) y_s^2 \right] \\
&\qquad \left. + 2 \left[\left(\kappa + \frac{2\kappa}{\kappa+1} \right) z_t^2 - \frac{2\kappa}{\kappa+1} 2 z_t z_s + \left(1 + \frac{2\kappa}{\kappa+1} \right) z_s^2 \right] \right\} ,
\end{aligned}
\tag{4.4}
$$

where $\top$ denotes transposition. The Lagrangian is then

$$
\begin{aligned}
\mathcal{L}_{crystal} &= \frac{1}{2}\mu m_s \dot{\mathbf{r}}_t^2 + \frac{1}{2} m_s \dot{\mathbf{r}}_s^2 - \kappa \frac{1}{2} m_s \omega_{cs} \left(\dot{x}_t y_t - \dot{y}_t x_t \right) - \frac{1}{2} m_s \omega_{cs} \left(\dot{x}_s y_s - \dot{y}_s x_s \right) \\
&\quad + \frac{1}{4} m_s \omega_{zs}^2 \left\{ - \left[\left(\kappa + \frac{2\kappa}{\kappa+1} \right) x_t^2 - \frac{2\kappa}{\kappa+1} 2 x_t x_s + \left(1 + \frac{2\kappa}{\kappa+1} \right) x_s^2 \right] \right. \\
&\qquad - \left[\left(\kappa + \frac{2\kappa}{\kappa+1} \right) y_t^2 - \frac{2\kappa}{\kappa+1} 2 y_t y_s + \left(1 + \frac{2\kappa}{\kappa+1} \right) y_s^2 \right] \\
&\qquad \left. + 2 \left[\left(\kappa + \frac{2\kappa}{\kappa+1} \right) z_t^2 - \frac{2\kappa}{\kappa+1} 2 z_t z_s + \left(1 + \frac{2\kappa}{\kappa+1} \right) z_s^2 \right] \right\} ,
\end{aligned}
\tag{4.5}
$$

and the equations of motion are

$$
\mu m_s \ddot{x}_t = \frac{1}{2} m_s \omega_{zs}^2 \left(\kappa + \frac{2\kappa}{\kappa+1} \right) x_t + \kappa m_s \omega_{cs} \dot{y}_t - \frac{1}{2} m_s \omega_{zs}^2 \frac{2\kappa}{\kappa+1} x_s \tag{4.6a}
$$

$$
m_s \ddot{x}_s = \frac{1}{2} m_s \omega_{zs}^2 \left(1 + \frac{2\kappa}{\kappa+1} \right) x_s + m_s \omega_{cs} \dot{y}_s - \frac{1}{2} m_s \omega_{zs}^2 \frac{2\kappa}{\kappa+1} x_t \tag{4.6b}
$$

$$
\mu m_s \ddot{y}_t = \frac{1}{2} m_s \omega_{zs}^2 \left(\kappa + \frac{2\kappa}{\kappa+1} \right) y_t - \kappa m_s \omega_{cs} \dot{x}_t - \frac{1}{2} m_s \omega_{zs}^2 \frac{2\kappa}{\kappa+1} y_s \tag{4.6c}
$$

$$
\ddot{m}_s y_s = \frac{1}{2} m_s \omega_{zs}^2 \left(1 + \frac{2\kappa}{\kappa+1} \right) y_s - m_s \omega_{cs} \dot{x}_s - \frac{1}{2} m_s \omega_{zs}^2 \frac{2\kappa}{\kappa+1} y_t \tag{4.6d}
$$

$$
\mu m_s \ddot{z}_t = - \left(\kappa + \frac{2\kappa}{\kappa+1} \right) \omega_{zs}^2 z_t + m_s \omega_{zs}^2 \frac{2\kappa}{\kappa+1} z_s \tag{4.6e}
$$

$$
\ddot{m}_s z_s = - m_s \omega_{zs}^2 \left(1 + \frac{2\kappa}{\kappa+1} \right) z_s + m_s \omega_{zs}^2 \frac{2\kappa}{\kappa+1} z_t \, . \tag{4.6f}
$$

These are equivalent to the equations presented in Ref. [97][3] for $\kappa = 1$. To write these in matrix form in a compact manner, it is useful to define the matrices

$$\mathbb{M} = m_s \begin{pmatrix} \mu & 0 & 0 & 0 & 0 & 0 \\ 0 & 1 & 0 & 0 & 0 & 0 \\ 0 & 0 & \mu & 0 & 0 & 0 \\ 0 & 0 & 0 & 1 & 0 & 0 \\ 0 & 0 & 0 & 0 & \mu & 0 \\ 0 & 0 & 0 & 0 & 0 & 1 \end{pmatrix} \tag{4.7}$$

(known as the *mass matrix*),

$$\mathbb{B} = m\omega_{cs} \begin{pmatrix} 0 & 0 & \kappa & 0 & 0 & 0 \\ 0 & 0 & 0 & 1 & 0 & 0 \\ -\kappa & 0 & 0 & 0 & 0 & 0 \\ 0 & -1 & 0 & 0 & 0 & 0 \\ 0 & 0 & 0 & 0 & 0 & 0 \\ 0 & 0 & 0 & 0 & 0 & 0 \end{pmatrix}, \tag{4.8}$$

which captures the effects of the magnetic field,

$$\mathbb{V} = \frac{1}{2} m_s \omega_{zs}^2 \begin{pmatrix} \kappa & 0 & 0 & 0 & 0 & 0 \\ 0 & 1 & 0 & 0 & 0 & 0 \\ 0 & 0 & \kappa & 0 & 0 & 0 \\ 0 & 1 & 0 & 1 & 0 & 0 \\ 0 & 1 & 0 & 0 & -2\kappa & 0 \\ 0 & 1 & 0 & 0 & 0 & -2 \end{pmatrix}, \tag{4.9}$$

which accounts for the effects of the trapping field, and

$$\mathbb{K} = \frac{1}{2} m_s \omega_{zs}^2 \frac{2\kappa}{\kappa + 1} \begin{pmatrix} 1 & -1 & 0 & 0 & 0 & 0 \\ -1 & 1 & 0 & 0 & 0 & 0 \\ 0 & 0 & 1 & -1 & 0 & 0 \\ 0 & 0 & -1 & 1 & 0 & 0 \\ 0 & 0 & 0 & 0 & -2 & 2 \\ 0 & 0 & 0 & 0 & 2 & -2 \end{pmatrix}, \tag{4.10}$$

[3]The order of the equations has changed, however, to instead match that of Ref. [100]. That makes Secs. 4.1.5 and 4.1.6 easier to read.

which comprises all terms arising from the Coulomb interation. Eqs. 4.6 can then simply be written as

$$\mathbb{M}\ddot{\mathbf{r}}^{\top} - \mathbb{B}\dot{\mathbf{r}}^{\top} - (\mathbb{V} + \mathbb{K})\,\mathbf{r}^{\top} = \mathbb{O}_{6\times 1}\,, \tag{4.11}$$

where $\mathbf{r} = (x_t, x_s, y_t, \dots)$ contains all the coordinates and again $\mathbb{O}$ is the zero matrix and $\top$ denotes transposition. Introducing the matrix $\mathbb{E} = \mathbb{V} + \mathbb{K}$ and the ansatz $\mathbf{r} = \boldsymbol{\rho} e^{-i\Omega t}$, a new quadratic eigenvalue problem results:

$$\left[\Omega^2\mathbb{M} - i\Omega\mathbb{B} + \mathbb{E}\right]\boldsymbol{\rho}^{\top} = \mathbb{O}_{6\times 1}\,. \tag{4.12}$$

Since the radial and axial parts of the problem are decoupled in this approximation, they can be studied separately. Dividing by $m_s\omega_{cs}^2$ and $m_s\omega_{zs}^2$, respectively, two quadratic eigenvalue problems are obtained:

$$\begin{aligned}
&\left[\left(\frac{\Omega}{\omega_{cs}}\right)^2\begin{pmatrix}\mu & 0 & 0 & 0\\ 0 & 1 & 0 & 0\\ 0 & 0 & \mu & 0\\ 0 & 0 & 0 & 1\end{pmatrix} - i\left(\frac{\Omega}{\omega_{cs}}\right)\begin{pmatrix}0 & 0 & \kappa & 0\\ 0 & 0 & 0 & 1\\ -\kappa & 0 & 0 & 0\\ 0 & -1 & 0 & 0\end{pmatrix}\right.\\
&\qquad\left.+\frac{1}{2}\left(\frac{\omega_{zs}}{\omega_{cs}}\right)^2\begin{pmatrix}\kappa+\frac{2\kappa}{\kappa+1} & -\frac{2\kappa}{\kappa+1} & 0 & 0\\ -\frac{2\kappa}{\kappa+1} & 1+\frac{2\kappa}{\kappa+1} & 0 & 0\\ 0 & 0 & \kappa+\frac{2\kappa}{\kappa+1} & -\frac{2\kappa}{\kappa+1}\\ 0 & 0 & -\frac{2\kappa}{\kappa+1} & 1+\frac{2\kappa}{\kappa+1}\end{pmatrix}\right]\cdot\begin{pmatrix}\rho_{x,t}\\ \rho_{x,s}\\ \rho_{y,t}\\ \rho_{y,s}\end{pmatrix} =\\
&\qquad = Q_r\left(\frac{\Omega}{\omega_{cs}}\right)\cdot\begin{pmatrix}\rho_{x,t}\\ \rho_{x,s}\\ \rho_{y,t}\\ \rho_{y,s}\end{pmatrix} = \mathbb{O}_{4\times 1}
\end{aligned} \tag{4.13a}$$

$$\begin{aligned}
&\left[\left(\frac{\Omega}{\omega_{zs}}\right)^2\begin{pmatrix}\mu & 0\\ 0 & 1\end{pmatrix} + \begin{pmatrix}-\left(\kappa+\frac{2\kappa}{\kappa+1}\right) & \frac{2\kappa}{\kappa+1}\\ \frac{2\kappa}{\kappa+1} & -\left(1+\frac{2\kappa}{\kappa+1}\right)\end{pmatrix}\right]\cdot\begin{pmatrix}\rho_{zt}\\ \rho_{zs}\end{pmatrix} =\\
&\qquad = Q_z\left(\frac{\Omega}{\omega_{zs}}\right)\cdot\begin{pmatrix}\rho_{z,t}\\ \rho_{z,s}\end{pmatrix} = \begin{pmatrix}0\\ 0\end{pmatrix}
\end{aligned} \tag{4.13b}$$

Note that the only trap-dependent quantity is the ratio $r = \omega_{zs}/\omega_{cs}$ acompanying

the last term in $Q_r\,(\Omega/\omega_{cs})$.

These eigenvalue problems will be solved and discussed in the following, using the procedures introduced in Chapter 2 (see in particular Eqs. 2.12 and 2.13). The modes will be characterized by their frequency and their *amplitude ratio*, that is, the ratio of oscillation amplitudes of the individual ions when the mode in question is the only mode in play. The amplitude ratio can be found simply by dividing the coefficients of the eigenvector of the mode in question.

Before the general case is addressed, however, the case $\mu = \kappa = 1$ (balanced crystal) will be studied first. Although it is irrelevant from the mass spectrometry point of view, it is much easier to solve, and it gives some insight into the general case. In particular, it will shed some light into the stability condition that arises for the stretch radial motions.

4.1.1 The balanced crystal

The axial eigenvalue problem (Eq. 4.13b) for a balanced crystal takes the form

$$\left[\left(\frac{\Omega}{\omega_{cs}}\right)^2\begin{pmatrix}1 & 0\\ 0 & 1\end{pmatrix}+\begin{pmatrix}-2 & 1\\ 1 & -2\end{pmatrix}\right]\cdot\begin{pmatrix}\rho_{zt}\\ \rho_{zs}\end{pmatrix}=Q_z\left(\frac{\Omega}{\omega_{cs}}\right)\cdot\begin{pmatrix}\rho_{z,t}\\ \rho_{z,s}\end{pmatrix}=\mathbb{O}_{2\times1}\,. \tag{4.14}$$

The resulting eigenvalues are

$$\det\left[Q_z\left(\frac{\Omega}{\omega_{cs}}\right)\right]=0\implies\left(\frac{\Omega_z^{\pm}}{\omega_{zs}}\right)^2=2\pm1\implies\left|\Omega_z^{\pm}\right|=\sqrt{2\pm1}\,\omega_{zs}\,. \tag{4.15}$$

Note that each frequency is a solution with positive or negative sign. The associated eigenvectors are

$$Q_r\left(\frac{\Omega^{\pm}}{\omega_{cs}}\right)\cdot\begin{pmatrix}\rho_{z,t}^{\pm}\\ \rho_{z,s}^{\pm}\end{pmatrix}=\mathbb{O}_{2\times1}\implies\begin{pmatrix}\rho_{z,t}^{\pm}\\ \rho_{z,s}^{\pm}\end{pmatrix}=\frac{1}{\sqrt{2}}\begin{pmatrix}1\\ \mp1\end{pmatrix}\,. \tag{4.16}$$

Therefore, there are two axial motions, and the axial coordinates of the individual ions can be written in terms of those:

$$\left.\begin{aligned} Z^+ &= \mathrm{P}_z^+ \cos\left(\Omega_z^+ t + \phi_z^+\right) \\ Z^- &= \mathrm{P}_z^- \cos\left(\Omega_z^- t + \phi_z^-\right) \end{aligned}\right\} \implies$$
$$\implies \begin{pmatrix} z_t \\ z_s \end{pmatrix} = \frac{1}{\sqrt{2}} \begin{pmatrix} 1 & 1 \\ -1 & 1 \end{pmatrix} \cdot \begin{pmatrix} Z^+ \\ Z^- \end{pmatrix} = \frac{1}{\sqrt{2}} \begin{pmatrix} \mathrm{P}_z^+ \cos\left(\Omega_z^+ t + \phi_z^+\right) + \mathrm{P}_z^- \cos\left(\Omega_z^- t + \phi_z^-\right) \\ -\mathrm{P}_z^+ \cos\left(\Omega_z^+ t + \phi_z^+\right) + \mathrm{P}_z^- \cos\left(\Omega_z^- t + \phi_z^-\right) \end{pmatrix} . \tag{4.17}$$

If only the mode of frequency $\Omega_z^- = \omega_{zs}$ is excited, both ions oscillate in phase with the same amplitude. In that case, the center of mass of the ions oscillates, while the relative distance among them remains constant. Therefore, the mode of frequency Ω_z^- is called *axial center-of-mass mode*. If instead only the mode of frequency $\Omega_z^+ = \sqrt{3}\omega_{zs}$, the relative distance between the ions oscillates and the center of mass remains stationary. Therefore, the mode with frequency Ω_z^+ is called *axial breathing mode*.

On the other hand, the radial eigenvalue problem (Eq. 4.13a) for the balanced crystal is

$$\left[\left(\frac{\Omega}{\omega_{cs}}\right)^2 \begin{pmatrix} 1 & 0 & 0 & 0 \\ 0 & 1 & 0 & 0 \\ 0 & 0 & 1 & 0 \\ 0 & 0 & 0 & 1 \end{pmatrix} - i\frac{\Omega}{\omega_{cs}} \begin{pmatrix} 0 & 0 & 1 & 0 \\ 0 & 0 & 0 & 1 \\ 1 & 0 & 0 & 0 \\ 0 & 1 & 0 & 0 \end{pmatrix} + \frac{1}{2}\left(\frac{\omega_{zs}}{\omega_{cs}}\right)^2 \begin{pmatrix} 2 & -1 & 0 & 0 \\ -1 & 2 & 0 & 0 \\ 0 & 0 & 2 & -1 \\ 0 & 0 & -1 & 2 \end{pmatrix} \right] \cdot \begin{pmatrix} \rho_{x,t} \\ \rho_{x,s} \\ \rho_{y,t} \\ \rho_{y,s} \end{pmatrix} =$$
$$= Q_r\left(\frac{\Omega}{\omega_{cs}}\right) \cdot \begin{pmatrix} \rho_{x,t} \\ \rho_{x,s} \\ \rho_{y,t} \\ \rho_{y,s} \end{pmatrix} = \mathbb{O}_{4\times 1} . \tag{4.18}$$

The eigenvalues are found, as usual, by forcing the determinant of $Q_r\left(\Omega/\omega_{cs}\right)$ to be zero. This results in four second-degree algebraic equations,

$$\begin{aligned}\det\left[Q_r\left(\frac{\Omega}{\omega_{cs}}\right)\right] &= \left[\left(\frac{\Omega}{\omega_{cs}}\right)^2 - \left(\frac{\Omega}{\omega_{cs}}\right) + \frac{1}{2}\left(\frac{\omega_{zs}}{\omega_{cs}}\right)^2\right]\left[\left(\frac{\Omega}{\omega_{cs}}\right)^2 + \left(\frac{\Omega}{\omega_{cs}}\right) + \frac{1}{2}\left(\frac{\omega_{zs}}{\omega_{cs}}\right)^2\right] \\ &\cdot \left[\left(\frac{\Omega}{\omega_{cs}}\right)^2 - \left(\frac{\Omega}{\omega_{cs}}\right) + \frac{3}{2}\left(\frac{\omega_{zs}}{\omega_{cs}}\right)^2\right]\left[\left(\frac{\Omega}{\omega_{cs}}\right)^2 + \left(\frac{\Omega}{\omega_{cs}}\right) + \frac{3}{2}\left(\frac{\omega_{zs}}{\omega_{cs}}\right)^2\right] \\ &= 0\,. \end{aligned} \tag{4.19}$$

The second term in square brackets (resp. fourth) is equivalent to the first (resp. third) with $\Omega \to -\Omega$. Therefore, as in the axial case, the eigenfrequencies are duplicated, with positive and negative sign. Further, since the balanced crystal's axial frequencies are $\Omega_z^{\pm} = \sqrt{2 \pm 1}\,\omega_{zs}$, the equations associated to the first and third terms in square brackets in Eq. 4.19 can be rewritten as

$$\left(\frac{\Omega^{\pm}}{\omega_{cs}}\right)^2 - \left(\frac{\Omega^{\pm}}{\omega_{cs}}\right) + \frac{1}{2}\left(\frac{\Omega_z^{\pm}}{\omega_{cs}}\right)^2 = 0\,. \tag{4.20}$$

The superindex $\pm$ has been added to indicate the radial frequencies that are associated with the stretch and common axial frequencies. The solution to these is equivalent to that of a single ion,

$$\frac{\Omega_{\pm}^{\pm}}{\omega_{cs}} = \frac{1}{2}\left(1 \pm \sqrt{1 - 2\left(\frac{\Omega_z^{\pm}}{\omega_{cs}}\right)}\right)\,. \tag{4.21}$$

The subindex identifies the sign of the square root (i.e. the frequency regime). Note that Eq. 4.21 is identical to that of the radial frequencies of the single ion (Eq. 2.13), using the frequencies of the two axial modes in place of the single ion's axial frequency. For that reason, the frequencies resulting from the + sign of the square root inherit the name *reduced-cyclotron* frequencies[4], and those that result from the − sign, *magnetron* frequencies. Similarly, the frequencies associated to the center-of-mass or axial breathing frequency also inherit these adjectives. Thus, Ω_+^+ is the *cyclotron breathing frequency*, Ω_+^- is the *cyclotron center-of-mass frequency*, and so on. The frequency hierarchy will be $\Omega_+^- > \Omega_+^+ > \Omega_-^+ > \Omega_-^-$.

The eigenvectors associated to the eigenfrequencies are

[4]In the following the adjective *reduced* will be dropped from crystal modes and frequencies

$$Q_r\left(\frac{\Omega_{\pm}^{\pm}}{\omega_{cs}}\right)\cdot\begin{pmatrix}\rho_{x,t}^{\pm}\\ \rho_{x,s}^{\pm}\\ \rho_{y,t}^{\pm}\\ \rho_{y,s}^{\pm}\end{pmatrix}=0 \implies \begin{pmatrix}\rho_{x,t}^{\pm}\\ \rho_{x,s}^{\pm}\\ \rho_{y,t}^{\pm}\\ \rho_{y,s}^{\pm}\end{pmatrix}=\frac{1}{2}\begin{pmatrix}1\\ -i\\ \mp 1\\ \pm i\end{pmatrix}, \tag{4.22}$$

The sub-index (cyclotron or magnetron motion) has been removed from the eigenvectors because each of the eigenvectors is actually associated with two frequencies, that is, the eigenvectors of both breathing motions are the same (and so are those of the common modes). The same happened for the single ion, where the radial eigenvectors were associated to both radial eigenfrequencies. Further, the solutions with the opposite sign of Ω also result in the sign reversal of the imaginary units, so that the relative phase between the y and x coordinates remains the same.

The trajectories can again be obtained from the eigenvectors:

$$\begin{aligned}x_t = \frac{1}{2}\big[&\mathrm{P}_+^-\cos\left(\Omega_+^- t+\phi_+^-\right)+\mathrm{P}_+^+\cos\left(\Omega_+^+ t+\phi_+^+\right)\\ &+\mathrm{P}_-^+\cos\left(\Omega_-^+ t+\phi_-^+\right)+\mathrm{P}_-^-\cos\left(\Omega_-^- t+\phi_-^-\right)\big]\end{aligned} \tag{4.23a}$$

$$\begin{aligned}x_s = \frac{1}{2}\big[&\mathrm{P}_+^-\cos\left(\Omega_+^- t+\phi_+^-\right)-\mathrm{P}_+^+\cos\left(\Omega_+^+ t+\phi_+^+\right)\\ &-\mathrm{P}_-^+\cos\left(\Omega_-^+ t+\phi_-^+\right)+\mathrm{P}_-^-\cos\left(\Omega_-^- t+\phi_-^-\right)\big]\end{aligned} \tag{4.23b}$$

$$\begin{aligned}y_t = \frac{1}{2}\big[&-\mathrm{P}_+^-\sin\left(\Omega_+^- t+\phi_+^-\right)-\mathrm{P}_+^+\sin\left(\Omega_+^+ t+\phi_+^+\right)\\ &-\mathrm{P}_-^+\sin\left(\Omega_-^+ t+\phi_-^+\right)-\mathrm{P}_-^-\sin\left(\Omega_-^- t+\phi_-^-\right)\big]\end{aligned} \tag{4.23c}$$

$$\begin{aligned}y_s = \frac{1}{2}\big[&-\mathrm{P}_+^-\sin\left(\Omega_+^- t+\phi_+^-\right)+\mathrm{P}_+^+\sin\left(\Omega_+^+ t+\phi_+^+\right)\\ &+\mathrm{P}_-^+\sin\left(\Omega_-^+ t+\phi_-^+\right)-\mathrm{P}_-^-\sin\left(\Omega_-^- t+\phi_-^-\right)\big]\,.\end{aligned} \tag{4.23d}$$

By analyzing the trajectories that result when only one of the amplitudes is non-zero, it becomes apparent that the modes of frequency $\Omega_{\pm}^-$, which were classified as *center of mass modes* due to their association with the axial center-of-mass frequency Ω_z^-, are actually center-of-mass modes in their own right, i.e. they result in a motion

where the relative position of the ions does not change. Similarly, the modes of frequency $\Omega_{\pm}^{+}$ are proper breathing modes, since they result in a stationary center of mass.

As anticipated, a new stability condition results from the radial breathing frequencies (Eq. 4.21):

$$\frac{\Omega_{\pm}^{+}}{\omega_{cs}} \in \mathbb{R} \implies \frac{\Omega_{z}^{+}}{\omega_{cs}} = \sqrt{3}\,\frac{\omega_{zs}}{\omega_{cs}} < \frac{1}{\sqrt{2}} \implies r = \frac{\omega_{zs}}{\omega_{cs}} < \frac{1}{\sqrt{6}}\,, \tag{4.24}$$

This condition is stricter than the criterion for axial orientation of the crystal shown in Ref. [98], $\omega_{zs} < \omega_1 \implies \omega_{zs}/\omega_{cs} < 1/\sqrt{3}$. Similarly to the case of a single trapped ion, at the stability limit ($r = 1/\sqrt{6}$) the stretch radial eigenfrequencies verify $\Omega_{+}^{+} = \Omega_{-}^{+} = \omega_{cs}/2$.

4.1.2 The unbalanced crystal: axial motion

The eigenfrequencies of the axial motion of the unbalanced two-ion crystal (Eq. 4.13b) are again found by zeroing out the determinant of the matrix $Q_z\left(\Omega/\omega_{zs}\right)$:

$$\begin{aligned} &\det\left[Q\left(\frac{\Omega}{\omega_{zs}}\right)\right] = 0 \implies \\ &\implies \left(\frac{\Omega_{z}^{\pm}}{\omega_{zs}}\right)^{2} = \frac{\left[\left(\frac{\kappa}{\mu}+1\right)+\left(\frac{1}{\mu}+1\right)\frac{2\kappa}{\kappa+1}\right] \pm \sqrt{\left[\left(\frac{\kappa}{\mu}+1\right)+\left(\frac{1}{\mu}+1\right)\frac{2\kappa}{\kappa+1}\right]^{2} - 12\frac{\kappa}{\mu}}}{2}\,. \end{aligned} \tag{4.25}$$

The associated eigenvectors are

$$\begin{pmatrix}\rho_{z,t}\\ \rho_{z,s}\end{pmatrix} \propto \begin{pmatrix} \frac{1}{2}\left\{\left[\left(\frac{\kappa}{\mu}-1\right)+\left(\frac{1}{\mu}-1\right)\frac{2\kappa}{\kappa+1}\right] \pm \sqrt{\left[\left(\frac{\kappa}{\mu}+1\right)+\left(\frac{1}{\mu}+1\right)\frac{2\kappa}{\kappa+1}\right]^{2} - 12\frac{\kappa}{\mu}}\right\} \\ -\frac{2\kappa}{\kappa+1} \end{pmatrix} \tag{4.26}$$

with a certain normalization factor. This factor disappears when the ratio between the target and sensor ion's amplitudes, $\rho_{z,s}/\rho_{z,t}$ is considered. This ratio is of great importance, since only the sensor ion can be detected optically – the greater this ratio, the easier it is to optically detect energy stored in the mode in question.

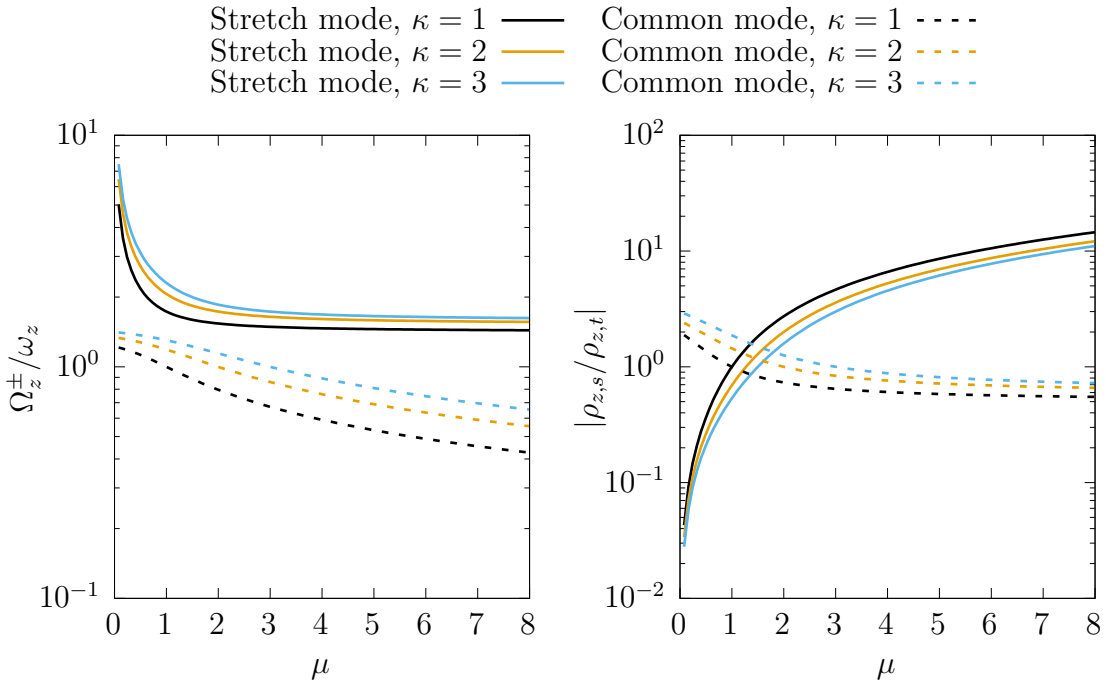

Figure 4.1: Axial modes of the unbalanced two-ion crystal. The left panel shows the mode frequencies (normalized to the sensor ion's axial frequency), and the right panel the ratio between the target and sensor ion's amplitudes associated to each mode.

In the case of the mode of frequency Ω_z^+ the amplitude ratio is negative. This was expected, since for the balanced crystal the mode of frequency Ω_z^+ was the *breathing mode*, in which the ions move in *antiphase* with equal amplitude, resulting in a stationary center of mass and an ion-ion distance that oscillates with the axial breathing frequency. However, the center of mass of the crystal is not stationary in the general case. For this reason, the mode with frequency Ω_z^+ is called *axial stretch mode* as a generalization of the breathing mode. Similarly, the mode of frequency Ω_z^-, results in a crystal with varying ion-ion distance, even though the ions still move in phase; for that reason, the mode is called *axial common mode*.

Figure 4.1 presents the axial mode frequencies and amplitude ratios for charge ratios of 1, 2 and 3. These are (in the particular case $\kappa = 1$) consistent with the results reported in Ref. [42, 97] for the axial modes of a two-ion crystal.

4.1.3 The unbalanced crystal: radial motion

Analytical solutions to the radial motion of the unbalanced crystal (described by Eq. 4.13a) exist – however, the resulting expressions are significantly more complex

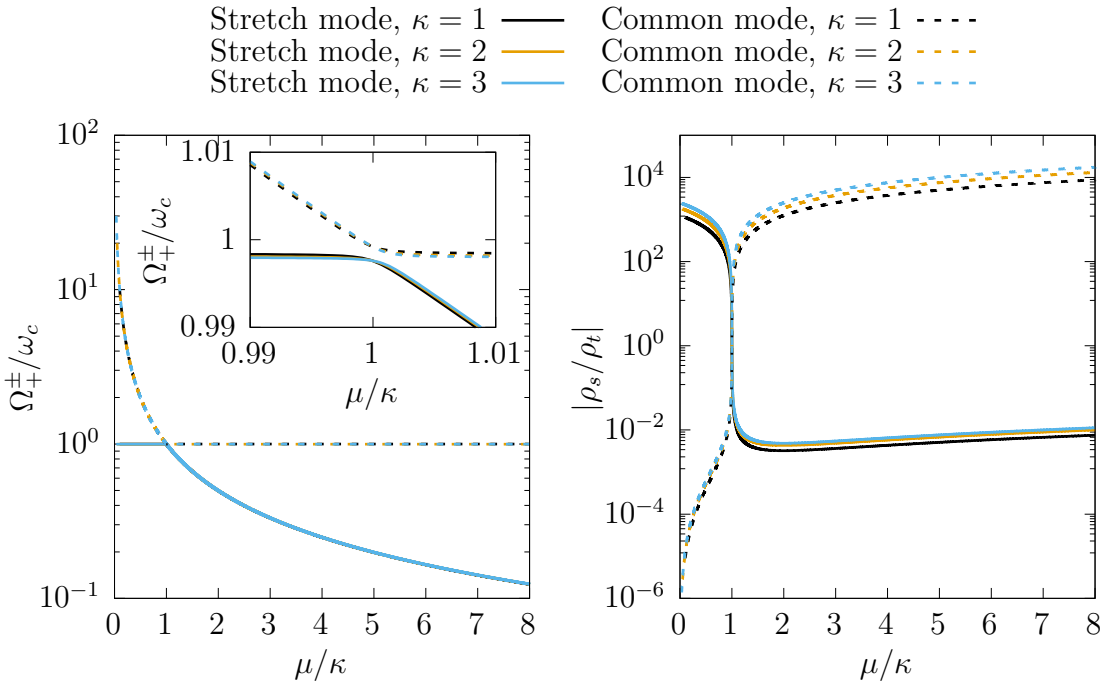

Figure 4.2: Cyclotron modes of motion of the unbalanced two-ion crystal. The left panel shows the mode frequencies (normalized to the sensor ion's free cyclotron frequency) and the right panel shows the the ratio between the target and sensor ion's amplitudes associated to each mode. Note that the abscissa is not the mass ratio μ, but μ/κ; this makes the curves for different values of κ nearly overlap. The inset in the left panel shows the region $\mu/\kappa \sim 1$ in detail, where the reduced-cyclotron frequencies of target and sensor ion are most similar. This is the only range where coupling between the individual modified-cyclotron motions is significant; several orders of magnitude separate the amplitudes of target and sensor ion everywhere else.

than those of the balanced crystal or the axial mode. For that reason, numerical solutions [103], which are only valid for a given ratio $r = \omega_{zs}/\omega_{cs}$, will be presented instead. Figs. 4.2 and 4.3 present the eigenfrequencies and amplitude ratios of the radial modes for $r \simeq 0.04$ (configuration used in the laser cooling experiments). The behavior of the system for other values of r will be discussed in Sec. 4.1.4.

Four modes of motion appear when solving Eq. 4.13a, as expected – two with high frequency and two of low frequency. For each pair there is a mode where the ions move in phase coincidence and another one where the ions move in phase opposition. Their frequencies and amplitude ratios at $\mu = \kappa = 1$ match those of the balanced crystal. They are therefore generalizations of these, and will be referred to as *common(stretch) cyclotron(magnetron) modes*, depending on the frequency regime and relative phase of the individual ions. Common ($-$) and stretch ($+$) are again differentiated with the superindex, whereas the subindex indicates the frequency regime

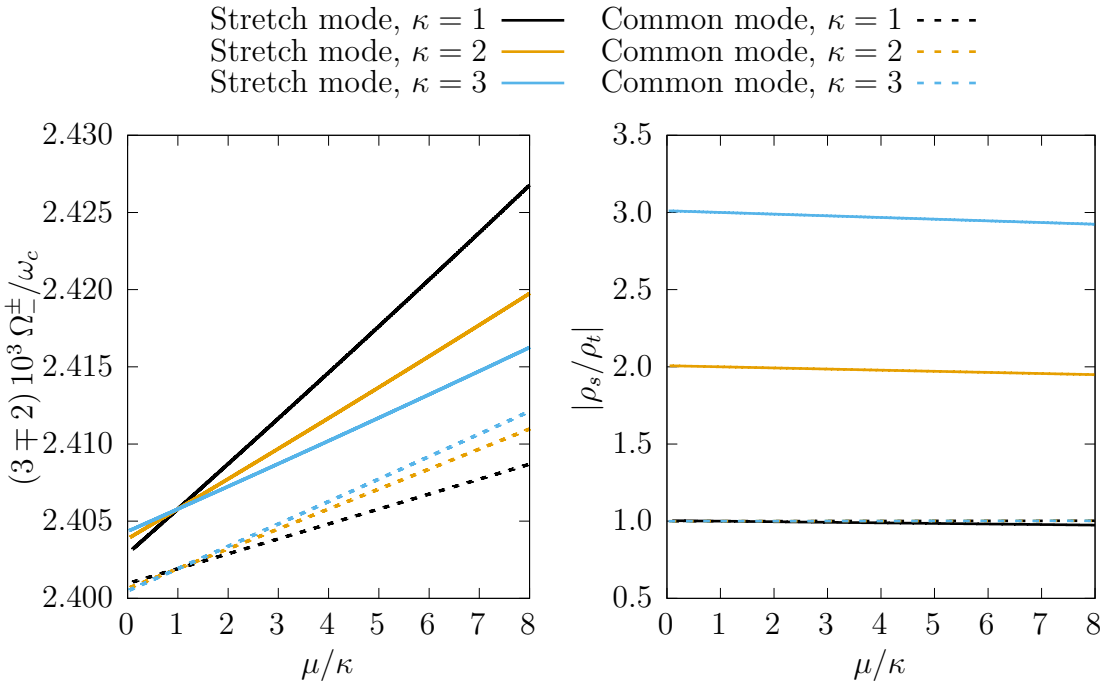

Figure 4.3: Magnetron modes of motion of the unbalanced two-ion crystal. Note that the common mode frequencies, Ω_-^-, are scaled by a factor of three so that they fall roughly in the same range as the stretch mode frequencies, Ω_-^+.

($-$ for the magnetron and $+$ for the cyclotron).

It is worthwhile to notice that if the frequencies are grouped according to the relative phase, the behavior of the single ion frequencies is maintained, i.e., the stretch modes have the highest of the axial and magnetron frequencies, but the lowest of the cyclotron ones.

The coupling strength between the individual ion's modes of motion is evidenced by the amplitude ratio depicted in Figs. 4.1, 4.2 and 4.3 – ratios closer to unity means that both ions are involved in that particular mode of motion. This is the case of the axial and magnetron modes. These are therefore best understood as a collective crystal motion. In the case of the crystal cyclotron modes, however, the coupling is weak whenever $\mu/\kappa \not\approx 1$. These modes are best described, as in Ref. [99], as slightly modified versions of the individual modified-cyclotron motions, instead of as a collective crystal mode.

To test this hypothesis, the coupling terms (off-diagonal elements of the third 4×4 matrix in Eq. 4.13a are neglected. The resulting eigenvalue problem can be separated for each of the ions. After multiplying the equation of the target ion by μ/κ^2, the eigenvalue problems are

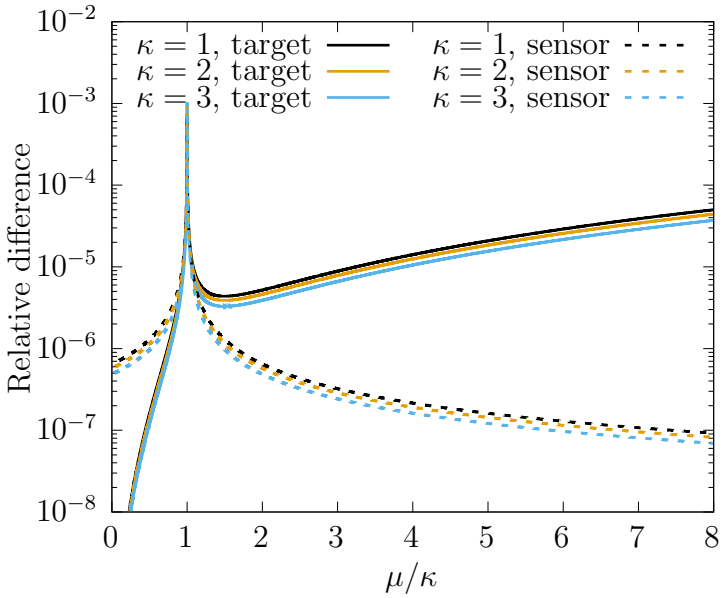

Figure 4.4: Relative error committed using the no-coupling approximation to determine the reduced-cyclotron frequencies of the unbalanced crystal.

$$\left[\left(\frac{\Omega}{\omega_{ct}}\right)^2 \begin{pmatrix} 1 & 0 \\ 0 & 1 \end{pmatrix} - i \left(\frac{\Omega}{\omega_{ct}}\right) \begin{pmatrix} 0 & 0 \\ -1 & 0 \end{pmatrix} + \frac{1}{2}\left(1 + \frac{2}{\kappa+1}\right)\left(\frac{\omega_{zt}}{\omega_{ct}}\right)^2 \begin{pmatrix} 1 & 0 \\ 0 & 1 \end{pmatrix} \right] \cdot \begin{pmatrix} \rho_{x,s} \\ \rho_{y,s} \end{pmatrix} = \begin{pmatrix} 0 \\ 0 \end{pmatrix} \quad (4.27a)$$

$$\left[\left(\frac{\Omega}{\omega_{cs}}\right)^2 \begin{pmatrix} 1 & 0 \\ 0 & 1 \end{pmatrix} - i \left(\frac{\Omega}{\omega_{cs}}\right) \begin{pmatrix} 0 & 0 \\ -1 & 0 \end{pmatrix} + \frac{1}{2}\left(1 + \frac{2\kappa}{\kappa+1}\right)\left(\frac{\omega_{zs}}{\omega_{cs}}\right)^2 \begin{pmatrix} 1 & 0 \\ 0 & 1 \end{pmatrix} \right] \cdot \begin{pmatrix} \rho_{x,t} \\ \rho_{y,t} \end{pmatrix} = \begin{pmatrix} 0 \\ 0 \end{pmatrix} \quad (4.27b)$$

for the target and sensor ion, respectively. These are equivalent to the eigenvalue problem of the single ion (see Eq. 2.12) if the axial frequencies were instead $\omega'_{zt} = \omega_{zt}\sqrt{1 + \frac{2}{\kappa+1}}$ (in the case of the target ion) and $\omega'_{zs} = \omega_{zs}\sqrt{1 + \frac{2\kappa}{\kappa+1}}$ (in the case of the sensor ion). Inserting these altered axial frequencies into Eq. 2.13, the altered

reduced-cyclotron frequencies

$$\omega'_{+,t} = \frac{\omega_{ct}}{2}\left(1+\sqrt{1-2\left(1+\frac{2}{\kappa+1}\right)\left(\frac{\omega_{zt}}{\omega_{ct}}\right)^2}\right) \tag{4.28a}$$

$$\omega'_{+,s} = \frac{\omega_{cs}}{2}\left(1+\sqrt{1-2\left(1+\frac{2\kappa}{\kappa+1}\right)\left(\frac{\omega_{zs}}{\omega_{cs}}\right)^2}\right) \tag{4.28b}$$

are obtained. Comparing these to the frequencies obtained by studying the full crystal dynamics (i.e. comparing with the frequencies shown in Fig. 4.2) serves as a test of this no-coupling approximation. The relative error commited in this approximation is shown in Fig. 4.4. It is clear that far from $\mu/\kappa \simeq 1$ the approximation predicts frequencies that are quite close to the real ones. One can therefore conclude that the cyclotron crystal modes can be thought of as individual ion modes.

4.1.4 Effects of the trap parameters

The modes of the ion crystal, as shown in the previous Section, are characterized by their frequency and amplitude ratio (meaning the amplitude ratio of the individual ions when only that crystal mode is oscillating). In this Section the effect of the only trap-dependent quantity, $r = \omega_{zs}/\omega_{cs}$ (see Eq. 4.13a) on the frequencies and amplitude ratios will be analyzed. Given that the solution of the axial motion of the unbalanced crystal is independent of r, only the radial motion will be addressed. The presented results are restricted to $\kappa = 1$ – the behavior for other values of κ is very similar.

To address the dependency of the cyclotron crystal frequencies with r, one may study how well the no-coupling approximation holds. By trial and error it becomes clear that two curves for a different r value are roughly scaled by a constant (this does not hold as well around $\mu/\kappa \simeq 1$, where the approximation breaks down). Therefore, a good way to characterize this is to take a small r value as a reference, and study the constant by which the error is increased for other trap configurations. The left panel of Fig. 4.5 shows exactly this. Each of the datapoints is calculated by averaging the ratio of a relative error curve (such as the ones shown in Fig. 4.4) with respect to that of $r = 0.005$. Only $\kappa = 1$ was considered, and datapoints within $\mu \simeq 1$ were omitted, since the approximation is not valid in that case. The standard deviation is used as an estimation of the uncertainty. By plotting the relative error ratio

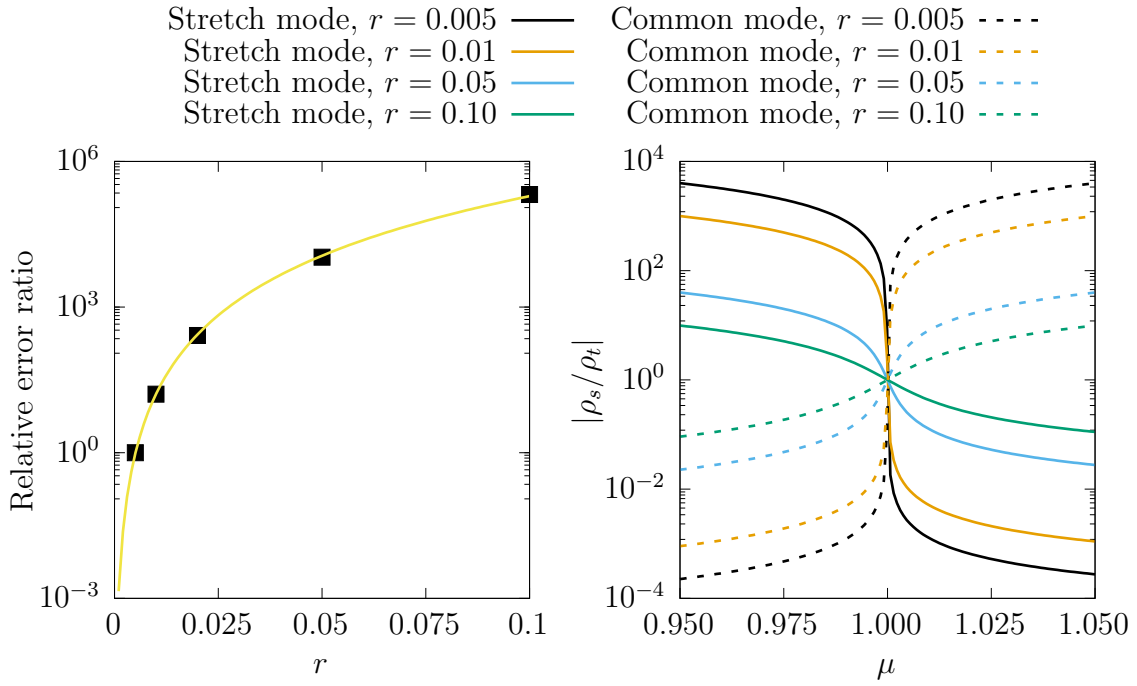

Figure 4.5: The left panel shows the scaling factor of the error committed using the no-coupling approximation for $r = \omega_{zs}/\omega_{cs} = 0.01$, 0.02, 0.05 and 0.10, with $r = 0.005$ as reference. The solid line is a power law fit. The right panel shows the amplitude ratios. The region of strong coupling (i.e. where both ions have similar amplitudes) extends further as r increases.

as a function of r in a double logarithmic scale, a power law dependency becomes apparent. A fit yields an exponent of 4.077 (29) with a coefficient of determination such that $1 - R^2 \sim 10^{-4}$. The conclusion to be drawn here is that as r increases the coupling strength grows as well, and the cyclotron modes cannot be considered as modes of the individual ions anymore. For such values of r a resolution of the full eigenvalue problem (i.e. solving Eq. 4.13a instead of Eq. 4.27) is needed to accurately predict the cyclotron crystal frequencies.

The behavior of the amplitude ratios of the cyclotron crystal modes near $\mu = 1$ is presented in the right panel of Fig 4.5. The region of strong coupling, where $\rho_s/\rho_t \sim 1$, extends further as $r = \omega_{zs}/\omega_{cs}$ is increased.

As per the magnetron modes, Fig. 4.6 shows the behavior for the same set of trap configurations (r values). The datapoints in the left panel are calculated by averaging (across $\mu \in [0, 8]$) the ratio of the magnetron frequencies for a given r with respect to those of $r = 0.005$. The standard deviations are used errorbars. A power law fit (solid line) yields an exponent of 2.0044(17), in close agreement with the behavior of the single ion (see Eq. 2.17). The coefficient of determination is such

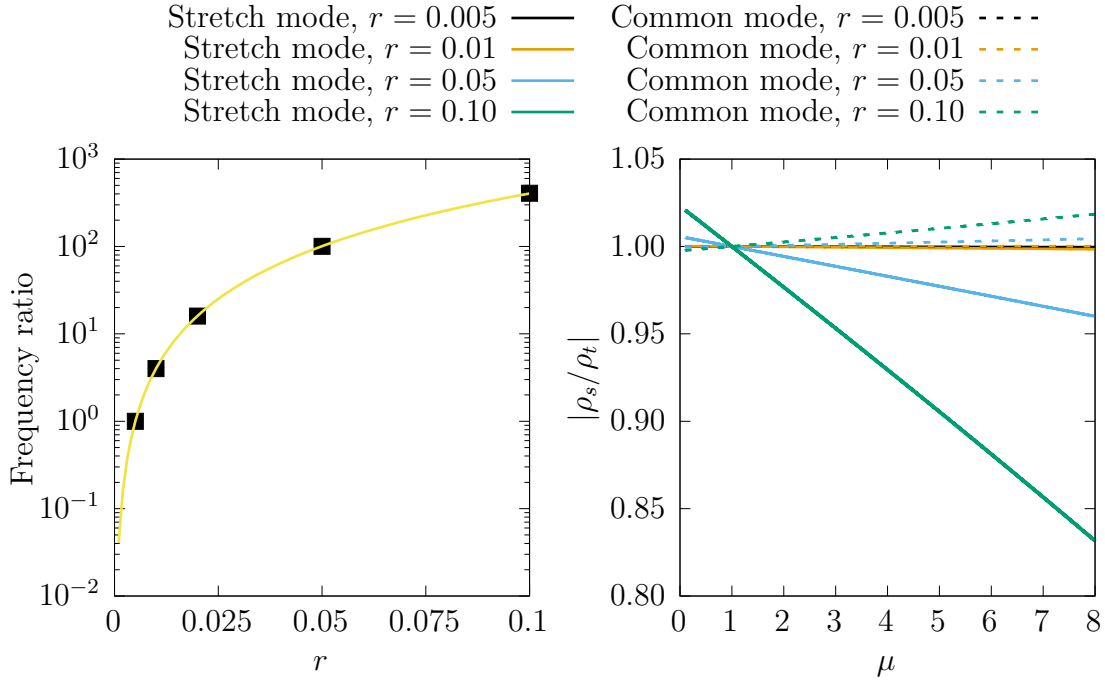

Figure 4.6: The left panel presents the ratio of the magnetron mode frequencies (averaged over μ) for several trap configurations, $r = \omega_{zs}/\omega_{cs} = 0.01$, 0.02, 0.05 and 0.10. The frequencies of the configuration $r = \omega_{zs}/\omega_{cs} = 0.005$ are taken as a reference. The solid line is a power law fit resulting in, as is the case in a single trapped ion, in a linear dependence of the magnetron frequencies with respect to the trapping voltage. The right panel shows the amplitude ratios for the four trap configurations considered.

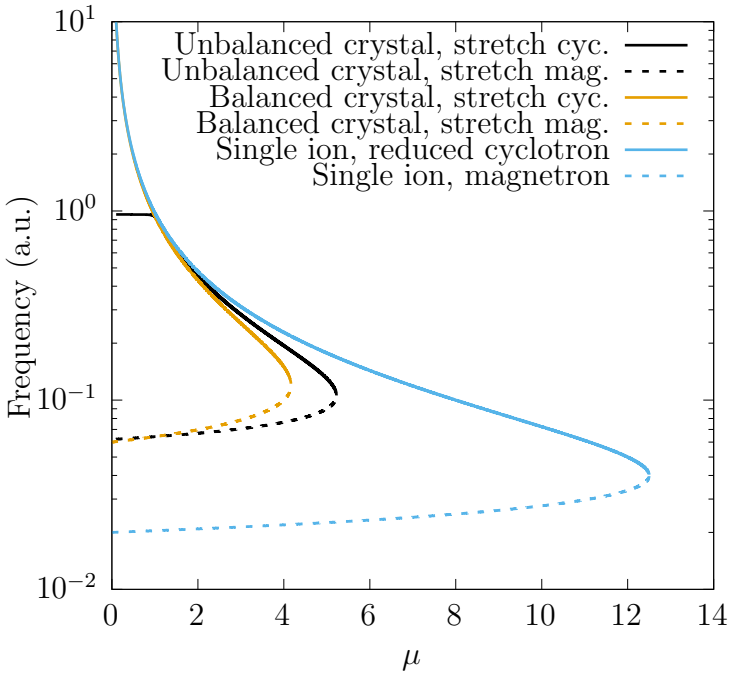

Figure 4.7: Relevant frequencies to understand the stability of the single ion, balanced crystal and unbalanced crystal. In all cases, $r = 0.2$ and $\kappa = 1$. The loss of stability of the unbalanced crystal happens for an intermediate mass, greater than the case of a balanced crystal, but smaller than that of the single ion.

that $1 - R^2 \sim 10^{-6}$. The right panel, on the other hand, shows the amplitude ratio (sensor over target ion) for the three configurations. As r grows, the degeneracy of the magnetron frequencies of the individual ions lessens. For example, the magnetron frequency of the target and sensor ions differ by up to 5 % for $r = 0.1$ and $\mu = 8$, as opposed to under 1 % for $r = 0.05$ or even less than 100 ppm for $r = 0.005$. As the frequencies grow appart, the coupling of the individual magnetron motions weakens, as evidenced by the change in amplitude ratio.

Finally, it is worth to revisit the crystal orientation and stability. Equation 2.16 presented the maximum mass-to-charge ratio (of a single ion) that can be confined in a given Penning trap. In this section, however, the parameter r is being used to characterize the trap configuration – writing Eq. 2.16 in terms of r, μ and κ yields

$$\frac{\omega_{zt}}{\omega_{ct}} = \frac{\sqrt{\frac{\kappa}{\mu}}\omega_{zs}}{\frac{\kappa}{\mu}\omega_{cs}} = \sqrt{\frac{\mu}{\kappa}}r < \frac{1}{\sqrt{2}} \implies \frac{\mu}{\kappa} < \frac{1}{2r^2}\,. \tag{4.29}$$

This is the stability condition for a single ion of mass μm_s and charge κq_s stored in a trap characterized by r. For an ion at the limit of stability the radial frequencies would verify $\omega_{+,t} = \omega_{-,t}$.

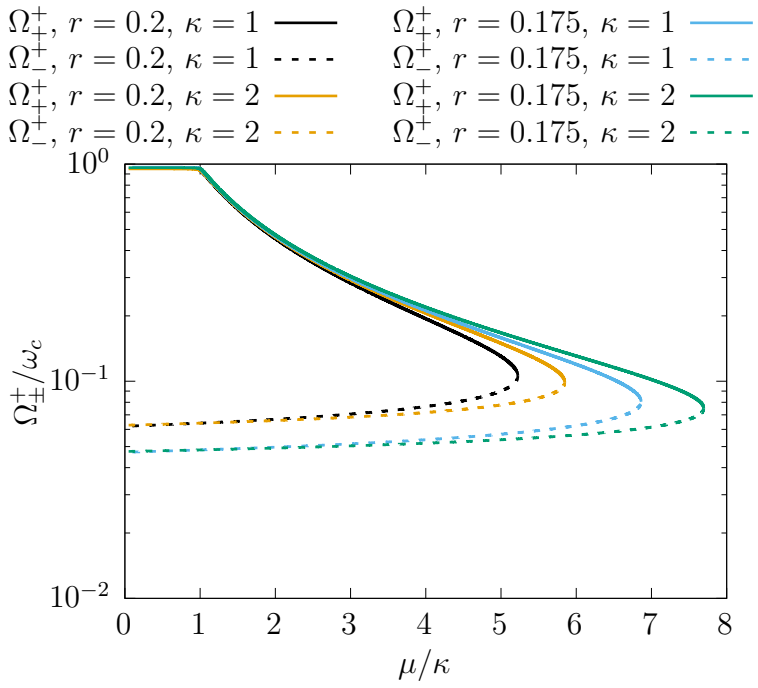

Figure 4.8: Frequencies of the stretch radial motions of the unbalanced two-ion crystal. The motions becomes unstable when the stretch cyclotron and magnetron frequencies coincide.

The presence of a second ion in the trap makes the confinement less stable. Equation 4.24 showed that for a balanced crystal with two ions of mass m_s and charge q_s, stability was lost when $r < \frac{1}{\sqrt{6}}$ (instead of $r < \frac{1}{\sqrt{2}}$ for the single ion of the same mass and charge). This is because of the stretch radial motions, as shown in Sec. 4.1.1. If the trap configuration (value of r) is fixed and the ions are swapped with two ions of mass μm_s and charge κq_s, stability is lost when

$$\frac{\omega_{zt}}{\omega_{ct}} = \sqrt{\frac{\mu}{\kappa}} r < \frac{1}{\sqrt{6}} \implies \frac{\mu}{\kappa} < \frac{1}{6r^2}\,. \tag{4.30}$$

Again, the stretch cyclotron and stretch magnetron frequencies become equal at the limit of stability.

In the case of the unbalanced ion, the situation is similar. Increasing μ/κ brings the stretch cyclotron and stretch axial frequencies closer and closer, until they become equal – beyond that point, increasing μ/κ gives the frequencies an imaginary component, resulting in an exponential growth of the mode amplitude (i.e. instability). Figure 4.7 compares the relevant frequencies of the single ion of mass μm_s and charge κm_s, of the balanced crystal with two such ions, and of the unbalanced crystal. The loss of stability of the unbalanced crystal happens for an intermediate

mass, greater than the case of a balanced crystal, but smaller than that of the single ion.

Figure 4.8, on the other hand, shows the stretch radial frequencies of the unbalanced crystal as a function of μ/κ for a few values of r and κ. In all cases, stability of the stretch modes is lost before the predicted change of orientation (see the discussion in Sec. 4.1) happens. Regardless, the values of r (that is, the trapping potentials) that need to be used to cause instability of the stretch radial motions for reasonable masses is too high. In short, one can be confident that for normal operating conditions the unbalanced crystal will be stable and oriented axially.

4.1.5 Generalized invariance theorem

Back in Chapter 2, the *invariance theorem*, $\omega_{cs}^2 = \omega_+^2 + \omega_{zs}^2 + \omega_{zs}^2$ (see Ref. [11]), which holds under certain kinds of trap imperfections, was presented. Recently, a more general version of the invariance theorem was derived in Ref. [100]. The *generalized invariance theorem* is obtained for a two-dimensional array of N microfabricated Penning traps, where ions interact via Coulomb repulsion, but the inter-ionic distance is determined almost exclusively by the position of the individual traps. Under these conditions, the $3N$ motional frequencies (whose deviation from the un-perturbed frequencies depends mainly on the distance between individual traps) verify

$$\sum_{\lambda=1}^{3N} \omega_\lambda^2 = \sum_{j=1}^{N} \omega_{c,j}^2 \,. \tag{4.31}$$

Here, ω_λ are each of the motional frequencies and $\omega_{c,j}$ is the free cyclotron frequency of the ion with index j. This result is valid under the same set of trap imperfections as the original invariance theorem.

On the following it will be shown that the two-ion crystal considered in this work also verifies the generalized invariance theorem – the expressions involved are, indeed, identical to those shown in Ref. [100]. The first step would be to linearize Eqs. 4.6, i.e. to introduce additional variables $\mathbf{v} = \dot{\mathbf{r}}$ so that the equations of motion can be written as a set of first order differential equations with twice the size:

$$\begin{cases} \dot{\mathbf{r}} = \mathbf{v} \\ \dot{\mathbf{v}} = f\left(\mathbf{r}, \mathbf{v}\right) \end{cases} . \tag{4.32}$$

In matrix form,

$$\begin{pmatrix} \mathbb{I}_6 & \mathbb{O}_{6x6} \\ \mathbb{O}_{6x6} & \mathbb{M} \end{pmatrix} \cdot \begin{pmatrix} \dot{\mathbf{r}}^\top \\ \dot{\mathbf{v}}^\top \end{pmatrix} = \begin{pmatrix} \mathbb{O}_{6x6} & \mathbb{I}_6 \\ \mathbb{E} & \mathbb{B} \end{pmatrix} \cdot \begin{pmatrix} \mathbf{r}^\top \\ \mathbf{v}^\top \end{pmatrix} , \tag{4.33}$$

where $\mathbb{I}$ is the identity matrix.

Introducing the ansatz $\mathbf{r} = \boldsymbol{\rho} e^{-i\Omega t}$, an algebraic system of equations results that can be written as

$$\begin{pmatrix} \mathbb{O}_{6x6} & -i\mathbb{I}_6 \\ \mathbb{E} & -i\mathbb{B} \end{pmatrix} \cdot \begin{pmatrix} \boldsymbol{\rho}^\top \\ \Omega\boldsymbol{\rho}^\top \end{pmatrix} = \Omega \begin{pmatrix} -i\mathbb{I}_6 & \mathbb{O}_{6x6} \\ \mathbb{O}_{6x6} & -\mathbb{M} \end{pmatrix} \cdot \begin{pmatrix} \boldsymbol{\rho}^\top \\ \Omega\boldsymbol{\rho}^\top \end{pmatrix} . \tag{4.34}$$

This is known as a *linearization of the first companion form* (see e.g. Ref. [52]), and results in a *generalized eigenvalue problem*. Inverting the right-hand side matrix (which is trivial, since it is diagonal) turns it into a standard eigenvalue problem,

$$\begin{pmatrix} \mathbb{O}_{6x6} & \mathbb{I}_6 \\ -\mathbb{M}^{-1}\mathbb{E} & i\mathbb{M}^{-1}\mathbb{B} \end{pmatrix} \cdot \begin{pmatrix} \boldsymbol{\rho}^\top \\ \Omega\boldsymbol{\rho}^\top \end{pmatrix} = \Omega \cdot \begin{pmatrix} \boldsymbol{\rho}^\top \\ \Omega\boldsymbol{\rho}^\top \end{pmatrix} . \tag{4.35}$$

Once the problem has been expressed in this form, the treatment used in Ref. [100] can be used. If Ω is an eigenvalue of the left hand matrix, Ω^2 will be an eigenvalue of the squared matrix with the same eigenvectors. Computing the trace of the squared matrix one finds that the crystal's eigenfrequencies verify

$$\sum \Omega^2 = \omega_{ct}^2 + \omega_{cs}^2 . \tag{4.36}$$

During the trace computation it becomes clear that the contribution of a misaligned magnetic field or electric fields whose Taylor expansion to second order is exact (e.g. an elliptic deviation from the ideal trapping field) do not affect Eq. 4.36.

4.1.6 Quantized motion

As a previous step to the quantization of the motion, the classical Hamiltonian must be derived. Using the notation introduced in Sec. 4.1.5, the canonical momenta associated with the cartesian coordinates of the individual ions are

$$p_i = \frac{\partial \mathcal{L}}{\partial \dot{r}_i} = \{\mu, 1\}\, m\dot{r}_i + \{\kappa, 1\}\, qA_i , \tag{4.37}$$

where either of the terms between curly brackets is used depending on the ion in question. The Hamiltonian function is therefore given by

$$\mathcal{H} = \sum_{i=1}^{6} p_i r_i - \mathcal{L} = \frac{\left(\mathbf{p}_t - \kappa q A\left(\mathbf{r}_t\right)\right)^2}{2\mu m} + \frac{\left(\mathbf{p}_s - q A\left(\mathbf{r}_s\right)\right)^2}{2m} + V_{crystal}\,, \tag{4.38}$$

which, using the matrices defined in Sec. 4.1 and introducing $\mathbb{T} = \mathbb{B}\mathbb{M}^{-1}\mathbb{B}$, can be rewritten as

$$\mathcal{H} = \sum_{i=1}^{6}\left(\frac{p_i^2}{2\mathbb{M}_{ii}} + \frac{1}{4\mathbb{M}_{ii}}\sum_{j=1}^{6}\mathbb{B}_{ij}p_i r_j - \sum_{j=1}^{6}\frac{\mathbb{B}_{ij}}{4\mathbb{M}_{ii}} r_i p_j - \frac{1}{8}\sum_{j=1}^{6}\mathbb{T}_{ij} r_i r_j + \frac{1}{2}\sum_{j=1}^{6}\mathbb{E}_{ij} r_i r_j\right). \tag{4.39}$$

This is identical to the expression obtained in Ref. [100], so the same quantization can be used. In a general way, the ladder operators for each mode can be written as

$$\hat{a}_\lambda^\dagger = \sum_{i=1}^{6}\left(\alpha_{\lambda k}\hat{p}_k + \beta_{\lambda k}\hat{r}_k\right) \text{ and } \hat{a}_\lambda = \sum_{i=1}^{6}\left(\alpha_{\lambda k}^*\hat{p}_k + \beta_{\lambda k}^*\hat{r}_k\right) \tag{4.40}$$

(since $\hat{p}_i$ and $\hat{r}_i$ are self-adjoint). The Hamiltonian operator, in the adequate basis, will be the sum of several harmonic oscillators,

$$\hat{\mathcal{H}} = \sum_{\lambda=1}^{6}\hbar\Omega_\lambda\left(\hat{a}_\lambda^\dagger\hat{a}_\lambda + \frac{1}{2}\right), \tag{4.41}$$

Since p_i and r_i are canonical conjugates, the associated operators $\hat{p}_i$ and $\hat{r}_i$ verify the usual commutation rules, i.e.

$$[\hat{r}_i, \hat{r}_j] = 0 \;\; [\hat{p}_i, \hat{p}_j] = 0 \;\; [\hat{r}_i, \hat{p}_j] = i\hbar\delta_{ij}\,. \tag{4.42}$$

If the ladder operators also verify the usual commutation rule, $\left[a_\lambda, a_{\lambda'}^\dagger\right] = i\hbar\delta_{\lambda\lambda'}$, it is easy to see that $\left[\hat{\mathcal{H}}, \hat{a}_\lambda^\dagger\right] = \hbar\Omega_\lambda\hat{a}_\lambda^\dagger$ holds. Calculating all the terms in this commutator (see Ref. [104]) the expressions

$$\begin{cases} -i\mathbb{M}^{-1}\boldsymbol{\beta}_\lambda + \frac{i}{2}\mathbb{M}^{-1}\mathbb{B}\boldsymbol{\alpha}_\lambda = \Omega_\lambda\boldsymbol{\alpha}_\lambda \\ \left(\Omega_\lambda^2\mathbb{M} - i\Omega_\lambda\mathbb{B} - \mathbb{E}\right)\boldsymbol{\alpha}_\lambda^\top = 0 \end{cases} \tag{4.43}$$

are obtained. The second expression is none other than the original eigenvalue

problem (Eq. 4.11), and therefore the resulting modes match the ones previously obtained in frequency and amplitude ratio.

4.2 Manipulation of the two-ion crystal

In this Section the effects of an external electromagnetic field, in the form of a dipolar driving, on the unbalanced two-ion crystal will be studied. This is very relevant since the method to determine the crystal's eigenfrequencies needs to drive each of the modes with such a field. For identification for example, one could use the axial motion and observe the oscillation amplitude when the crystal is simultaneously driven and laser cooled (see Refs. [105] and [102]). When direct observation of a particular mode is not possible (see e.g. the cyclotron modes of the crystal in Sec. 4.1.3, which are almost decoupled), the energy on that mode has to be transferred to another mode that involves large oscillations of the sensor ion. This is done by means of a quadrupolar driving, much like the case of the single ion (see Sec. 2.3.2).

The introduction of a dipolar driving in the axial direction can be accounted for with an additional term in the equations of motion,

$$\begin{cases} \ddot{z}_t = -\frac{1}{\mu}\left(\kappa + \frac{2\kappa}{\kappa+1}\right)\omega_{zs}^2 z_t + \frac{1}{\mu}\frac{2\kappa}{\kappa+1}\omega_{zs}^2 z_s + \frac{\kappa}{\mu}\frac{\alpha q V_{RF}}{d_{elec}}\sin\left(\omega_{RF}t + \phi_{RF}\right) \\ \ddot{z}_s = -\left(1 + \frac{2\kappa}{\kappa+1}\right)\omega_{zs}^2 z_t + \frac{2\kappa}{\kappa+1}\omega_{zs}^2 z_s + \frac{\alpha q V_{RF}}{d_{elec}}\sin\left(\omega_{RF}t + \phi_{RF}\right) \end{cases} . \tag{4.44}$$

A change of base is required to write these in terms of the eigenmodes of the crystal. It can be obtained from the eigenvectors (Eq. 4.26) or, equivalently, from the modes' amplitude ratios presented in Fig. 4.1. The change of base matrix is

$$\mathbf{Z}^{\pm} = \frac{1}{\sqrt{1 + (\rho_{zs}/\rho_{zt})^2}} \begin{pmatrix} 1 \\ \rho_{zs}/\rho_{zt} \end{pmatrix} = \begin{pmatrix} a_z^{\pm} \\ b_z^{\pm} \end{pmatrix} \implies \begin{pmatrix} Z^+ \\ Z^- \end{pmatrix} = \begin{pmatrix} a_z^+ & b_z^+ \\ a_z^- & b_z^- \end{pmatrix} \begin{pmatrix} z_t \\ z_s \end{pmatrix} . \tag{4.45}$$

The normalization is such that the components of the eigenvectors verify $(a_z^{\pm})^2 + (b_z^{\pm})^2 = 1$. The equations of motion in this basis are

$$\begin{cases} \ddot{Z}^{+} = -\left(\Omega_z^{+}\right)^2 Z^{+} + \frac{q}{m}\left(\frac{\kappa}{\mu}a_z^{+} + b_z^{+}\right)\frac{\alpha V_{RF}}{d_{elec}}\sin\left(\omega_{RF}t + \phi_{RF}\right) \\ \ddot{Z}^{-} = -\left(\Omega_z^{-}\right)^2 Z^{-} + \frac{q}{m}\left(\frac{\kappa}{\mu}a_z^{-} + b_z^{-}\right)\frac{\alpha V_{RF}}{d_{elec}}\sin\left(\omega_{RF}t + \phi_{RF}\right) \end{cases} . \tag{4.46}$$

Comparing with Eq. 2.29, it is clear that the amplitude of the modes evolves according to

$$\mathrm{P}_z^{\pm} \simeq \frac{q}{m}\left(\frac{\kappa}{\mu}a_z^{\pm} + b_z^{\pm}\right)\frac{\alpha V_{RF} T_{RF}}{2\Omega_z^{\pm} d_{elec}}\mathrm{sinc}\left(\frac{\Delta\omega}{2}T_{RF}\right) \tag{4.47}$$

when driven near resonance. The quantity

$$q/m\big|_z^{\pm} = \frac{q}{m}\left(\frac{\kappa}{\mu}a_z^{\pm} + b_z^{\pm}\right) \tag{4.48}$$

is defined as the *effective charge-to-mass ratio* of the given mode, since it quantifies how strongly the mode responds to the electric field.

The radial eigenmotions, on the other hand, have eigenvectors of the form $(a, -ia, b, -ib)$. a and b are obtained by solving Eq. 4.13a, resulting in

$$\begin{pmatrix} R_+^- \\ R_+^+ \\ R_-^+ \\ R_-^- \end{pmatrix} = \begin{pmatrix} a_+^- & ia_+^- & b_+^- & ib_+^- \\ a_+^+ & ia_+^+ & b_+^+ & ib_+^+ \\ a_-^+ & ia_-^+ & b_-^+ & ib_-^+ \\ a_-^- & ia_-^- & b_-^- & ib_-^- \end{pmatrix} \cdot \begin{pmatrix} x_t \\ y_t \\ x_s \\ y_s \end{pmatrix} , \tag{4.49}$$

where $a_\pm^\pm$ and $b_\pm^\pm$ are again calculated from the modes' amplitude ratios (see Figs. 4.2 and 4.3) and the modes have been sorted in order of decreasing frequency.

The radial equations of motion with the addition of the driving term in the x direction are

$$\begin{cases} \ddot{x}_t = \frac{1}{2}\frac{1}{\mu}\left(\kappa + \frac{2\kappa}{\kappa+1}\right)\omega_{zs}^2 x_t + \frac{\kappa}{\mu}\omega_{cs}\dot{y}_t - \frac{1}{2}\frac{1}{\mu}\frac{2\kappa}{\kappa+1}\omega_{zs}^2 x_s + \frac{\kappa}{\mu}\frac{q}{m}\frac{\alpha V_{RF}}{d_{elec}}\sin\left(\omega_{RF}t + \phi_{RF}\right) \\ \ddot{y}_t = \frac{1}{2}\frac{1}{\mu}\left(\kappa + \frac{2\kappa}{\kappa+1}\right)\omega_{zs}^2 y_t - \frac{\kappa}{\mu}\omega_{cs}\dot{x}_t - \frac{1}{2}\frac{1}{\mu}\frac{2\kappa}{\kappa+1}\omega_{zs}^2 y_s \\ \ddot{x}_s = \frac{1}{2}\left(1 + \frac{2\kappa}{\kappa+1}\right)\omega_{zs}^2 x_s + \omega_{cs}\dot{y}_s - \frac{1}{2}\frac{2\kappa}{\kappa+1}\omega_{zs}^2 x_t + \frac{q}{m}\frac{\alpha V_{RF}}{d_{elec}}\sin\left(\omega_{RF}t + \phi_{RF}\right) \\ \ddot{y}_s = \frac{1}{2}\left(1 + \frac{2\kappa}{\kappa+1}\right)\omega_{zs}^2 y_s - \omega_{cs}\dot{x}_s - \frac{1}{2}\frac{2\kappa}{\kappa+1}\omega_{zs}^2 y_t \end{cases} , \tag{4.50}$$

which in the eigenmode basis are

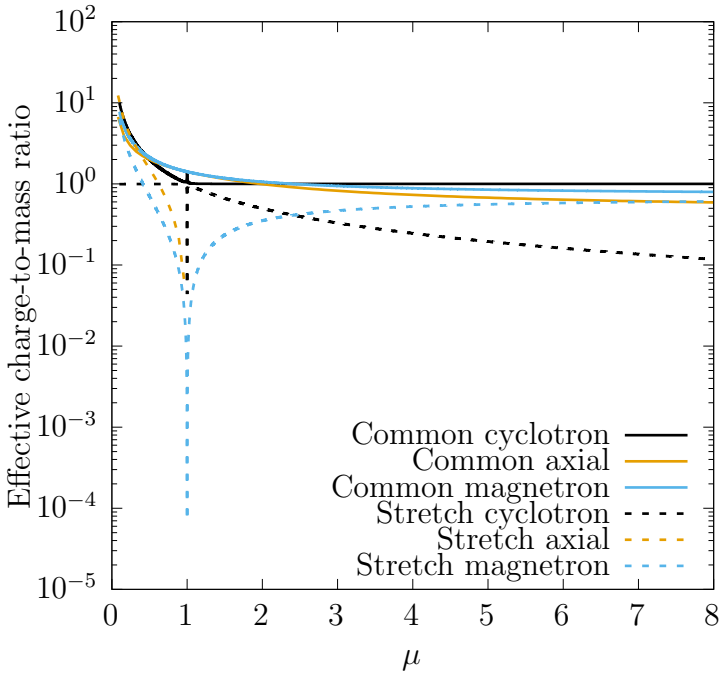

Figure 4.9: Absolute value of the effective charge-to-mass ratio of the different crystal modes (see Eqs. 4.48 and 4.53) under dipolar driving. The values are normalized to the charge-to-mass ratio of the sensor ion, q/m. Note that all stretch modes have an effective charge-to-mass of zero when $\mu = 1$.

$$\begin{cases} \ddot{U}_+^- = -\left(\Omega_+^-\right)^2 U_+^- + \frac{q}{m}\left(\frac{\kappa}{\mu}a_+^- + b_+^-\right)\frac{\alpha V_{RF}}{d_{elec}}\sin\left(\omega_{RF}t + \phi_{RF}\right) \\ \ddot{U}_+^+ = -\left(\Omega_+^+\right)^2 U_+^+ + \frac{q}{m}\left(\frac{\kappa}{\mu}a_+^+ + b_+^+\right)\frac{\alpha V_{RF}}{d_{elec}}\sin\left(\omega_{RF}t + \phi_{RF}\right) \\ \ddot{U}_-^+ = -\left(\Omega_-^+\right)^2 U_-^+ + \frac{q}{m}\left(\frac{\kappa}{\mu}a_-^+ + b_-^+\right)\frac{\alpha V_{RF}}{d_{elec}}\sin\left(\omega_{RF}t + \phi_{RF}\right) \\ \ddot{U}_-^- = -\left(\Omega_-^-\right)^2 U_-^- + \frac{q}{m}\left(\frac{\kappa}{\mu}a_-^- + b_-^-\right)\frac{\alpha V_{RF}}{d_{elec}}\sin\left(\omega_{RF}t + \phi_{RF}\right) \end{cases} . \tag{4.51}$$

The evolution of the mode amplitudes is therefore identical to that of the axial modes,

$$\mathrm{P}_\pm^\pm \simeq \frac{q}{m}\left(\frac{\kappa}{\mu}a_\pm^\pm + b_\pm^\pm\right)\frac{\alpha V_{RF} T_{RF}}{2\Omega_\pm^\pm d_{elec}}\mathrm{sinc}\left(\frac{\Delta\omega}{2}T_{RF}\right) , \tag{4.52}$$

and so is their effective charge-to-mass ratio,

$$q/m\big|_\pm^\pm = \frac{q}{m}\left(\frac{\kappa}{\mu}a_\pm^\pm + b_\pm^\pm\right) . \tag{4.53}$$

Figure 4.9 presents the effective charge-to-mass ratio of the different modes. Note that the absolute value is given; some of the effective charge-to-mass ratios, as

calculated in this Section, are negative. This is an artifact due to the choice of sign on the components of the eigenvectors (the first component is always taken as positive).

All stretch modes present zero effective charge-to-mass ratio at $\mu = 1$ (equal masses). This is due to the geometry of the stretch modes: since both ions move with equal amplitudes in opposite directions, a force exerted on them with equal magnitude and direction does not favor an increase in amplitude.

The cyclotron modes' effective charge-to-mass ratio are very close to q/m and $\kappa q/\mu m$, i.e., to the charge-to-mass ratios of the sensor and target ion, respectively. This is expected, since the cyclotron modes can be considered as modes of motion of the individual ions (see Sec. 4.1.3).

4.3 Anharmonicities and systematic effects

By using a small-displacement approximation around the equilibrium configuration of the crystal, the crystal's motion has been shown to be the superposition of six harmonic eigenmotions. However, the Coulomb interaction between the ions is highly anharmonic, since its expansion reads $|z-d|^{-1} = 1/d \cdot \sum_{n=0}^{\infty} (z/d)^n$. Therefore, a quantification of the frequency shifts is needed. Two approaches have been followed in this regard. If a measurement procedure similar to the one outlined in Ref. [102] is to be used, the amplitudes would be in the order of d – thus, a classical perturbative treatment of the first few terms in the Taylor expansion of the Coulomb potential would not suffice. Therefore, a numerical approach was chosen, where the complete, $1/r$ interaction is computed. An ad-hoc program that simulates the trajectories of the two ions and then performs a Fast Fourier Transform (FFT) to obtain the motional frequencies was created. In view of the results obtained in this way, a study of the frequency shifts in the quantum regime is required.

4.3.1 Shifts in the classical regime

The program created for this section can solve an arbitrary number of differential equations, so it is possible to switch between the small-displacement (Eqs. 4.6) and full-interaction (Eqs. 4.2) pictures.

The amplitude-dependent shift is the difference between the frequency observed in the small amplitude regime (see Sec. 4.1) and the actual oscillation frequency at

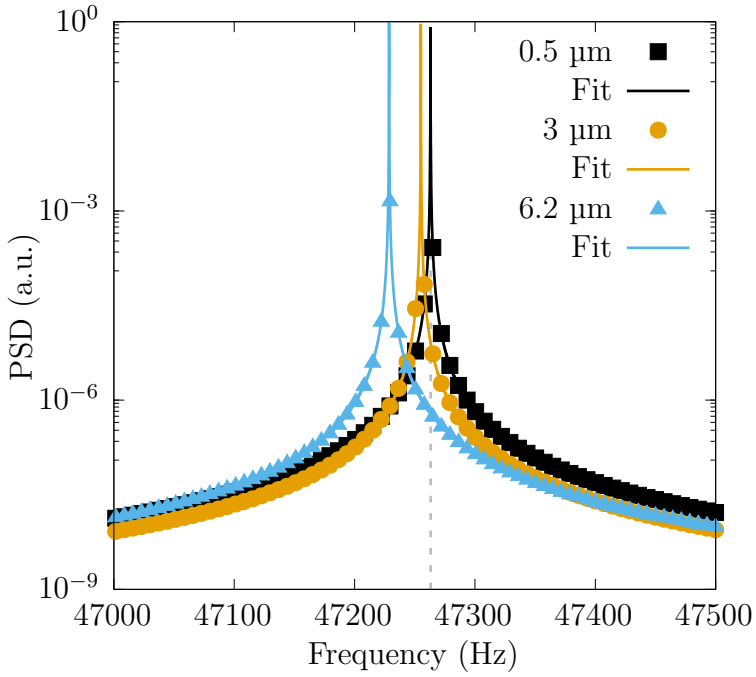

Figure 4.10: Amplitude-dependent shift of the common axial motion. The target ion is $^{257}Rf^+$, and the trap configuration is $\omega_{zs} = 2\pi \cdot 100\,\text{kHz}$ and $\omega_{cs} = 2\pi \cdot 2.689\,\text{MHz}$. The simulation is 140 ms long with a step of 2 ns. The vertical dashed line indicates the oscillation frequency in the small amplitude regime. The shifts obtained from the Lorentzian fits are -8.030122(69) Hz for 3 µm and -34.435650(74) Hz for 6.2 µm.

that amplitude. An example is shown in Fig. 4.10. The datapoints correspond to a $^{257}Rf^+$–$^{40}Ca^+$ crystal oscillating in the common axial mode with the target ion oscillating the amplitudes of amplitudes 0.5 µm, 3 µm and 6.2 µm. The resulting shifts are -8.030122(69) Hz for 3 µm and -34.435650(74) Hz for 6.2 µm. They therefore scale roughly with the square of the oscillation amplitude. This fact could be used to correct the shift from the optically determined amplitude, reducing (up to a point) the weight of the shift.

In an actual experiments like those presented in Refs. [102, 101], one observes the steady state attained when the energy the ion gains due to the driving and the energy removed by the laser cooling. Therefore, the amplitude of oscillation is constant during the detection process. If a different method, where the driving and detection are separated in time, were used, the ion would sweep through a range of oscillation amplitudes, each of them associated to different frequencies. Consider for example Fig. 4.11, which shows the target ion's oscillation amplitude when the $^{257}Rf^+$–$^{40}Ca^+$ crystal is driven from rest with a certain driving amplitude. It becomes clear that the amplitude reached is lower than it would be in absence of anharmonicites (e.g.

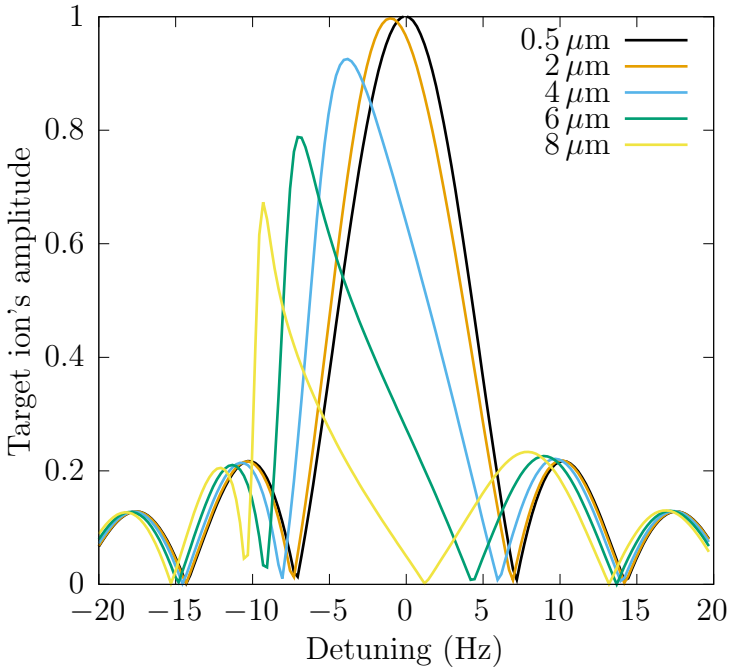

Figure 4.11: Resulting amplitude of the target ion as a function of the driving frequency when the $^{257}Rf^{+}$–$^{40}Ca^{+}$ crystal's common axial mode is driven at different amplitudes. Each of the curves is normalized to the amplitude that would be reached if the anharmonicities are neglected (indicated in the labels). The parameters used in the simulation are as in Fig. 4.10, with the addition of a dipolar axial driving, also 140 ms long.

the maximum amplitude for the yellow curve is 5.4 µm, whereas 8 µm would be reached if no amplitude dependent shifts were present). It is also clear that the maximum is between the unperturbed and amplitude-shifted frequencies.

The case of the common axial mode is not the least favorable when it comes to frequency shifts. The approximation of the Coulomb interaction to a harmonic potential is broken when the ion-ion distance changes. Therefore, the stretch magnetron and stretch axial modes (where the ions move in phase opposition) present the largest shifts. For the same reason, the common magnetron mode (where the ions move in phase with almost identical amplitudes, see Sec. 4.1.3) presents negligible shifts. The cyclotron modes, being almost decoupled, result in small frequency shifts, similar to one another. The next section provides numbers that back up this qualitative analysis.

Due to the large shifts that are obtained for the stretch magnetron and axial modes, any measurement in the classical regime that involves these frequencies is not feasible. It is possible to determine the crystal's mass ratio μ from the common axial

frequency (see Sec. 4.4.1). However, the effects of the Doppler-cooled stretch magnetron mode will have to be quantified experimentally, since (as shown in the next section) the any amplitude in the stretch magnetron mode significantly affects all the modes' frequencies.

4.3.2 Shifts in the quantum regime

If the crystal motion is in the quantum regime (resulting in amplitudes significantly smaller than the inter-ion distance d) the importance of the successive terms in the Coulomb potential's expansion does indeed decrease as their order grows. Therefore, a perturbative treatment is appropriate. Ref. [106] will be followed here. Since the contribution of odd order terms of the expansion vanishes, the next contribution comprises both the third term of the Coulomb's expansion to second order perturbation theory and the fourth order term of the expansion to first order perturbation theory:

$$\Delta E = \langle n_{\lambda_1} \dots n_{\lambda_6} | \, V^{(4)}_{Coul} \, | n_{\lambda_1} \dots n_{\lambda_6} \rangle + \sum_{\substack{\{n'_{\lambda_1} \dots n'_{\lambda_6}\} \neq \\ \{n_{\lambda_1} \dots n_{\lambda_6}\}}} \frac{\langle n'_{\lambda_1} \dots n'_{\lambda_6} | \, V^{(3)}_{Coul} \, | n_{\lambda_1} \dots n_{\lambda_6} \rangle}{\sum_\lambda \hbar \Omega_\lambda \left(n_\lambda - n'_\lambda \right)} \,, \tag{4.54}$$

where the succesive n_{λ_i} are the number of phonons in each of the modes[5].

In order to calculate the corrections, the expansion of the Coulomb potential must be written in terms of these modes of the crystal. The first step [106] is to change to the mass-weighted coordinates, $r'_i = \sqrt{m_i} r_i$. Since $\partial / \partial r'_i = \left(1/\sqrt{m_i} \right) \partial / \partial r_i$, the third and fourth order terms of the expansion can be written as

$$V^{(3)}_{Coul} = \sum_{i,j,k} \frac{1}{3!} \frac{1}{\sqrt{m_i m_j m_k}} \frac{\partial^3 V_{Coul}}{\partial r_i \partial r_j \partial r_k} r'_i r'_j r'_k \tag{4.55}$$

and

$$V^{(4)}_{Coul} = \sum_{i,j,k,l} \frac{1}{4!} \frac{1}{\sqrt{m_i m_j m_k m_l}} \frac{\partial^4 V_{Coul}}{\partial r_i \partial r_j \partial r_k \partial r_l} r'_i r'_j r'_k r'_l \,, \tag{4.56}$$

[5]Each of the λ_i labels correspond to one of the modes of oscillation of the crystal ($n_{\lambda_1} = n^-_+$, $n_{\lambda_2} = n^+_+$, $n_{\lambda_2} = n^+_z$, ...). Using this notation allows for more compact expressions, since sums over the crystal modes appear in many places.

respectively. Introducing

$$A'^{(3)}_{ijk} = \frac{1}{3!}\frac{1}{\sqrt{m_i m_j m_k}}\frac{\partial^3 V_{Coul}}{\partial r_i \partial r_j \partial r_k} \text{ and } A'^{(4)}_{ijkl} = \frac{1}{4!}\frac{1}{\sqrt{m_i m_j m_k m_l}}\frac{\partial^4 V_{Coul}}{\partial r_i \partial r_j \partial r_k \partial r_l}, \quad (4.57)$$

these can be written as $V^{(3)}_{Coul} = \sum_{i,j,k} A'^{(3)}_{ijk} r'_i r'_j r'_k$ and $V^{(4)}_{Coul} = \sum_{i,j,k,l} A'^{(4)}_{ijkl} r'_i r'_j r'_k r'_l$, respectively.

Another change of base, this time between the mass-weighted coordinates and the normal modes, needs to be derived to write the expansion in terms of the normal modes. This can be done transposing Eqs. 4.45 and 4.49. In that case, defining

$$G'^{(3)}_{ijk} = \sigma'_{\lambda_1}\sigma'_{\lambda_2}\sigma'_{\lambda_3}\sum_{i,j,k} e'^{i}_{\lambda_1} e'^{j}_{\lambda_2} e'^{k}_{\lambda_3} A'^{(3)}_{ijk} \text{ and } G'^{(4)}_{ijkl} = \sigma'_{\lambda_1}\sigma'_{\lambda_2}\sigma'_{\lambda_3}\sigma'_{\lambda_4}\sum_{i,j,k,l} e'^{i}_{\lambda_1} e'^{j}_{\lambda_2} e'^{k}_{\lambda_3} e'^{l}_{\lambda_4} A'^{(4)}_{ijkl} \quad (4.58)$$

(where $\sigma'_\lambda = \sqrt{\hbar/(2\Omega_\lambda)}$) and taking into account that the position operators associated to each of the modes, R'_λ, that accompany these can be written in terms of the ladder operators as $R'_\lambda = \sigma'_\lambda\left(\hat{a}^\dagger_\lambda + \hat{a}_\lambda\right)$,

$$V^{(3)}_{Coul} = \sum_{\lambda_1,\lambda_2,\lambda_3} G'^{(3)}_{ijk}\left(\hat{a}^\dagger_{\lambda_1} + \hat{a}_{\lambda_1}\right)\left(\hat{a}^\dagger_{\lambda_2} + \hat{a}_{\lambda_2}\right)\left(\hat{a}^\dagger_{\lambda_3} + \hat{a}_{\lambda_3}\right) \quad (4.59)$$

and

$$V^{(4)}_{Coul} = \sum_{\lambda_1,\lambda_2,\lambda_3,\lambda_4} G'^{(4)}_{ijkl}\left(\hat{a}^\dagger_{\lambda_1} + \hat{a}_{\lambda_1}\right)\left(\hat{a}^\dagger_{\lambda_2} + \hat{a}_{\lambda_2}\right)\left(\hat{a}^\dagger_{\lambda_3} + \hat{a}_{\lambda_3}\right)\left(\hat{a}^\dagger_{\lambda_4} + \hat{a}_{\lambda_4}\right) \quad (4.60)$$

result. Once these are available, calculating the correction to the energy is a matter of evaluating brackets of combinations of ladder operators (see Ref. [106]). The shift of the transition $n_\lambda \leftrightarrow n_\lambda + 1$, obtained by subtracting the corrections to the $n_\lambda + 1$ and n_λ levels (with all other occupation numbers constant) is then

$$\hbar\Delta\Omega_\lambda\left(\{n_{\lambda'}\},n_\lambda\right)=12\left[\left(n_\lambda+1\right)G'^{(4)}_{\lambda\lambda\lambda\lambda}+\sum_{\lambda'\neq\lambda}G'^{(4)}_{\lambda'\lambda'\lambda\lambda}\left(2n_{\lambda'}+1\right)\right]$$
$$-\frac{36}{\hbar}\sum_{\lambda'\neq\lambda}\left(2n_{\lambda'}+1\right)\left[\frac{2\Omega_{\lambda'}\left(G'^{(3)}_{\lambda'\lambda'\lambda}\right)^2}{4\Omega_{\lambda'}^2-\Omega_\lambda^2}+\frac{2\Omega_\lambda\left(G'^{(3)}_{\lambda\lambda\lambda'}\right)^2}{4\Omega_\lambda^2-\Omega_{\lambda'}^2}+\frac{G'^{(3)}_{\lambda\lambda\lambda}G'^{(3)}_{\lambda'\lambda'\lambda}}{\Omega_\lambda}+\frac{G'^{(3)}_{\lambda'\lambda\lambda}G'^{(3)}_{\lambda'\lambda'\lambda'}}{\Omega_{\lambda'}}\right]$$
$$-\frac{6}{\hbar}\left(n_\lambda+1\right)\left[10\frac{(G'^{(3)}_{\lambda\lambda\lambda})^2}{\Omega_\lambda}-6\sum_{\lambda'\neq\lambda}\frac{\left(G'^{(3)}_{\lambda\lambda\lambda'}\right)^2\Omega_{\lambda'}}{4\Omega_\lambda^2-\Omega_{\lambda'}^2}+12\sum_{\lambda'\neq\lambda}\frac{\left(G'^{(3)}_{\lambda'\lambda\lambda}\right)^2}{\Omega_{\lambda'}}\right]$$
$$-\frac{72}{\hbar}\sum_{\lambda'\neq\lambda}\sum_{\lambda''\neq\lambda',\lambda}\left(G'^{(3)}_{\lambda'\lambda''\lambda}\right)^2\left[\frac{\left(n_{\lambda'}-n_{\lambda''}\right)\left(\Omega_{\lambda''}-\Omega_{\lambda'}\right)}{\left(\Omega_{\lambda''}-\Omega_{\lambda'}\right)^2-\Omega_\lambda^2}+\frac{\left(n_{\lambda'}+n_{\lambda''}+1\right)\left(\Omega_{\lambda''}+\Omega_{\lambda'}\right)}{\left(\Omega_{\lambda''}+\Omega_{\lambda'}\right)^2-\Omega_\lambda^2}\right]$$
$$-\frac{36}{\hbar}\sum_{\lambda'\neq\lambda}\frac{G'^{(3)}_{\lambda'\lambda\lambda}}{\Omega_{\lambda'}}\left[\sum_{\lambda''\neq\lambda',\lambda}G'^{(3)}_{\lambda'\lambda''\lambda''}\left(2n_{\lambda''}+1\right)\right]..\tag{4.61}$$

The so-called *cross-coupling matrix*, which relates frequency shifts with occupation numbers, is obtained by differentiating with respect to the occupation numbers. In the case of the diagonal terms,

$$S_{\lambda\lambda}=\frac{\partial\left(h\Delta f_\lambda\right)}{\partial n_\lambda}=12G'^{(4)}_{\lambda\lambda\lambda\lambda}-\frac{6}{\hbar}\left[10\frac{\left(G'^{(3)}_{\lambda\lambda\lambda}\right)^2}{\Omega_\lambda}-6\sum_{\lambda'\neq\lambda}\frac{\left(G'^{(3)}_{\lambda'\lambda'\lambda}\right)^2\Omega_\lambda}{4\Omega_{\lambda'}-\Omega_\lambda}+12\sum_{\lambda'\neq\lambda}\frac{\left(G'^{(3)}_{\lambda\lambda'\lambda'}\right)^2}{\Omega_{\lambda'}}\right],\tag{4.62}$$

whereas for the off-diagonal ones,

$$
\begin{aligned}
S_{\lambda\lambda'} &= \frac{\partial\left(h\Delta f_\lambda\right)}{\partial n_{\lambda'}} \\
&= 24G'^{(4)}_{\lambda'\lambda'\lambda\lambda} \\
&\quad - \frac{72}{\hbar}\Bigg[\frac{2\Omega_{\lambda'}\left(G'^{(3)}_{\lambda'\lambda'\lambda}\right)^2}{4\Omega_{\lambda'}^2-\Omega_\lambda^2} + \frac{2\Omega_\lambda\left(G'^{(3)}_{\lambda\lambda\lambda'}\right)^2}{4\Omega_\lambda^2-\Omega_{\lambda'}^2} + \frac{G'^{(3)}_{\lambda\lambda\lambda}G'^{(3)}_{\lambda'\lambda'\lambda}}{\Omega_\lambda} + \frac{G'^{(3)}_{\lambda'\lambda\lambda}G'^{(3)}_{\lambda'\lambda'\lambda'}}{\Omega_{\lambda'}} \\
&\quad + \sum_{\lambda''\neq\lambda',\lambda}\Bigg(\left[\left(G'^{(3)}_{\lambda'\lambda''\lambda}\right)^2+\left(G'^{(3)}_{\lambda''\lambda'\lambda}\right)^2\right]\left[\frac{\Omega_{\lambda''}-\Omega_{\lambda'}}{\left(\Omega_{\lambda''}-\Omega_{\lambda'}\right)^2-\Omega_\lambda^2}+\frac{\Omega_{\lambda''}+\Omega_{\lambda'}}{\left(\Omega_{\lambda''}+\Omega_{\lambda'}\right)^2-\Omega_\lambda^2}\right] \\
&\qquad\qquad + \frac{G'^{(3)}_{\lambda'\lambda\lambda}G'^{(3)}_{\lambda'\lambda''\lambda''}}{\Omega_{\lambda'}}\Bigg)\Bigg].
\end{aligned}
\tag{4.63}
$$

The cross-coupling matrix for e.g. the $^{257}\mathrm{Rf}^+$–$^{40}\mathrm{Ca}^+$ pair under the trap configuration $\omega_{zs} = 2\pi \cdot 100$ kHz and $\omega_{cs} = 2\pi \cdot 2.689$ MHz is [97]

$$
\begin{pmatrix}\Delta\Omega_+^- \\ \Delta\Omega_+^+ \\ \Delta\Omega_z^+ \\ \Delta\Omega_z^- \\ \Delta\Omega_-^+ \\ \Delta\Omega_-^-\end{pmatrix} = 2\pi\cdot\begin{pmatrix}
0.0004 & 0.0016 & -0.0162 & -0.0012 & 0.3967 & 0.0000 \\
0.0016 & 0.0004 & -0.0124 & -0.0010 & 0.4942 & 0.0004 \\
-0.0162 & -0.0124 & 0.0469 & 0.0172 & -1.2477 & 0.0000 \\
-0.0012 & -0.0010 & 0.0172 & -0.0014 & 2.0643 & 0.0000 \\
0.3967 & 0.4942 & -1.2477 & 2.0643 & -0.4094 & -0.0003 \\
0.0000 & 0.0000 & 0.0000 & 0.0000 & -0.0003 & 0.0000
\end{pmatrix}\cdot\begin{pmatrix}n_+^- \\ n_+^+ \\ n_z^+ \\ n_z^- \\ n_-^+ \\ n_-^-\end{pmatrix}\ \mathrm{Hz}.
\tag{4.64}
$$

It is relevant to see that a presence of even a few quanta in the stretch magnetron motion introduces significant shifts in the frequencies of all modes. The next mode in terms of size of the arising shifts is the axial stretch mode.

4.4 Mass measurements using the unbalanced two-ion crystal

Once the motion of the unbalanced two-ion crystal has been characterized, a way to measure the relevant frequencies and, from these, obtain the crystal's mass ratio μ is needed. Given the large amplitude-dependent shifts that appear due to the Coulomb

interaction's anharmonicity (see Sec. 4.3), especially in the stretch magnetron and stretch axial modes, a procedure similar to that presented in Refs. [101, 102] to measure all the crystal's eigenfrequencies becomes unfeasible. Two possibilities remain. The common axial mode alone, whose frequency can be linked to the mass ratio, can be used by itself to perform non-destructive identification of an ion. This mode presents a moderate amplitude dependent frequency shift that must nevertheless be accounted for (see Sec. 6.4). This could potentially be corrected, given that the sensor ion's oscillation amplitude is the actual measured quantity. If better performance is required, all modes need to be involved. This can only be done in the quantum regime, where the shifts are smaller and, more importantly, non-classical measurement procedures can be used [107]. This section will present both possibilities.

4.4.1 Heavy ion identification using the common axial mode

From Eq. 4.13b, zeroing out the determinant of the matrix $Q_z\left(\Omega/\omega_{zs}\right)$,

$$\det\left[Q\left(\frac{\Omega}{\omega_{zs}}\right)\right]=0 \implies \mu=\frac{1}{\left(\frac{\Omega_z^{\pm}}{\omega_{zs}}\right)^2}\left[\frac{\left(\frac{2\kappa}{\kappa+1}\right)^2}{\left(\frac{\Omega_z^{\pm}}{\omega_{zs}}\right)^2-\left(1+\frac{2\kappa}{\kappa+1}\right)}+\left(\kappa+\frac{2\kappa}{\kappa+1}\right)\right]. \tag{4.65}$$

Differentiating with respect to the frequency ratio $\Omega_z^{\pm}/\omega_{zs}$, and taking into account that

$$\Delta\left(\frac{\Omega_z^{\pm}}{\omega_{zs}}\right)=\frac{\Omega_z^{\pm}}{\omega_{zs}}\sqrt{\left(\frac{\Delta\Omega_z^{\pm}}{\Omega_z^{\pm}}\right)^2+\left(\frac{\Delta\omega_{zs}}{\omega_{zs}}\right)^2}\simeq\frac{\Omega_z^{\pm}}{\omega_{zs}}\frac{\Delta\Omega_z^{\pm}}{\Omega_z^{\pm}}, \tag{4.66}$$

(where $\Delta\omega_{zs}/\omega_{zs}$ is neglected because ω_{zs} is the axial frequency of the sensor ion and is therefore not subjected to the systematics introduced by the presence of a second ion), the uncertainty in μ can be expressed as

$$\Delta\mu=\left|\frac{\partial\mu}{\partial\left(\Omega_z^{\pm}/\omega_{zs}\right)}\right|\Delta\left(\frac{\Omega_z^{\pm}}{\omega_{zs}}\right)\simeq\left|\frac{\partial\mu}{\partial\left(\Omega_z^{\pm}/\omega_{zs}\right)}\right|\frac{\Omega_z^{\pm}}{\omega_{zs}}\frac{\Delta\Omega_z^{\pm}}{\Omega_z^{\pm}} \implies$$
$$\implies \frac{\Delta\mu/\mu}{\Delta\Omega_z^{\pm}/\Omega_z^{\pm}}=\frac{1}{\mu}\frac{\Omega_z^{\pm}}{\omega_{zs}}\left|\frac{\partial\mu}{\partial\left(\Omega_z^{\pm}/\omega_{zs}\right)}\right|. \tag{4.67}$$

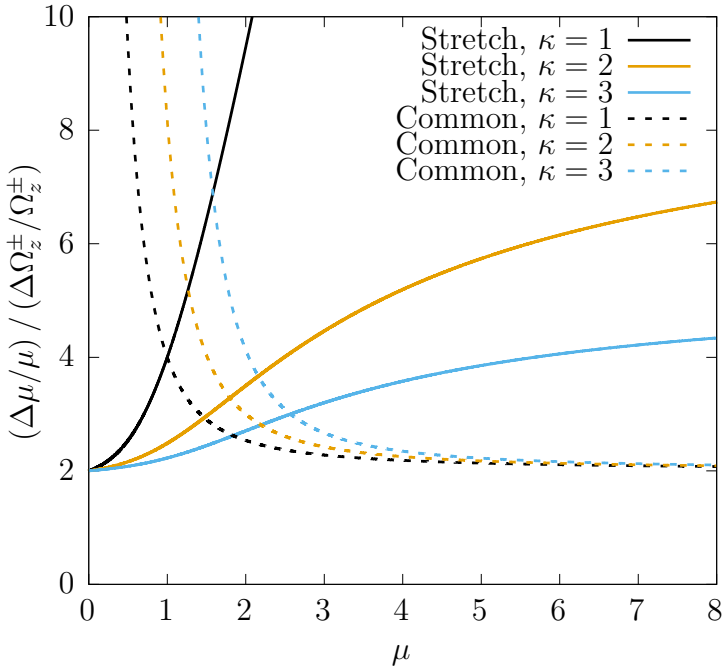

Figure 4.12: Relationship between relative uncertainties in mass and axial frequencies.

The relationship between the relative uncertainty in the mass ratio μ and the axial eigenfrequencies of the crystal $\Omega_z^{\pm}$ that arises from these expressions is shown in Fig. 4.12. The dependency in the charge ratio κ is implicit in the derivative on the right-hand side of Eq. 4.67. The stretch modes are shown for completeness only, since the large systematic errors that would arise when measuring its frequency (see Sec. 4.3). It becomes clear that for target ions significantly heavier than the sensor ion one obtains

$$\frac{\Delta\mu}{\mu} \simeq 2\frac{\Delta\Omega_z^-}{\Omega_z^-}\,. \tag{4.68}$$

This enables a determination of the mass ratio of the two ions by measuring only two frequencies, only one of which is a crystal frequency. However, since these are axial frequencies (determined by the electrostatic field) the voltage stability becomes paramount. As shown in Sec. 4.1.2, the crystal's eigenfrequencies are proportional to the axial frequency of the sensor ion. Since the latter responds to trapping voltage fluctuations as $\delta\omega_{z,s}/\omega_{z,s} = \delta U/2U$, the fluctuations of the common axial frequency would be $\delta\Omega_z^-/\Omega_z^- = \Omega_z^-/\omega_{z,s} \cdot \delta U/2U$. For our expected value of $\delta U/2U \sim 10^{-7}$, this should be second to the amplitude dependent shifts in limiting the achievable uncertainty. This procedure may therefore be best suited for non-destructive iden-

tification of heavy ions, e.g. monitoring the mass of a trapped SHE by driving the crystal near the resonance frequency until an α decay happens. At that point the driving will no longer be on resonance, and the sensor ion will no longer oscillate visibly.

4.4.2 Heavy ion mass determination using all modes of motion

As presented in Sec. 4.1.5, there is a relationship between the crystal's eigenfrequencies and the target ion's free cyclotron frequency (and therefore the target mass). However, the frequency shifts that arise due to the Coulomb interaction's anharmonicity are not among the imperfections the generalized invariance theorem is impervious to. Therefore, an excelent level of control of each of the modes of motion is required.

Ref. [108] studies the limits of Doppler and sideband cooling of a single ion in a Penning trap. Doppler cooling with *axialization* (coupling of the radial modes) is shown to cool down to ∼100 quanta for both the magnetron and modified-cyclotron motions in a wide range of trap configurations. The large shifts that arise with such quantum numbers, especially for the stretch magnetron motion, hinder any attempts to precisely measure all six of the crystal's eigenfrequencies. Cooling to the ground state of motion is therefore a must if such a measurement is to be done. For a single ion in a Penning trap, occupation numbers $\langle n_+ \rangle < 1$ and $\langle n_- \rangle \sim 1$ have been reported [108]. It remains to be seen how these will translate into an asymmetric cristal. Cooling to near the ground state of unbalanced crystals has already been achieved in Paul traps [109, 110].

Once cooling to the ground state of the unbalanced ion has been translated into the Penning trap, there are several possibilities to determine the eigenfrequencies of the unbalanced crystal. Procedures using non-classical methods have been employed to measure motional frequencies [107] of a single ion in a Paul trap. A thorough study of the possibilities is being developed for this particular case [111].

It is relevant to note that, depending on the desired precision, it may not be necessary to measure all six of the crystal's eigenfrequencies using the target ion. A more readily available ion may be used in some cases, since some of the frequencies (stretch cyclotron and both magnetron frequencies) are quite mass insensitive. For example, the difference between the stretch cyclotron frequencies of the crystals $^{257}Rf^{2+}$–$^{40}Ca^{+}$

and $^{208}Pb^{2+}$–$^{40}Ca^{+}$ is under 0.3 Hz – using this value would introduce a systematic error in the order of $6 \cdot 10^{-7}$. The variation in the magnetron frequencies is larger, with 0.7 and 3 Hz for the common and stretch magnetron modes, respectively. The systematic errors that would be introduced are $\sim 10^{-9}$ and $\sim 10^{-8}$. Depending on the desired precision, these frequencies will have to be measured, or the estimation will suffice. One could also correct the reference values, based on the existing mass value for the target ion.

Chapter 5

Control system for unbalanced two-ion crystal experiments

The previous Chapter presented the search for a non-destructive mass measurement technique using a laser-cooled ion as a detector. The motion of the resulting two-ion crystal was studied. Six modes of motion appear, described extensively in Sec. 4.1. After studying the effects of the Coulomb interaction's anharmonicity (see Sec. 4.3), there are two possibilities: either a measurement based on the determination of the common axial mode's frequency (similar to those presented in Refs. [102, 101]) for identification at Doppler limit energies, or a measurement of all the crystal's eigenfrequencies in the quantum regime.

An advanced system for the control of the experiment and data acquisition is required in order to perform these measurements. There are many types of devices involved, such as lasers (up to 13 beams for the simplest approach to Doppler and ground state cooling, see Sec. 2.4), power supplies, fast switches and radiofrequency sources for the control portion, and Electron-Multiplying Charge-Coupled Devices (EMCCD) cameras or PhotoMultiplier Tubes (PMT) for acquisition. Precise timing control is required e.g. to transport and manipulate ions or to synchronize control and acquisition.

Before and during a significant portion of this work, the aforementioned tasks were achieved with a mix of software solutions. To define the timing and to control RF generators, GSI's *CS* framework [112, 113, 114] in combination with MSU's *MM6* sequencer and GUI [115, 116, 117] were used. More details on the implementation of these in the laboratory can be found in Ref. [59]. While this combination has many advantages, it was never made to perform laser cooling or optical detection.

Instead, a customized program was used to control the lasers [118] and the EMCCD and PMT general purpose software, provided by the manufacturers, were used for acquisition. Analysis of the images was then performed manually after the measurements had been carried out. Therefore, there was no unified control and data acquisition software in the laser experiments reported in Refs. [102, 105, 119], nor feedback during the measurements due to the lack of simultaneous analysis.

A unified software solution, and especially automated analysis, was therefore needed. A system based on ARTIQ (*Advanced Real-Time Infrastructure for Quantum physics* – see Ref. [120]) was chosen. This Chapter will justify the choice and report on the creation of an integrated control and data acquisition system for mass measurements based on optical detection using unbalanced two-ion crystals. The control of the experiment, except for the lasers[1], as well as the acquisition, have been addressed.

5.1 The ARTIQ ecosystem

The ARTIQ ecosystem consists of software and hardware. The software is referred to as ARTIQ as well, whereas the hardware is called *Sinara*. Both are open source.

The software uses a Python dialect as a programming language to describe the experiments. An interpreted language is not the best solution when precise timing is required – that is why the quasi-Python code is compiled and run on an FPGA card. This results in nanosecond-level resolution and sub-microsecond-level latencies. It can therefore maintain the exacting timing performance needed for experiments involving ion manipulation and transport, while enabling the use of optical detection hardware, namely EMCCD cameras and PMTs. Given its Python roots, many existing packages can be used to automate analysis as well.

The Sinara hardware, on the other hand, revolves around a FPGA card and is modular. The FPGA carrier presents *Eurocard Extension Module* (EEM) connectors, to which a number of devices can be connected[2]. The Sinara hardware cannot fulfill

[1] In the short term, control of the lasers will be integrated by using ARTIQ's DAC in combination with the double pass AOM setup described in Ref. [118]. However, that relies solely on calibration, since there is no feedback of the resulting laser frequency. To solve this, the existing ARTIQ software to control a HighFinesse wavemeter or custom drivers for the Menlo frequency comb [121] can be used to have live frequency feedback. There are two alternative solutions. In an online conference (*ARTIQ day*) within the COST Action CA17113, two possibilities were presented: either the Master Control Program (MCP) package, created by K. Singer, or even new firmware for the wavemeter created by ARTIQ's parent company, could be used.

[2] Development of new modules is still ongoing. The best place to look for the existing and in-development modules is Sinara's GitHub page and, in particular, the Wiki [122].

all of the experimental requirements. However, ARTIQ is prepared to work with devices outside its ecosystem using the so-called *Simple Python Communications* (SyPiCo) library, provided a driver is created for the purpose. Thanks to this possibility, devices already present in the laboratory (such as DC voltage power supplies, arbitrary function generators or the EMCCD camera) could be incorporated in the new system.

The most relevant Sinara modules for this particular use case are the *Digital Input-Output* modules, that provide TTL signals for timing control. Three modules, with eight channels each, were chosen when configuring the crate. The features, which are sufficient for the experiments envisioned in this work, include an output channel impedance of 50 Ω, a minimum pulse width of 3 ns, and a maximum toggle rate of 150 MHz with 50 % duty cycle.

The other modules incorporated in the crate configuration are:

- *Zotino*: 32 channel *Digital-to-Analog Converter* (DAC) with a ±10 V range and 16-bit resolution
- *Urukul*: 4 channel *Direct Digital Synthesis* (DDS)-based frequency synthesizer with a 1-400 MHz range and 32-bit frequency resolution
- *Sampler*: 8 channel *Analog-to-Digital Converter* (ADC) with 16-bit resolution and a sample rate up to 1.5 MHz
- *Grabber*: a *frame grabber* that reads the EMCCD output using the *CameraLink* interface, therefore bypassing the slow USB connection. However, it does not allow the use of the full sensor – instead, the number of counts within several *Regions Of Interest* (ROIs) is read out.

A detailed description of the full capabilities and usage of the base ARTIQ software is beyond the scope of this work. Such a description can be found in the manual [123]. A description of some concepts, however, is relevant to understand the work done to incorporate new devices to the control system aiming at monitoring the two-ion crystal and to analyze the data on-line.

In terms of timing performance, the devices that form the control system can be classified into those that can provide good temporal resolution and low latency, which are referred to as *realtime hardware*. These are the Sinara modules, connected via EEM to the FPGA carrier. On the other hand, devices that communicate

using slower channels, such as USB, and therefore cannot achieve the same timing performance, are referred to as *non-realtime hardware*. In ARTIQ, the former are controlled by code that is compiled and runs at the FPGA (the so-called *kernels*), whereas the latter are controlled by regular Python code that is run in a PC.

A kernel can execute Python code in a PC using the *Remote Procedure Call* (RPC) mechanism. This procedure is transparent to the user. The RPC mechanism is used, among other things, to communicate with the non-realtime hardware. The software that controls this hardware and enables communication is called *Network Device Support Package* (NDSP). They are composed of two main parts:

- The *driver*: this is the Python code that actually communicates with the device. For it to be part of a NDSP, the driver functions must be methods of a single object, an a *simulation mode* and *ping* method must be implemented.
- The *controller*, which instantiates, initializes and terminates the driver. It is usually started by one of ARTIQ's components (the *controller manager*) and is kept running continuously. It then receives commands from the client (either over the network or from the PC in which it is running through the *localhost* interface), performs the actions and returns the results. It can be configured to run the driver in simulation mode (e.g. for debugging), and it calls the ping method every 30 s to verify that the connection with the device is still working.

Optionally the NDSP can also have a *client* (a generic one, provided with ARTIQ, often suffices) and a *mediator* when core devices (such as a TTL channel) are to be used within the driver.

In the following, the creation of a few NDSPs to incorporate additional hardware into the control system is presented.

5.2 Extending ARTIQ

The devices (already available in the lab) used to address the experimental requirements that fall outside of the Sinara modules' capabilities are:

- Two Agilent 33210A function generators for signals under 1 MHz, which will be used to drive the motional modes (since only one of the modes is above 1 MHz for ions heavier than ~ 100 u for usual operating conditions, see Chapter 4)

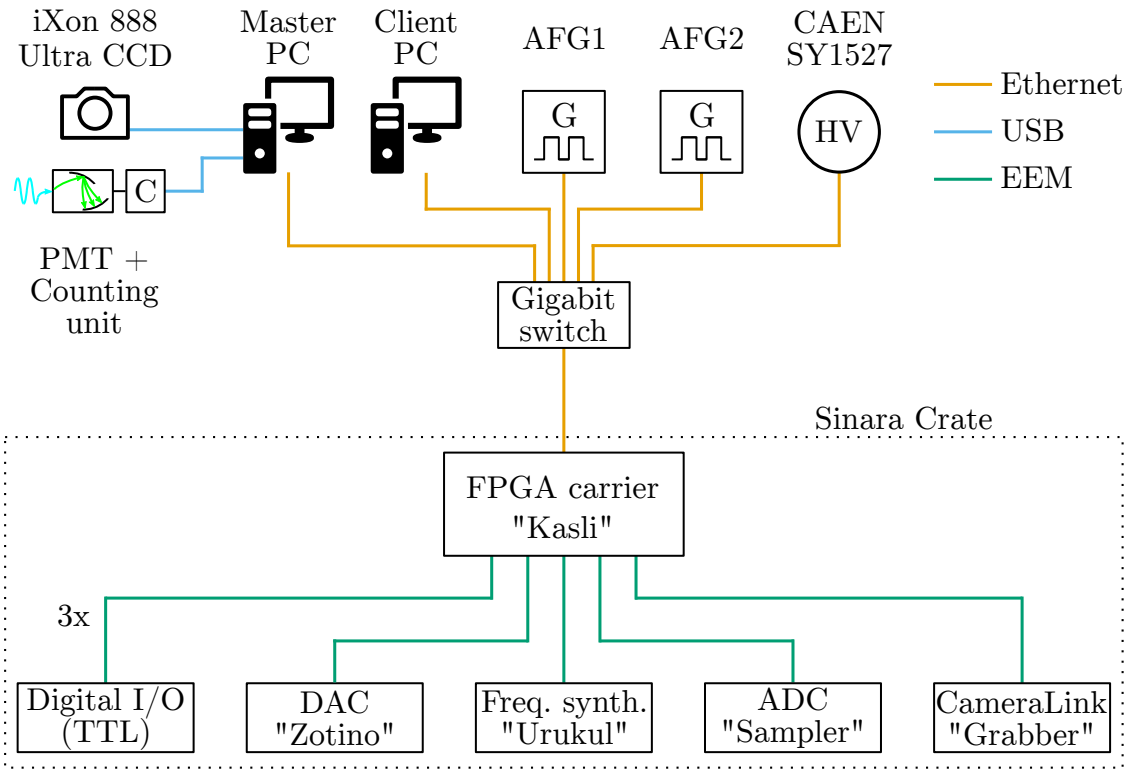

Figure 5.1: Sketch of the devices involved in the control and acquisition system. The Sinara crate contains the FPGA card and the TTL outputs used to control the timing. The voltages can be provided either by Sinara's Zotino card or the CAEN SY1527 crate. The USB connection is used instead of the crate's frame grabber card to obtain the full camera image.

- A CAEN SY1527 crate with several boards, including a CAEN A1510 12-channel floating power supply with 100 V range and 20 mV resolution, that will be used to set the voltages of any trap electrodes requiring more than 10 V

- An Andor iXon Ultra 888 EMCCD camera used to image the laser-cooled ions, and

- A Hamamatsu PMT connected to the C8855-01 counting unit which is used if the spatial distribution of the fluorescence is not relevant

The complete setup, including the Sinara crate and these devices, together with the connections that join them, is shown in Fig. 5.1. NDSPs were created to incorporate these devices into the control system – they will be presented in the following, classified according to the method used to communicate with the device.

5.2.1 Trapping potentials: CAEN power supply

To operate the open-ring Penning trap, voltages larger than 10 V are required. This means that the Zotino DC power supply integrated in the Sinara module does not suffice for this purpose. In the past, the CAEN SY1527 has been used to bias the trap electrodes. This system can be used in custom software, since the vendor provides the CAENHVWrapper library [124]. This library, given as a `.lib` file, is statically linked. This means that the common method using to integrate C code into Python (the `ctypes` library) will not work. That does not mean that such libraries cannot be used – statically linked C libraries can be integrated in Python if one builds a *Python Extension Module* (PEM) [125].

To create a PEM, Python's *Application Programming Interface* (API), a C library that contains Python-like structures, is used. The API is provided by the Python installation – one needs to use an `include` preprocessing directive that tells the compiler where this library can be found. One would then *wrap* the functions from the original library using only the Python-like data structures for input and output. This is considered a *thin* wrapper, since it does not perform actions on its own – it just converts data structures and calls functions from the vendor library. For example, to wrap the initialization procedure, whose signature is

```
CAENHVRESULT CAENHV_InitSystem( CAENHV_SYSTEM_TYPE_t system,
            int LinkType, void *Arg, const char *UserName,
            const char *Passwd, int *handle);
```

one would create something akin to the C function shown in Snippet 5.1. Two conversions are made in that function: the first (from Python data structures to C data structures) is carried out by the `PyArg_ParseTuple` function. This function parses the `args` variable, which is a *tuple* that contains the arguments given when called (in Python) and stores them into C variables, in this case, `IP`, `status`, `user` and `password`. If there is a problem during the parsing process, the function returns `false`, and the call to the vendor's library does not take place. The second conversion takes place at the return statement: the C integer handle is converted to a Python integer using the `PyLong_FromLong` function. For other types of returned variables there are similar functions, such as `PyFloat_FromDouble` or `PyUnicode_FromStringAndSize`. Note that no attempt to manage errors has been made, other than returning a negative handle value if there is a problem. This is again because the PEM is a thin layer created to deal only with the conversion between C and Python data structures – all the error handling is done in Python,

```
#include "/path/to/Python.h"

static PyObject *method_initsystem(PyObject *self, PyObject *args)
{
    char *IP, *user, *passwd;
    int status=-1, handle=-1;

    if(!PyArg_ParseTuple(args, "siss", &IP, &status, &user, &passwd))
        handle=-1;

    else
    {   // SY1527, LINKTYPE_TCPIP are constants defined elsewhere
        status=CAENHV_InitSystem(SY1527,LINKTYPE_TCPIP,IP,user,
                                                    passwd, &handle);
        if (status!=CAENHV_OK) handle=-1;
    }

    return PyLong_FromLong(handle);
}
```

Snippet 5.1: Extract of the CAEN shim layer.

taking advantage of its features.

Once the necessary functions have been wrapped, a `distutils` package is created to install the wrapper into the Python environment. With these thin wrappers available in the Python environment, the NDSP can be created.

Due to timeout issues, the CAEN NDSP is slightly different from those of the Agilent function generators and EMCCD camera (see Secs. 5.2.2 and 5.2.3). Instead of initiating communication with the hardware when the controller is started, dummy `init` and `ping` methods are implemented, and the kernels must open and close the connection to perform any voltage changes. A use example is given in Snippet 5.2. The interaction between the different layers of the NDSP is presented as a *execution specification UML diagram* in Fig. 5.2.

5.2.2 Driving of the crystal's eigenmotions: radiofrequency generators

To drive any of the modes of motion of the crystal the use of function generators other than Urukul are needed, since most of the eigenfrequencies are below 1 MHz. Two Agilent 33210A are used for this purpose. In this case, the vendor does not provide any drivers that can be used. However, the generators can be controled

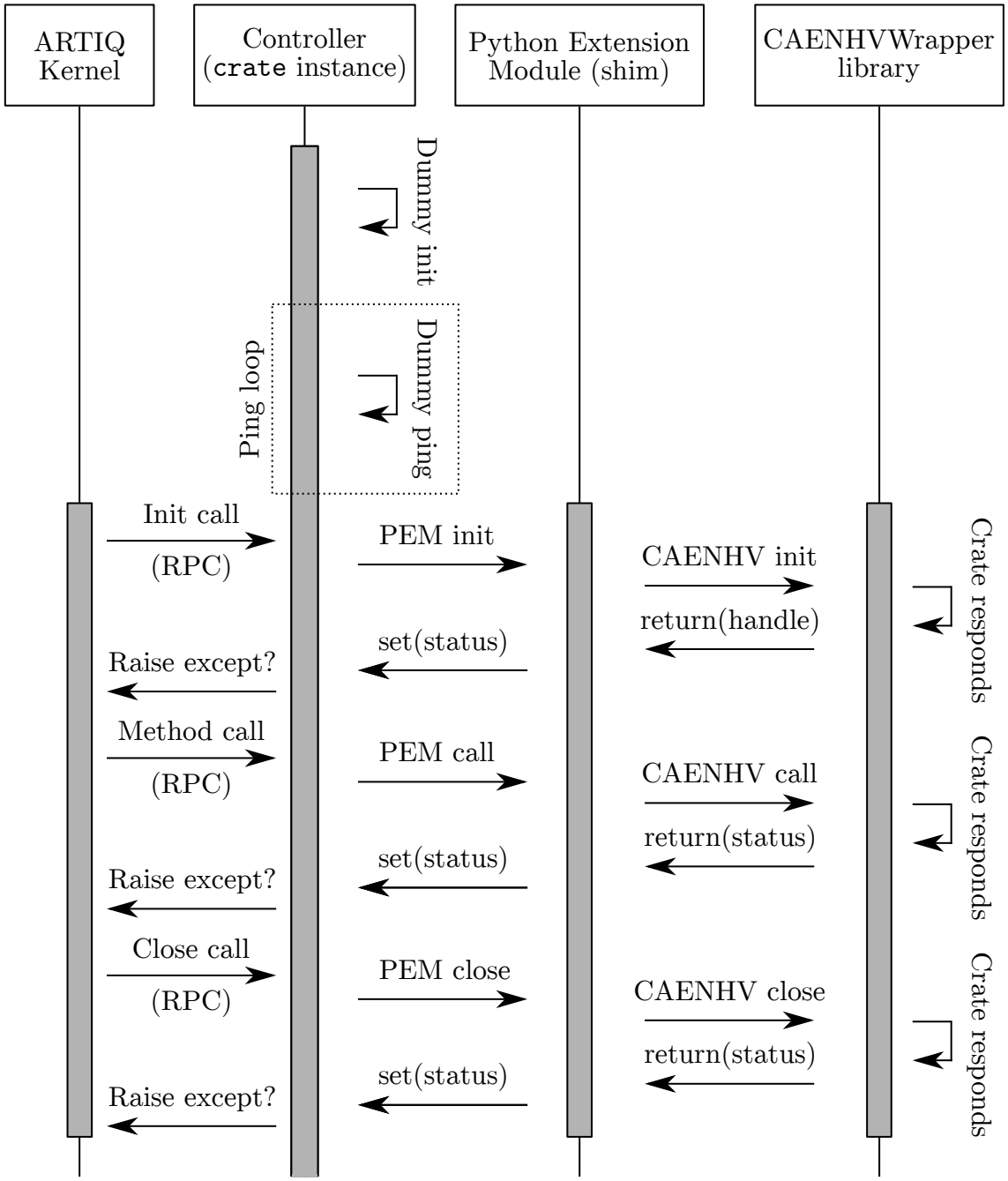

Figure 5.2: Execution specification UML diagram of the CAEN ARTIQ NDSP. The Python Extension Module (PEM) is a very thin wrapper that deals only with the conversion between the original (CAENHVWrapper library) data structures and those of Python. Error handling and other processing is done at the driver level. The controller deviates from a standard NDSP in that the `init` and `ping` methods are dummies (see text for details).

```
import pycaen # This is the PEM layer

class crate():
    def __init__ (self, simulation = True):
        self.simulation = simulation
        self.handle = self.status = -1

    def open (self, IP, simulation = True, user, passwd):
        if not self.simulation:
            self.handle=pycaen.initsystem(IP,user,passwd,self.status)
            if(self.handle < 0):
                # Deal with error
        else:
            self.status=0
            self.handle=0

    def set_voltage(self,slot,channel,value):
        if not self.simulation:
            self.status=pycaen.setvoltage(self.handle,self.status,
                                          slot,channel,value)
            if(self.status != 0):
                # Deal with error
        else:
            pass
```

Snippet 5.2: Extract of the code required to control the CAEN SY1527 power supply with ARTIQ.

using the *Virtual Instrument Software Architecture* (VISA) standard. There are several Python modules to use VISA – in this case, `pyVISA` was chosen.

To control a device using `pyVISA`, an instance of the *resource manager* class is created. Then, the method `open_resource` of this object is called. This call returns an object representing the instrument one wants to control. The methods `write` and `query` are used to communicate with the instrument. The commands that must be submitted to manipulate the device depends on the device itself, so the manual of the particular instrument must be consulted.

In this experiment, only a few of the capabilities of the function generator are actually needed. The frequency and amplitude of the signal, as well as the output status (on or off) need to be manipulated. The gated burst mode (where the output is only applied when the device is triggered externally) is also utilized. A sample of the code, containing the initialization procedure and the method that sets the output frequency, is shown in Snippet 5.3. The rest of the methods are largely

```
class AgilentFunGen:
    def __init__(self, IP, simulation = True):
        self.simulation = simulation
        if not self.simulation:
            rm = pyvisa.ResourceManager()
            self.fg = rm.open_resource(
                        'tcpip0::{}::inst0::instr'.format(IP) )
        else:
            pass

    def frequency(self, freq):
        if not self.simulation:
            self.fg.write('frequency {}'.format(freq))
        else:
            pass
```

Snippet 5.3: Extract of the code required to control Agilent AFGs with ARTIQ.

```
from ctypes import cdll, c_int, byref
library = cdll.LoadLibrary('/path/to/sharedlibrary.so')
my_c_int = c_int()
library.foo( byref( my_c_int ) )
my_py_int = my_c_int.value # "value" is a c_int attribute
```

Snippet 5.4: Example of ctypes usage. The ctypes module enables the use of C shared libraries in a Python environment.

identical. Figure 5.3 shows the interaction between the NDSP layers.

5.2.3 Optical detection: camera and photomultiplier tube

The manufacturer of the EMCCD camera provides drivers in the form of a *dynamically linked library* (the so-called *AndorSDK*). Shared libraries can be used in Python code using the `ctypes` module [125]. `ctypes` provides C-equivalent data structures and allows calling C functions contained in a shared library from Python. In that sense, the integration process is somewhat reversed with respect to what was done for the CAEN power supply in Sec. 5.2.1.

For example, to call a function named `foo` within a library called `sharedlibrary.so` that receives a pointer to an integer and modifies it, one would proceed as shown in Snippet 5.4.

Several things are important in this example. First is the use of ctypes' `byref` function, which passes a variable by reference. Second is the use of the `c_int` class

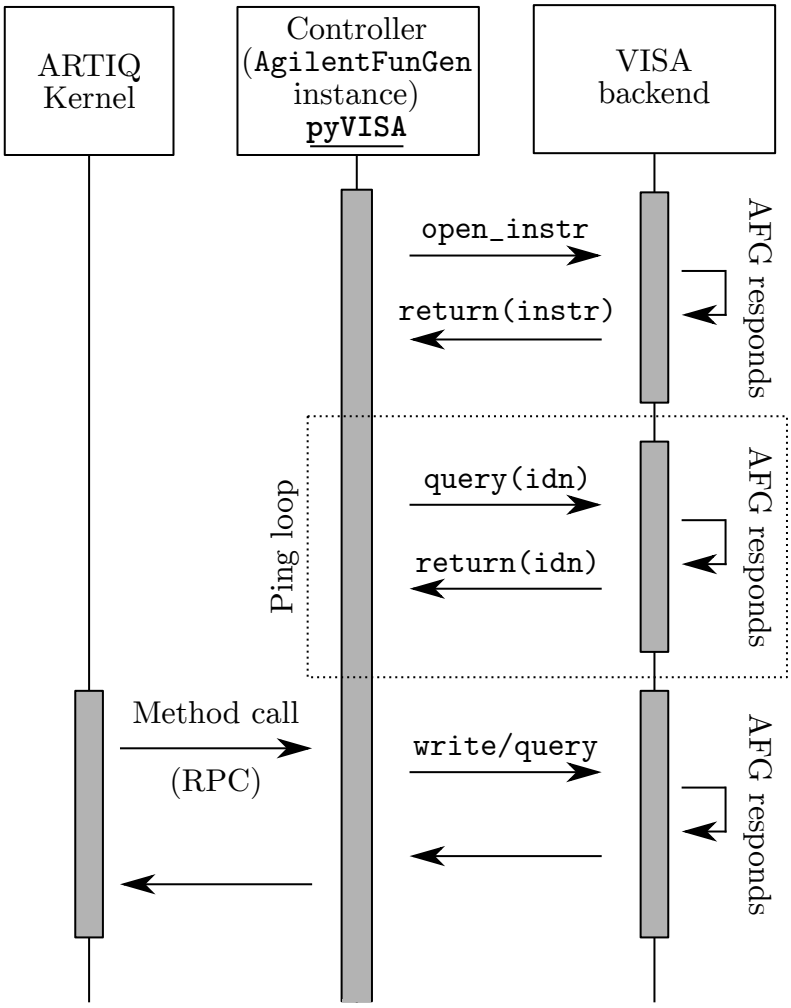

Figure 5.3: Execution specification UML diagram of the Agilent AFG ARTIQ NDSP.

– `my_c_int` is not a regular Python integer, but instead is a C-like integer provided by `ctypes`. Other classes are provided to represent other C data types in Python, e.g. `c_char`, `c_float`, etc. In this manner, a Python wrapper can be made so that the manufacturer's libraries can be used. In the case of the Andor cameras, wrappers do exist that can be adapted for use in ARTIQ by adding a ping method and a simulation mode, to comply with the NDSP requirements. The final driver for the two-ion crystal experiment was created in this work, although several of these wrappers [126, 127] were consulted, especially when it comes to retrieving the image from the EMCCD.

The final structure of the driver contains a class, called `ixon` (middle layer in Fig. 5.5). The class attributes represent the different parameters (e.g. sensor temperature, exposure time, gain, ...). The class methods are used to modify and consult those parameters (*setters* and *getters*) as well as start the acquisition and

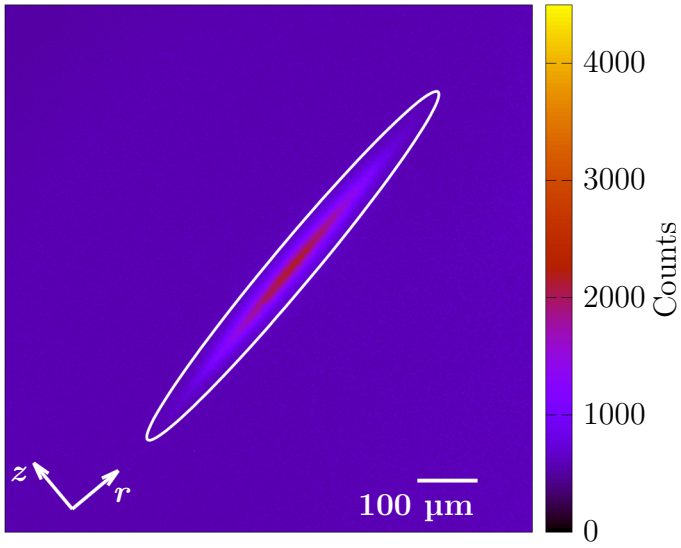

Figure 5.4: Image of a laser-cooled ion cloud obtained using ARTIQ and the Andor EMCCD NDSP. The ellipse is a 3σ contour resulting from a gaussian fit. The gaussian's widths in terms of cloud size are 11.713(83) µm in the axial direction and 125.91(89) µm in the radial direction. Only the axial lasers were present in this case.

retrieve the resulting image (which is stored in another of the class attributes), all using the AndorSDK functions (right layer in Fig. 5.5). The *ping* method calls the AndorSDK function that retrieves the camera's serial name – if the retrieved number is correct, the communication is deemed to be working adequately. The kernels (left layer in Fig. 5.5 call methods of the `ixon` class to perform the desired tasks. This NDSP has already been used to image ion clouds, which are trapped and laser cooled in the Penning trap, as shown in Fig. 5.4.

The EMCCD camera connected via USB will not be the best solution once the quantum regime is obtained. In that moment, the detection is made via a projective measurement that detects whether the ion is in the lower or upper state of its qubit transition. As usual, this is done through the Doppler cooling process – fluorescence is only achieved if the ion is in its ground state. In this scenario the spatial distribution of the fluorescence is no longer relevant, and a faster detection is desirable. Sinara's frame grabber card allows the definition of tens of ROIs, for which the number of counts (but not the count distribution) is read. The frame grabber bypasses the slow USB connection, achieving much lower latencies. Since this is part of Sinara, no drivers have to be created.

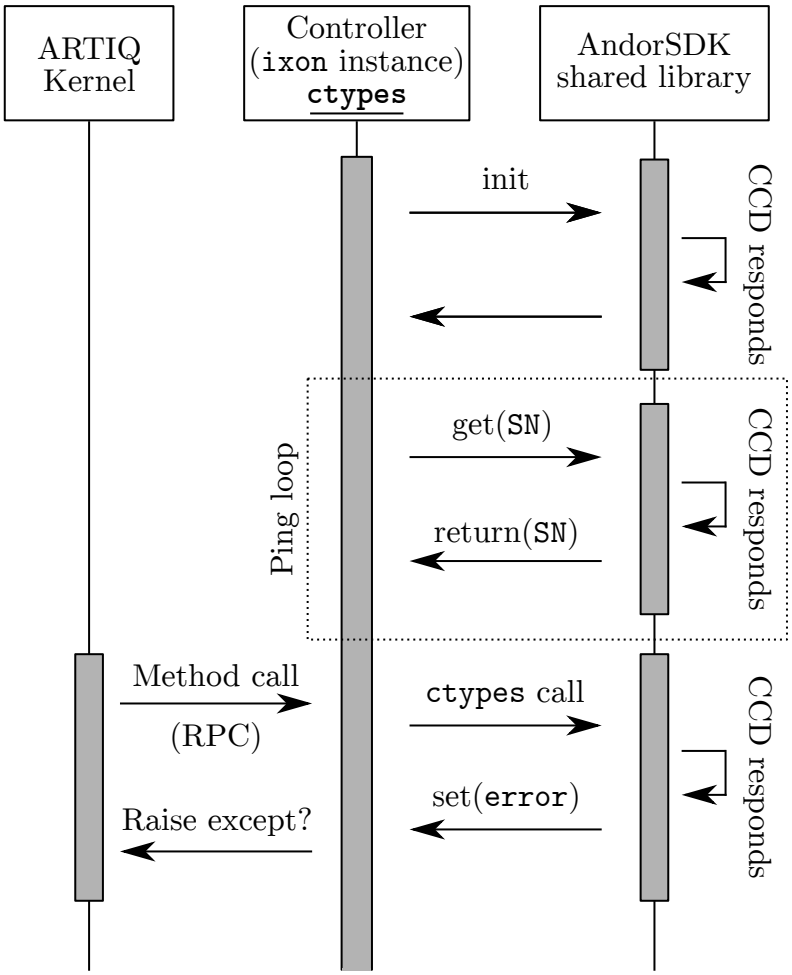

Figure 5.5: Execution specification UML diagram of the Andor iXon ARTIQ NDSP. The controller, which contains an instance of the `ixon` class (the driver) that wraps the vendor-provided library, called AndorSDK. The controller instantiates the driver and pings every 30 s. When an experiment is run, calls are sent to the controller using the Remote Procedure Call (RPC) mechanism.

Alternatively, the use of a PMT has been considered. Tests have been carried out [69] that validate the suitability of the Hamamatsu PMT and counting unit present in the laboratory. The manufacturer provides a dynamically linked library. Therefore, its integration into ARTIQ will be carried out using `ctypes` as well.

Chapter 6

Experimental setup and formation of the two-ion crystal

The Ion Traps and Lasers Laboratory in Granada started its path in 2012, with the primary goal of implementing a novel single-ion-sensitive mass measurement technique. With this aim a Penning-trap facility has been built. This Chapter will present the relevant parts of the Penning-trap facility with emphasis on the developments carried out as part of this Thesis, as well as the characterization results. Special focus will be put on the core of the experiment, the open-ring Penning trap, a novel geometry that has shown great potential for laser-based experiments. Part of the contents of this Chapter were published in Ref. [119].

6.1 The experimental setup

6.1.1 General overview

Figure 6.1 shows a sketch of the Penning traps beamline in the two configurations used in this Thesis. The first configuration, which uses an external ion source and a preparation Penning Trap, was used to perform a TOF-ICR measurements of calcium to precisely determine the magnetic field. The second configuration uses an internal ion source to perform laser cooling experiments. Both configurations could be merged if the photoionization lasers were inserted together with the other axial laser beams, or if the ion source is placed at a 90-degree angle with the rest of the beamline. Indeed, a new source, produced at GSI [128], is being installed at the quadrupole bender.

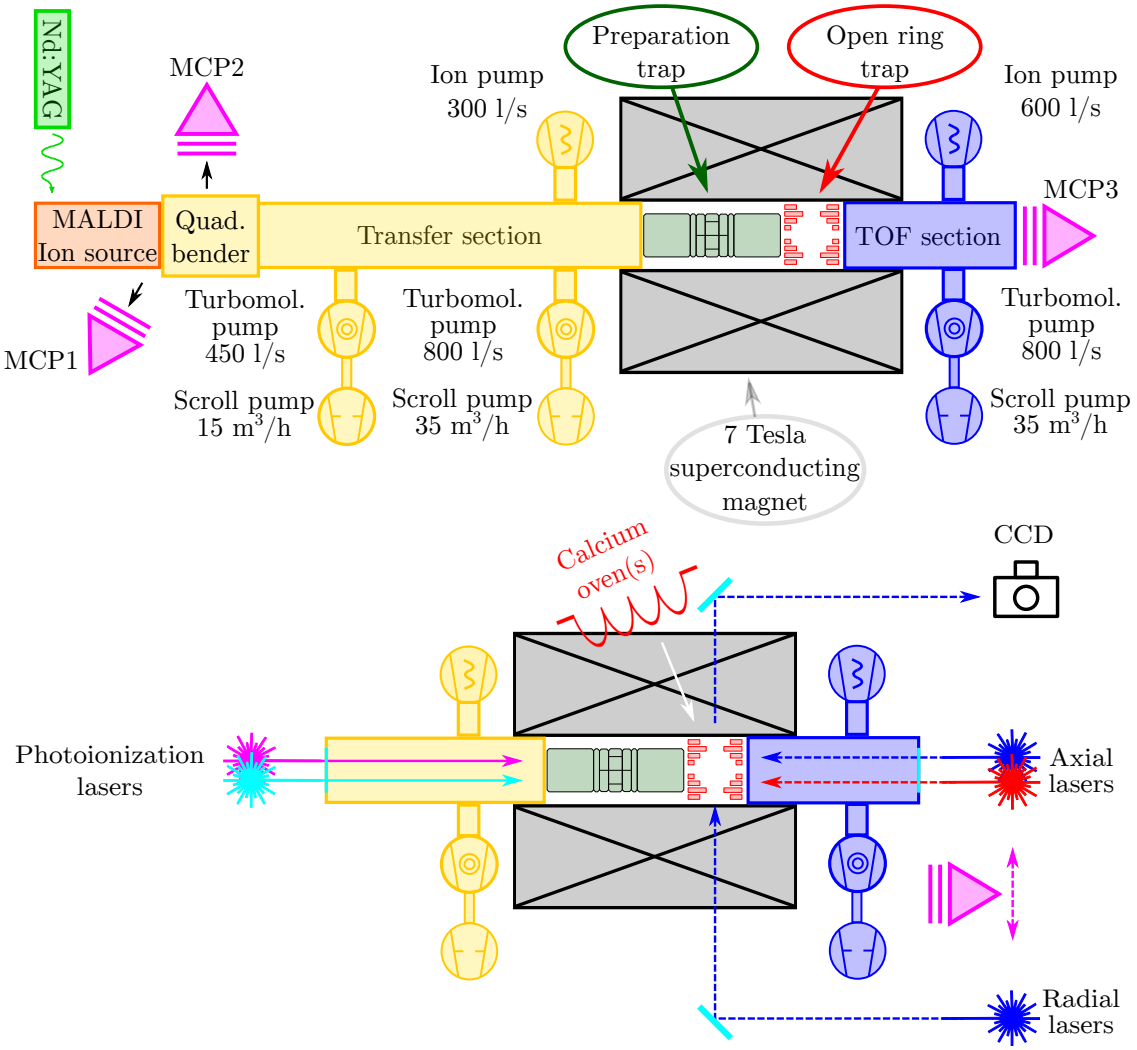

Figure 6.1: Sketch of the two configurations of the Penning trap setup used in this Thesis. See text for details. Top: configuration used to perform TOF-ICR with the open-ring Penning trap with any ion species produced in the laser desorption ion source. This, the transfer section and preparation Penning trap [59] are used in this configuration. The ions are detected by means of an MCP. Bottom: configuration used to perform laser cooling. The internal (photoionization) ion source developed in this Thesis is used. Cooling lasers are inserted axially and radially, while repumping lasers are inserted only in the axial direction. An adjustable mirror mount placed inside the magnet can be used to adjust the position of the radial laser beams. The scattered photons are also collected in the radial direction. Note that the radial laser injection and fluorescence collection systems are in a CF100 vacuum tube in the room-temperature magnet bore; they are depicted outside this tube for clarity. The MCP detector (MCP3) is maintained for diagnosis purposes. Labels common to both configurations are omitted to improve readability.

In the following, a general overview will be presented – Sec. 6.1.2 will delve deeper into the improvements implemented during the course of this work.

Ion production

Ions can be produced at one of two places: either at a metallic plate by laser desorption [129, 130] (which was used to prove cooling resonances [59] and TOF-ICR [119]) or directly at the trap center through photoionization of neutral calcium atoms evaporated from a comercial oven (see Sec. 6.1.2).

The laser desorption ion source is a slightly modified version of the commercial system Reflex III from Brucker Analytical Systems. A movable plate with several samples, including calcium, gold, rhenium, osmium and a small sample of isotopically enriched ^{48}Ca, provides several choices of ionic species. A Q-switched, frequency doubled Nd:YAG laser ($\lambda \simeq 532$ nm) from the Litron Nano series is used for the desorption process. The system originally incorporates a MicroChannel Plate (MCP), which is now used for diagnostics. An Edwards scroll pump and two Pfeiffer turbomolecular pumps provide vacuum at the ion source.

Laser desorption will be also carried out using a target coupled to a miniature Radio Frequency Quadrupole (mini-RFQ) structure filled with helium gas built at GSI [128]. Such a system is currently under commissioning, placed in a vacuum CF160 cross where an electrostatic quadrupole bender (see Fig. 6.1) is placed. The mini-RFQ is oriented perpendicular to rest of the beamline, so that it does not interfere with the axial lasers.

Transfer section

Downstream from the ion source, the so-called *transfer section* starts. Its purpose is to transport the ions produced in the laser desorption ion source by means of electrostatic lenses to the Penning traps.

The first element in the transfer section is the aforementioned quadrupole bender. At one side of the quadrupole bender there is another MCP, while at the other is the mini-RFQ, currently under commissioning. Previously a surface ionization source [131] was placed in this spot.

After that, an open-ring Paul trap initially tested for laser cooling in a separate setup [102, 105, 132] has been installed to inject calcium ions in the Penning trap [133]. The structure of the trap, made of cylinders, does not interfere with the beam

transport.

A number of Einzel lenses (one of which has been used at times as a pulsed cavity) and two electrostatic deflectors are utilized to ensure efficient injection into the preparation Penning trap – more details on these can be found in Ref. [59]. DC voltages for the transfer section, as well as the traps and other elements, are provided by a CAEN SY1527 system, run through Stahl switches when needed. The RF for the Paul trap is delivered by a resonant amplifier. The vacuum system on the transfer line comprises one set of Edwards scroll and turbomolecular pumps, and a Gamma Vacuum ion pump (see Fig. 6.1). If the desorption ion source is connected, an additional scroll-turbo pair is used in the extra length. Pressure readings at the ion pumps are around 10^{-10} mbar.

Penning traps

The source of magnetic field is a superconducting solenoid from Agilent [51] that is used in other four Penning trap facilities [61, 134, 135, 136]. It has a field intensity of 7 T and two homogeneous regions, separated by 200 mm and equidistant from the solenoid center.

The first homogeneous region (100 ppm in $1\,\mathrm{cm}^3$) hosts the preparation trap, build as a part of a previous Thesis [59, 137]. It follows the design created for the MATS setup at FAIR [138]. Its main difference with respect to the usual cylindrical trap geometry is the segmentation of the endcaps (each of them is formed from a stack of ten smaller electrodes). This allows a nested configuration where electrons could be trapped along the endcaps and the ions of interest in the trap center. This was intended to perform sympathetic cooling of highly-charged ions (see e.g. Ref. [139] for the nested trap configuration). In this work, the preparation trap has been used to prepare the ions from the laser desorption source via cooling resonance [53] in order to perform TOF-ICR.

The second homogeneous region (measured at 0.14(10) ppm in $1\,\mathrm{cm}^3$) hosts the open-ring trap, thoroughly characterized in this Thesis. The geometry and associated systems for ion creation and optical detection merit a more in-depth analysis, which can be found in the following.

Downstream from the open-ring trap one encounters the time-of-flight section. Its purpose is to guide the ions ejected from the open-ring trap towards MCP3 for detection. The measurements carried using this method of detection will be presented

in Sec. 6.2. On this side of the solenoid, another set of Edwards scroll and turbo-molecular pumps (see Fig. 6.1), along with a larger Gamma Vacuum ion pump, are installed.

Laser beam delivery

A big part of the laser delivery system for Doppler cooling, as well as the first iteration of the optical detection system, were created before this work – see Refs. [59, 140, 118, 81].

Nine external-cavity diode lasers are used to perform Doppler cooling in the 7 T magnetic field (see Sec. 2.4.4). All of them drive transitions with $\Delta m_J = \pm 1$. This configuration is chosen so that each laser can drive the corresponding transition independently of its alignment relative to the magnetic field [81, 82].

Three of these lasers, of wavelength ∼397 nm, are used to drive the two cooling transitions both in the axial and radial directions. One of them delivers more power, and is split for the axial and radial directions. The remaining two are set to the same frequency and used in one direction each. Four of the remaining lasers have wavelengths of ∼866 nm and are used to pump the $D_{3/2}$ metastable state. The other two lasers ($\lambda \sim 854$ nm) are used to pump the $D_{5/2}$ metastable state. An Electro-Optic Modulator (EOM) (see Sec. 6.1.2 and Refs. [81, 141]) is used to obtain six wavelengths[1] from the two lasers.

The delivery of the laser light is done using separate optical fibers for the UV (cooling) and infrared (pumping) lasers. The light exits the fibers in front of the vacuum chamber and is delivered to the trap as shown in Fig. 6.2.

Optical detection system

The first fluorescence measurements were carried out with a group of seven optical lenses within the vacuum chamber, which collimate and transport the fluorescence photons towards an Electron Multiplying Charge-Coupled Device (EMCCD). The first lens, placed in the radial plane of the trap (see Fig. 6.2) was an aspheric with a 25 mm focal distance placed 25 mm away from the trap center. Therefore,

[1] Only the $m_J = \pm 1/2, \pm 3/2$ sublevels must be pumped for Doppler cooling (see Sec. 2.4.4). However, pumping of one of the $m_J = \pm 5/2$ sublevels will be used in the future to accelerate ground state cooling. The EOM driving scheme developed in this work has already accounted for this (see Sec. 6.1.2). For sideband spectroscopy, however, it would be preferable to be able to forego pumping of the upper level of the qubit transition.

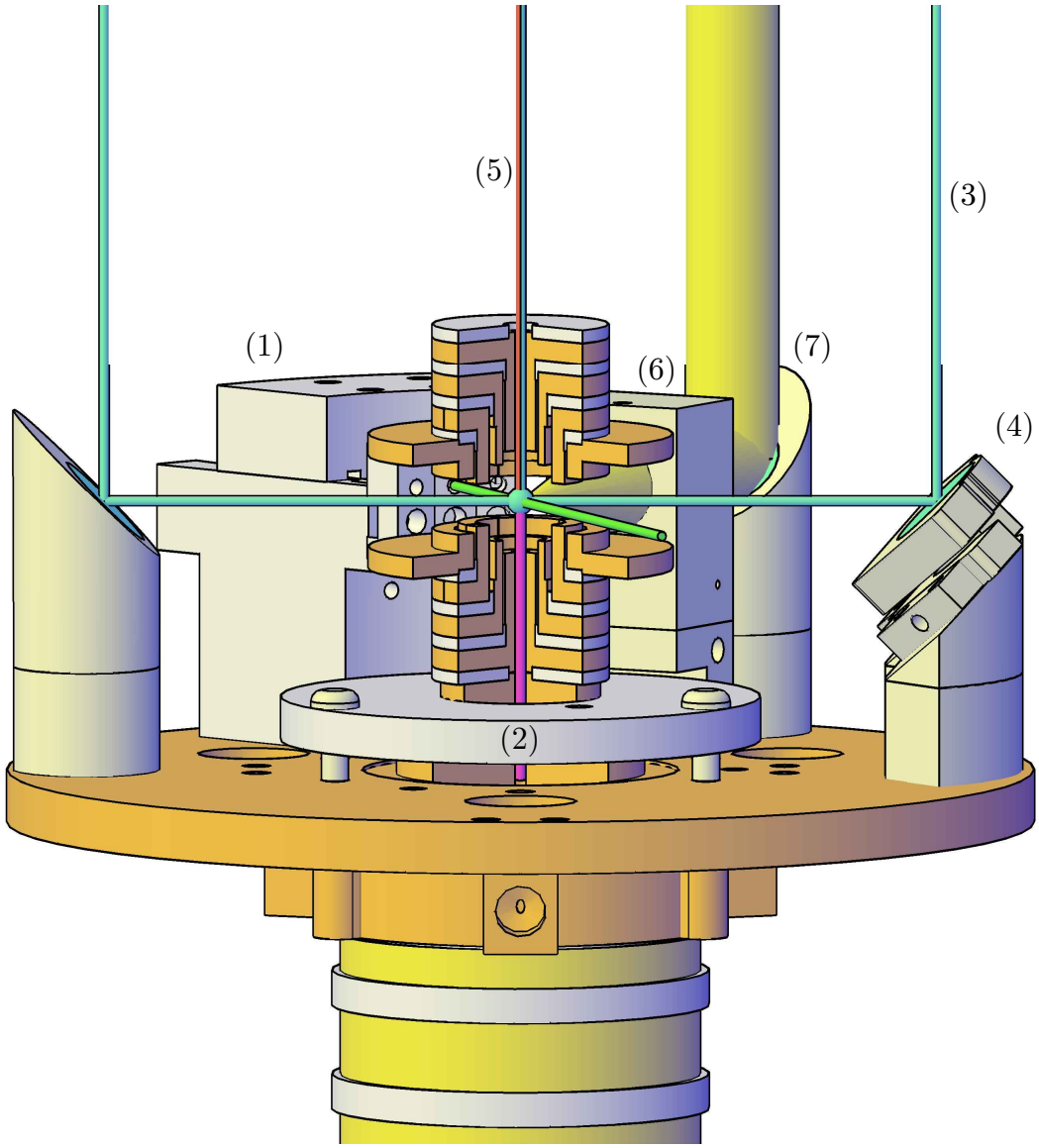

Figure 6.2: CAD drawing of the open-ring trap and associated elements. Some structural parts (as well as the first extraction electrostatic lens) have been omitted for clarity. The oven assembly (1) produces a collimated beam of calcium atoms that travels in the radial direction. The photoionization laser beams (2) enter the trap in the axial direction from the injection side, crossing the atom beam at the trap center. The radial cooling beams (3) enter parallel to the magnetic field and are directed towards the trap center by virtue of a mirror supported by an adjustable mount (4). Axial cooling and repumping beams (5) enter from the extraction side. An aspheric lens (6) collects fluorescence from the ions; the fluorescence is then reflected in a mirror (7) and extracted axially through the remaining (plano-convex spherical) lenses.

the fluorescence photons are collimated. The lens' surface results in a coverage of 1.6 % of the 4π solid angle. After reflecting in a mirror placed at a 45-degree angle, the fluorescence travels parallel to the magnetic field through a set of plano-convex spherical lenses, providing a side view of the cloud without compromising the magnetic field homogeneity with radial viewports.

The six remaining lenses were placed so that the separation among them is equal to the sum of their focal distances. Such a configuration could suffer from vignetting, but it is also optimal in terms of stability (small shifts of lenses along their axis result in minimal perturbation of the image).

After that, outside the vacuum chamber, an additional lens and a variable magnification objective are attached to the EMCCD. The overall length of the optical system from trap center to EMCCD is about 2 m. The sensor has 1024 by 1024 pixels, with 13 µm pixel size. The overall magnification factor was determined to be 3.2(5) (see Sec. 6.3) when the variable magnification objective was set to its minimum setting.

This configuration has been changed for one with greatly increased resolution as part of a different work (Ref. [69]). This improved system has enabled the visualization of the two-ion crystal.

6.1.2 New developments

In this section, the modifications to the setup carried out during the course of the present work will be presented. Besides these, other improvements have been made, such as improving the stability of the optical elements shown in Fig. 6.2, dispensing with the in-vacuum optical fibers and changing the mounting system for the optical lenses contained in the vacuum chamber to one more robust.

The open-ring Penning trap

The choice of trap geometry for a given experiment is not a trivial matter. The particular needs of the experiment must be assessed and ranked, so that the more stringent constraints of the experiment are satisfied. For the purposes of using laser-cooled ions as an auxiliary system to measure motional frequencies, the requirements were discussed in length in Ref. [44]. By order of priority they can be summed up as:

- Easy access in the radial and axial direction for both cooling and visualization

of the ion(s)

- As close to an ideal quadrupolar potential as possible, to minimize systematic effects
- Tunability for a wide range of mass-to-charge ratios
- Ability to capture ions created outside the magnetic field. The most common method is to have a trap with mirror symmetry around $z = 0$ (plane containing the trap center), so that the trap halves can be switched individually.
- Revolution symmetry around the magnetic field axis

The hyperbolic Penning trap, as shown in Sec. 2.1, has a geometry that gives rise, in principle, to a quadrupolar electrostatic field. In practice, the hyperbolic geometry has several disadvantages. Limitations in trap size and machining accuracy introduce field imperfections that must be taken into account. Often, an additional pair of *correction* electrodes are placed in the gap between the truncated ring and endcaps to mitigate this issue, although studying the field created by such electrodes cannot be done analytically. Access to the trap is not possible unless holes or slits in the electrodes are created. Even though their contribution to the electric field has been characterized (see Ref. [50] and references therein), a trap geometry that has inherent access paths and is easier to fabricate with high accuracy is desirable.

Historically, the first non-hyperbolic geometry was the closed-endcap cylindrical trap [142]. This geometry is simpler to machine, and with careful design and possibly by adding correction electrodes its harmonicity can surpass that of hyperbolic traps. The access to the trapping volume, however, is just as difficult.

The open-endcap cylindrical trap [143] provides easy access in the axial direction. The potential created by such a a geometry can be calculated analytically (unlike that of a truncated hyperboloid). That, together with the ease of manufacturing and the axial access, makes this geometry the most prevalent, being used in Penning traps for many different purposes [7, 15, 28, 29, 39]. More elaborated versions exist, with additional electrodes intended to correct the trap harmonicity to a higher degree or even to create more than one potential well (see for example Refs. [137, 138]). If radial or oblique access for laser delivery or image collection is required, holes in the electrodes are still needed (see e.g. Refs. [144, 145]). The electrostatic imperfections created by the holes have to be characterized using numerical methods and tuned out using the trap potentials.

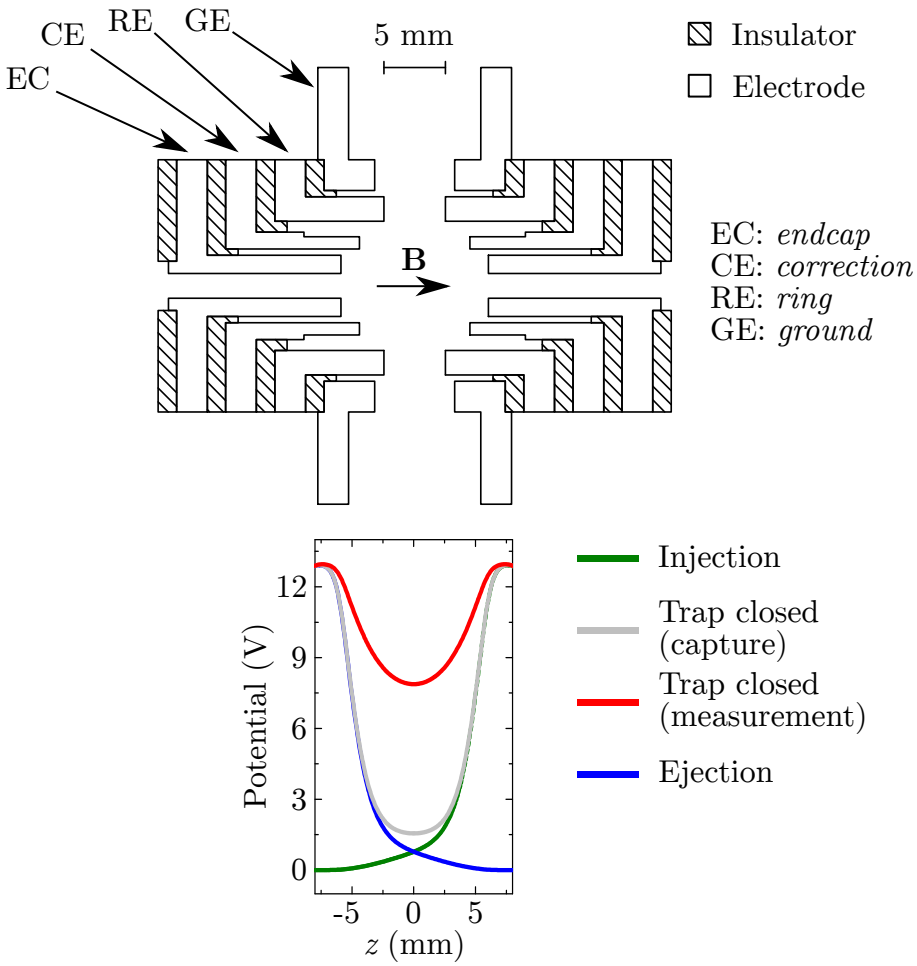

Figure 6.3: CAD drawing showing a cross section of the open-ring trap and the potential along the z axis during the different stages of a TOF-ICR measurement. The trap has revolution symmetry around the z (magnetic field) axis and mirror symmetry with respect to the plane $z = 0$, that contains the trap center. Two closed configurations are used to have a greater trap depth during capture.

The open-ring trap geometry, unlike the previously mentioned designs, has no electrode in the radial plane. Instead, it is formed of two sets of concentric rings, which have mirror symmetry with respect to a plane (the trap center) perpendicular to the revolution axis. Figure 6.3 shows a CAD drawing of the version installed in the magnet bore. This geometry allows axial and radial access. It is a modified version of a Paul trap built for $\beta-\nu$ correlation experiments at GANIL [146]. The Paul trap with the original configuration was also used to perform laser cooling experiments [132]. The modified version featured in this work was used as a Penning trap for the first time in Refs. [81, 119]. Since space is a much bigger constraint in Penning traps, due to the small diameter of the magnet bore, the open-ring Penning trap differs from the original Paul trap in size, shape and assembly method. The trap

used in this work is a factor of two smaller than the Paul trap from Refs. [132, 146], and has an additional electrode (innermost ring). It also features four-fold segmentation of one of the electrodes (RE in Fig. 6.3) to enable coupling among any of the eigenmotions. The geometry, together with the potential along the z axis during injection, capture, measurement and ejection, is also shown in Fig. 6.3.

The tuning of the trap potentials has been studied numerically and experimentally. In principle, due to the linearity of the Laplace equation, if one finds the potential $\varphi_i(\mathbf{r})$ arising from applying a voltage to the pair of electrodes i with e.g. $V_{ref,i}$, the resulting potential when arbitrary voltages V_i are applied must be

$$\varphi(\mathbf{r}) = \sum_i \frac{V_i}{V_{ref,i}} \varphi_i(\mathbf{r}) \,. \tag{6.1}$$

Given that both sides of the trap are biased equally, the potential is always symmetric in z, and each of the φ_i can therefore be written as

$$\varphi_i(r=0,z) = \sum_k C_{2k,i} z^{2k} = C_{0,i} + C_{2,i} z^2 + C_{4,i} z^4 + \dots \,, \tag{6.2}$$

and the overall potential would have

$$C_{2k} = \sum_i \frac{V_i}{V_{ref,i}} C_{2k,i} \,. \tag{6.3}$$

This means that if one computes $\varphi_i(\mathbf{r})$ numerically for each of the electrodes and fits the potential along the trap axis using a polynomial with only even terms, tuning the trap becomes a matter of solving a system of algebraic equations for V_i. Either SIMION or an ad-hoc program were used to calculate the potentials created by each of the electrodes. The custom program solves the Laplace equation in cylindrical coordinates. By imposing the revolution symmetry, the angular terms of the Laplacian vanish, and the differential equation becomes

$$\nabla^2 \varphi = \left(\frac{\partial^2}{\partial \rho^2} + \frac{1}{\rho} \frac{\partial}{\partial \rho} + \frac{\partial^2}{\partial z^2} \right) \varphi = 0 \,. \tag{6.4}$$

This transforms a 3D problem into a 2D problem, and therefore it is greatly memory- and computation-efficient. However, a singularity appears when $\rho \to 0$. Since that is precisely the most relevant part of the geometry, simply avoiding the calculations along $\rho = 0$ does not suffice. From a symmetry argument it follows that $\partial\varphi/\partial\rho = 0$

at $\rho = 0$. Therefore, one can apply L'Hôpital's rule to the problematic term [147]

$$\lim_{\rho\to 0} \frac{\partial\varphi/\partial\rho}{\rho} = \frac{\frac{\partial}{\partial\rho}\partial\varphi/\partial\rho}{\frac{\partial}{\partial\rho}\rho} = \frac{\partial^2\varphi}{\partial\rho^2}\,. \tag{6.5}$$

This results in an equivalent differential equation for $\rho = 0$ that can be used for the points along the z axis,

$$\nabla^2\varphi\big|_{\rho\to 0} = \left(2\frac{\partial^2}{\partial\rho^2} + \frac{\partial^2}{\partial z^2}\right)\varphi = 0\,, \tag{6.6}$$

that is actually equivalent to the equation at the z axis using cartesian coordinates. However, the fitting routines limit the precision that can be reached with this method. Therefore, the initial set of V_i resulting from this process is used as a starting point for an iterative process, where one of the electrode voltages is varied and one of the resulting C_{2k} is observed. Once an optimal value has been found, a different (V_i, C_{2k}) pair is chosen and optimized, until satisfactory values for all C_{2k} parameters are obtained. The number of tunable C_{2k} coefficients is, of course, limited by the number of electrodes. Figure 6.4 shows an example of this process, where the voltage applied to the correction electrode is scanned and C_4 is observed. This is repeated for several values of the endcap voltage, resulting in different axial frequencies.

In-trap ion production

In the first laser experiments aiming at a the detection of fluorescence photons and Doppler cooling, and eventually in the realization of Coulomb crystals, the production of calcium ions was implemented directly in the trap. Calcium *ovens* (stainless steel cylinders containing calcium and an indium seal, prepared in an inert atmosphere by Alfa Vakuo) are Joule heated, evaporating calcium atoms. These are then ionized, in this case, using one of two step photoionization proceses [148, 149]. Photoionization has several advantages with respect to laser desorption. The number of ions in the trap can be made larger by increasing the current through the oven or the loading time. Since the first step (or both in the second case) of the photoionization process is resonant, only the desired species is produced (although formation of oxides in the trap has been observed under suboptimal vacuum conditions). Additionally, the ions are produced close to the trap center with thermal energies (under 100 meV due to the high temperature of the oven) without a cooling

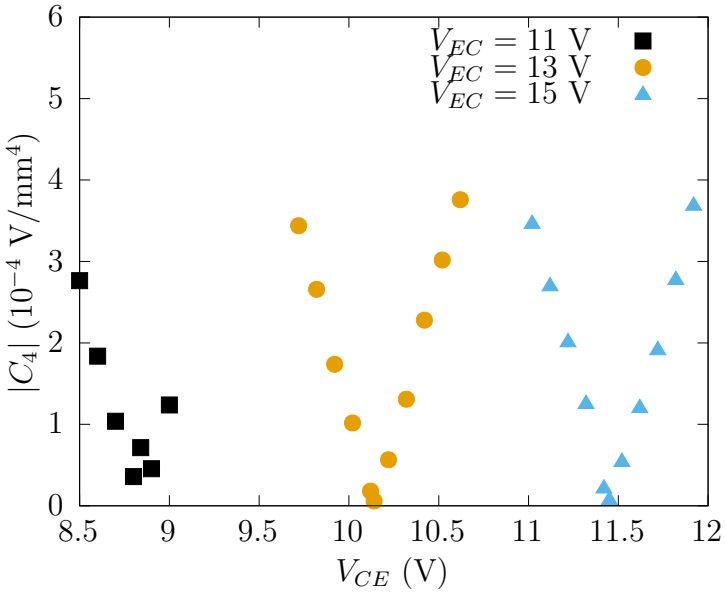

Figure 6.4: Example of the tuning of one of the open-ring trap electrodes. The absolute value of the C_4 coefficient is tracked for several correction electrode voltages (V_{CE}). The data points are obtained after fitting with the numerically obtained potential with the polynomial $C_0 + C_2 z^2 + C_4 z^4$.

stage at the preparation trap. The use of the later in combination with the laser cooling process in the open-ring trap requires a more restrictive pumping barrier than the one currently installed – this would only make sense when performing an experiment on rare isotopes. The preparation of ions produced outside the magnet can be done with a radiofrequency quadrupole structure filled with gas [128] – this approach is currently being pursued in the experiment.

Given the complexities associated with the installation and removal of the traps, several ovens were installed so that the traps could be kept in the bore in the event of oven failure. Due to space available in the bore, and since the trap vicinity is already crowded with the optical elements needed to introduce the lasers and collect the fluorescence photons (see Fig. 6.2), the design proved challenging. Custom ovens from Alfa Vakuo (slightly shorter than the standard ones) could be made, and a MACOR© ceramic structure, shown in context in Fig. 6.2 and in more detail in Fig. 6.5, was designed and constructed.

Regarding the lasers used for the two-step photoionization, one has again to consider the influence of the magnetic field on the electronic structure of the atom. The process $^{40}\mathrm{Ca} \rightarrow^{40} \mathrm{Ca}^* \rightarrow^{40} \mathrm{Ca}^+ + \mathrm{e}^-$ needs to be carried out. The initial electronic configuration of the atom is $^1\mathrm{S}_0$, and the resulting ion will have $^2\mathrm{S}_{1/2}$. The free electron can be considered a plane wave [150]. The plane wave's expansion into

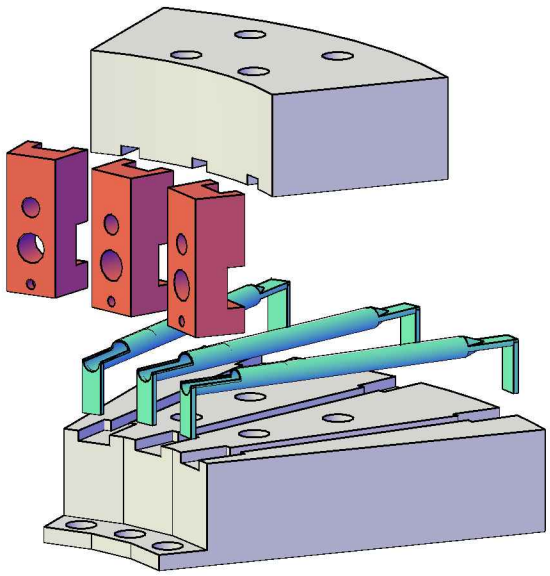

Figure 6.5: Exploded view of the calcium oven assembly. The ovens (in blue) are sandwiched between two ceramic pieces (in white). The grooves ensure the ovens are correctly aligned. Three smaller ceramic pieces (in red) are placed in front of each oven, with a small hole so that only the atoms directed towards the trap center make it through. The larger holes in the collimating pieces are threaded, so that a screw is used to press together the oven and a cable – a similar arrangement is used in the rear part. The front cable is common, whereas one rear cable is available for each individual oven, so that they can be heated individually.

spherical harmonics is usually done by choosing the quantization direction to be aligned with the electron's direction of motion, so that only the $m = 0$ components survive. In this case, however, the quantization axis is defined by the magnetic field, and therefore there are components for all L, m.

Since only transitions with $m_J = \pm 1$ can be driven using axial lasers [81, 82], the intermediate state must have $m_J = \pm 1$. Using a dedicated 422 nm tunable diode laser available in the laboratory, the $^1P_1$ state can be reached – the sublevel with $m_J = +1$ is chosen to enable the use of axial beams. This level is affected by linear Zeeman effect, resulting in a correction of +98 GHz with respect to the value for $B = 0$. For the second step, two choices were tested: a dedicated 375 nm laser can ionize the excited atom non-resonantly, or one of the 397 nm lasers used for cooling can be repurposed to resonantly excite the atom up to the $3p^6 4s17d\ ^1D_2$ level, which is 50 meV away from ionization [149] and can be ionized due to e.g. background

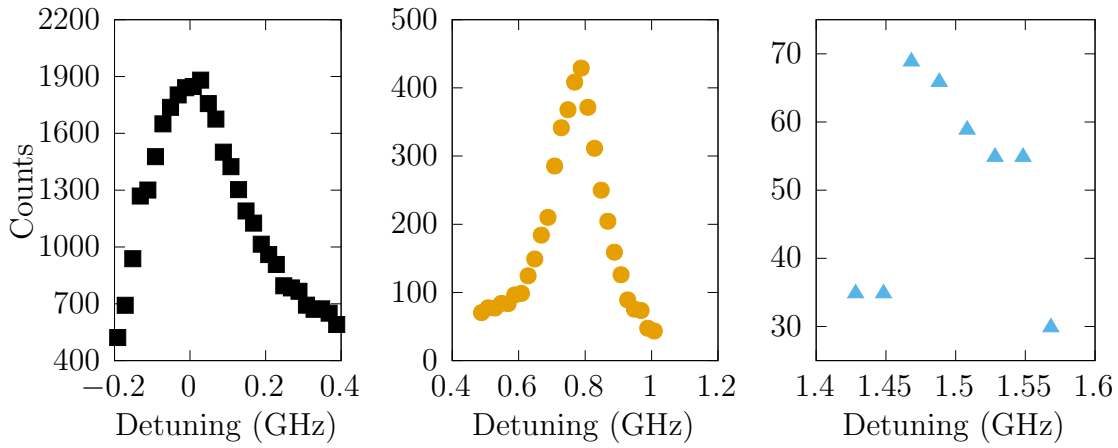

Figure 6.6: Resonance frequency of the first ionization step for different calcium isotopes. Interaction between the calcium atoms and the lasers is allowed for a fixed amount of time. The resulting ions are then ejected towards MCP3 for detection. From left to right, these are ^{40}Ca, ^{44}Ca and ^{48}Ca. The $^{48}Ca^{+}$ count rate is much lower than the rest due to its lower abundance (0.19 %, as opposed to 2.1 % and 96.6 % for ^{44}Ca and ^{40}Ca, respectively). The detuning is given with respect to the resonance frequency for the ^{40}Ca isotope.

thermal radiation. Given that both methods resulted in similar efficiencies, the first approach was chosen due to its simplicity.

Since the first step of the photoionization process is resonant, and the calcium ovens are not isotopically enriched, it is possible to selectively ionize the different calcium isotopes within their natural abundance percentages. An estimate of the isotope shift is needed to narrow down the frequencies to a feasible range. According to Ref. [151], the isotope shift in calcium is dominated by the increased nuclear mass, and not by the change in charge distribution (i.e. the so called *field shift* can be neglected for the purposes of this estimation). Further, the electron correlation effects present in two-electron atoms can also be neglected. The isotope shifts are then given simply by

$$\frac{\nu_H - \nu_L}{\nu_L} = \frac{m_e\,(m_H - m_L)}{m_L\,(m_H + m_e)}\,, \tag{6.7}$$

where the subindices refer to the heavier (H) and lighter (L) isotopes, and m_e is the electron's mass. This simple estimation suffices to find the resonances, which are shown in Fig. 6.6.

Even though the isotope shifts are much larger than the transition linewidth, the larger abundance of $^{40}Ca^{+}$ means that this isotope is present in the trap in significant

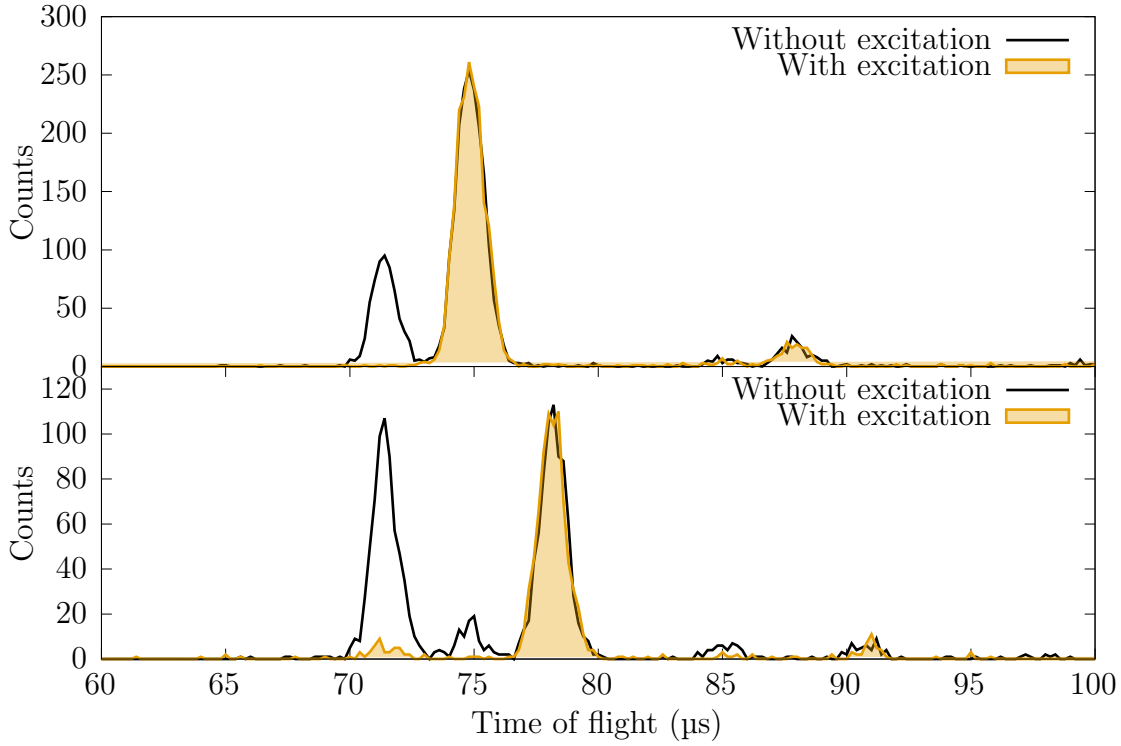

Figure 6.7: TOF spectrum when using the ^{44}Ca (top) and ^{48}Ca (bottom) resonant frequencies for the $^1S_0 \rightarrow {}^1P_1$ transition. See text for further details.

amounts when the laser is tuned for the other isotopes (see Fig. 6.7). Therefore, if one wants to have exclusively $^{44}Ca^+$ or $^{48}Ca^+$, the undesired species have to be removed from the trap. In the case of $^{44}Ca^+$, only $^{40}Ca^+$ is present, so a dipolar excitation at the reduced-cyclotron frequency suffices. In the case of $^{48}Ca^+$, however, both $^{40}Ca^+$ and $^{44}Ca^+$ are present. Therefore, a *Stored Waveform Inverse Fourier Transform* (SWIFT) [152] excitation that sweeps a frequency range containing the reduced-cyclotron frequencies of both species is used. The corresponding oxides are produced due to a continuous interaction of the ions and molecules from the residual gas in suboptimal vacuum conditions, and were not detected anymore when the vacuum conditions improved.

These results provide an interesting possibility. As observed in Fig. 6.7, when the laser is set to the resonance frequency of the ^{48}Ca isotope, $^{40}Ca^+$ and $^{48}Ca^+$ are produced with almost equal rates. This anticipates a way of producing an unbalanced $^{40}Ca^+$–$^{48}Ca^+$ crystal to put the results presented in Chapter 4 to the test.

Electro-optic modulator

Electro-optic modulators (EOMs) consist on a material whose refractive index can be modified by an externally applied electric field. A laser traversing this medium acquires an additional phase that depends on the voltage applied to the EOM. Therefore, the phase can be modulated by applying a driving voltage $V\cos(\omega_d t)$. If the relationship between the refractive index and applied voltage is linear, the resulting laser electric field can be written as

$$E = E_0 e^{i(\omega_L t + \alpha\cos(\omega_d t))} = E_0 e^{i\omega_L t}\sum_{n=-\infty}^{+\infty} J_n(\alpha)\, e^{in\omega_d t} = \\ = \left[J_0(\alpha) + \sum_{n=1}^{+\infty} i^n J_n(\alpha)\left(e^{in\omega_d t} + (-1)^n e^{-in\omega_d t}\right)\right], \quad (6.8)$$

where the Jacobi-Anger expansion and the property of the Bessel functions of the first kind $J_{-n}(\alpha) = (-1)^n J_n(\alpha)$ have been used, and α is proportional to the driving amplitude[2]. Therefore, sidebands at $\pm n\omega_d$ appear, with intensities given by $I_n = I_0 J_n^2(\alpha)$.

The EOM sideband generation scheme shown in Ref. [81] intended to use carrier and first sidebands at ∼13 GHz to depopulate the $D_{5/2}$ metastable states. However, it failed to take into account the non-linear nature of the Zeeman splitting at such high magnetic fields (see Sec. 2.4.4). The frequencies reported in Ref. [81] were therefore around 1 GHz away from resonance. Given that only three parameters (two laser frequencies and the EOM driving frequency) are available, the best case scenario, using a least-squares approach, would have detunings as high as 500 MHz for the sidebands, thus requiring an alternative approach.

The approach chosen applies two driving fields to the EOM. This was studied in Ref. [153], although for a different reason (in that case the Zeeman splitting is still linear, but only one 854 nm laser was available). If two driving fields are applied, allowing for a phase ϕ among them, the resulting electric field is

[2]It can simply be written as $\alpha = \pi V/V_\pi$, where V_π, a parameter that is usually given by EOM vendors, is the voltage required to introduce a π phase shift.

Table 6.1: EOM configurations to pump the $D_{5/2}$ metastable states. The laser frequencies (ω_{L1} and ω_{L2}) are given with the $B = 0$ transition frequency as a reference. n and m are the order of the sidebands of the first and second driving, respectively. See text for details.

Configuration	Parameters (GHz)	Transition $D_{5/2} \rightarrow P_{3/2}$	Sideband (n, m)	Detuning (MHz)
1	$\Delta\omega_{L1} = 110.568$ $\Delta\omega_{L2} = -111.553$ $\omega_1 = 13.099$ $\omega_2 = 0.475$	$m_J = -5/2 \rightarrow -3/2$	$(-1, +1)$	-11
		$m_J = -3/2 \rightarrow -1/2$	$(0, 0)$	$+23$
		$m_J = -1/2 \rightarrow +1/2$	$(+1, -1)$	-11
		$m_J = +1/2 \rightarrow -1/2$	$(-1, -1)$	-23
		$m_J = +3/2 \rightarrow +1/2$	$(0, 0)$	$+47$
		$m_J = +5/2 \rightarrow +3/2$	$(+1, +1)$	-23
2	$\Delta\omega_{L1} = 110.545$ $\Delta\omega_{L2} = -111.600$ $\omega_1 = 12.656$ $\omega_2 = 0.848$	$m_J = -5/2 \rightarrow -3/2$	$(-1, 0)$	-67
		$m_J = -3/2 \rightarrow -1/2$	$(0, 0)$	0
		$m_J = -1/2 \rightarrow +1/2$	$(+1, 0)$	0
		$m_J = +1/2 \rightarrow -1/2$	$(-1, -1)$	0
		$m_J = +3/2 \rightarrow +1/2$	$(0, 0)$	0
		$m_J = +5/2 \rightarrow +3/2$	$(+1, +1)$	-140
3	$\Delta\omega_{L1} = 110.579$ $\Delta\omega_{L2} = -111.530$ $\omega_1 = 13.099$ $\omega_2 = 0.475$	$m_J = -5/2 \rightarrow -3/2$	$(-1, +1)$	0
		$m_J = -3/2 \rightarrow -1/2$	$(0, 0)$	$+33$
		$m_J = -1/2 \rightarrow +1/2$	$(+1, -1)$	0
		$m_J = +1/2 \rightarrow -1/2$	$(-1, -1)$	0
		$m_J = +3/2 \rightarrow +1/2$	$(0, 0)$	$+70$
		$m_J = +5/2 \rightarrow +3/2$	$(+1, +1)$	0

$$E = E_0 e^{i(\omega_L t + \alpha_1 \sin(\omega_1 t) + \alpha_2 \sin(\omega_2 t + \phi))} = \\ = E_0 e^{i\omega_L t} \sum_{n=-\infty}^{+\infty} J_n(\alpha_1)\, e^{in\omega_1 t} \sum_{m=-\infty}^{+\infty} J_m(\alpha_2)\, e^{im(\omega_2 t + \phi)}. \quad (6.9)$$

Therefore, each of the terms in the sum over n (the sidebands that arise from the first driving) has its own set of sidebands at $\pm m\omega_2$. Now there are four parameters that can be manipulated to match the six transitions. There is no need to use sidebands other than $n, m \in 0, \pm 1$. This also means that, in this case, the phase ϕ between the two drivings can be disregarded, since there will be only one (n, m) pair for each of the relevant frequencies, and therefore no interference. The intensity of each sideband is thus $I = I_0 J^2_{|n|}(\alpha_1)\, J^2_{|m|}(\alpha_2)$. With this in mind, several configurations were thought out:

- Minimizing all detunings simultaneously (least-squares). After some trial and error the optimal configuration is found to be the one labeled as *configuration 1* in Tab. 6.1.

- Neglecting the $m_J = \pm 5/2$ sublevels. While this is valid for Doppler cooling, since there is no decay from $P_{1/2}$ to these sublevels (see Sec. 2.4.4), driving them is desirable to accelerate sideband cooling to the ground state. This corresponds to *configuration 2* from Tab. 6.1.

- Neglecting the $m_J = \pm 3/2$ sublevels results in $\omega_1 = 12.098$ GHz and $\omega_2 = 475$ MHz. This corresponds to *configuration 3* from Tab. 6.1.

Configuration 3 was chosen in this case. Since the detuned transitions are driven by carriers (i.e. $n = m = 0$), which will (depending on the driving amplitudes α_1 and α_2) carry greater intensity, the off-resonance driving is somewhat compensated by the power broadening of the transition. Nevertheless, changing the frequencies in a broad range in the actual experiment (up to hundreds of megahertz) results in almost no variation in the fluorescence signal. This is attributed to intensities that are well above saturation for all transitions (see Sec. 2.4.4).

6.2 Motional frequency measurements using destructive detection

In the first period of this Thesis the performance of the open-ring trap was investigated by measuring ν_+, ν_z, ν_-, and ν_c, as well as running SIMION simulations of the time-of-flight spectrum of $^{40}Ca^+$ ions from the open-ring trap to the MCP3 through the TOF section. The average time of flight of the ions from the center of the trap to the MCP detector is given by Eq. 3.6. Therefore, an increase of any of the amplitudes results in a decrease of the time of flight. The size of this reduction is related to the motion's frequency. Figure 6.8 shows the time of flight versus the driving frequency when the modified-cyclotron (left) or axial (right) motions are driven using a dipolar excitation.

Comparing these and other measurements with SIMION simulations lead to the conclusion that about 2.1 eV of axial energy are imparted to the ions during ejection. Taking that into account, the modified-cyclotron radius required to reduce the time of flight as shown in the left part of the figure is $\rho_+ \approx 250$ µm. The axial amplitude

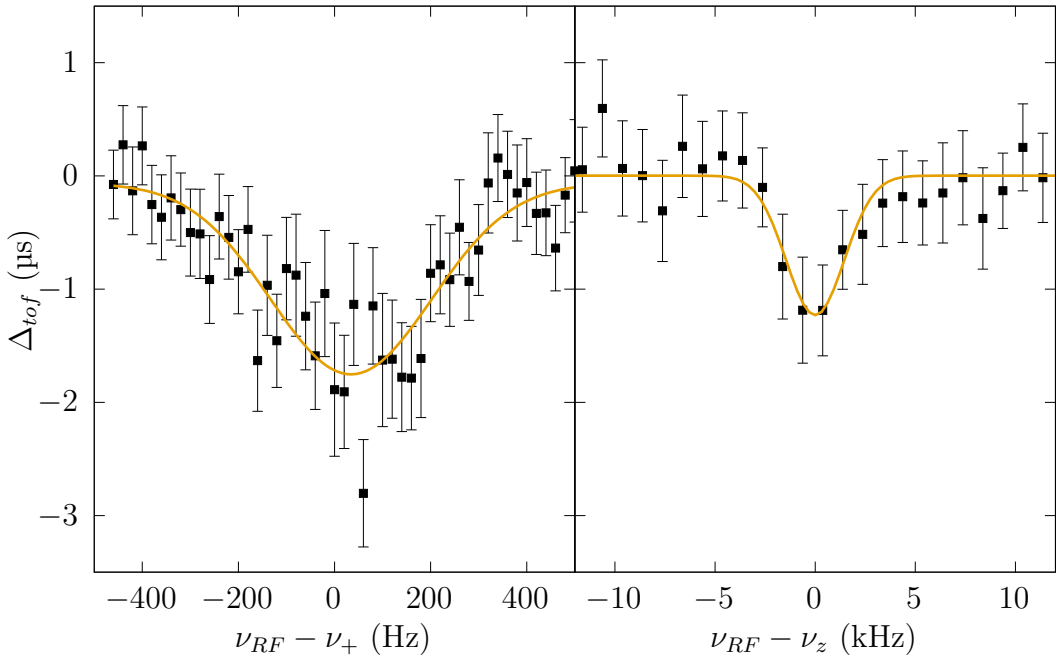

Figure 6.8: Average change in time-of-flight of the ions after dipolar driving. Left: modified-cyclotron motion. Right: axial motion. The dipolar driving field was applied during 100 ms. The lines are gaussian fits to the datapoints.

needed to reduce the time of flight as shown in the right part of the figure is $\rho_z = 4.6$ mm, equivalent to an energy of 1.7 eV. The eigenfrequencies obtained using this method are shown in Tab. 6.2. Several values of V_{CE} are listed, which result in different eigenfrequencies. Comparing these with results from simulations can be used to estimate the leading anharmonic term, C_4, whose effect on the axial frequency is given by

$$\Delta\nu_z = \frac{3qC_4E_z}{8\pi^2m^2\nu_z^3}\,, \tag{6.10}$$

with E_z the energy stored in the axial mode. However, the large errors resulting from

Table 6.2: Eigenfrequencies for $^{40}Ca^+$ obtained by probing the axial and modified-cyclotron motions with a dipolar driving (Fig. 6.8). The potentials not listed in the table are $V_{EC} = 13$ V, $V_{RE} = 5.8$ V, and $V_{GE} = 0$ V.

V_{CE} (V)	ν_+ (MHz)	ν_z (kHz)
9.82	2.685203(11)	149.916(93)
10.14	2.685135(17)	150.277(231)
10.42	2.685090(27)	152.109(679)

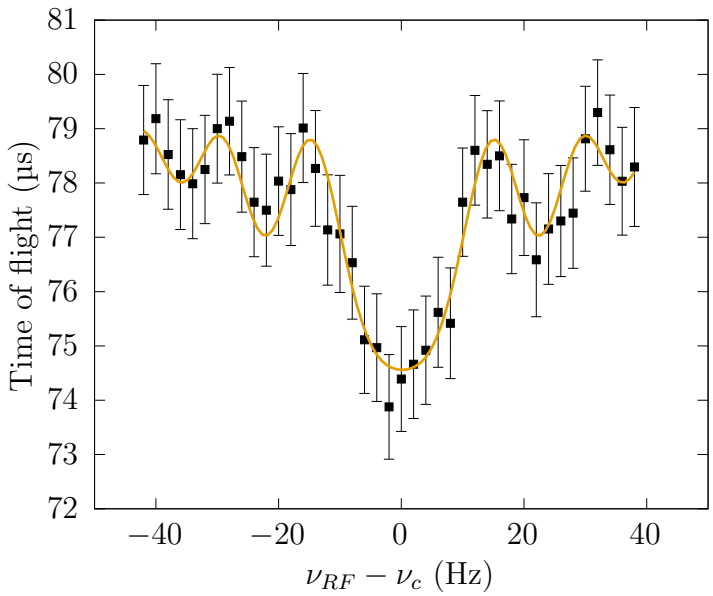

Figure 6.9: Time-Of-Flight Ion-Cyclotron-Resonance for $^{40}Ca^+$ ions. ν_c is the cyclotron frequency resulting from fitting Eq. 3.6 to the datapoints (solid line). The driving time was 100 ms, and the driving amplitude, 76 mV_{pp}, resulting in five full conversions.

the fitting routines mean that no precise values are possible. It can be concluded, however, that the values of C_4 predicted during the tuning process (see Fig. 6.4) are of the same order as those obtained here. Further validation of the tuning procedure will be shown in Sec. 6.3.

Time-of-flight resonances have been obtained with the open-ring trap. Figure 6.9 shows one of these for $^{40}Ca^+$. The value ν_c=2.6893743(7) MHz was obtained, with a resolving power $m/\Delta m \simeq 7 \cdot 10^5$. A measurement with very low statistics for $^{187}Re^+$ was only tested, yielding $\nu_c = 574.8861\,(25)$ kHz with a driving time of 25 ms and a resulting resolving power $m/\Delta m \simeq 2 \cdot 10^4$. From the test with this excitation time, the resulting value of ν_c was in agreement with the masses found in the literature.

6.3 Measurements using non-destructive detection

In this section, the experimental results obtained using non-destructive detection methods will be presented. First, circuits for induced image current detection are used to experimentally certify the effectiveness of the tuning method presented in Sec. 6.1.2. These circuits, developed in Refs. [69, 59, 154], use a quartz crystal as a resonator, instead of the usual coil or SQUID. After that, laser cooling of $^{40}Ca^+$ ions

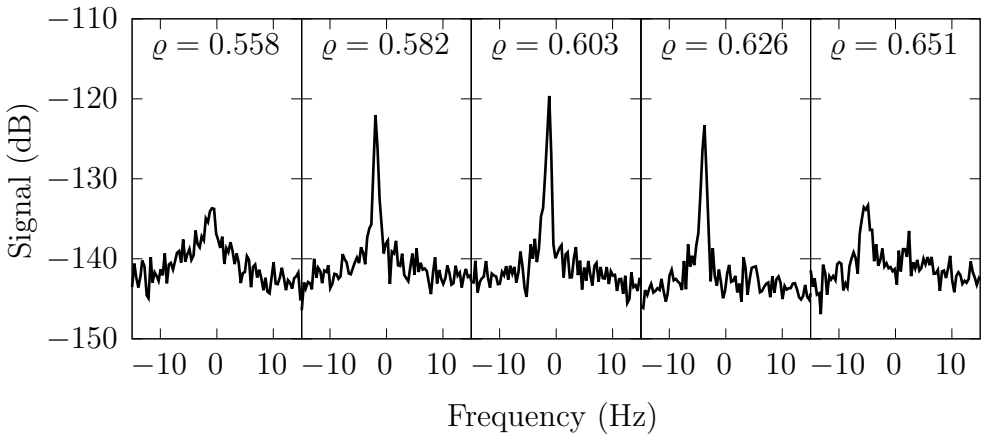

Figure 6.10: Spectrum of the induced image current signal for different voltage configurations. Besides the effect on the power of the signal, which is used to determine the optimal trap configuration, a shift of the signal is observed – this is because the change in voltage on one electrode is not compensated with the remaining one to keep C_2 constant. Frequencies are given with respect to the circuit's resonance frequency.

in the 7 T Penning trap is reported, starting from the first fluorescence detection and evidences of cooling, up to the formation of Coulomb crystals, with ion numbers ranging from several hundreds down to two [133]. The formation of a balanced two-ion crystal is an importan prerequisite to perform the envisaged experiments with unbalanced two-ion crystals as described in Chapter 4.

6.3.1 Induced image current detection: trap tuning

Restricting the analysis presented in Sec. 6.1.2 to the case where only two electrodes are biased, one obtains

$$C_2 = V_1 \frac{C_{2,1}}{V_{ref,1}} + V_2 \frac{C_{2,2}}{V_{ref,2}} \qquad \text{and} \qquad C_4 = V_1 \frac{C_{4,1}}{V_{ref,1}} + V_2 \frac{C_{4,2}}{V_{ref,2}} \,. \tag{6.11}$$

Therefore,

$$C_4 = 0 \implies \frac{V_1}{V_2} = -\frac{C_{4,2}}{C_{4,1}} \frac{V_{ref,1}}{V_{ref,2}} = \varrho \tag{6.12}$$

and, as long as the potentials are kept at this ratio, any C_2 (and therefore any axial frequency) can be obtained,

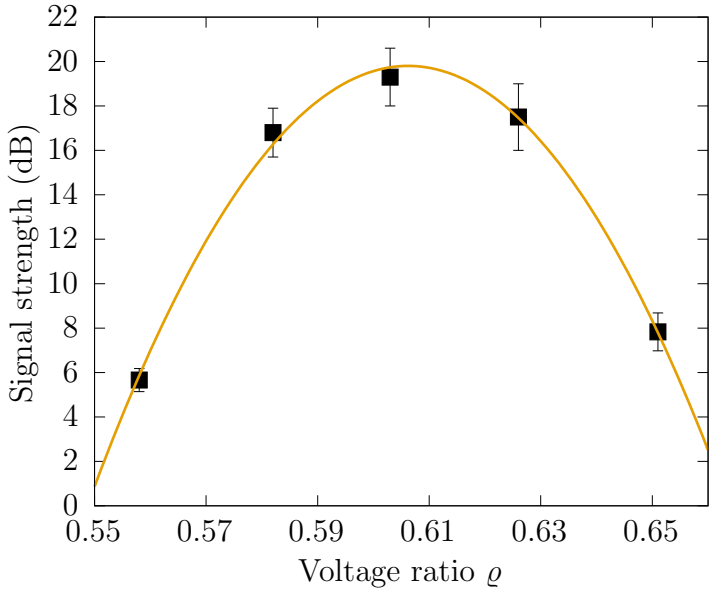

Figure 6.11: Induced current signal strength as a function of the electrodes' voltage ratio. The solid line is a gaussian fit to the datapoints, from which an optimal value (i.e. maximum signal) is obtained at $\varrho = 0.60625(89)$.

$$C_2 = V_2 \left(\varrho \frac{C_{2,1}}{V_{ref,1}} + \frac{C_{2,2}}{V_{ref,2}} \right) , \tag{6.13}$$

while keeping anharmonicities arising from C_4 to a minimum.

The presence and magnitude of anharmonicities in the trap can be determined by resonantly detecting the image current induced by the ion(s). During the detection, the ion(s)' energy is dissipated in the resonant circuit. Relatively large initial oscillation amplitudes (in the order of mm) are used. The ion(s) therefore oscillate within a range of oscillation frequencies, depending on the initial amplitude. The presence of non-zero C_4 (or higher order terms) can therefore result in a lower, wider peak in the frequency spectrum.

To test this, the circuits developed in Refs.[154, 35] based on the designed in Ref. [59] were used (see Ref. [37] for the most recent results). These use a quartz crystal oscillator, instead of the usual superconducting coil or SQUID. They have been shown to perform exceptionally well at room temperature, whereas the previous alternatives require operation at 4 K in order to achieve similar feature. Figure 6.10 shows the acquired signal's spectrum for a range of electrode potentials. By studying the signal strength as a function of the voltage ratio ϱ as shown in Fig. 6.11 it is possible to derive the optimal value, in this case, $\varrho = 0.60625(89)$. This is in good agreement with the value that results from the process described in Sec. 6.1.2.

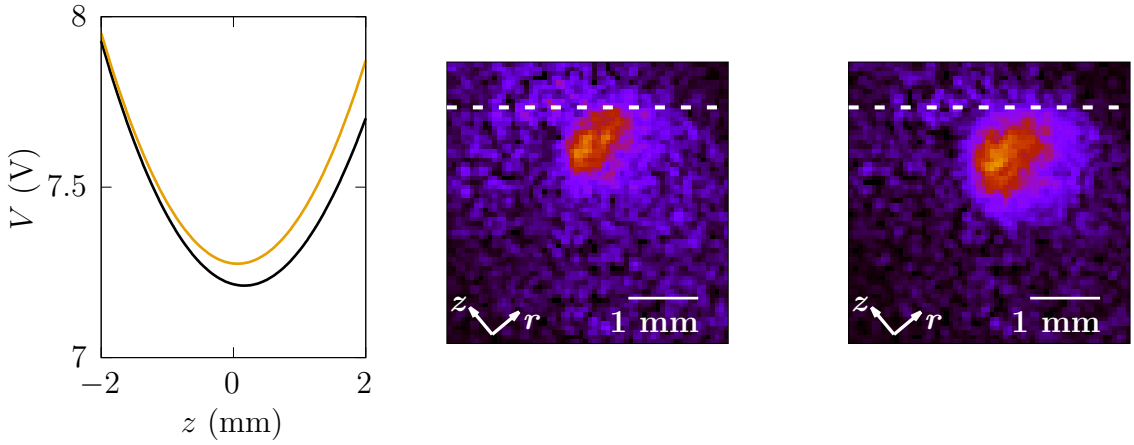

Figure 6.12: First images of Doppler cooled $^{40}Ca^{+}$ ion clouds and determination of the magnification. In all cases the detunings were -20 MHz for the cooling lasers and -30 MHz for the pumping ones. Accumulation times at the EMCCD were set to 5 s, with 16×16 binning to increase the signal-to-noise ratio. Left panel: two voltage configurations. The light curve is symmetric, whereas the dark curve has the voltage applied to one of the endcaps lowered by 2 V. This is used to determine the overall magnification of the optical system (see text for details). Center panel: fluorescence for the symmetric endcap configuration. Right panel: fluorescence for the asymmetric configuration. The dashed line serves to highlight the ion cloud displacement.

6.3.2 First evidences of laser cooling ions in the open-ring trap

After the changes presented in this Chapter were implemented, the first evidence of Doppler cooling on a cloud of $^{40}Ca^{+}$ ions was observed. Figure 6.12 shows some of the first images obtained. Due to the way the fluorescence collection system is set up, a side view of the ion cloud is achieved, with an angle indicated in the lower left corner of the images. In this case, ions were produced directly at the trap center via photoionization, and no radial laser beams were present. The maximum fluorescence signal was recorded with a detuning of about -20 MHz for the cooling lasers and -30 MHz for the pumping ones.

By causing a known displacement of the ion cloud (see Fig. 6.12) it is possible to determine the overall magnification factor of the optical system. A displacement of 265 µm is introduced by lowering one of the endcaps' voltage by 2 V. 2D Gaussian fits to the images yield trap centers (in pixel units) (34.6,18.6) and (37.1,21.8). This results in a magnification factor of 3.2(5) with the variable magnification objective set to its lowest value.

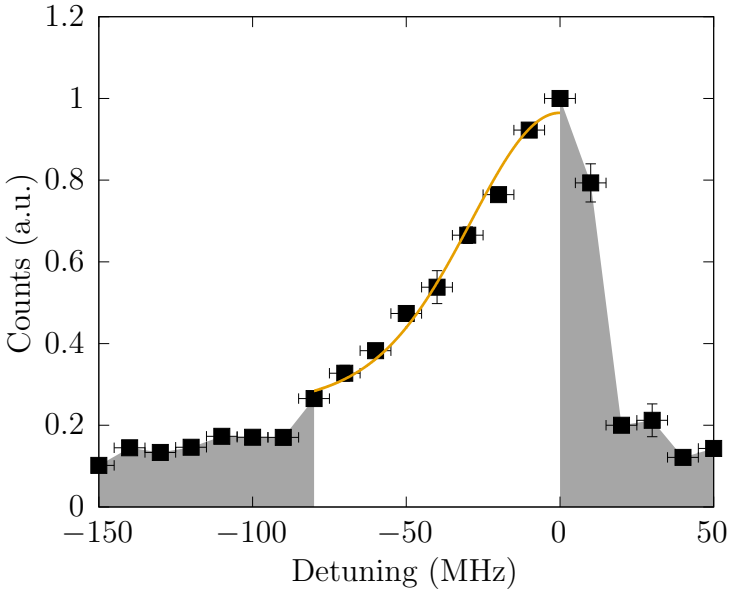

Figure 6.13: Fluorescence rate (normalized to the maximum value) as a function of the cooling laser's detuning, with fixed pumping frequencies. Each data point is the average of three measurements. The solid line is the Voigt fit of the datapoints without the shaded area, from which a temperature of 570(120) mK is obtained. The datapoints in the shaded area are not considered in the fit, since no reduction in cloud size was observed – including them would result in a temperature of about 1.28(16) K with a worse fit ($1 - R^2$ increased by an order of magnitude).

Evidence of cooling was also observed. The size of the ion clouds were reduced several times after 1 s of accumulation time on the EMCCD. An upper bound of the cloud temperature can be obtained, as described in Refs. [68, 132] by recording the fluorescence rate as a function of the detuning of the cooling laser. This measurement is shown in Fig. 6.13. The fluorescence curve has a Lorentzian component due to the natural linewidth of the transition and a Gaussian component due to the ion's motion. Therefore, a Voigt function is used to fit the datapoints. The temperature of the ion cloud is then related to the width of the Gaussian component as

$$T = \frac{mc^2}{8k_B \ln 2} \left(\frac{\Delta\nu_G}{\nu_L} \right)^2 , \tag{6.14}$$

where ν_L is the cooling transition's frequency and k_B is Boltzmann's constant. Disregarding the datapoints in the shaded area, for which no evidence of cooling (i.e. no reduction in cloud size) was observed, a temperature of 570(120) mK is obtained. Although this is over an order of magnitude away from the Doppler limit, it is well below the initial (thermal) energies.

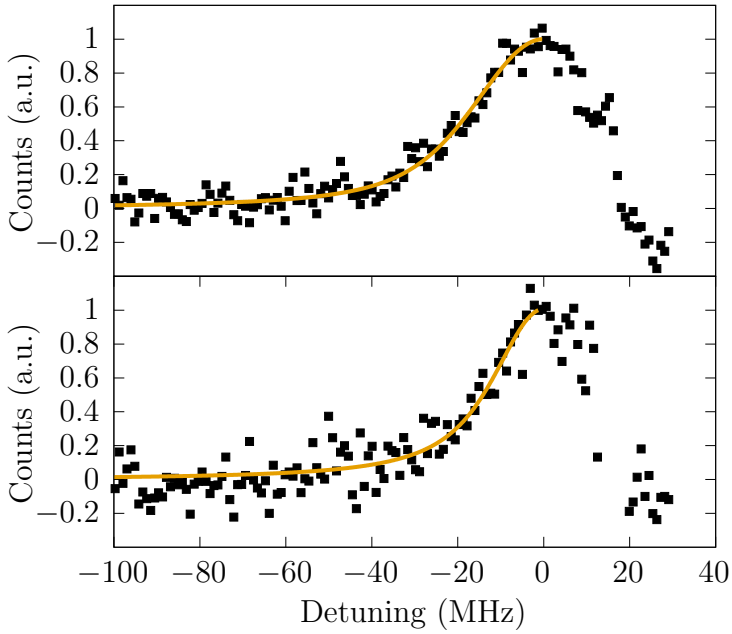

Figure 6.14: Fluorescence rate as a function of axial and radial laser frequencies. Each data point is the average of tens of measurements with 200 ms exposure each. The rates are normalized to their maximum value. Top: radial laser. The fit (solid line) results in a temperature of 87(10) mK. Bottom: axial laser. The resulting temperature in this case is 22(10) mK.

An important limiting factor at the date these (first) measurements were taken was the vacuum level. By combining the fluorescence detection with time-of-flight spectra taken in similar experimental conditions, the rate of fluorescence loss was linked to the formation of $^{40}CaO^+$ in the trap.

6.4 Formation of the two-ion crystal

As the vacuum conditions improved, and with the radial laser beams in an optimized position [69], new upper bounds of the cloud temperature were obtained. For these measurements no quadrupolar driving was present, so the degree to which the magnetron motion was cooled was solely up to the positioning of the radial lasers, as explained in Sec. 2.4.3. Figure 6.14 shows the fluorescence level when scanning the axial or radial laser cooling frequencies, keeping all other laser frequencies constant. This results in temperatures bound by 22(10) mK and 87(10) mK, as obtained from scanning the axial and radial lasers' frequency. These are much closer to the Doppler limit (around 1 mK, depending on the saturation parameter, see Sec. 2.4.1) than

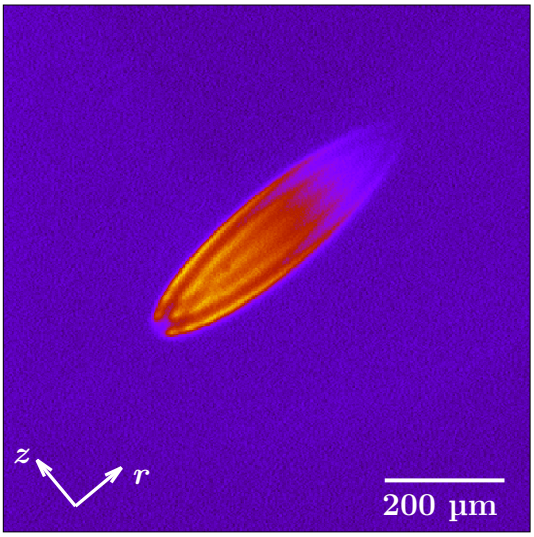

Figure 6.15: Image of the first Coulomb crystal obtained in the open-ring Penning trap. Radial lasers were present, but their position was not optimal. A quadrupolar field at ω_c was introduced to provide additional cooling of the magnetron motion.

the first results, but still one order of magnitude above it. Other techniques, such as sideband spectroscopy of a single ion [155] or thermometry based on the so-called *dark resonances* [156], could be used for a better temperature determination. Work in the former is ongoing, with the commissioning of a 729 nm laser locked to a high-finesse cavity ($\mathcal{F} \simeq 280000$, as measured at the factory) [121].

Three further modifications to the setup were made between the previous results and those that follow. The details will be presented in Ref. [69]. These are:

- Installation of a copper insert in the trap vicinity, cooled down to 40 K, to reduce background gas in the trap volume
- Installation of a new optical system: the previous optical system was diffraction limited and insufficient to resolve individual ions. A new system with much better resolution was designed and installed
- Fine alignment of the radial laser beams: a systematic study of the position of the radial laser beams and its effect on the cooling of the ion clouds was carried out

These modifications, together with those presented in Sec. 6.1.2, enabled the visual-

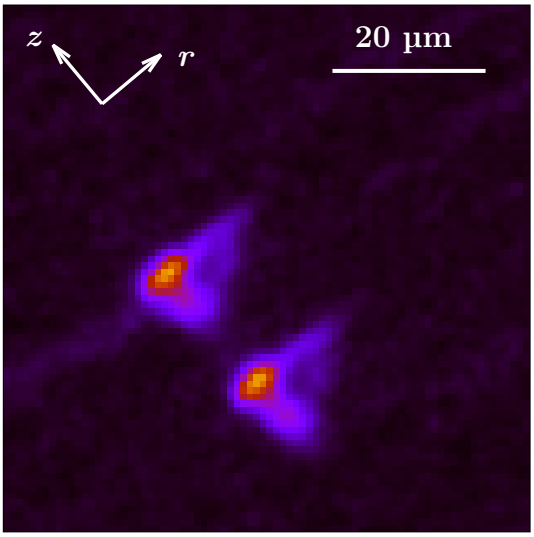

Figure 6.16: Image of the first two-ion Coulomb crystal obtained in the open-ring trap. Some comatic aberration (attributed to a slight misplacement of the first lens in the optical system) is observed.

ization of the first crystallized ion clouds. Figure 6.15 shows one of the first crystals obtained in this way. Thereafter it was possible to observe a two-ion crystal by lowering the oven current. Such a crystal is shown in Fig. 6.16. From this image, with the axial frequency known to be at $\Omega_z^- = \omega_z = 2\pi \cdot 170$ kHz from the tuning procedure, a magnification factor of 15.1(1) is obtained. This is in agreement with the optical system's design, which will be presented elsewhere [69].

By analyzing the axial projection of the fluorescence of the two ion crystal shown in Fig. 6.16, widths of 1.40(14) µm are obtained. Therefore, the oscillation of the sensor ion will be resolved by the optical system if it oscillates with an amplitude greater than $2 \cdot 1.40(14) = 2.80(28)$ µm. If the sensor ion was part of an unbalanced crystal together with a heavy ion, the target ion would be oscillating with roughly twice this amplitude (see Sec. 4.1.2). This puts the best-case amplitude dependent shift at around 35 Hz (see Fig. 4.10), although it can be corrected for (up to a point). The simulations carried out in Sec. 4.3 show a quadratic dependence between amplitude and shift – therefore, a shift $\delta\nu$ can be corrected with $\Delta(\delta\nu)/\delta\nu = 2\Delta\rho_{z,s}/\rho_{z,s}$. An experimental characterization of the shifts will be needed.

At this stage, the balanced crystal can be used to test the determination of frequencies of the common crystal modes, as described in Sec. 4.2. The use of the

new control and data acquisition system presented in Chapter 5 will simplify this task greatly, with the ability to take a succession of images for a range of driving frequencies. Especially relevant will be the study of the common axial mode, which can be used to identify the target ion through its mass using non-destructive detection, as shown in Sec. 4.4.1. Unbalanced crystals formed with different calcium isotopes will also be studied in the short-term future, using the production method described in Sec. 6.1.2. The study of the $^{40}Ca^{+}$–$^{232}Th^{+}$ crystal, which is part of an ongoing project, will be carried out using the new mini-RFQ [128], currently under commissioning.

It is worth noting that single ions have been observed as well – a study of the sensitivity of the single ion in the Penning trap to external electric fields, as the ones reported earlier in this group in Refs. [102, 105, 132], are also possible. Improvements with respect to the Paul trap system are expected due to the purely DC nature of the trapping fields in a Penning trap. Furthermore, since the single ion is not subject to the same frequency shifts as the unbalanced crystal, it is the perfect platform to study other systematic effects, such as those arising from stability of the lasers, magnetic field and power supplies.

Chapter 7

Conclusions and future work

This Thesis was motivated on exploring a new way to perform mass measurements of a single ion with a novel approach relying on optical (rather than electronic) detection. The method consists in having two different ions stored in the same Penning trap, forming a Coulomb Crystal, which we have termed *unbalanced two-ion crystal*. One of the ions (the *sensor ion*) is directly laser cooled – the photons it scatters allow a determination of the oscillation amplitude of the crystal. In the following, the theoretical and experimental aspects addressed in this work, as well as the outcomes, will be summarized. At the end, the next steps to be taken will be outlined.

The first requirement is to study in detail the motion of the two ions from different species when they are simultaneously confined in the same Penning trap. This is done in Chapter 4. The ions form a crystal when laser cooling is applied to the sensor ion, and the trap is configured so that the crystal is aligned with the magnetic field.

When the crystal is formed, the initial three eigenmotions per ion are transformed into six modes of motion. For each eigenmotion of the single ion (modified-cyclotron, axial and magnetron) two crystal modes appear, one where the ions oscillate in phase coincidence, called *common mode*, and one where they oscillate in phase opposition, called *stretch mode*. Each mode is characterized by the frequency and amplitude ratio, that is, the ratio of the oscillation amplitudes of the sensor and target ion if only that given mode is excited. The values of these are calculated for a wide range of target-to-sensor ion mass ratios (denoted as $\mu = m_t/m_s$) and for charge ratios $\kappa = q_t/q_s = 1, 2, 3$. The axial and magnetron modes of motion involve both ions, whereas the modified-cyclotron modes are pretty much decoupled – the presence of the second (target) ion manifests itself mostly as a shift in frequency with respect

to the one the ion would have if isolated in the trap. These frequencies scale mostly as would do those of a single ion, as shown in Sec. 4.1.4.

More important than the particular values of the motional frequencies, however, is to link them to the free cyclotron frequency (and therefore the mass) of the target ion. Ref. [100] introduces the so-called *generalized invariance theorem* for an array of Penning traps which, as shown in Sec. 4.1.5, also applies to the unbalanced two-ion crystal. Therefore, the free cyclotron frequencies of the two ions are related to the crystal's motional frequencies as

$$\omega_{ct}^2 + \omega_{cs}^2 = \sum_{\lambda} \Omega_{\lambda}^2 \,,$$

where Ω_λ are the crystal frequencies and ω_{ct} and ω_{cs} are the target and sensor ion's free cyclotron frequencies, respectively. There is no linear combination of frequencies that yields the target ion's free cyclotron frequency and thus to perform precise mass measurements one needs to determine the six crystal's eigenfrequencies. For experiments on rare isotopes, and depending on the required precision, one could measure only three of the eigenfrequencies directly (stretch cyclotron, stretch axial and common axial modes) – the remaining frequencies, that are pretty much mass-independent, could be measured using a more abundant species with relatively low impact into the attainable precision. In any case, a very precise measurement of the free cyclotron frequency of the target ion will not be possible in the classical regime. In order to progress, all of the crystal modes of motion must be cooled to the ground state, and the measurement procedure will require a non-classical approach, different from the one initially foreseen following experiments with one and two ions in a Paul trap [105, 102]. This is currently being addressed from a theoretical standpoint [111] as well as experimentally in two on-going PhD theses [69, 157].

The experimental part of this thesis has been focused in two issues, describing the advances made towards the implementation of the technique using an unbalanced two-ion crystal. On the one hand, a new control system has been initiated, including the most significant devices to control the creation and observation of the crystal, as well as data acquisition (Chapter 5). On the other hand, the Penning-trap system was characterized, and modifications were carried out towards the final implementation of a two-ion crystal (Chapter 6).

The above-mentioned control and data acquisition system is based on ARTIQ [120],

since this has an excellent timing performance and is easily extensible. The hardware provided by the company is not sufficient to perform all the proceses required to form and study the crystal, and therefore some of the existing devices in the laboratory were integrated. Three of these devices, integrated through different mechanisms, have been discussed. The first (for trapping), controlled with statically linked libraries, has been integrated by building a *Python Extension Module*. The second (for driving) uses the VISA standard and thus an additional Python package, called `pyVISA`, was used. For the third one (observation and detection), the software provided by the manufacturer was given as a shared library, and was integrated into ARTIQ using the `ctypes` Python package. With these extensions built, having on-line analysis is just a matter of reusing the existing Python analysis routines (or creating new ones) taking advantage of ARTIQ's *Remote Procedure Call* mechanism. The basic building blocks and protocols to extend the detection capabilities further (for example, to incorporate the PMT's counting unit) are in place as a result of this Thesis.

The experimental platform has been initially characterized using destructive detection techniques. The system required several important developments in order to perform Doppler cooling of $^{40}Ca^{+}$ and achieve the formation of the crystal:

- A tuning procedure for the open-ring Penning trap was developed, using a customized Laplace-equation solver, to find the operating voltages that provide a quadrupolar electrostatic field at the desired frequency.

- The laser frequencies to carry out Doppler cooling in 7 Tesla, the largest magnetic field in these kinds of experiments, motivated detailed calculations up to third-order perturbation theory and the implementation of additional devices to obtain 13 laser frequencies out of 9 lasers.

- A new in-trap ion source was designed and installed, with the goal of increasing the number of ions (produced by two-step photoionization) and decreasing their initial energy. This enabled the very first observation of fluorescence. Production of other ions from the naturally-abundant calcium isotopes (^{40}Ca, ^{44}Ca and ^{48}Ca) was later reached

These led initially to the observation of Doppler cooling of an ion cloud. The signal-to-noise ratio became larger in a step-by-step process, circumventing problems with the vacuum, the cooling of the radial motion and increasing the resolution of the

image-collection system Ref. [69]. This eventually led to the formation of the first two-ion crystal, which opens the possibility to start performing motional frequency measurements.

The next steps involve the use of a new laser system locked to a high-finesse cavity, which is under commissioning, to drive the transition $S_{1/2} \rightarrow D_{5/2}$. This will be used to perform sideband spectroscopy and sideband cooling, as well as the read-out operation of the generated qubit. It will initially be utilized on a single ion or a balanced crystal in a linear Paul trap, which is used as test bench [157]. On top of this, the second-generation open-ring Penning trap is now in the first stage of commissioning (cryogenic operation and electrical connections) in a separate system [69].

Appendix A

Mathematical calculations

This Appendix will contain those mathematical deductions that are deemed too long to be in the main body of the Thesis.

A.1 Transient response of the driven harmonic oscillator

Each of the three modes of motion of the trapped ion is a harmonic oscillator (see Sec. 2.2). Therefore, to study the effect of a dipolar driving on the ion's motion, it sufices to study the transient behavior of the driven harmonic oscillator. The differential equation governing the harmonic oscillator with a driving in $t \in [0, T_d]$ is

$$\ddot{x} + \omega^2 x = H(t)\, H(T_d - t)\, f_d \sin(\omega_d t) \ , \tag{A.1}$$

where f_d is the amplitude of the driving force per mass unit, ω_d the driving frequency, ω the oscillator's natural frequency and H the Heaviside step function. The general solution for $t \notin [0, T_d]$ is the usual one, i.e., $x = A \sin(\omega t + \phi)$; inside that range, however, an additional term must be added. Let us assume the additional term is an oscillation with the same frequency as the driving, allowing for a phase shift, that is, $x_p(t) = A' \sin(\omega_d t + \phi)$. Inserting this ansatz in the original equation yields

$$\begin{aligned}
\ddot{x} + \omega^2 x = & \\
&= -\omega_d^2 A' \sin(\omega_d t + \phi) + \omega^2 A' \sin(\omega_d t + \phi) = \\
&= A' \left(\omega^2 - \omega_d^2\right) \sin(\omega_d t + \phi) = \\
&= A' \left(\omega^2 - \omega_d^2\right) \left[\cos(\omega_d t) \sin\phi + \sin(\omega_d t) \cos\phi\right] = \\
&= f_d \sin(\omega_d t)\ \forall t \implies \begin{cases} \sin\phi = 0 \implies \phi = n\pi \\ A' \left(\omega^2 - \omega_d^2\right) = f_d \end{cases}
\end{aligned} \tag{A.2}$$

The general solution for $t \in [0, T_d]$ is therefore

$$x(t) = A \sin(\omega t) + B \cos(\omega t) + \frac{f_d}{\omega^2 - \omega_d^2} \sin(\omega_d t)\ . \tag{A.3}$$

If the initial conditions $x,\ \dot{x} = 0$ are imposed, values for A and B are readily found. The solution for this set of initial conditions in $t \in [0, T_d]$ is

$$x_r(t) = \frac{f_d}{\omega^2 - \omega_d^2} \left[\sin(\omega_d t) - \frac{\omega_d}{\omega} \sin(\omega t)\right]\ \forall t \in (0, T_d)\ , \tag{A.4}$$

which is labeled x_r to remark that it results from an oscillator initially at rest.

At $t = T_d$, the driving is interrupted, and the trajectory must conform to that of the harmonic oscillator. Since the disconinuity in acceleration is finite, position and velocity must be preserved. This can be used to determine the amplitude and phase after the driving:

$$\begin{cases} x_r\left(T_d^-\right) = x_r\left(T_d^+\right) \\ \dot{x}_r\left(T_d^-\right) = \dot{x}_r\left(T_d^+\right) \end{cases} \implies \begin{cases} \frac{f_d}{\omega^2 - \omega_d^2} \left[\sin(\omega_d T_d) - \frac{\omega_d}{\omega} \sin(\omega T_d)\right] = A_r \sin(\omega T_d + \phi_r) \\ \frac{f_d \omega_d}{\omega^2 - \omega_d^2} \left[\cos(\omega_d T_d) - \cos(\omega T_d)\right] = \omega A_r \cos(\omega T_d + \phi_r) \end{cases} \tag{A.5}$$

The amplitude is therefore

$$
\begin{aligned}
|A_r| &= \sqrt{\left[A_r \sin\left(\omega T_d + \phi_r\right)\right]^2 + \left[A_r \cos\left(\omega T_d + \phi_r\right)\right]^2} \\
&= \frac{f_d}{\omega^2 - \omega_d^2}\Big[\sin^2\left(\omega_d T_d\right) + \frac{\omega_d^2}{\omega^2}\sin^2\left(\omega T_d\right) - 2\frac{\omega_d}{\omega}\sin\left(\omega_d T_d\right)\sin\left(\omega T_d\right) \\
&\qquad + \frac{\omega_d^2}{\omega^2}\left(\cos^2\left(\omega_d T_d\right) + \cos^2\left(\omega T_d\right) - 2\cos\left(\omega_d T_d\right)\cos\left(\omega T_d\right)\right)\Big]^{1/2} \\
&= \frac{f_d}{|\omega^2 - \omega_d^2|}\Bigg[2 + \frac{\omega_d^2 - \omega^2}{\omega^2}\cos^2\left(\omega_d T_d\right) \\
&\qquad - 2\frac{\omega_d}{\omega}\left(\sin\left(\omega_d T_d\right)\sin\left(\omega T_d\right) + \frac{\omega_d}{\omega}\cos\left(\omega_d T_d\right)\cos\left(\omega T_d\right)\right)\Bigg]^{1/2},
\end{aligned}
\tag{A.6}
$$

and the phase is simply

$$
\phi_r = \operatorname{atan}\left(\frac{\sin\left(\omega T_d + \phi_r\right)}{\cos\left(\omega T_d + \phi_r\right)}\right) - \omega T_d = \operatorname{atan}\left(\frac{\frac{\omega}{\omega_d}\sin\left(\omega_d T_d\right) - \sin\left(\omega T_d\right)}{\cos\left(\omega_d T_d\right) - \cos\left(\omega T_d\right)}\right) - \omega T_d\,,
\tag{A.7}
$$

taking into consideration that the information about the sign of A_r (which can be accounted for with an additional phase $\frac{\pi}{2}\left(1 - \operatorname{sgn} A_r\right)$, with $\operatorname{sgn}(x) = x/|x|$ the *sign* function) is lost in Eq. A.6.

These expressions can be simplified if the drive's detuning, $\Delta\omega = \omega_d - \omega$, verifies $\Delta\omega \ll \omega$. In that case, $\omega_d/\omega \simeq 1$ and $\omega_d + \omega \simeq 2\omega$, and the position and velocity at $t = T_d^-$ can be rewritten as

$$
\begin{aligned}
x_r\left(T_d^-\right) &= \frac{f_d}{\omega^2 - \omega_d^2}\left[\sin\left(\omega_d T_d\right) - \frac{\omega_d}{\omega}\sin\left(\omega T_d\right)\right] \\
&\simeq \frac{-f_d}{2\omega\Delta\omega}\left[\sin\left(\omega_d T_d\right) - \sin\left(\omega T_d\right)\right] \\
&= \frac{-f_d}{\omega\Delta\omega}\sin\left(\frac{\Delta\omega}{2}T_d\right)\cos\left(\left[\omega + \frac{\Delta\omega}{2}\right]T_d\right) \\
&= \frac{f_d T_d}{2\omega}\operatorname{sinc}\left(\frac{\Delta\omega}{2}T_d\right)\left[\sin\left(\omega T_d\right)\sin\left(\frac{\Delta\omega}{2}T_d\right) - \cos\left(\omega T_d\right)\cos\left(\frac{\Delta\omega}{2}T_d\right)\right]
\end{aligned}
\tag{A.8}
$$

and

$$\begin{aligned}\dot{x}_r\left(T_d^-\right) &= \frac{f_d\omega_d}{\omega^2-\omega_d^2}\left[\cos\left(\omega_d T_d\right)-\cos\left(\omega T_d\right)\right] \\ &\simeq \frac{f_d}{\Delta\omega}\sin\left(\frac{\Delta\omega}{2}T_d\right)\sin\left(\left[\omega+\frac{\Delta\omega}{2}\right]T_d\right) \\ &= \frac{f_d T_d}{2}\mathrm{sinc}\left(\frac{\Delta\omega}{2}T_d\right)\left[\cos\left(\omega T_d\right)\sin\left(\frac{\Delta\omega}{2}T_d\right)+\sin\left(\omega T_d\right)\cos\left(\frac{\Delta\omega}{2}T_d\right)\right],\end{aligned} \tag{A.9}$$

respectively. Here the function $\mathrm{sinc}\left(x\right) = \sin\left(x\right)/x$ is introduced, and several trigonometric identities have been used[1]. Comparing Eqs. A.8 and A.9 with the position and velocity after the driving,

$$\begin{cases} x_r\left(T_d^+\right) = A_r\sin\left(\omega T_d+\phi_r\right) = A_r\left[\sin\left(\omega T_d\right)\cos\phi_r+\cos\left(\omega T_d\right)\sin\phi_r\right] \\ \dot{x}_r\left(T_d^+\right) = \omega A_r\cos\left(\omega T_d+\phi_r\right) = \omega A_r\left[\cos\left(\omega T_d\right)\cos\phi_r-\sin\left(\omega T_d\right)\sin\phi_r\right] \end{cases}, \tag{A.10}$$

it is clear that both position and velocity are continuous if

$$A_r \simeq \frac{f_d T_d}{2\omega}\mathrm{sinc}\left(\frac{\Delta\omega}{2}T_d\right) \tag{A.11}$$

and

$$\begin{cases} \sin\left(\frac{\Delta\omega}{2}T_d\right) \simeq \cos\phi_r \\ \cos\left(\frac{\Delta\omega}{2}T_d\right) \simeq -\sin\phi_r \end{cases} \implies \phi_r \simeq \frac{\Delta\omega}{2}T_d - \frac{\pi}{2}\,. \tag{A.12}$$

Therefore, the oscillator's full trajectory for the initial conditions $x,\,\dot{x}=0$ is

$$x_r\left(t\right) \simeq \begin{cases} 0 & \forall t<0 \\ \frac{f_d}{\omega^2-\omega_d^2}\left[\sin\left(\omega_d t\right)-\frac{\omega_d}{\omega}\sin\left(\omega t\right)\right] & \forall t\in\left(0,T_d\right) \\ -\frac{f_d T_d}{2\omega}\mathrm{sinc}\left(\frac{\Delta\omega}{2}T_d\right)\cos\left(\omega t+\frac{\Delta\omega}{2}T_d\right) & \forall t>T_d \end{cases}. \tag{A.13}$$

The information about amplitude and phase after driving is presented in Fig. A.1. If the oscillator has non-vanishing initial amplitude, that is, $x_0 = A_0\sin\left(\omega t+\phi_0\right)$ for $t<0$, it is clear that

[1] Namely, $\sin a-\sin b = 2\sin\left(\frac{a-b}{2}\right)\cos\left(\frac{a+b}{2}\right)$, $\cos a-\cos b = -2\sin\left(\frac{a-b}{2}\right)\sin\left(\frac{a+b}{2}\right)$, $\cos\left(a+b\right) = \cos a\cos b-\sin a\sin b$ and $\sin\left(a+b\right) = \sin a\cos b+\cos a\sin b$.

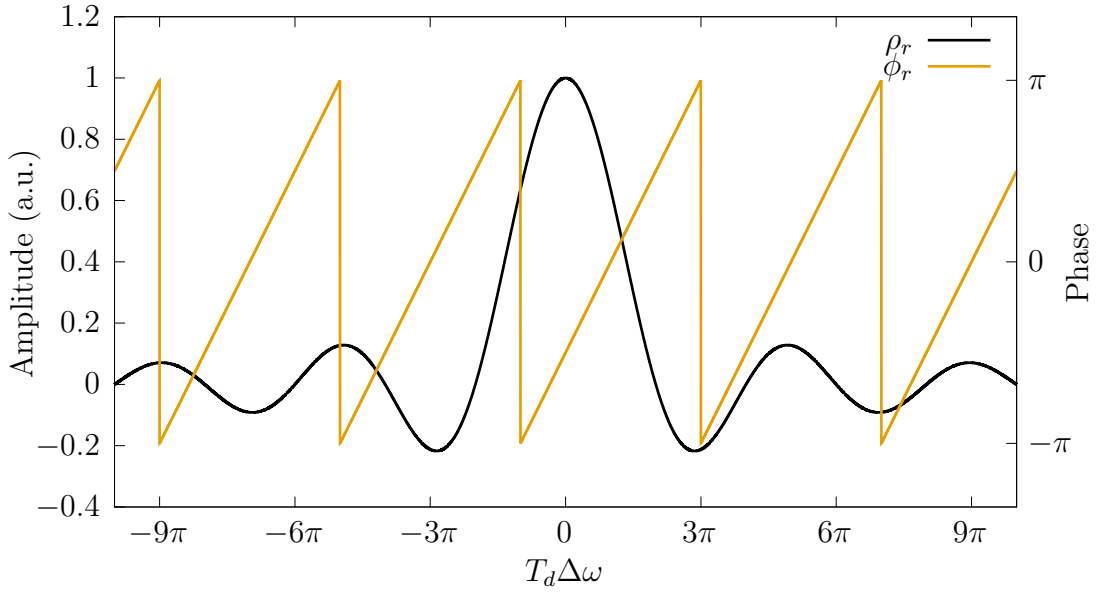

Figure A.1: Amplitude and phase of the harmonic oscillator after being driven for a time T_d at a frequency $\omega_d = \omega + \Delta\omega$.

$$x(t) = x_0(t) + x_r(t) = \begin{cases} A_0 \sin(\omega t + \phi_0) & \forall t < 0 \\ A_0 \sin(\omega t + \phi_0) + \frac{f_d}{\omega^2 - \omega_d^2}\left[\sin(\omega_d t) - \frac{\omega_d}{\omega}\sin(\omega t)\right] & \forall t \in (0, T_d) \\ A_0 \sin(\omega t + \phi_0) + A_r \sin(\omega t + \phi_r) & \forall t > T_d \end{cases} \tag{A.14}$$

fulfills Eq. A.1 at all points and conserves position and velocity at $t = 0$ and $t = T_d$. It must therefore be the solution. The solution for $t > T_d$ can be rewritten as

$$\begin{aligned} x(t > T_d) &= A_0 \sin(\omega t + \phi_0) + A_r \sin(\omega t + \phi_r) \\ &= \sin(\omega t)(A_0 \cos\phi_0 + A_r \cos\phi_r) + \cos(\omega t)(A_0 \sin\phi_0 + A_r \sin\phi_r) \end{aligned} \tag{A.15}$$

Since there is no driving for $t > T_d$, this must be of the form

$$x = A \sin(\omega t + \phi) = A \sin(\omega t)\cos\phi + A\cos(\omega t)\sin\phi\,. \tag{A.16}$$

The only way for Eqs. A.15 and A.16 to be equal for all values of t is to have the coefficients multiplying the terms in $\sin(\omega t)$ and $\cos(\omega t)$ match; therefore,

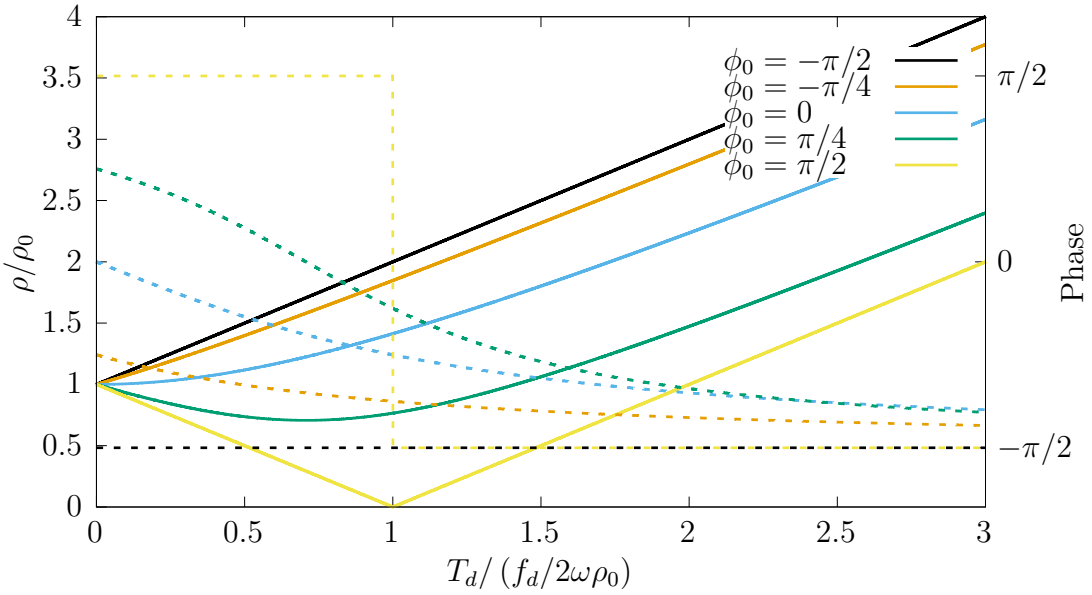

Figure A.2: Amplitude (solid lines) and phase (dashed lines) of a harmonic oscillator with initial amplitude A_0 being driven on-resonance for a time T_d for several initial phases ϕ_0. Figure inspired by Ref. [30].

$$\begin{cases} A_0 \cos\phi_0 + A_r \cos\phi_r = A\cos\phi \\ A_0 \sin\phi_0 + A_r \sin\phi_r = A\sin\phi \end{cases} . \tag{A.17}$$

The final values of ϕ and A are, respectively,

$$\phi = \operatorname{atan}\left(\frac{\sin\phi}{\cos\phi}\right) = \operatorname{atan}\left(\frac{A_0\sin\phi_0 + A_r\sin\phi_r}{A_0\cos\phi_0 + A_r\cos\phi_r}\right) \tag{A.18}$$

and

$$\begin{aligned} A &= \sqrt{(A\sin\phi)^2 + (A\cos\phi)^2} \\ &= \sqrt{A_0^2 + A_r^2 + 2A_0A_r\left(\cos\phi_0\cos\phi_r - \sin\phi_0\sin\phi_r\right)} \\ &= \sqrt{A_0^2 + A_r^2 + 2A_0A_r\cos\left(\phi_0 - \phi_r\right)}\,. \end{aligned} \tag{A.19}$$

The amplitude and phase an oscillator with an initial amplitude A_0 and phase ϕ_0 attains after being driven on resonance for a time T_d with force mf_d is shown, for several initial phases ϕ_0, in Fig. A.2. The fastest changes in amplitude happen for $\phi_0 = \pm\pi/2$, which is when the ion's *velocity* is in phase (or in phase opposition)

with the driving force, therefore maximizing the power transferred to the oscillator.

A.2 Quadrupolar driving of the trapped ion

When the coupling potential $\varphi_{RF} = -xy\frac{2\alpha V_{RF}}{d_{elec}^2}\cos\left(\omega_{RF}t + \phi_{RF}\right)$ is superimposed to the trapping potential of the Penning trap, the Hamiltonian in the eigenmode basis is

$$\begin{aligned}\mathcal{H} = &\frac{1}{2}\omega_+\left(q_+^2 + p_+^2\right) - \frac{1}{2}\omega_-\left(q_-^2 + p_-^2\right) + \frac{1}{2}\omega_z\left(q_3^2 + p_3^2\right) \\ &- H\left(t\right)H\left(T_d - t\right)k_0\cos\left(\omega_{RF}t + \phi_{RF}\right)\left(q_+ + q_-\right)\left(p_+ - p_-\right)\ , \end{aligned} \tag{A.20}$$

where $k_0 = \frac{2\alpha q V_{RF}}{m\omega_1 d_{elec}^2}$. The resulting equations of motion while the quadrupolar driving is applied are

$$\begin{cases} \dot{p}_+ = -\frac{\partial\mathcal{H}}{\partial q_+} = -\omega_+ q_+ + k_0\cos\theta_{RF}\left(p_+ - p_-\right) \\ \dot{q}_+ = \frac{\partial\mathcal{H}}{\partial p_+} = \omega_+ p_+ - k_0\cos\theta_{RF}\left(q_+ + q_-\right) \\ \dot{p}_- = -\frac{\partial\mathcal{H}}{\partial q_-} = \omega_- q_- + k_0\cos\theta_{RF}\left(p_+ - p_-\right) \\ \dot{q}_- = \frac{\partial\mathcal{H}}{\partial p_-} = -\omega_- p_- + k_0\cos\theta_{RF}\left(q_+ + q_-\right) \end{cases} . \tag{A.21}$$

A procedure similar to the one shown in Ref. [13] can be used to solve these equations. $q_\pm = A_\pm e^{\pm\theta_\pm}$ and $p_\pm = iq_\pm$ (where again $\theta_\pm = \omega_\pm t + \phi_\pm$) are solutions of Eq. A.21 for $k_0 = 0$. Based on this, the *ansatz*

$$q_\pm = A_\pm\left(t\right)e^{\pm\theta_\pm} \tag{A.22a}$$

$$p_\pm = iq_\pm \tag{A.22b}$$

is introduced[2]. Therefore, the effects of the quadrupolar driving are contained in $A_\pm\left(t\right)$. Introducing the ansatz in Eq. A.21, the following differential equations are obtained:

[2]By preserving the relationship $p_\pm = iq_\pm$, the assumption of circular trajectories made in Ref. [13] is implicit.

$$\begin{cases} \dot{A}_+ e^{i\theta_+} = k_0 \cos\theta_{RF} \left(A_+ e^{i\theta_+} - A_- e^{-i\theta_-} \right) \\ \dot{A}_+ e^{i\theta_+} = k_0 \cos\theta_{RF} \left(-A_+ e^{i\theta_+} - A_- e^{-i\theta_-} \right) \\ \dot{A}_- e^{-i\theta_-} = k_0 \cos\theta_{RF} \left(A_+ e^{i\theta_+} - A_- e^{-i\theta_-} \right) \\ \dot{A}_- e^{-i\theta_-} = k_0 \cos\theta_{RF} \left(A_+ e^{i\theta_+} + A_- e^{-i\theta_-} \right) \end{cases} \tag{A.23}$$

There is a clear disagreement between the two pairs of equations arising from the circularity assumption. However, if the cosine is written as $\cos\theta_{RF} = \left(e^{i\theta_{RF}} + e^{-i\theta_{RF}}\right)/2$ and only the lowest frequency term of the product is kept (*rotating wave approximation*), the discordant terms are among those neglected. The final equations are

$$\dot{A}_\pm = \mp\frac{k_0}{2} e^{\pm i(\theta_{RF} - \theta_+ - \theta_-)} A_\mp = \mp\frac{k_0}{2} e^{\pm i\Delta\omega\cdot t} e^{\pm i\Delta\phi} A_\mp \tag{A.24}$$

where $\Delta\omega = \omega_{RF} - \omega_c$ and $\Delta\phi = \phi_{RF} - \phi_+ - \phi_-$. Taking the time derivative of the $\dot{A}_+$ equation and inserting the $\dot{A}_-$ equation yields

$$\ddot{A}_+ - i\Delta\omega\dot{A}_+ + \left(\frac{k_0}{2}\right)^2 A_+ = 0\,, \tag{A.25}$$

whose solution is

$$A_+ = a_1' e^{i\Delta\omega/2\cdot t} e^{+i\omega_B t} + a_2' e^{i\Delta\omega/2\cdot t} e^{-i\omega_B t} = e^{i\Delta\omega/2\cdot t} \left[a_1 \cos(\omega_B t) + a_2 \sin(\omega_B t)\right]\,. \tag{A.26}$$

Here, $\omega_B = \sqrt{\Delta\omega^2 + k_0^2}/2$ has been introduced. A_- can be found using the $\dot{A}_+$ equation:

$$\begin{aligned} A_- &= -\frac{2}{k_0} e^{-i\Delta\omega t} e^{-i\Delta\phi} \dot{A}_+ \\ &= -\frac{2}{k_0} e^{-i\Delta\omega/2\cdot t} e^{-i\Delta\phi} \left[\left(i\frac{\Delta\omega}{2} a_1 + \omega_B a_2 \right) \cos(\omega_B t) + \right. \\ &\qquad \left. \left(i\frac{\Delta\omega}{2} a_2 - \omega_B a_1 \right) \sin(\omega_B t) \right] \end{aligned} \tag{A.27}$$

The values of a_1 and a_2 are obtained from adequate boundary conditions. These are, as shown in Appendix A.1, continuity in position and velocity. Given the coordinate transformation (Eq. 2.22) and the ansatz used (Eq. A.22), this is equivalent to

imposing continuity in the amplitudes (radii):

$$\begin{cases} A_+\left(0^-\right) = \sqrt{m\omega_1}\rho_+ = A_+\left(0^+\right) \\ A_-\left(0^-\right) = \sqrt{m\omega_1}\rho_- = A_-\left(0^+\right) \end{cases} \implies \begin{cases} a_1 = \sqrt{m\omega_1}\rho_+ \\ a_2 = -\frac{\sqrt{m\omega_1}}{2\omega_B}\left(k_0 e^{i\Delta\phi}\rho_- + i\Delta\omega\cdot\rho_+\right) \end{cases} \tag{A.28}$$

The amplitudes during the driving are therefore

$$A_\pm\left(t\right) = \sqrt{m\omega_1}\rho_\pm\left(t\right) = \sqrt{m\omega_1}e^{\pm i\Delta\omega/2\cdot t}\left[\rho_\pm\cos\left(\omega_B t\right) \mp \frac{i\Delta\omega\cdot\rho_\pm + k_0 e^{\pm i\Delta\phi}\rho_\mp}{2\omega_B}\sin\left(\omega_B t\right)\right] \tag{A.29}$$

If the initial radii are $\rho_+\left(0\right) = 0$ and $\rho_-\left(0\right) = \rho_-$, and the driving time is such that the conversion is complete when the driving is on resonance ($k_0 T_d = \pi$),

$$\begin{aligned} \rho_+\left(t > T_d\right) &= -\rho_- \frac{k_0 e^{i(\Delta\omega/2\cdot T_d + \phi_{RF} - \phi_-)}}{2\omega_B}\sin\left(\omega_B T_d\right) \\ &= \rho_- e^{i(\Delta\omega/2\cdot T_d + \phi_{RF} - \phi_- + \pi)}\frac{\pi}{2}\frac{1}{T_d\omega_B}\sin\left(\omega_B T_d\right) \\ &= \rho_- e^{i(\Delta\omega/2\cdot T_d + \phi_{RF} - \phi_- + \pi)}\frac{\pi}{2}\mathrm{sinc}\left(\omega_B T_d\right) \\ &= \rho_- e^{i(\Delta\omega/2\cdot T_d + \phi_{RF} - \phi_- + \pi)}\frac{\pi}{2}\mathrm{sinc}\left(\frac{\pi}{2}\sqrt{\left(\frac{\Delta\omega\cdot T_d}{\pi}\right)^2 + 1}\right) \end{aligned} \tag{A.30}$$

Fig. A.3 shows the resulting cyclotron radius and phase.

On the other hand, if the initial radii are instead $\rho_-\left(0\right) = 0$ and $\rho_+\left(0\right) = \rho_+$, the driving is on-resonance ($\Delta\omega = 0$) and a full conversion takes place,

$$\rho_-\left(t > T_d\right) = e^{-i(\phi_{RF} - \phi_+)}\rho_+ \implies q_-\left(t > T_d\right) = \sqrt{m\omega_1}\rho_+ e^{-i(\omega_- t - \phi_+)}e^{-i\phi_{RF}} \tag{A.31}$$

This expression explicitly shows that the resulting magnetron phase opposes the original cyclotron phase (plus a constant factor) and that the final magnetron radius is the same as the original cyclotron one.

On the other hand,

Eq. A.31 and A.30 will be useful when discussing several of the PTMS techniques.

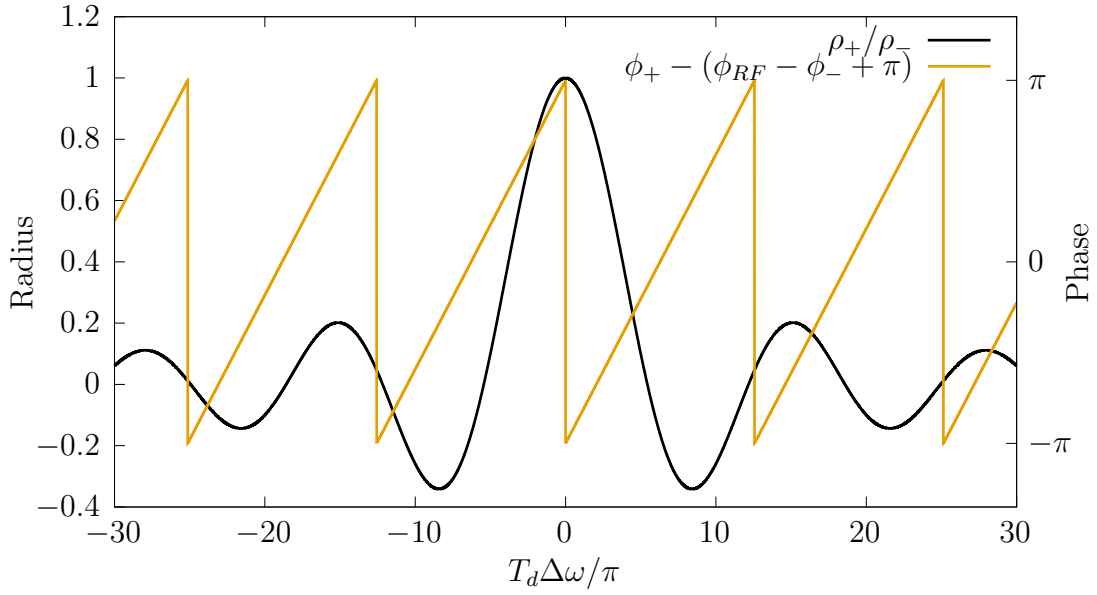

.pdf

Figure A.3: Amplitude and phase of a trapped ion after a quadrupolar RF driving. The driving settings are such that the conversion is complete when the driving is on resonance.

A.3 Perturbation theory and Zeeman effect

In order to study the modified electronic structure of the $^{40}Ca^{+}$ under magnetic fields beyond the linear regime of the Zeeman effect, perturbation theory can be used, as long as the splitting is much smaller than the separation due to the fine structure. The Hamiltonian is

$$\hat{\mathcal{H}} = \hat{\mathcal{H}}_0 + \hat{\mathcal{H}}' \tag{A.32}$$

where $\hat{\mathcal{H}}_0$ is the unperturbed Hamiltonian (including fine structure) and

$$\hat{\mathcal{H}}' = \mu_B B \left(\hat{L}_z + g\hat{S}_z\right)/\hbar \tag{A.33}$$

is the perturbation. Since the eigenstates of the unperturbed Hamiltonian have well defined L, S and J, whereas the perturbation is proportional to M_L and M_S, the coefficients of the base change between the two bases (i.e. the *Clebsch-Gordan coefficients*) will appear often in the calculations.

The first, second and third order corrections to the energy of the state $\left|i^{(0)}\right\rangle$ (eigenstate of the unperturbed Hamiltonian $\hat{\mathcal{H}}_0$) are given by [71]

$$\Delta E^{(1)} = \left\langle i^{(0)} \right| \hat{\mathcal{H}}' \left| i^{(0)} \right\rangle , \tag{A.34}$$

$$\Delta E^{(2)} = \sum_{j:E_i^{(0)} \neq E_j^{(0)}} \frac{\left| \left\langle j^{(0)} \right| \hat{\mathcal{H}}' \left| i^{(0)} \right\rangle \right|^2}{E_i^{(0)} - E_j^{(0)}} \tag{A.35}$$

and [80]

$$\begin{aligned} \Delta E_i^{(3)} = & \sum_{j:E_j^{(0)} \neq E_i^{(0)}} \sum_{k:E_k^{(0)} \neq E_i^{(0)}} \frac{\left\langle i^{(0)} \right| \hat{\mathcal{H}}' \left| j^{(0)} \right\rangle \left\langle j^{(0)} \right| \hat{\mathcal{H}}' \left| k^{(0)} \right\rangle \left\langle k^{(0)} \right| \hat{\mathcal{H}}' \left| i^{(0)} \right\rangle}{\left(E_i^{(0)} - E_j^{(0)} \right) \left(E_i^{(0)} - E_k^{(0)} \right)} \\ & - \sum_{j:E_j^{(0)} \neq E_i^{(0)}} \frac{\left\langle i^{(0)} \right| \hat{\mathcal{H}}' \left| j^{(0)} \right\rangle \left\langle j^{(0)} \right| \hat{\mathcal{H}}' \left| i^{(0)} \right\rangle \left\langle i^{(0)} \right| \hat{\mathcal{H}}' \left| i^{(0)} \right\rangle}{\left(E_i^{(0)} - E_j^{(0)} \right)^2} , \end{aligned} \tag{A.36}$$

respectively.

Note that these expressions deviate from the usual ones at the sum indices. The sums only iterate outside of the degenerate subspace that contains $\left| i^{(0)} \right\rangle$, i.e. over states whose energy differs from that of $\left| i^{(0)} \right\rangle$. In a hydrogen-like atomic system with fine structure that means that $\left| i^{(0)} \right\rangle$ and $\left| j^{(0)} \right\rangle$ must differ at least in one of the quantum numbers L or J. This is a valid way to apply non-degenerate perturbation theory to a degenerate $\hat{\mathcal{H}}_0$ if the perturbation is diagonalized in each of the degenerate subspaces [71]. Later on it will be shown that the perturbation $\hat{\mathcal{H}}'$ verifies this condition from the onset.

In the previous expressions all the brackets that appear are matrix elements of the perturbation $\hat{\mathcal{H}}'$ in the base of the eigenstates of the unperturbed Hamiltonian $\hat{\mathcal{H}}_0$. If these are known, the bracket $\left\langle i^{(0)} \right| \hat{\mathcal{H}}' \left| j^{(0)} \right\rangle$ can be substituted by matrix element h_{ij}, greatly simplifying these expressions. The matrix elements will be calculated in the present Appendix.

The diagonal terms are given by

$$
\begin{aligned}
&\langle LS; JM_J|\hat{\mathcal{H}}'\,|LS; JM_J\rangle \\
&\quad= \left(\sum_{M_L,M_S} \langle LS; JM_J|\ LM_LSM_S\rangle\,\langle LM_LSM_S|\right) \\
&\qquad\qquad \hat{\mathcal{H}}'\left(\sum_{M'_L,M'_S} \langle LM'_LSM'_S|\ LS; JM_J\rangle\,|LM'_LSM'_S\rangle\right) \\
&\quad= \mu_B B\left(\sum_{M_L,M_S} \langle LS; JM_J|\ LM_LSM_S\rangle\,\langle LM_LSM_S|\right) \\
&\qquad\qquad \left(\sum_{M'_L,M'_S} (M'_L + gM'_S)\,\langle LM_LSM_S|\ LS; JM_J\rangle\,|LM'_LSM'_S\rangle\right) \\
&\quad= \mu_B B \sum_{M_L,M_S,M'_L,M'_S} [(M'_L + gM'_S)\,\langle LS; JM_J|\ LM_LSM_S\rangle \\
&\qquad\qquad \langle LM_LSM_S|\ LS; JM_J\rangle\,\langle LM_LSM_S|\ LM'_LSM'_S\rangle] \\
&\quad= \mu_B B \sum_{M_L,M_S,M'_L,M'_S} [(M'_L + gM'_S)\,\langle LS; JM_J|\ LM_LSM_S\rangle \\
&\qquad\qquad \langle LM_LSM_S|\ LS; JM_J\rangle\,\delta_{M_LM'_L}\delta_{M_SM'_S}] \\
&\quad= \mu_B B \sum_{M_L,M_S} (M'_L + gM'_S)\,|\langle LS; JM_J|\ LM_LSM_S\rangle|^2 \\
&\quad= \mu_B B \sum_{M_L} (M'_L + gM'_S)\,|\langle LS; JM_J|\ LM_LSM_S\rangle|^2\ . \qquad \text{(A.37)}
\end{aligned}
$$

The brackets that appear in the last term are, as anticipated, Clebsch-Gordan coefficients. The last step takes into account that, for the Clebsch-Gordan coefficient to be non-zero, $M_S = M_J - M_L$, and therefore no summing over M_S is needed. If, as is the case of $^{40}Ca^+$, $S = 1/2$ is fixed, the state $|L\,S; L\,M_J\rangle$ in the perturbation base is given by

$$
\left|L\,\frac{1}{2}; J\,M_J\right\rangle = a\left|L\ M_J + \frac{1}{2}\ \frac{1}{2}\ \frac{-1}{2}\right\rangle + b\left|L\ M_J - \frac{1}{2}\ \frac{1}{2}\ \frac{+1}{2}\right\rangle\ , \qquad \text{(A.38)}
$$

with a and b the corresponding Clebsch-Gordan coefficients. The matrix element is then

$$
\langle LS; JM_J|\,\hat{\mathcal{H}}'\,|LS; JM_J\rangle = \mu_B B\left[a\left(M_J + \frac{1}{2} - \frac{g}{2}\right) + b\left(M_J - \frac{1}{2} + \frac{g}{2}\right)\right] \qquad \text{(A.39)}
$$

The off-diagonal elements, on the other hand, are given by

$$
\begin{aligned}
&\langle L'S';J'M'_J|\,\hat{\mathcal{H}}'\,|LS;JM_J\rangle = \\
&= \left(\sum_{L'',M''_L,S'',M''_S} \langle L'S';J'M'_J|\;L''M''_LS''M''_S\rangle\,\langle L''M''_LS''M''_S|\right) \\
&\qquad \hat{\mathcal{H}}'\left(\sum_{L''',M'''_L,S''',M'''_S} \langle L'''M'''_LS'''M'''_S|\;LS;JM_J\rangle\,|L'''M'''_LS'''M'''_S\rangle\right) \\
&= \mu_B B\left(\sum_{L'',M''_L,S'',M''_S} \langle L'S';J'M'_J|\;L''M''_LS''M''_S\rangle\,\langle L''M''_LS''M''_S|\right) \\
&\qquad \left(\sum_{L''',M'''_L,S''',M'''_S} (M'''_L+gM'''_S)\,\langle L'''M'''_LS'''M'''_S|\;LS;JM_J\rangle\,|L'''M'''_LS'''M'''_S\rangle\right) \\
&= \mu_B B\Bigg(\sum_{L'',M''_L,S'',M''_S,L''',M'''_L,S''',M'''_S} (M'''_L+gM'''_S)\,\langle L'S';J'M'_J|\;L''M''_LS''M''_S\rangle \\
&\qquad \langle L'''M'''_LS'''M'''_S|\;LS;JM_J\rangle\,\langle L''M''_LS''M''_S|\;L'''M'''_LS'''M'''_S\rangle\Bigg) \\
&= \mu_B B\Bigg(\sum_{L'',M''_L,S'',M''_S,L''',M'''_L,S''',M'''_S} (M'''_L+gM'''_S)\,\langle L'S';J'M'_J|\;L''M''_LS''M''_S\rangle \\
&\qquad \langle L'''M'''_LS'''M'''_S|\;LS;JM_J\rangle\,\delta_{L''L'''}\delta_{M''_LM'''_L}\delta_{S''S'''}\delta_{M''_SM'''_S}\Bigg) \\
&= \mu_B B\sum_{L'',M''_L,S'',M''_S} (M''_L+gM''_S)\,\langle L'S';J'M'_J|\;L''M''_LS''M''_S\rangle\,\langle L''M''_LS''M''_S|\;LS;JM_J\rangle \\
&= \mu_B B\sum_{M''_L} (M''_L+gM''_S)\,\langle LS;J'M'_J|\;LM''_LSM''_S\rangle\,\langle LM''_LSM''_S|\;LS;JM_J\rangle \qquad \text{(A.40)}
\end{aligned}
$$

Again, the brackets in the final term are Clebsch-Gordan coefficients. The last step takes into account that for both Clebsch-Gordan to be simultaneously non-zero, $L = L' = L''$, $S = S' = S''$ and $M_J = M'_J$ are required, J being the only quantum number that can differ[3]. This also restricts M''_S to $M''_S = M_J - M''_L$. Therefore, given that $L \neq L'$ results in zeros, sorting the base by increasing values of L yields a block diagonal matrix:

[3]In fact, $J \neq J'$ is a requirement as well – otherwise, the element being calculated is not off-diagonal to begin with, since all quantum numbers are equal!

$$\hat{\mathcal{H}}' = \begin{pmatrix} \hat{\mathcal{H}}'_{\mathrm{S}} & \mathbb{O}_{6\mathrm{x}6} & \mathbb{O}_{10\mathrm{x}10} \\ \mathbb{O}_{4\mathrm{x}4} & \hat{\mathcal{H}}'_{\mathrm{P}} & \mathbb{O}_{10\mathrm{x}10} \\ \mathbb{O}_{4\mathrm{x}4} & \mathbb{O}_{6\mathrm{x}6} & \hat{\mathcal{H}}'_{\mathrm{D}} \end{pmatrix} \tag{A.41}$$

Also, since matrix elements involving $M_J \neq M'_J$ result in zeroes, the diagonal form of $\hat{\mathcal{H}}'$ within each of the degenerate subspaces (equal J) is proven, and the use of Eqs. A.34, A.35 and A.36 is justified.

If $S = 1/2$ (as in the case of $^{40}Ca^{+}$), two values of J are possible for each L – or even just one, if $L = 0$:

- If $L = 0$, there is no other state with different J but equal M_J; therefore, off-diagonal elements are zero if they involve an S state.

- If $L \neq 0$, the restriction $M_J = M'_J$ still applies. For the term to be non-zero there must exist a state with $J' \neq J$ but $M_J = M'_J$. Therefore, states with $J = L + 1/2$ and $|M_J| = L + \frac{1}{2}$ won't have non-zero off-diagonal elements, since a state with $J = L - 1/2$ can't have $M_J = \pm\left|L + \frac{1}{2}\right|$. For the remaining states ($L \neq 0$ and $|M_J| < L + \frac{1}{2}$), only a single off-diagonal term is non-zero – that of $L = L'$, $J \neq J'$ and $M_J = M'_J$.

The pairs of states with equal L and M_J but different J can be decomposed in the basis of the perturbation as

$$\left|L\ \frac{1}{2}; L + \frac{1}{2}\ M_J\right\rangle = a\left|L\ M_J + \frac{1}{2}\ \frac{1}{2}\ \frac{-1}{2}\right\rangle + b\left|L\ M_J - \frac{1}{2}\ \frac{1}{2}\ \frac{+1}{2}\right\rangle \tag{A.42}$$

and

$$\left|L\ \frac{1}{2}; L - \frac{1}{2}\ M_J\right\rangle = b\left|L\ M_J + \frac{1}{2}\ \frac{1}{2}\ \frac{-1}{2}\right\rangle - a\left|L\ M_J - \frac{1}{2}\ \frac{1}{2}\ \frac{+1}{2}\right\rangle, \tag{A.43}$$

where a and b are the Clebsh Gordan coefficients, verifying $a, b > 0$ and $a^2 + b^2 = 1$. Applying the perturbation to e.g. the second,

$$
\begin{aligned}
&(L_z + gS_z)\left|L\ \frac{1}{2}; L-\frac{1}{2}\ M_J\right\rangle = \\
&\qquad = (L_z + gS_z)\left(b\left|L\ M_J+\frac{1}{2}\ \frac{1}{2}\ \frac{-1}{2}\right\rangle - a\left|L\ M_J-\frac{1}{2}\ \frac{1}{2}\ \frac{+1}{2}\right\rangle\right) = \\
&= b\left(M_J+\frac{1}{2}-\frac{g}{2}\right)\left|L\ M_J+\frac{1}{2}\ \frac{1}{2}\ \frac{-1}{2}\right\rangle - a\left(M_J-\frac{1}{2}+\frac{g}{2}\right)\left|L\ M_J-\frac{1}{2}\ \frac{1}{2}\ \frac{+1}{2}\right\rangle
\end{aligned}
\tag{A.44}
$$

and multiplying by the first,

$$
\begin{aligned}
&\left\langle L\ \frac{1}{2}; L+\frac{1}{2}\ M_J\right| L_z + gS_z \left|L\ \frac{1}{2}; L-\frac{1}{2}\ M_J\right\rangle = \\
&\qquad = \left(a\left\langle L\ M_J+\frac{1}{2}\ \frac{1}{2}\ \frac{-1}{2}\right| + b\left\langle L\ M_J-\frac{1}{2}\ \frac{1}{2}\ \frac{+1}{2}\right|\right) \\
&\left(b\left[M_J+\frac{1}{2}-\frac{g}{2}\right]\left|L\ M_J+\frac{1}{2}\ \frac{1}{2}\ \frac{-1}{2}\right\rangle - a\left[M_J-\frac{1}{2}+\frac{g}{2}\right]\left|L\ M_J-\frac{1}{2}\ \frac{1}{2}\ \frac{+1}{2}\right\rangle\right) = \\
&\quad = ab\left(\left[M_J+\frac{1}{2}-\frac{g}{2}\right]-\left[M_J-\frac{1}{2}+\frac{g}{2}\right]\right) = ab\,(1-g) = -ab\,(g-1)\ ,
\end{aligned}
\tag{A.45}
$$

the off-diagonal matrix elements are obtained.

Putting the focus on the particular case of $^{40}Ca^{+}$, whose unperturbed electronic structure was shown in Sec. 2.4.4 (see Fig. 2.5), the previous conclusions can be applied to a concrete physical case. Only the P states with $|M_J| \leq \frac{1}{2}$ and the D states with $|M_J| \leq \frac{3}{2}$ will have non-zero off-diagonal terms. If the states within a given L value are sorted by increasing J and then by increasing M_J (i.e. the ordering of e.g. the P states is $J = 1/2$, $M_J = -1/2$, then $J = 1/2$, $M_J = +1/2$, then $J = 3/2$, $M_J = -3/2$, ...) the sub-matrices introduced in Eq. A.41 are

$$
\hat{\mathcal{H}}'_{\mathrm{S}} = \mu_B B \begin{pmatrix} -\frac{g}{2} & 0 \\ 0 & \frac{g}{2} \end{pmatrix}
\tag{A.46}
$$

within the $L = 0$ subspace,

$$\hat{\mathcal{H}}'_{\mathrm{P}} = \mu_B B \begin{pmatrix} -\left(\frac{2}{3} - \frac{g}{6}\right) & 0 & 0 & -\frac{\sqrt{2}}{3}(g-1) & 0 & 0 \\ 0 & +\left(\frac{2}{3} - \frac{g}{6}\right) & 0 & 0 & -\frac{\sqrt{2}}{3}(g-1) & 0 \\ 0 & 0 & -\left(1 + \frac{g}{2}\right) & 0 & 0 & 0 \\ -\frac{\sqrt{2}}{3}(g-1) & 0 & 0 & -\left(\frac{1}{3} + \frac{g}{6}\right) & 0 & 0 \\ 0 & -\frac{\sqrt{2}}{3}(g-1) & 0 & 0 & +\left(\frac{1}{3} + \frac{g}{6}\right) & 0 \\ 0 & 0 & 0 & 0 & 0 & +\left(1 + \frac{g}{2}\right) \end{pmatrix} \tag{A.47}$$

within the $L = 1$ subspace and finally, within the $L = 2$ subspace,

$$\hat{\mathcal{H}}'_{\mathrm{D}} = \mu_B B \begin{pmatrix}
-\left(\frac{9}{5}-\frac{3g}{10}\right) & 0 & 0 & 0 & 0 & -\frac{2}{5}(g-1) & 0 & 0 & 0 & 0 \\
0 & -\left(\frac{3}{5}-\frac{g}{10}\right) & 0 & 0 & 0 & 0 & -\frac{\sqrt{6}}{5}(g-1) & 0 & 0 & 0 \\
0 & 0 & +\left(\frac{3}{5}-\frac{g}{10}\right) & 0 & 0 & 0 & 0 & -\frac{\sqrt{6}}{5}(g-1) & 0 & 0 \\
0 & 0 & 0 & +\left(\frac{9}{5}-\frac{3g}{10}\right) & 0 & 0 & 0 & 0 & -\frac{2}{5}(g-1) & 0 \\
0 & 0 & 0 & 0 & -\left(2+\frac{g}{2}\right) & 0 & 0 & 0 & 0 & 0 \\
-\frac{2}{5}(g-1) & 0 & 0 & 0 & 0 & -\left(\frac{6}{5}+\frac{3g}{10}\right) & 0 & 0 & 0 & 0 \\
0 & -\frac{\sqrt{6}}{5}(g-1) & 0 & 0 & 0 & 0 & -\left(\frac{2}{5}+\frac{g}{10}\right) & 0 & 0 & 0 \\
0 & 0 & -\frac{\sqrt{6}}{5}(g-1) & 0 & 0 & 0 & 0 & +\left(\frac{2}{5}+\frac{g}{10}\right) & 0 & 0 \\
0 & 0 & 0 & -\frac{2}{5}(g-1) & 0 & 0 & 0 & 0 & +\left(\frac{6}{5}+\frac{3g}{10}\right) & 0 \\
0 & 0 & 0 & 0 & 0 & 0 & 0 & 0 & 0 & +\left(2+\frac{g}{2}\right)
\end{pmatrix} \tag{A.48}$$

Resumen extenso y conclusiones

La presente Tesis doctoral tiene como motivación el desarrollo de una nueva técnica de medidas de masa en trampas Penning basada en la detección óptica. Para ello tiene tres pilares principales: uno teórico (estudio del *cristal asimétrico de dos iones*), otro de desarrollo de software (para crear un sistema de control que facilite la realización de los experimentos) y otro experimental (en el que se ha mejorado el sistema hasta conseguir la cristalización de iones en la trampa Penning).

Introducción

Las medidas de masa son muy relevantes en numerosos campos. Las medidas de masa de alta precisión se han utilizado para poner a prueba teorías fundamentales, estudiar la nucleosíntesis estelar o incluso para contribuir al acotamiento de la masa del neutrino (véase el Capítulo 1). Todos los métodos de medidas de masa en trampas Penning se basan en la medida de las frecuencias de movimiento del ion en la trampa, que se pueden relacionar con la frecuencia que el ion tendría si sólo actuase el campo magnético de la trampa (*frecuencia ciclotrón libre*) y, a partir de ésta, con la masa del ion (véase el Capítulo 2).

El foco de esta tesis está en los los elementos *superpesados* o *transactínidos*, producidos en unas pocas instalaciones en todo el mundo [23, 24, 25, 26]. Estos elementos se producen en cantidades minúsculas, con eficiencias tanto menores cuanto más pesados son estos núcleos. La determinación de su masa (y, por tanto, de su energía de ligadura) permite estudiar la estructura nuclear en condiciones extremas. Además, mapear la energía de ligadura de los diferentes elementos superpesados ayudará a localizar la *isla de la estabilidad*, donde el cierre de capa en el núcleo confiere de una estabilidad superior a la de las especies de similar composición. Con tasas de producción tan bajas como unos pocos iones a la semana, la capacidad de medir la masa a partir de un solo ion es fundamental. Las técnicas actuales de medidas de masa, aunque muy exitosas, no pueden alcanzar esta sensibilidad (véase el Capítulo 3).

Algunas especies iónicas tienen una estructura electrónica que permite manipularlas medi-

ante el uso de láseres, con lo que se pueden enfriar a temperaturas de milikelvin o incluso hasta el estado fundamental del pozo de potencial de la trampa (véase la Sección 2.4). El uso de estas especies iónicas como sensores para el estudio de otras especies sin las mismas propiedades ha sido muy exitoso [40, 41].

La técnica aquí propuesta se basa en el uso de un ion $^{40}Ca^{+}$ (el ion *sensor*) para estudiar la masa de un ion arbitrario (ion *de interés*) encontrándose los dos atrapados en la misma trampa Penning. Cuando el ion sensor es enfriado por láser, ambos forman un *cristal de Coulomb*. Para determinar la masa del ion de interés es necesario caracterizar en detalle la dinámica de dicho cristal.

Cristal asimétrico de dos iones

El primer paso llevado a cabo en el Capítulo 4 es el estudio de la dinámica de un cristal con dos iones idénticos, denominado *cristal simétrico* El tratamiento matemático en este caso es más sencillo. Aunque este cristal no tiene relevancia desde el punto de vista de la espectrometría de masas, su estudio sirve para interpretar mejor los resultados de un cristal genérico, que se ha denominado *cristal asimétrico*. En ambos casos, el cristal tiene seis modos de movimiento. Los modos del cristal tienen además características similares a los modos de un solo ion, por lo que heredan los nombres de éstos. Los modos radiales de alta frecuencia, cercana a la frecuencia que el ion tendría en un campo magnético de la misma intensidad, se denominan *modos ciclotrón*. Los modos radiales de baja frecuencia, que aparecen debido al campo electrostático de la trampa, heredan el nombre de *modos magnetrón*. También aparecen dos *modos axiales*, que no están influidos por el campo magnético de la trampa. Estas tres parejas de modos se pueden clasificar en dos categorías, puesto que en cada pareja hay un modo en el que ambos iones se mueven en coincidencia de fase (*modos comunes*) y otro en el que se mueven en oposición de fase (*modos vibracionales*).

Además de caracterizar los modos, en esta tesis se muestra cómo el *teorema de invariancia generalizado*, obtenido para trampas Penning microfabricadas, en las que cada trampa contiene únicamente un ion [100], es aplicable también al caso del cristal asimétrico de dos iones. Por tanto, las frecuencias de los seis modos del cristal, Ω_λ, se pueden relacionar con las frecuencias ciclotrón de los iones de interés y sensor, ω_{ct} y ω_{cs}, según

$$\sum_{\lambda} \Omega_\lambda^2 = \omega_{ct}^2 + \omega_{cs}^2$$

Puesto que en el estudio del cristal habrá que someterlo a campos electromagnéticos oscilantes (*excitaciones*) a distintas frecuencias para encontrar aquellas que resuenan con sus modos de movimiento, es importante caracterizar la respuesta del cristal a dichos

campos externos. Esto se ha llevado a cabo en la Sección 4.2. Se encuentra que la respuesta es equivalente a la de un solo ion si se introduce una *relación carga/masa efectiva*, característica de cada uno de los modos. Especialmente interesante es que los modos vibracionales del cristal simétrico no responden a las excitaciones.

En el estudio de la dinámica del cristal se ha de realizar una aproximación de desplazamientos pequeños alrededor de la posición de equilibrio. Dada la no-armonicidad de la repulsión culombiana entre los iones, esto introduce corrimientos en la frecuencia de los modos que dependen de la amplitud de oscilación. Es fundamental, por tanto, estudiar estos corrimientos en frecuencia. Esto tiene lugar en la Sección 4.3. El estudio de los corrimientos en el régimen clásico mediante simulaciones de las trayectorias de los iones muestra que algunos modos (especialmente el modo magnetrón vibracional y, en menor medida, el axial vibracional) tienen corrimientos en frecuencia muy significativos. El estudio de los corrimientos en frecuencia en el régimen cuántico, llevado a cabo mediante teoría de perturbaciones, evidencia ademas que el modo magnetrón vibracional introduce corrimientos significativos no solo en su propia frecuencia, sino en la del resto de modos.

Desarrollo del nuevo sistema de control y adquisición

En cuanto a la parte de desarrollo de software, en esta Tesis se ha sustituido el sistema anteriormente utlizado (que realiza el control del experimento y la adquisición de datos de forma separada) por un sistema unificado, como se muestra en el Capítulo 5. Un sistema unificado simplifica la realización de experimentos, por ejemplo, permitiendo realizar un experimento para varios valores de un parámetro experimental y registrar los resultados asociándolos al valor utilizado, o automatizar el análisis de forma que se puedan visualizar los resultados *en vivo*, pudiendo actuar el operador en consecuencia.

Como punto de partida se ha elegido el sistema *ARTIQ* (Advanced Real-Time Infrastructure for Quantum Physics). No solo presenta una muy buena resolución temporal, lo cual es imprescindible para realizar experimentos con iones atrapados, sino que además es fácilmente extensible. El software, basado en Python, es compilado y ejecutado en un procesador dedicado (Field-Programmable Gate Array, o FPGA) para aquellas tareas que requieren el mayor rendimiento, pudiendo ejecutarse en un ordenador convencional todas aquellas tareas que no tengan esas restricciones, usando llamadas a procedimientos remotos (Remote Procedure Calls, o RPCs).

ARTIQ tiene asociada una familia de dispositivos (*Sinara*) capaces de suplir muchas de las necesidades de un laboratorio. Sin embargo, no todos los requisitos del experimento son alcanzables usando únicamente hardware Sinara. Es en este punto donde la base Python del software es especialmente útil – dada la gran popularidad del lenguaje, así como la posibilidad de ejecutar código en un ordenador convencional mediante RPCs, casi

cualquier dispositivo puede integrarse en un sistema ARTIQ. En esta Tesis se han resuelto de este modo varias necesidades del experimento:

- Potenciales de atrapamiento: la fuente de alimentación de Sinara está limitada a ±10 V, por lo que no alcanza los voltajes necesarios para confinar iones en la trampa Penning en las condiciones deseadas. Por eso se integró la fuente de alimentación CAEN SY1527 en el nuevo sistema de control. El fabricante proporciona una librería estática codificada en C. Este tipo de librerías se integran en Python creando un *módulo de extensión*, un programa en C que utiliza la interfaz de programación (Application Programming Interface, o API) de Python, de modo que el código resultante sea compatible con el mismo.

- Excitación de los modos de movimiento del cristal: los sintetizadores de frecuencia de Sinara no operan por debajo de 1 MHz. La mayoría de frecuencias de movimiento del cristal se encuentran por debajo de este valor. Por tanto, una pareja de generadores de radiofrecuencia Agilent fueron integrados en el sistema de control. Éstos se controlan mediante el estándar *Virtual Instrument Software Architecture* (VISA). Existen varias librerías Python que pueden controlar dispositivos mediante este estándar. En este caso, `pyVISA` fue utilizada.

- Detección de fotones dispersados por el ion sensor: la cámara EMCCD que se utilizaba en los experimentos con anterioridad fue integrada en el nuevo sistema. El fabricante de la cámara proporciona una librería dinámica codificada en C para utilizar la cámara en programas personalizados. El paquete `ctypes` permite utilizar dichas librerías en Python. Además, el tubo fotomultiplicador disponible en el laboratorio, cuyo fabricante también proporciona una librería del mismo tipo, será integrado siguiendo el mismo proceso en los próximos meses.

El nuevo sistema de control está actualmente en uso en el laboratorio.

Observación del cristal de dos iones

La parte experimental del trabajo tiene dos componentes: la caracterización de la trampa de anillos abierta, por un lado, y las modificaciones llevadas a cabo hacia la consecución del cristal de dos iones, por otro.

La trampa de anillos abierta, a diferencia de las geometrías de trampas Penning más comunes, no tiene electrodos en el plano radial. Esto otorga una gran facilidad de acceso, sea para láseres, recolección de fotones, o cualquier otro propósito. Un paso importante es la sintonización de la trampa. Para ello se ha creado un protocolo, basado en un programa de resolución de potenciales electrostáticos, que permite elegir una frecuencia minimizando

los términos no armónicos. Se ha conseguido verificar experimentalmente la armonicidad del potencial resultante. La trampa se ha utilizado para medir frecuencias de movimiento de iones de calcio usando detección destructiva mediante un detector de microcanales, así como para realizar resonancias por tiempo de vuelo. Éstas últimas sirvieron además para obtener un valor preciso del campo magnético para los cálculos del efecto Zeeman.

De cara al enfriamiento por láser, diferentes modificaciones del setup fueron implementadas, entre las que destacan:

- Diseño y fabricación de una nueva fuente de iones. En lugar de usar la fuente por desorción láser empleada anteriormente, se diseñó una estructura para colocar hornos de calcio dentro del campo magnético. Éstos evaporan átomos de calcio, que después son fotoionizados en el centro de la trampa en un proceso con dos pasos, de los cuales el primero es resonante. Esto permite ionizar sólo calcio, permitiendo incluso selectividad isotópica. Además, permite incrementar el número de iones de forma sencilla, y la energía inicial de los mismos es bastante baja.

- Diseño del esquema de operación de un modulador electro-óptico: el estudio del efecto del campo magnético en la estructura electrónica del ion sensor (*efecto Zeeman*) llevado a cabo en la Sección 2.4.4 permitió diseñar un esquema de operación del modulador electro-óptico que permite bombear los seis sub-niveles del estado metaestable $D_{5/2}$. Este estado, que en principio no debería estar involucrado en el proceso de Doppler cooling, es puesto en juego debido al efecto de mezclado de momentos angulares del campo magnético. Además, la alta intensidad del campo magnético hace que el efecto Zeeman entre en un régimen no lineal, de modo que una sola señal aplicada al EOM no es suficiente. Varias configuraciones con dos señales fueron analizadas, y una de ellas implementada.

Estas modificaciones permitieron la observación de fluorescencia y las primeras evidencias de enfriamiento láser de $^{40}Ca^{+}$ en un campo magnético de tal intensidad. Mejoras incrementales en el vacío en la trampa, así como un rediseño del sistema óptico como parte de otra tesis doctoral [69] permitieron además la cristalización de nubes de iones de $^{40}Ca^{+}$. Una vez observada la cristalización se pudo conseguir un cristal de dos iones (en este caso iguales) reduciendo la corriente que circula por el horno de calcio.

Conclusiones

Este trabajo ha estudiado la viabilidad del uso de un cristal asimétrico de dos iones como plataforma sobre la que realizar medidas de masa utilizando detección óptica.

En primer lugar, se ha estudiado la dinámica de dicho cristal. Un estudio detallado del movimiento de los iones, apoyado en la intuición que proporciona el estudio del cristal

simétrico, así como la dinámica de un solo ion, permite caracterizar los seis modos de movimiento resultantes. Especialmente importante, sin embargo, ha sido demostrar la aplicabilidad del *teorema de invariancia generalizado*. Éste permite relacionar las frecuencias del cristal con las frecuencias ciclotrón libres de los iones sensor y de interés, que son las cantidades a partir de las que, en última instancia, se deriva el valor de la masa. Se ha estudiado también la mayor limitación del método (los corrimientos en frecuencia debidos a la no-armonicidad de la interacción de Coulomb). Los grandes corrimientos causados por los modos vibracionales impiden realizar un proceso de medida basado en las seis frecuencias del cristal que sea puramente clásico. Se proponen dos posibilidades. El primer consiste en una medida en el régimen clásico de la frecuencia axial común, a partir de la cual se puede obtener la masa, aunque con una precisión limitada. Esto se podría emplear a modo de método de identificación no destructivo. Un método en el régimen cuántico que determine al menos tres de lase seis frecuencias del cristal (dependiendo de la precisión deseada) usando métodos de medida no clásicos [107] está siendo estudiado para este caso particular [111].

Además, esta Tesis ha conseguido por primera vez el enfriamiento de iones de $^{40}Ca^{+}$ en un campo magnético de 7 Tesla. A diferencia de las implementaciones realizadas en otros grupos, es necesario tener en cuenta el efecto Zeeman hasta tercer orden para poder localizar las frecuencias de transición. Con una trampa de geometría novedosa y debidamente caracterizada, se ha conseguido observar la cristalización de una nube de iones. Se ha conseguido también observar un cristal simétrico de dos iones. A partir de la imagen del cristal se ha podido estimar la mínima amplitud con la que se podrían realizar medidas de masa usando únicamente el modo axial común. Esto ha permitido, por tanto, estimar el corrimiento en frecuencia – en el mejor de los casos, la resonancia se verá desplazada unos 30 Hz. Sin embargo, dado que la amplitud de oscilación es directamente observada, este corrimiento se puede corregir hasta cierto punto, por lo que este método puede ser utilizado para realizar identificaciones no destructivas de iones desconocidos a partir de su masa, o para monitorizar la desintegración de los mismos. Por otro lado se está progresando en el terreno experimental hacia las medidas en el régimen cuántico. Un láser de 729 nm asociado a una cavidad de alta fineza han sido instalados y caracterizados. Éste láser permitirá llevar a cabo enfriamiento al estado cero, así como medidas con números de fonones muy bajos y métodos de medida no clásicos.

Bibliography

[1] T.W. Hänsch. Nobel Lecture: Passion for precision. *Rev. Mod. Phys.*, **78** 1297–1309, 2006.

[2] T. Fortier and E. Baumann. 20 years of developments in optical frequency comb technology and applications. *Commun. Phys.*, **2**(1) 153, 2019.

[3] A. Beyer, L. Maisenbacher, A. Matveev, R. Pohl, K. Khabarova, A. Grinin, T. Lamour, D.C. Yost, T.W. Hänsch, N. Kolachevsky, and T. Udem. The Rydberg constant and proton size from atomic hydrogen. *Science*, **358**(6359) 79–85, 2017.

[4] R. Pohl, A. Antognini, F. Nez, F.D. Amaro, F. Biraben, J.M.R. Cardoso, D.S. Covita, A. Dax, S. Dhawan, L.M.P. Fernandes, A. Giesen, T. Graf, T.W. Hänsch, P. Indelicato, L. Julien, C.Y. Kao, P. Knowles, E.O. Le Bigot, Y.W. Liu, J.A.M. Lopes, L. Ludhova, C.M.B. Monteiro, F. Mulhauser, T. Nebel, P. Rabinowitz, J.M.F. dos Santos, Lukas A. Schaller, K. Schuhmann, C. Schwob, D. Taqqu, J.F.C.A. Veloso, and F. Kottmann. The size of the proton. *Nature*, **466**(7303) 213–216, 2010.

[5] W. Xiong, A. Gasparian, H. Gao, D. Dutta, M. Khandaker, N. Liyanage, E. Pasyuk, C. Peng, X. Bai, L. Ye, K. Gnanvo, C. Gu, M. Levillain, X. Yan, D.W. Higinbotham, M. Meziane, Z. Ye, K. Adhikari, B. Aljawrneh, H. Bhatt, D. Bhetuwal, J. Brock, V. Burkert, C. Carlin, A. Deur, D. Di, J. Dunne, P. Ekanayaka, L. ElFassi, B. Emmich, L. Gan, O. Glamazdin, M.L. Kabir, A. Karki, C. Keith, S. Kowalski, V. Lagerquist, I. Larin, T. Liu, A. Liyanage, J. Maxwell, D. Meekins, S.J. Nazeer, V. Nelyubin, H. Nguyen, R. Pedroni, C. Perdrisat, J. Pierce, V. Punjabi, M. Shabestari, A. Shahinyan, R. Silwal, S. Stepanyan, A. Subedi, V.V. Tarasov, N. Ton, Y. Zhang, and Z.W. Zhao. A small proton charge radius from an electron–proton scattering experiment. *Nature*, **575**(7781) 147–150, 2019.

[6] G. Schneider, A. Mooser, M. Bohman, N. Schön, J. Harrington, T. Higuchi, H. Nagahama, S. Sellner, C. Smorra, K. Blaum, Y. Matsuda, W. Quint, J. Walz, and

S. Ulmer. Double-trap measurement of the proton magnetic moment at 0.3 parts per billion precision. *Science*, **358**(6366) 1081–1084, 2017.

[7] C. Smorra, S. Sellner, M.J. Borchert, J.A. Harrington, T. Higuchi, H. Nagahama, T. Tanaka, A. Mooser, G. Schneider, M. Bohman, K. Blaum, Y. Matsuda, C. Ospelkaus, W. Quint, J. Walz, Y. Yamazaki, and S. Ulmer. A parts-per-billion measurement of the antiproton magnetic moment. *Nature*, **550**(7676) 371–374, 2017.

[8] D. Hanneke, S. Fogwell Hoogerheide, and G. Gabrielse. Cavity control of a single-electron quantum cyclotron: Measuring the electron magnetic moment. *Phys. Rev. A*, **83** 052122, 2011.

[9] R.M. Godun, P.B.R. Nisbet-Jones, J.M. Jones, S.A. King, L.A.M. Johnson, H.S. Margolis, K. Szymaniec, S.N. Lea, K. Bongs, and P. Gill. Frequency Ratio of Two Optical Clock Transitions in $^{171}Yb^{+}$ and Constraints on the Time Variation of Fundamental Constants. *Phys. Rev. Lett.*, **113** 210801, 2014.

[10] J. Dilling, K. Blaum, M. Brodeur, and S. Eliseev. Penning-Trap Mass Measurements in Atomic and Nuclear Physics. *Annu. Rev. Nucl. Part. Sci.*, **68**(1) 45–74, 2018.

[11] L.S. Brown and G. Gabrielse. Geonium theory: Physics of a single electron or ion in a Penning trap. *Rev. Mod. Phys.*, **58** 233–311, 1986.

[12] L.S. Brown and G. Gabrielse. Precision spectroscopy of a charged particle in an imperfect Penning trap. *Phys. Rev. A*, **25** 2423–2425, 1982.

[13] M. König, G. Bollen, H.-J. Kluge, T. Otto, and J. Szerypo. Quadrupole excitation of stored ion motion at the true cyclotron frequency. *Int. J. Mass Spectrom.*, **142**(1) 95–116, 1995.

[14] S. Ulmer, C. Smorra, A. Mooser, K. Franke, H. Nagahama, G. Schneider, T. Higuchi, S. Van Gorp, K. Blaum, Y. Matsuda, W. Quint, J. Walz, and Y. Yamazaki. High-precision comparison of the antiproton-to-proton charge-to-mass ratio. *Nature*, **524**(7564) 196–199, 2015.

[15] D. Rodríguez, V.S. Kolhinen, G. Audi, J. Äystö, D. Beck, K. Blaum, G. Bollen, F. Herfurth, A. Jokinen, A. Kellerbauer, H.-J. Kluge, M. Oinonen, H. Schatz, E. Sauvan, and S. Schwarz. Mass Measurement on the *rp*-Process Waiting Point ^{72}Kr. *Phys. Rev. Lett.*, **93** 161104, 2004.

[16] A.A. Valverde, M. Brodeur, G. Bollen, M. Eibach, K. Gulyuz, A. Hamaker, C. Izzo, W.-J. Ong, D. Puentes, M. Redshaw, R. Ringle, R. Sandler, S. Schwarz, C.S. Sumithrarachchi, J. Surbrook, A.C.C. Villari, and I.T. Yandow. High-Precision Mass

Measurement of ^{56}Cu and the Redirection of the *rp*-Process Flow. *Phys. Rev. Lett.*, **120** 032701, 2018.

[17] J.C. Hardy and I.S. Towner. Superallowed $0^+ \to 0^+$ nuclear β decays: 2020 critical survey, with implications for V_{ud} and CKM unitarity. *Phys. Rev. C*, **102** 045501, 2020.

[18] K. Blaum, S. Eliseev, F.A. Danevich, V. I. Tretyak, S. Kovalenko, M.I. Krivoruchenko, Yu.N. Novikov, and J. Suhonen. Neutrinoless double-electron capture. *Rev. Mod. Phys.*, **92** 045007, 2020.

[19] J.A. Formaggio, A.L.C. de Gouvêa, and R.G.H. Robertson. Direct measurements of neutrino mass. *Phys. Rep.*, **914** 1–54, 2021.

[20] M. Acker et al. The Design, Construction, and Commissioning of the KATRIN Experiment. *arXiv*, 2021. 2103.04755 [physics.ins-det].

[21] M. Acker et al. Improved Upper Limit on the Neutrino Mass from a Direct Kinematic Method by KATRIN. *Phys. Rev. Lett.*, **123** 221802, 2019.

[22] L. Gastaldo et al. The electron capture in ^{163}Ho experiment – ECHo. *Eur. Phys. J. Spec. Top.*, **226**(8) 1623–1694, 2017.

[23] S. Hofmann, V. Ninov, F.P. Heßberger, P. Armbruster, H. Folger, G. Münzenberg, H.J. Schött, A.G. Popeko, A.V. Yeremin, S. Saro, R. Janik, and M. Leino. The new element 112. *Z. Phys. A*, **354**(3) 229–230, 1996.

[24] Yu.Ts. Oganessian, V.K. Utyonkov, Yu.V. Lobanov, F. Sh. Abdullin, A.N. Polyakov, R.N. Sagaidak, I.V. Shirokovsky, Yu.S. Tsyganov, A.A. Voinov, G.G. Gulbekian, S.L. Bogomolov, B.N. Gikal, A.N. Mezentsev, S. Iliev, V.G. Subbotin, A.M. Sukhov, K. Subotic, V.I. Zagrebaev, G.K. Vostokin, M.G. Itkis, K.J. Moody, J.B. Patin, D.A. Shaughnessy, M.A. Stoyer, N.J. Stoyer, P.A. Wilk, J.M. Kenneally, J.H. Landrum, J.F. Wild, and R.W. Lougheed. Synthesis of the isotopes of elements 118 and 116 in the ^{249}Cf and ^{245}Cm $+^{48}$ Ca fusion reactions. *Phys. Rev. C*, **74** 044602, 2006.

[25] K. Morita, K. Morimoto, D. Kaji, T. Akiyama, S. Goto, H. Haba, E. Ideguchi, R. Kanungo, K. Katori, H. Koura, H. Kudo, T. Ohnishi, A. Ozawa, T. Suda, K. Sueki, H.S. Xu, T. Yamaguchi, A. Yoneda, A. Yoshida, and Y.L. Zhao. Experiment on the Synthesis of Element 113 in the Reaction ^{209}Bi(^{70}Zn, n)^{278}113. *J. Phys. Soc. Japan*, **73**(10) 2593–2596, 2004.

[26] A. Ghiorso, J.M. Nitschke, J.R. Alonso, C.T. Alonso, M. Nurmia, G.T. Seaborg, E.K. Hulet, and R.W. Lougheed. Element 106. *Phys. Rev. Lett.*, **33** 1490–1493, 1974.

[27] H. Kragh. *From Transuranic to Superheavy Elements*. Springer International Publishing, Switzerland, 2018.

[28] E. Minaya Ramirez, D. Ackermann, K. Blaum, M. Block, C. Droese, Ch. E. Düllmann, M. Dworschak, M. Eibach, S. Eliseev, E. Haettner, F. Herfurth, F.P. Heßberger, S. Hofmann, J. Ketelaer, G. Marx, M. Mazzocco, D. Nesterenko, Yu.N. Novikov, W.R. Plaß, D. Rodríguez, C. Scheidenberger, L. Schweikhard, P.G. Thirolf, and C. Weber. Direct Mapping of Nuclear Shell Effects in the Heaviest Elements. *Science*, **337**(6099) 1207–1210, 2012.

[29] M. Block, D. Ackermann, K. Blaum, C. Droese, M. Dworschak, S. Eliseev, T. Fleckenstein, E. Haettner, F. Herfurth, F.P. Heßberger, S. Hofmann, J. Ketelaer, J. Ketter, H.-J. Kluge, G. Marx, M. Mazzocco, Yu.N. Novikov, W.R. Plaß, A. Popeko, S. Rahaman, D. Rodríguez, C. Scheidenberger, L. Schweikhard, P.G. Thirolf, G.K. Vorobyev, and C. Weber. Direct mass measurements above uranium bridge the gap to the island of stability. *Nature*, **463**(7282) 785–788, 2010.

[30] O.T. Kaleja. *High-precision mass spectrometry of nobelium, lawrencium and rutherfordium isotopes and studies of long-lived isomers with SHIPTRAP*. PhD thesis, Johannes Gutenberg-Universität Mainz, Mainz, 2020.

[31] S. Rau, F. Heiße, F. Köhler-Langes, S. Sasidharan, R. Haas, D. Renisch, C.E. Düllmann, W. Quint, S. Sturm, and K. Blaum. Penning trap mass measurements of the deuteron and the HD^+ molecular ion. *Nature*, **585**(7823) 43–47, 2020.

[32] M.P. Bradley, J.V. Porto, S. Rainville, J.K. Thompson, and D.E. Pritchard. Penning Trap Measurements of the Masses of ^{133}Cs, ^{87,85}Rb, and ^{23}Na with Uncertainties ≤ 0.2 ppb. *Phys. Rev. Lett.*, **83** 4510–4513, 1999.

[33] O. Kaleja, B. Anđelić, K. Blaum, M. Block, P. Chhetri, C. Droese, Ch.E. Düllmann, M. Eibach, S. Eliseev, J. Even, S. Götz, F. Giacoppo, N. Kalantar-Nayestanaki, M. Laatiaoui, E. Minaya Ramirez, A. Mistry, T. Murböck, S. Raeder, L. Schweikhard, and P.G. Thirolf. The performance of the cryogenic buffer-gas stopping cell of SHIPTRAP. *Nucl. Instrum. Methods Phys. Res., B*, **463** 280 – 285, 2020.

[34] Z. Andelkovic, G. Birkl, S. Fedotova, V. Hannen, F. Herfurth, K. König, N. Kotovskiy, B. Maaß, J. Vollbrecht, T. Murböck, D. Neidherr, W. Nörtershäuser, S. Schmidt, M. Vogel, G. Vorobjev, and C. Weinheimer. Status of deceleration and laser spectroscopy of highly charged ions at HITRAP. *Hyperfine Interactions*, **235**(1) 37–44, 2015.

[35] S. Lohse, J. Berrocal, M. Block, S. Chenmarev, J.M. Cornejo, J.G. Ramírez, and D. Rodríguez. A quartz amplifier for high-sensitivity Fourier-transform ion-cyclotron-resonance measurements with trapped ions. *Rev. Sci. Instrum.*, **90**(6) 063202, 2019.

[36] S. Lohse, J. Berrocal, S. Böhland, J. van de Laar, M. Block, S. Chenmarev, Ch.E. Düllmann, Sz. Nagy, J.G. Ramírez, and D. Rodríguez. Quartz resonators for Penning traps toward mass spectrometry on the heaviest ions. *Rev. Sci. Instrum.*, **91**(9) 093202, 2020.

[37] J. Berrocal, S. Lohse, F. Domínguez, M.J. Gutiérrez, F.J. Fernández, M. Block, J.J. García-Ripoll, and D. Rodríguez. Non-equilibrium Coupling of a Quartz Resonator to Ions for Penning-Trap Fast Resonant Detection (accepted). *Quantum Sci. Technol.*

[38] A. Hamaker, G. Bollen, M. Eibach, C. Izzo, D. Puentes, M. Redshaw, R. Ringle, R. Sandler, S. Schwarz, and I. Yandow. Sipt - an ultrasensitive mass spectrometer for rare isotopes. *Hyperfine Interact.*, **240**(1) 34, 2019.

[39] S. Schmidt, T. Murböck, Z. Andelkovic, G. Birkl, K. König, W. Nörtershäuser, R.C. Thompson, and M. Vogel. Sympathetic cooling in two-species ion crystals in a Penning trap. *J. Mod. Opt*, **65**(5-6) 538–548, 2018.

[40] P.O. Schmidt, T. Rosenband, C. Langer, W.M. Itano, J.C. Bergquist, and D.J. Wineland. Spectroscopy Using Quantum Logic. *Science*, **309**(5735) 749–752, 2005.

[41] M. Niemann, T. Meiners, J. Mielke, M.J. Borchert, J.M. Cornejo, S. Ulmer, and C. Ospelkaus. Cryogenic $^{9}Be^{+}$ Penning trap for precision measurements with (anti-)protons. *Meas. Sci. Technol.*, **31**(3) 035003, 2020.

[42] G. Morigi and H. Walther. Two-species Coulomb chains for quantum information. *Eur. Phys. J. D*, **13**(2) 261–269, 2001.

[43] D. Rodríguez. A quantum sensor for high-performance mass spectrometry. *Appl. Phys. B*, **107**(4) 1031–1042, 2012.

[44] J.M. Cornejo, M.J. Gutiérrez, E. Ruiz, A. Bautista-Salvador, C. Ospelkaus, S. Stahl, and D. Rodríguez. An optimized geometry for a micro Penning-trap mass spectrometer based on interconnected ions. *Int. J. Mass Spectrom.*, **410** 22–30, 2016.

[45] R.A. Rica, F. Domínguez, M.J. Gutiérrez, J. Bañuelos, J.J. del Pozo, and D. Rodríguez. A double paul trap system for the electronic coupling of ions. *Eur. Phys. J. Spec. Top.*, **227**(3) 445–456, 2018.

[46] R. Weinstock. On a fallacious proof of Earnshaw's theorem. *Am. J. Phys.*, **44**(4) 392–393, 1976.

[47] D. Leibfried, R. Blatt, C. Monroe, and D. Wineland. Quantum dynamics of single trapped ions. *Rev. Mod. Phys.*, **75** 281–324, 2003.

[48] J.D. Jackson. *Classical Electrodynamics*. Wiley, New York, 3rd edition, 1975.

[49] B.J. McMahon, C. Volin, W.G. Rellergert, and B.C. Sawyer. Doppler-cooled ions in a compact reconfigurable Penning trap. *Phys. Rev. A*, **101** 013408, 2020.

[50] M. Vogel. *Particle Confinement in Penning Traps*. Springer International Publishing, Switzerland, 2018.

[51] Agilent. *Manual for the 7.0T/160mm actively screened magnet system for ion trap application.*

[52] F. Tisseur and K. Meerbergen. The Quadratic Eigenvalue Problem. *SIAM Review*, **43**(2) 235–286, 2001.

[53] G. Savard, St. Becker, G. Bollen, H.-J. Kluge, R.B. Moore, Th. Otto, L. Schweikhard, H. Stolzenberg, and U. Wiess. A new cooling technique for heavy ions in a Penning trap. *Phys. Lett. A*, **158**(5) 247–252, 1991.

[54] H. Goldstein, C.P. Poole, and J.L. Safko. *Classical Mechanics (New International Edition)*. Pearson, London, 2014.

[55] M. Kretzschmar. The Ramsey method in high-precision mass spectrometry with Penning traps: Theoretical foundations. *Int. J. Mass Spectrom.*, **264**(2) 122–145, 2007.

[56] L. Schweikhard and A.G. Marshall. Excitation modes for Fourier transform-ion cyclotron resonance mass spectrometry. *J. Am. Soc. Mass Spectrom.*, **4**(6) 433–452, 1993.

[57] E.A. Cornell, R.M. Weisskoff, K.R. Boyce, and D.E. Pritchard. Mode coupling in a penning trap: π pulses and a classical avoided crossing. *Phys. Rev. A*, **41** 312–315, 1990.

[58] F.G. Major, V.N. Gheorghe, and G. Werth. *Charged Particle Traps*. Springer-Verlag, Berlin, 1st edition, 2005.

[59] J.M. Cornejo. *The preparation Penning trap and recent developments on high-performance ion detection for the project TRAPSENSOR*. PhD thesis, Universidad de Granada, Granada, 2016.

[60] M. Mukherjee, D. Beck, K. Blaum, G. Bollen, J. Dilling, S. George, F. Herfurth, A. Herlert, A. Kellerbauer, H.-J. Kluge, S. Schwarz, L. Schweikhard, and C. Yazidjian. ISOLTRAP: An on-line Penning trap for mass spectrometry on short-lived nuclides. *Eur. Phys. J. A*, **35**(1) 1–29, 2008.

[61] M. Block, D. Ackermann, K. Blaum, A. Chaudhuri, Z. Di, S. Eliseev, R. Ferrer, D. Habs, F. Herfurth, F.P. Heßberger, S. Hofmann, H.-J. Kluge, G. Maero, A. Martín, G. Marx, M. Mazzocco, M. Mukherjee, J.B. Neumayr, W.R. Plaß, W. Quint, S. Rahaman, C. Rauth, D. Rodríguez, C. Scheidenberger, L. Schweikhard, P.G. Thirolf, G. Vorobjev, and C. Weber. Towards direct mass measurements of nobelium at SHIPTRAP. *Eur. Phys. J. D*, **45**(1) 39–45, 2007.

[62] W.M. Itano and D.J. Wineland. Laser cooling of ions stored in harmonic and Penning traps. *Phys. Rev. A*, **25** 35–54, 1982.

[63] F. Diedrich, J.C. Bergquist, W.M. Itano, and D.J. Wineland. Laser Cooling to the Zero-Point Energy of Motion. *Phys. Rev. Lett.*, **62** 403–406, 1989.

[64] G. Morigi, J. Eschner, and C.H. Keitel. Ground State Laser Cooling Using Electromagnetically Induced Transparency. *Phys. Rev. Lett.*, **85** 4458–4461, 2000.

[65] C.F Roos, D. Leibfried, A. Mundt, F. Schmidt-Kaler, J. Eschner, and R. Blatt. Experimental Demonstration of Ground State Laser Cooling with Electromagnetically Induced Transparency. *Phys. Rev. Lett.*, **85** 5547–5550, 2000.

[66] C. Monroe, D.M Meekhof, B.E King, S.R Jefferts, W.M Itano, D.J Wineland, and P. Gould. Resolved-Sideband Raman Cooling of a Bound Atom to the 3D Zero-Point Energy. *Phys. Rev. Lett.*, **75** 4011–4014, 1995.

[67] J. Berrocal. Implementación de una trampa lineal para simulaciones del modelo cuántico de rabi. Master's thesis, Universidad de Granada, Granada, 2018.

[68] K. Koo, J. Sudbery, D.M. Segal, and R.C. Thompson. Doppler cooling of Ca^+ ions in a Penning trap. *Phys. Rev. A*, **69** 043402, 2004.

[69] J. Berrocal. In preparation. PhD thesis, Universidad de Granada, Granada, Exp. 2022.

[70] H.F. Powell, D.M. Segal, and R.C. Thompson. Axialization of Laser Cooled Magnesium Ions in a Penning Trap. *Phys. Rev. Lett.*, **89** 093003, 2002.

[71] J.J. Sakurai and J. Napolitano. *Modern Quantum Mechanics*. Cambridge University Press, 2nd edition, 2017.

[72] A.L. Wolf, S.A. van den Berg, C. Gohle, E.J. Salumbides, W. Ubachs, and K.S.E. Eikema. Frequency metrology on the $4s\,^2S_{1/2} - 4p\,^2P_{1/2}$ transition in $^{40}Ca^+$ for a comparison with quasar data. *Phys. Rev. A*, **78** 032511, 2008.

[73] M. Hettrich, T. Ruster, H. Kaufmann, C.F. Roos, C.T. Schmiegelow, F. Schmidt-Kaler, and U.G. Poschinger. Measurement of Dipole Matrix Elements with a Single Trapped Ion. *Phys. Rev. Lett.*, **115** 143003, 2015.

[74] Florian Gebert, Yong Wan, Fabian Wolf, Christopher N. Angstmann, Julian C. Berengut, and Piet O. Schmidt. Precision Isotope Shift Measurements in Calcium Ions Using Quantum Logic Detection Schemes. *Phys. Rev. Lett.*, **115** 053003, 2015.

[75] K. König, Ch. Geppert, J. Krämer, B. Maaß, E.W. Otten, T. Ratajczyk, and W. Nörtershäuser. First high-voltage measurements using Ca^+ ions at the ALIVE experiment. *Hyperfine Interact.*, **238**(1) 24, 2017.

[76] R. Gerritsma, G. Kirchmair, F. Zähringer, J. Benhelm, R. Blatt, and C.F. Roos. Precision measurement of the branching fractions of the 4p $^2P_{3/2}$ decay of Ca II. *Eur. Phys. J. D*, **50**(1) 13–19, 2008.

[77] A.L. Wolf, S.A. van den Berg, W. Ubachs, and K.S.E. Eikema. Direct Frequency Comb Spectroscopy of Trapped Ions. *Phys. Rev. Lett.*, **102** 223901, 2009.

[78] Hua Guan, Yao Huang, Pei-Liang Liu, Wu Bian, Hu Shao, and Ke-Lin Gao. Precision spectroscopy with a single $^{40}Ca^+$ ion in a Paul trap. *Chin. Phys. B*, **24**(5) 054213, 2015.

[79] Günter Werth. The g-factor of the bound electron as a test of quantum electrodynamics. *Phys. Scr.*, **89**(9) 098004, 2014.

[80] W. Quint and M. Vogel, editors. *Fundamentals of the Physics of Solids, Volume II: Electronic Properties*. Springer-Verlag, Heidelberg, 1st edition, 2009.

[81] M.J. Gutiérrez. Estudio de la fluorescencia de un ion de $^{40}Ca^+$ en una trampa magnética de 7 T. Master's thesis, Universidad de Granada, Granada, 2016.

[82] S. Mavadia. *Motional Sideband Spectra and Coulomb Crystals in a Penning Trap*. PhD thesis, Imperial College of Science, Technology and Medicine, London, 2013.

[83] D.R. Crick, S. Donnellan, D.M. Segal, and R.C. Thompson. Magnetically induced electron shelving in a trapped ca^+ ion. *Phys. Rev. A*, **81** 052503, 2010.

[84] S. Eliseev, K. Blaum, M. Block, A. Dörr, C. Droese, T. Eronen, M. Goncharov, M. Höcker, J. Ketter, E. Minaya Ramirez, D.A. Nesterenko, Yu.N. Novikov, and

L. Schweikhard. A phase-imaging technique for cyclotron-frequency measurements. *Appl. Phys. B*, **114**(1) 107–128, 2014.

[85] J. Sólyom. *Fundamental Physics in Particle Traps*. Springer-Verlag, Heidelberg, 1st edition, 2014.

[86] A. Kellerbauer, K. Blaum, G. Bollen, F. Herfurth, H.-J. Kluge, M. Kuckein, E. Sauvan, C. Scheidenberger, and L. Schweikhard. From direct to absolute mass measurements: A study of the accuracy of ISOLTRAP. *Eur. Phys. J. D*, **22**(1) 53–64, 2003.

[87] A. Kellerbauer. Recent improvements of ISOLTRAP: absolute mass measurements of exotic nuclides at 10^{-8} precision. *Int. J. Mass Spectrom.*, **229**(1) 107–115, 2003.

[88] S. George, K. Blaum, F. Herfurth, A. Herlert, M. Kretzschmar, S. Nagy, S. Schwarz, L. Schweikhard, and C. Yazidjian. The Ramsey method in high-precision mass spectrometry with Penning traps: Experimental results. *Int. J. Mass Spectrom.*, **264**(2) 110–121, 2007.

[89] S. Eliseev, C. Roux, K. Blaum, M. Block, C. Droese, F. Herfurth, M. Kretzschmar, M.I. Krivoruchenko, E. Minaya Ramirez, Yu.N. Novikov, L. Schweikhard, V.M. Shabaev, F. Šimkovic, I.I. Tupitsyn, K. Zuber, and N.A. Zubova. Octupolar-Excitation Penning-Trap Mass Spectrometry for Q-Value Measurement of Double-Electron Capture in ^{164}Er. *Phys. Rev. Lett.*, **107** 152501, 2011.

[90] G. Eitel, M. Block, A. Czasch, M. Dworschak, S. George, O. Jagutzki, J. Ketelaer, J. Ketter, Sz. Nagy, D. Rodríguez, C. Smorra, and K. Blaum. Position-sensitive ion detection in precision Penning trap mass spectrometry. *Nucl. Instrum. Methods Phys. Res., A*, **606**(3) 475–483, 2009.

[91] L. Schweikhard. Theory of quadrupole detection fourier transform-ion cyclotron resonance. *Int. J. Mass Spectrom.*, **107**(2) 281–292, 1991.

[92] W. Shockley. Currents to Conductors Induced by a Moving Point Charge. *J. Appl. Phys.*, **9**(10) 635–636, 1938.

[93] A. Weigel. *Detection Electronics Design and First Observation of Bound-Electron Spin Transitions at the ALPHATRAP g-Factor Experiment*. PhD thesis, Ruprecht-Karls-Universität Heidelberg, Heidelberg, 2019.

[94] H. Nyquist. Thermal Agitation of Electric Charge in Conductors. *Phys. Rev.*, **32** 110–113, 1928.

[95] D.J. Wineland and H.G. Dehmelt. Principles of the stored ion calorimeter. *J. Appl. Phys.*, **46**(2) 919–930, 1975.

[96] E.G. Myers. The most precise atomic mass measurements in Penning traps. *Int. J. Mass Spectrom.*, **349-350** 107–122, 2013. 100 years of Mass Spectrometry.

[97] M.J. Gutiérrez, J. Berrocal, F. Domínguez, I. Arrazola, M. Block, E. Solano, and D. Rodríguez. Dynamics of an unbalanced two-ion crystal in a Penning trap for application in optical mass spectrometry. *Phys. Rev. A*, **100** 063415, 2019.

[98] R.C. Thompson and D.C. Wilson. The motion of small numbers of ions in a Penning trap. *Z. Phys.*, **42**(4) 271–277, 1997.

[99] E.A. Cornell, K.R. Boyce, D.L.K. Fygenson, and D.E. Pritchard. Two ions in a Penning trap: Implications for precision mass spectroscopy. *Phys. Rev. A*, **45** 3049–3059, 1992.

[100] S. Jain, J. Alonso, M. Grau, and J.P. Home. Scalable Arrays of Micro-Penning Traps for Quantum Computing and Simulation. *Phys. Rev. X*, **10** 031027, 2020.

[101] M. Drewsen, A. Mortensen, R. Martinussen, P. Staanum, and J.L. Sørensen. Non-destructive Identification of Cold and Extremely Localized Single Molecular Ions. *Phys. Rev. Lett.*, **93** 243201, 2004.

[102] F. Domínguez, M.J. Gutiérrez, I. Arrazola, J. Berrocal, J.M. Cornejo, J.J. Del Pozo, R.A. Rica, S. Schmidt, E. Solano, and D. Rodríguez. Motional studies of one and two laser-cooled trapped ions for electric-field sensing applications. *J. Mod. Opt*, **65**(5-6) 613–621, 2018.

[103] J.W. Eaton, D. Bateman, S. Hauberg, and R. Wehbring. *GNU Octave version 5.2.0 manual: a high-level interactive language for numerical computations*, 2020.

[104] S. Jain. Micro-Fabricated Penning Trap Arrays for Quantum Simulation. Master's thesis, Eidgenössische Technische Hochschule Zürich, Zürich, 2018.

[105] F. Domínguez, I. Arrazola, J. Doménech, J.S. Pedernales, L. Lamata, E. Solano, and D. Rodríguez. A Single-Ion Reservoir as a High-Sensitive Sensor of Electric Signals. *Sci. Rep.*, **7**(1) 8336, 2017.

[106] J P Home, D Hanneke, J D Jost, D Leibfried, and D J Wineland. Normal modes of trapped ions in the presence of anharmonic trap potentials. *New J. Phys.*, **13**(7) 073026, 2011.

[107] F. Wolf, C. Shi, J.C. Heip, M. Gessner, L. Pezzè, A. Smerzi, M. Schulte, K. Hammerer, and P.O. Schmidt. Motional Fock states for quantum-enhanced amplitude and phase measurements with trapped ions. *Nat. Commun.*, **10**(1) 2929, 2019.

[108] P. Hrmo, M.K. Joshi, V. Jarlaud, O. Corfield, and R.C. Thompson. Sideband cooling of the radial modes of motion of a single ion in a Penning trap. *Phys. Rev. A*, **100** 043414, 2019.

[109] Y. Wan, F. Gebert, F. Wolf, and P.O. Schmidt. Efficient sympathetic motional-ground-state cooling of a molecular ion. *Phys. Rev. A*, **91** 043425, 2015.

[110] J.S. Chen, S.M. Brewer, C.W. Chou, D.J. Wineland, D.R. Leibrandt, and D.B. Hume. Sympathetic Ground State Cooling and Time-Dilation Shifts in an $^{27}Al^{+}$ Optical Clock. *Phys. Rev. Lett.*, **118** 053002, 2017.

[111] J. Cerrillo and D. Rodríguez. In preparation. *EPL*, 2021.

[112] D. Beck and H. Brand. CS - A Control System Framework for Experiments at GSI. In U. Grundinger, editor, *GSI Scientific Report 2002 [GSI Report 2003-1]*, volume 2003-1, page 210. GSI, Darmstadt, 2003.

[113] D. Beck, K. Blaum, H. Brand, F. Herfurth, and S. Schwarz. A new control system for ISOLTRAP. *Nucl. Instrum. Methods Phys. Res., A*, **527**(3) 567–579, 2004.

[114] D. Beck and H. Brand. CS Wiki.

[115] T. Sun. *High precision mass measurement of ^{37}Ca and developments for LEBIT*. PhD thesis, Michigan State University, East Lansing, 2006.

[116] D. Neidherr. *Nuclear structure studies in the xenon and radon region and the discovery of a new radon isotope by Penning-trap mass spectrometry*. PhD thesis, Johannes Gutenberg-Universität Mainz, Mainz, 2010.

[117] LEBIT software repository.

[118] P. Escobedo. Desarrollo de un sistema de control para láseres de diodo utilizando moduladores acústico-ópticos. Master's thesis, Universidad de Granada, Granada, 2014.

[119] M.J. Gutiérrez, J. Berrocal, J.M. Cornejo, F. Domínguez, J.J. Del Pozo, I. Arrazola, J. Bañuelos, P. Escobedo, O. Kaleja, L. Lamata, Rica. R.A., S. Schmidt, M. Block, E. Solano, and D. Rodríguez. The TRAPSENSOR facility: an open-ring 7 tesla Penning trap for laser-based precision experiments. *New J. Phys.*, **21**(2) 023023, 2019.

[120] S. Bourdeauducq, whitequark, R. Jördens, Y. Sionneau, enjoy digital, cjbe, D. Nadlinger, hartytp, JBoulder, D. Slichter, Drew, mntng, r srinivas, apatura iris, S. Mackenzie, Z. Smith, K. Paweł, M. Weber, kemstevens, F. Held, and D. Leibrandt. m-labs/artiq: A leading-edge control system for quantum information experiments, 2018.

[121] F. Domínguez et al. In preparation. 2020.

[122] Sinara's GitHub wiki.

[123] M-Labs. ARTIQ manual.

[124] CAEN SpA. CAEN HV Wrapper Library.

[125] The Python Software Foundation. *Python 3.9.1 documentation*, 2021.

[126] H. Ohadi. pyandor (AndorSDK wrapper).

[127] C. Balance. andorEmccd (AndorSDK wrapper).

[128] B. Anđelić, M. Block, P. Chhetri, J. Even, F. Giacoppo, N. Kalantar-Nayestanaki, O. Kaleja, T. Murböck, F. Schneider, and S. Raeder. Simulation studies of the laser ablation ion source at the SHIPTRAP setup. *Hyperfine Interact.*, **241**(1) 46, 2020.

[129] J.M. Cornejo, A. Lorenzo, D. Renisch, M. Block, Ch.E. Düllmann, and D. Rodríguez. Status of the project TRAPSENSOR: Performance of the laser-desorption ion source. *Nucl. Instrum. Methods Phys. Res., B*, **317** 522–527, 2013.

[130] A. Lorenzo. Adaptacion de una fuente de iones por desorción láser para su acoplamiento a un sistema de trampas magnéticas (*Penning traps*). Master's thesis, Universidad de Sevilla, Sevilla, 2012.

[131] C. Vivo. Estudio de una fuente de iones de superficie en el marco del proyecto TRAPSENSOR y primeros resultados de enfriamiento por láser (laser cooling) de iones de 40Ca+. Master's thesis, Universidad de Granada, Granada, 2014.

[132] J.M. Cornejo, M. Colombano, J. Doménech, M. Block, P. Delahaye, and D. Rodríguez. Extending the applicability of an open-ring trap to perform experiments with a single laser-cooled ion. *Rev. Sci. Instrum.*, **86**(10) 103104, 2015.

[133] J. Berrocal et al. In preparation. 2021.

[134] T. Eronen, V. S. Kolhinen, V.-V. Elomaa, D. Gorelov, U. Hager, J. Hakala, A. Jokinen, A. Kankainen, P. Karvonen, S. Kopecky, I. D. Moore, H. Penttilä, S. Rahaman, S. Rinta-Antila, J. Rissanen, A. Saastamoinen, J. Szerypo, C. Weber, and J. Äystö.

JYFLTRAP: a Penning trap for precision mass spectroscopy and isobaric purification. *Eur. Phys. J. A*, **48**(4) 46, 2012.

[135] V.S. Kolhinen, M. Bussmann, D. Habs, J.B. Neumayr, U. Schramm, C. Schürmann, M. Sewtz, J. Szerypo, and P.G. Thirolf. MLLTRAP: A Penning trap facility for high-accuracy mass measurements. *Nucl. Instrum. Methods Phys. Res., B*, **266**(19) 4547–4550, 2008.

[136] J. Ketelaer, J. Krämer, D. Beck, K. Blaum, M. Block, K. Eberhardt, G. Eitel, R. Ferrer, C. Geppert, S. George, F. Herfurth, J. Ketter, Sz. Nagy, D. Neidherr, R. Neugart, W. Nörtershäuser, J. Repp, C. Smorra, N. Trautmann, and C. Weber. TRIGA-SPEC: A setup for mass spectrometry and laser spectroscopy at the research reactor TRIGA Mainz. *Nucl. Instrum. Methods Phys. Res., A*, **594**(2) 162–177, 2008.

[137] J.M. Cornejo and D. Rodríguez. A preparation Penning trap for the TRAPSENSOR project with prospects for MATS at FAIR. *Nucl. Instrum. Methods Phys. Res., B*, **376** 288–291, 2016.

[138] D. Rodríguez et al. MATS and LaSpec: High-precision experiments using ion traps and lasers at FAIR. *Eur. Phys. J. Spec. Top.*, **183**(1) 1–123, 2010.

[139] S.L. Rolston and G. Gabrielse. Cooling antiprotons in an ion trap. *Hyperfine Interact.*, **44**(1) 233–245, 1989.

[140] J.M. Cornejo, P. Escobedo, and D. Rodríguez. Status of the project TRAPSENSOR. *Hyperfine Interact.*, **227**(1) 223–237, 2014.

[141] M. Colombano. Implementación y puesta a punto de un modulador electro-óptico y mejora de las prestaciones del sistema de deteción en el proyecto TRAPSENSOR. Master's thesis, Universidad de Granada, Granada, 2015.

[142] G. Gabrielse and F.C. Mackintosh. Cylindrical Penning traps with orthogonalized anharmonicity compensation. *Int. J. Mass Spectrom.*, **57**(1) 1–17, 1984.

[143] G. Gabrielse, L. Haarsma, and S.L. Rolston. Open-endcap Penning traps for high precision experiments. *Int. J. Mass Spectrom.*, **88**(2) 319–332, 1989.

[144] S. Bharadia. *Towards Laser Spectroscopy of Highly Charged Ions*. PhD thesis, Imperial College of Science, Technology and Medicine, London, 2011.

[145] M. Niemann. *Design and commissioning of an experiment for sympathetic cooling and coupling of ions in a cryogenic Penning trap*. PhD thesis, Leibniz Universität Hannover, Hannover, 2019.

[146] D. Rodríguez, A. Méry, G. Ban, J. Brégeault, G. Darius, D. Durand, X. Fléchard, M. Herbane, M. Labalme, E. Liénard, F. Mauger, Y. Merrer, O. Naviliat-Cuncic, J.C. Thomas, and C. Vandamme. The LPCTrap facility: A novel transparent Paul trap for high-precision experiments. *Nucl. Instrum. Methods Phys. Res., A*, **565**(2) 876–889, 2006.

[147] J.A. Porti. private communication.

[148] J. Doménech. Producción de iones de $^{40}Ca^{+}$ por el método de fotoionización y estudio de su utilización en el proyecto TRAPSENSOR. Master's thesis, Universidad de Granada, Granada, 2015.

[149] M. Block. private communication.

[150] C. García-Recio. private communication.

[151] W.H. King. *Isotope Shifts in Atomic Spectra*. Springer US, 1st edition, 1984.

[152] S. Guan and A.G. Marshall. Stored waveform inverse Fourier transform (SWIFT) ion excitation in trapped-ion mass spectometry: Theory and applications. *Int. J. Mass Spectrom.*, **157-158** 5–37, 1996.

[153] S. Donnellan. *Towards Sideband Cooling of a Single* $^{40}Ca^{+}$ *Ion in a Penning Trap*. PhD thesis, Imperial College London, London, 2011.

[154] S. Lohse. In preparation. PhD thesis, Johannes Gutenberg-Universität Mainz, Mainz, Exp. 2020.

[155] S. Mavadia, G. Stutter, J.F. Goodwin, D.R. Crick, R.C. Thompson, and D.M. Segal. Optical sideband spectroscopy of a single ion in a Penning trap. *Phys. Rev. A*, **89** 032502, 2014.

[156] J. Roßnagel, K.N. Tolazzi, F. Schmidt-Kaler, and K. Singer. Fast thermometry for trapped ions using dark resonances. *New J. Phys.*, **17**(4) 045004, 2015.

[157] F. Domínguez. In preparation. PhD thesis, Universidad de Granada, Granada, Exp. 2022.